



THE UNIVERSITY OF QUEENSLAND  
A U S T R A L I A

# Ground Testing at Superorbital Flight Conditions in a Large Scale Expansion Tube

Andreas Andrianatos

Bachelor of Engineering (Hons Class I)

*A thesis submitted for the degree of Doctor of Philosophy  
at The University of Queensland in 2019*

School of Mechanical and Mining Engineering  
Centre for Hypersonics

# **Abstract**

Testing superorbital reentry flow conditions typically uses a small scale model that requires binary ( $\rho L$ ) scaling to conserve similarity of flow features and non-equilibrium dissociation reactions between the scaled and full scale condition. However, binary scaling is only applicable for non-equilibrium binary reactions (dissociation and ionisation), not three-body reactions or the conditions near equilibrium. Additionally, binary scaling does not correctly scale the coupling of radiative cooling and mass flow into the shock layer. Therefore, if significant levels of coupling between radiation and flow properties exists, binary scaling may not conserve similarity of macroscopic flow properties between the scaled and full scale condition. The goal of this thesis is to examine the effects of scaling by developing a full scale ground experiment of the Hayabusa capsule at its peak radiation trajectory point and comparing it to data obtained from experiments performed in a smaller facility with a 1:5 scale model and binary scaled condition.

X3, a large free-piston driven expansion tube, is capable of producing test flows with a core flow diameter on the order of hundreds of millimetres with test times on the order of a millisecond. Large scale models can be experimented within X3, and in the case of Hayabusa, there is the potential to perform high-enthalpy radiation experiments with a full scale model, which avoids the need for binary scaling.

The current configuration of X3 had never been used for high-enthalpy radiation experiments; only two-dimensional Mach 10 scramjet experiments had been performed, using a model designed to reduce three dimensional effects of the flow. A lightweight piston had previously been designed but never fully tested. Reducing the mass of the piston increases the performance of the driver and enables the realisation of test conditions that require a higher performance facility to achieve.

This thesis is composed of two main parts; the design of new driver operating conditions and evaluation of the suitability of the conditions for producing high-enthalpy radiating flows, and experiments performed with a 1:5 scale and full scale Hayabusa model using a test condition representative of the unscaled peak radiative heating trajectory point.

Operating conditions for the lightweight piston were designed using L1d, a one-dimensional Lagrangian flow solver, to ensure the piston had a soft landing at the end of its trajectory. Calibrating the L1d model with blank-off experiments demonstrated the capability to predict piston motion and driver pressure accurately. A range of operating conditions were designed for 2mm and 3mm thick diaphragms.

The new driver operating conditions have been quantified by measuring shock speed and wall pressure targeting the 1:5 scaled flow condition used in X2. Results from the study found that although X2 and X3 have similar drivers, X3 was unable to match the performance of the condition used in X2. This was attributed to the relatively large mass of the diaphragms in X3 compared to X2, and additional losses

arising at the diaphragm. The most powerful driver comprised a 3mm thick steel primary diaphragm, 100% helium driver gas and an orifice plate to control the flow of driver gas.

A final condition, representative of Hayabusa's peak radiative heating trajectory point for unscaled flight, was designed using 4mm diaphragms scored to reduce shrapnel. The test flow had an equivalent flight velocity, density and enthalpy of  $10.76 \pm 0.12 \text{ km s}^{-1}$ ,  $0.33 \times 10^{-3} \pm 0.11 \times 10^{-3} \text{ kg m}^{-3}$  and  $57.5 \pm 1.9 \text{ MJ kg}^{-1}$  respectively, and a test time of  $600\mu\text{s}$ . The test time was limited by the nozzle start up process and initially off design operation for the Mach 12 nozzle.

1:5 scale and full scale Hayabusa models were used for the final experiments. High speed video of the shock layer and time-resolved spectroscopy of the stagnation streamline were obtained for both model sizes. Both methods agreed well in terms of shock stand-off. The normalised shock stand-off in front of the full scale model was found to be smaller than CFD values in literature, and scaled experiments performed in X2, possibly due to the condition having lower density than the trajectory point or the condition in X2 having a higher total pressure, which increases the importance of three-body recombinations, reducing density in the shock layer. Spectroscopic measurements were limited by the efficiency of available optics and intensifier sensitivity, with measurements only taken in two visible regions. The spectra show contaminants from the tertiary diaphragm are present and contaminants from the tube wall or primary diaphragm increase at the end of the test time.

To summarise, this thesis details the development of X3 as a facility for high-enthalpy radiating flows. The work completed on X3's driver opens the possibility to use a range of initial conditions to perform experiments at large scale with different flows. The long test times open up possibilities to conduct experiments that depend on examining phenomena at larger time constants or model surface. Time-resolved spectroscopic measurements were taken of the flow over two different sized models and while the optical arrangement still needs refining, the measurements are a first on facilities of this type and scale.

## **Declaration by author**

This thesis is composed of my original work, and contains no material previously published or written by another person except where due reference has been made in the text. I have clearly stated the contribution by others to jointly-authored works that I have included in my thesis.

I have clearly stated the contribution of others to my thesis as a whole, including statistical assistance, survey design, data analysis, significant technical procedures, professional editorial advice, financial support and any other original research work used or reported in my thesis. The content of my thesis is the result of work I have carried out since the commencement of my higher degree by research candidature and does not include a substantial part of work that has been submitted to qualify for the award of any other degree or diploma in any university or other tertiary institution. I have clearly stated which parts of my thesis, if any, have been submitted to qualify for another award.

I acknowledge that an electronic copy of my thesis must be lodged with the University Library and, subject to the policy and procedures of The University of Queensland, the thesis be made available for research and study in accordance with the Copyright Act 1968 unless a period of embargo has been approved by the Dean of the Graduate School.

I acknowledge that copyright of all material contained in my thesis resides with the copyright holder(s) of that material. Where appropriate I have obtained copyright permission from the copyright holder to reproduce material in this thesis and have sought permission from co-authors for any jointly authored works included in the thesis.

## **Publications included in this thesis**

No Publications Included

## **Submitted manuscripts included in this thesis**

No manuscripts submitted for publication

## **Other publications during candidature**

A. Andrianatos, D. Gildfind, and R. Morgan. “A study of radiation scaling of high enthalpy flows in expansion tubes”. In: *7th Asia-Pacific International Symposium on Aerospace Technology Conference*. 2015. DOI: 10.1007/978-3-319-91017-8\_37

A. Andrianatos, D. Gildfind, and R. Morgan. “Preliminary Development of High Enthalpy Conditions for the X3 Expansion Tube”. In: *20th Australasian Fluid Mechanics Conference, 20AFMC*. 2016

A. Andrianatos, D. Gildfind, and R. G. Morgan. “Driver Condition Development for High Enthalpy Operation of the X3 Expansion Tube”. In: *31st International Symposium on Shock Waves*. 2017. DOI: 10.1007/978-3-319-91017-8\_37

T. Hermann, S. Löhle, S. Fasoulas, and A. Andrianatos. “Tomographic optical emission spectroscopy of a high enthalpy air plasma flow”. In: *Applied optics* 55.36 (2016), pp. 10290–10298. DOI: 10.1364/AO.55.010290

T. Hermann, S. Löhle, R. Öfele, S. Fasoulas, and A. Andrianatos. “Tomographic optical emission spectroscopy for plasma wind tunnel testing”. In: *32nd AIAA Aerodynamic Measurement Technology and Ground Testing Conference*. 2016, p. 3203

P. Toniato, D. E. Gildfind, A. Andrianatos, and R. G. Morgan. “Full Free-stream Mach 12 Scramjet testing in expansion tubes”. In: *2018 Applied Aerodynamics Conference*. 2018, p. 3818. DOI: 10.2514/6.2018-3818

D. E. Gildfind, P. A. Jacobs, R. J. Gollan, P. Toniato, T. J. McIntyre, A. Andrianatos, C. M. James, and R. G. Morgan. “Flow characterization and modeling of the X2 and X3 expansion tubes”. In: *VKI Lecture Series* (2018)

## **Contributions by others to the thesis**

No contribution by others

## **Statement of parts of the thesis submitted to qualify for the award of another degree**

No works submitted towards another degree have been included in this thesis

## **Research involving humans or animal subjects**

No animal or human subjects were involved in this research

## **Acknowledgements**

Firstly, I would like to thank my supervisors, Dr David Gildfind and Prof. Richard Morgan, for all their support throughout the years, without whom I would never have been able to get through my thesis mostly unscathed. David, you always had a way to relate what I was doing back to the narrative I was trying to achieve, even when it wasn't clear and your attention to detail definitely helped me keep focus along the way. Richard, you could come up with a new direction for my work without fail when the previous one hit a dead end for one reason or another and were always able to provide insights to experiments in X3 that others could never hope to provide. I don't think I'll ever be able to condense a month of work into a five minute calculation in my head...

To the xLab technicians, Frans and Neil, while most of it was repairing the various parts of X3, without your support I would never have been able to complete my experiments. Thanks to all the other people whose support has not gone unnoticed: Barry, Keith and Sam, Jason and the workshop staff, Peter and the instrumentation staff, and Marilyn for solving all my financial woes. Peter and Rowan, thanks for all your help with CFD related stuff, although a lot of it never got off the ground.

Pierpaolo, we have both been to hell and back working with X3 but I wouldn't have done it with anyone else. Despite our best efforts, X3 is still standing. Juan and Augusto, you complete out circle quartet and have considerably eased my burden in listening to Pierpaolo's complaints. Although one of you was perpetually late to every single lunch, I'd happily wait again. The four of you have made the last four and a half years enjoyable and I'm sure we will continue our friendship in the future.

A special thanks to David, Fabs and Rishabh for letting me use your intensifier and answering any questions I had about it (and then still letting me use it). To Jens and Ryan, I know it was annoying sharing the Phantom, but without your cooperation I wouldn't have been able to complete my work. I'd also like to express my gratitude to the X3 operators who have given their blood, sweat and tears in helping me do my experiments: Pierpaolo, Juan, Sam, Daniel, Nils and Chris. To all the other xLabbers and T4 people, past and present, I have befriended over the years, it has been a pleasure.

To all my other friends and family, I thank you for your love and support, with a special mention to those who have followed up "What do you do for a living?" with "Oh, so you can work for NASA then?"

And finally, Erica, your infinite reservoir of love, support and patience, lots and lots of patience, have been instrumental in getting me through this thesis, especially during the last year. Of all the things I've accomplished and experienced throughout my thesis, meeting you easily surpasses them all.

## **Financial Support**

This research was supported by an Australian Government Research Training Program (RTP) Scholarship. This research was undertaken with support and funding of the Australian Research Council.

## **Keywords**

Expansion tube, radiation, scaling, condition development, spectroscopy, large scale, free-piston driver, shock stand-off, Hayabusa, superorbital

## **Australian and New Zealand Standard Research Classification (ANZSRC)**

ANZSRC code: 090107, Hypersonic Propulsion and Hypersonic Aerodynamics, 100%

## **Fields of Research (FoR) Classification**

FoR code: 0901, Aerospace Engineering, 100%

---

# Contents

<b>1. Introduction</b>	<b>1</b>
1.1. Research Context . . . . .	1
1.2. Research Aims . . . . .	4
1.2.1. Facility Development . . . . .	4
1.2.2. Radiation Experiments . . . . .	4
1.3. Thesis Outline . . . . .	6
<b>2. Literature Review</b>	<b>8</b>
2.1. Radiating Flows . . . . .	8
2.1.1. Early Experiments . . . . .	9
2.1.2. Facility and Measurement Developments . . . . .	10
2.1.3. Theoretical Models . . . . .	13
2.1.4. Flight Data . . . . .	16
2.1.5. Hayabusa . . . . .	17
2.2. Expansion Tubes . . . . .	20
2.2.1. Development . . . . .	20
2.2.2. Use of a Secondary Driver . . . . .	22
2.2.3. X2 . . . . .	23
2.2.4. X3 . . . . .	25
<b>3. X3's Driver</b>	<b>28</b>
3.1. Chapter Overview . . . . .	28
3.2. Expansion Tube Layout . . . . .	28
3.3. X3 Driver Introduction . . . . .	29
3.4. Previous 200kg Piston . . . . .	30
3.5. Analytical Methods . . . . .	33
3.5.1. Stalker's Method . . . . .	33
3.5.2. Hornung's Method . . . . .	36
3.6. Lightweight Piston - Analytical Results . . . . .	39
3.6.1. Analytical Analysis . . . . .	39

## Contents

3.7.	Numerical Model . . . . .	45
3.7.1.	X3 Geometry . . . . .	46
3.7.2.	Piston . . . . .	48
3.7.3.	Final Model Parameters . . . . .	52
3.8.	Blank-off Shots and Model Validation . . . . .	53
3.8.1.	Reservoir Extension . . . . .	53
3.8.2.	L1d Validation . . . . .	55
3.9.	Chapter Conclusion . . . . .	57
<b>4.</b>	<b>Driver Performance</b>	<b>58</b>
4.1.	Chapter Overview . . . . .	58
4.2.	Expansion Tube Layout . . . . .	59
4.3.	The Diaphragm in L1d . . . . .	60
4.3.1.	Diaphragm Object Adjustments . . . . .	60
4.3.2.	A Tuned Piston Condition . . . . .	62
4.4.	Experiments with a Rupturing Diaphragm . . . . .	63
4.5.	Driver Performance . . . . .	67
4.6.	Acceleration Tube . . . . .	71
4.7.	Secondary Driver . . . . .	73
4.8.	Shock Tube Length . . . . .	80
4.9.	Stronger Diaphragms . . . . .	82
4.10.	Chapter Conclusion . . . . .	84
<b>5.</b>	<b>Radiation Experiments</b>	<b>86</b>
5.1.	Chapter Overview . . . . .	86
5.2.	Expansion Tube Layout . . . . .	86
5.3.	Repeatability . . . . .	87
5.4.	Developing the New Condition . . . . .	93
5.4.1.	Pitot Rake Measurements . . . . .	94
5.4.2.	Nozzle Inlet Rake Measurements . . . . .	100
5.4.3.	Summary . . . . .	101
5.5.	Quantifying the Condition . . . . .	102
5.6.	Experimental Models . . . . .	109
5.7.	Optics Experiments . . . . .	111
5.7.1.	Optical Setup . . . . .	111
5.7.2.	High Speed Imaging . . . . .	113
5.7.3.	Time Resolved Spectra . . . . .	122
5.7.4.	Shock Stand-off Comparisons . . . . .	129
5.8.	Binary Scaling Assessment . . . . .	132

5.9. Chapter Conclusion . . . . .	139
<b>6. Conclusions and Recommendations</b>	<b>141</b>
6.1. Research Goals . . . . .	141
6.1.1. Facility Development . . . . .	141
6.1.2. Radiation Experiments . . . . .	142
6.2. Future Work and Recommendations . . . . .	143
6.2.1. The Driver and Condition Development . . . . .	143
6.2.2. The diaphragm problem . . . . .	145
6.2.3. Radiating flow experiments . . . . .	145
6.3. A Final Point . . . . .	146
<b>A. Experiment List</b>	<b>161</b>
<b>B. Shock Tube Wall Static Pressures</b>	<b>166</b>
<b>C. Acceleration Tube Wall Static Pressures</b>	<b>172</b>
<b>D. Spectral Line Comparisons</b>	<b>183</b>

---

# List of Figures

2.1.	AVCO Everett Research Laboratories experimental arrangement . . . . .	10
2.2.	Theoretical comparison with ballistic range data . . . . .	11
2.3.	Spectrograph example . . . . .	11
2.4.	Spatial variation of spectra . . . . .	12
2.5.	Comparison of theoretical and experimental shock tube data . . . . .	13
2.6.	Stagnation point heating of Fire II . . . . .	14
2.7.	EAST measurements with HARA and NEQAIR comparisons . . . . .	15
2.8.	Fire II experiment results . . . . .	17
2.9.	Apollo 4 instrumentation . . . . .	18
2.10.	Spectra obtained during Hayabusa observation . . . . .	18
2.11.	Idealised x-t diagram of an expansion tube . . . . .	21
2.12.	Two-stage piston used on X2 . . . . .	24
2.13.	Diagram of X2 and X3 . . . . .	25
2.14.	Typical optical setup . . . . .	26
3.1.	X3 layout for chapter 3 . . . . .	29
3.2.	200kg piston compression tube pressure trace . . . . .	31
3.3.	200kg piston trajectory . . . . .	32
3.4.	Compression tube pressure derived by Stalker . . . . .	35
3.5.	Lightweight piston compression ratios for various gas compositions and rupture pressures	36
3.6.	Required piston velocity for given compression ratios . . . . .	40
3.7.	Different types of piston trajectory . . . . .	41
3.8.	Tuned piston trajectory and compression tube pressure trace . . . . .	42
3.9.	Results of applying Horgung's methodology . . . . .	44
3.10.	Shock speeds using Hornung's methodology and an orifice plate . . . . .	45
3.11.	X3's launcher . . . . .	46
3.12.	Internals of X3's launcher . . . . .	47
3.13.	Geometry of X3's launcher in one dimension . . . . .	48
3.14.	Diagram of the chevron seal . . . . .	49

3.15. Effects of varying the friction factor . . . . .	50
3.16. Illustration of piston leaving the launcher . . . . .	51
3.17. Effects of changing the launcher length $L$ . . . . .	52
3.18. Sample blank-off shot . . . . .	53
3.19. Compression tube pressure with and without reservoir extension . . . . .	54
3.20. Compression tube pressure after launcher slots enlarged . . . . .	54
3.21. L1d validation with blank-off shots . . . . .	55
3.22. Welding electrode setup . . . . .	56
3.23. Piston location at end of stroke during blank-off shot . . . . .	57
4.1. Layout of X3 used in chapter 4 . . . . .	59
4.2. Variation of averaging regions in L1d . . . . .	61
4.3. Pressure distribution in compression tube at diaphragm rupture . . . . .	62
4.4. Variation of reservoir pressure and piston trajectory . . . . .	63
4.5. Original buffer design . . . . .	64
4.6. Blank-off shots performed of the final condition . . . . .	65
4.7. Compression tube traces for different mixtures . . . . .	66
4.8. Compression tube traces for the 2mm diaphragms . . . . .	67
4.9. Compression tube traces for the 3mm diaphragms . . . . .	68
4.10. Shock tube shock speeds with a 2mm diaphragm . . . . .	68
4.11. Shock tube shock speeds with a 3mm diaphragm . . . . .	70
4.12. Shock tube wall pressures for 2mm diaphragm, 100% argon 0% helium . . . . .	70
4.13. Shock tube wall pressures for 3mm diaphragm, 100% argon 0% helium . . . . .	71
4.14. Acceleration tube shock speeds with a 2mm diaphragm . . . . .	72
4.15. Acceleration tube shock speeds with a 3mm diaphragm . . . . .	73
4.18. X3 layout with a secondary driver . . . . .	73
4.16. Acceleration tube wall pressures for 2mm diaphragm, 100% argon 0% helium . . . . .	74
4.17. Acceleration tube wall pressures for 3mm diaphragm, 100% argon 0% helium . . . . .	75
4.19. Idealised x-t diagram with a secondary driver . . . . .	76
4.20. Performance increase due to a secondary driver . . . . .	77
4.21. Secondary driver in L1d . . . . .	78
4.22. Shock speeds with a secondary driver . . . . .	79
4.23. ST6, AT8 and test section pressure traces with and without a secondary driver . . . . .	79
4.24. X3 layout with a short shock tube . . . . .	80
4.25. Shock speeds with a long and short shock tube . . . . .	81
4.26. Wall pressure at AT8 and test section pressure for a long and short shock tube . . . . .	82
4.27. Compression tube pressure and piston trajectory for stronger 3mm diaphragms . . . . .	83
4.28. Piston damage . . . . .	84
5.1. Layout of X3 used in chapter 5 . . . . .	87

5.2.	Static and dynamic diaphragm rupture . . . . .	88
5.3.	Diaphragm test rig and ruptured diaphragms . . . . .	89
5.4.	85% helium driver gas compression tube traces . . . . .	90
5.5.	100% helium driver gas compression tube traces . . . . .	90
5.6.	Shock speeds for 85% and 100% helium driver gas . . . . .	91
5.7.	Wall pressure trace comparison for 85% driver gas . . . . .	92
5.8.	Wall pressure trace comparison for 100% driver gas . . . . .	92
5.9.	Shock speeds measured during fill pressure iteration . . . . .	93
5.10.	Wall pressures measured during fill pressure iteration . . . . .	94
5.11.	Average shock speeds for condition quantification and optical experiments . . . . .	95
5.12.	Test section pitot rake and nozzle inlet rake . . . . .	96
5.13.	Pitot rake measurements with 15° conical probes . . . . .	97
5.14.	Spatial and temporal distribution of fig. 5.13 . . . . .	97
5.15.	Pitot rake measurements with pitot probes . . . . .	98
5.16.	Spatial and temporal distribution of fig. 5.15 . . . . .	99
5.17.	Comparison of fig. 5.14 and fig. 5.16 . . . . .	99
5.18.	Pressure measurements with the nozzle inlet rake . . . . .	101
5.19.	Spatial and temporal distribution of fig. 5.18 . . . . .	102
5.20.	Analytical post shock pressure in the shock tube . . . . .	104
5.21.	Analytical wall pressure at end of acceleration tube . . . . .	105
5.22.	Analytical pressure after a conical shock over a 15° cone at the nozzle inlet . . . . .	106
5.23.	Analytical pressure after a conical shock over a 15° cone at the nozzle exit . . . . .	107
5.24.	Analytical pitot pressure at the nozzle exit . . . . .	107
5.25.	Final test condition comparison to Hayabusa trajectory . . . . .	109
5.26.	1:5 scale Hayabusa model . . . . .	110
5.27.	Full scale Hayabusa model . . . . .	110
5.28.	Optical Layout . . . . .	112
5.29.	Optical instrument timing . . . . .	113
5.30.	Sample 2D image with edge detection . . . . .	114
5.31.	Shock fitting demonstration . . . . .	116
5.32.	1:5 Hayabusa model shock stand-off measurements . . . . .	118
5.33.	Full scale Hayabusa model shock fitting . . . . .	118
5.34.	Full scale Hayabusa model shock stand-off measurements . . . . .	119
5.35.	Post shock density profiles . . . . .	120
5.36.	Qualitative spectral measurements at EAST . . . . .	122
5.37.	1:5 scale Hayabusa model sample spectral measurement . . . . .	124
5.38.	Full scale Hayabusa model sample spectral measurement . . . . .	125
5.39.	Spectral line comparison for the 1:5 scale Hayabusa model . . . . .	127
5.40.	Identified spectral features for spectra centred at 640nm . . . . .	128

5.41. Identified spectral features for spectra centred at 450nm . . . . .	128
5.42. Shock stand-off for 1:5 scale Hayabusa model measured with high speed video and spectra . . . . .	130
5.43. Shock stand-off for full scale Hayabusa model measured with high speed video and spectra . . . . .	130
5.44. Shock stand-off measured in X3 compared with X2 and CFD . . . . .	131
5.45. Post-shock density for the X2 conditions . . . . .	134
5.46. Binary scaling parameter for the X2 conditions . . . . .	134
5.47. Mole fraction and mole concentration . . . . .	135
5.48. Post-shock density for the X3 condition . . . . .	136
5.49. Binary scaling parameter for the X3 condition . . . . .	137
5.50. Additional Hayabusa trajectory point . . . . .	138
5.51. Post-shock density for equivalent altitude . . . . .	139
5.52. Binary scaling parameter for equivalent altitude . . . . .	139
B.1. Shock tube wall static pressure traces for x3s508 . . . . .	166
B.2. Shock tube wall static pressure traces for x3s509 . . . . .	167
B.3. Shock tube wall static pressure traces for x3s510 . . . . .	167
B.4. Shock tube wall static pressure traces for x3s511 . . . . .	168
B.5. Shock tube wall static pressure traces for x3s512 . . . . .	168
B.6. Shock tube wall static pressure traces for x3s527 . . . . .	169
B.7. Shock tube wall static pressure traces for x3s528 . . . . .	169
B.8. Shock tube wall static pressure traces for x3s529 . . . . .	170
B.9. Shock tube wall static pressure traces for x3s530 . . . . .	170
B.10. Shock tube wall static pressure traces for x3s508 . . . . .	171
B.11. Shock tube wall static pressure traces for x3s532 . . . . .	171
C.1. Acceleration tube wall static pressure traces for x3s508 . . . . .	173
C.2. Acceleration tube wall static pressure traces for x3s509 . . . . .	174
C.3. Acceleration tube wall static pressure traces for x3s511 . . . . .	175
C.4. Acceleration tube wall static pressure traces for x3s512 . . . . .	176
C.5. Acceleration tube wall static pressure traces for x3s527 . . . . .	177
C.6. Acceleration tube wall static pressure traces for x3s528 . . . . .	178
C.7. Acceleration tube wall static pressure traces for x3s529 . . . . .	179
C.8. Acceleration tube wall static pressure traces for x3s530 . . . . .	180
C.9. Acceleration tube wall static pressure traces for x3s531 . . . . .	181
C.10. Acceleration tube wall static pressure traces for x3s532 . . . . .	182
D.1. Comparison of shots x3s693, x3s694 and x3s696 line <i>a</i> for a wavelength region of 560–700nm. . . . .	184

*List of Figures*

D.2. Comparison of shots x3s693, x3s694 and x3s696 line <i>b</i> for a wavelength region of 560–700nm. . . . .	188
D.3. Comparison of shots x3s699 and x3s700 line <i>a</i> for a wavelength region of 380–500nm.	192
D.4. Comparison of shots x3s699 and x3s700 line <i>b</i> for a wavelength region of 380–500nm.	199
D.5. Comparison of shots x3s701, x3s702 and x3s703 line <i>a</i> for a wavelength region of 560–700nm. . . . .	206
D.6. Comparison of shots x3s701, x3s702 and x3s703 line <i>b</i> for a wavelength region of 560–700nm. . . . .	210
D.7. Comparison of shots x3s704 and x3s705 line <i>a</i> for a wavelength region of 380–500nm.	214
D.8. Comparison of shots x3s704 and x3s705 line <i>b</i> for a wavelength region of 380–500nm.	218

---

# List of Tables

1.1.	Goulard number for some entry vehicles . . . . .	3
3.1.	Sensor locations for chapter 3 . . . . .	29
3.2.	200kg piston operating condition . . . . .	31
3.3.	Lightweight piston compression ratios for various gas compositions and rupture pressures	36
3.4.	Results from Stalker analysis . . . . .	41
3.5.	Final parameters used in L1d . . . . .	52
4.1.	Tube wall static sensor locations . . . . .	59
4.2.	Orifice plate area restriction . . . . .	65
5.1.	Sensor locations . . . . .	87
5.2.	Analytically determined test condition . . . . .	108
5.3.	Optical exposures and timing . . . . .	114
5.4.	Post shock average densities . . . . .	121
5.5.	Binary scaling flow properties . . . . .	133
5.6.	Equivalent altitude trajectory point comparison . . . . .	138
A.1.	Shots performed with a 2mm thick primary diaphragm discussed in section 4.5. . . . .	162
A.2.	Shots performed with a 3mm thick primary diaphragm discussed in section 4.5. . . . .	162
A.3.	Shots that used a secondary driver with both 2mm and 3mm thick primary diaphragms, discussed in section 4.7. . . . .	163
A.4.	Shots performed with a short shock tube, discussed in section 4.8. . . . .	163
A.5.	Shots performed with the stronger 3mm diaphragms, discussed in section 4.9. . . . .	163
A.6.	Shots performed when developing and quantifying the full scale condition . . . . .	164
A.7.	Shots performed when taking optical measurements in front of a model . . . . .	165
D.1.	Appendix D figure descriptions . . . . .	183



# Introduction

Humankind has always been fascinated by space. Beginning with observations of the night sky by ancient civilisations, space is now an important factor in day to day life, whether it be communications, navigation, scientific research or general exploration. Increased availability and reduction in size and cost of electronics has led to an overall reduction in cost and size of satellite systems, which in turn means that the large launch systems of the 20th century are no longer required for most access to space applications. Simultaneously, a desire to reduce the cost and increase the resusability of launch systems has occurred, most notably with the development of SpaceX's Falcon rockets, a push towards reusable air-breathing stages with rocket-scramjet-rocket launch systems [8], and the development of multiple smaller launch systems, such as those by Rocket Lab [9] and Gilmour Space Technologies [10].

Despite the increased commercialisation there is still a desire to perform exploratory and scientific space missions, a subset of which involve returning to Earth with scientific payloads. Current missions are Hayabusa2 [11], OSIRIS-REx [12] and Chang'e-5 [13], which all have a mission objective to return to Earth from asteroids, or in the case of Chang'e-5, from the Moon. While these three examples have all travelled to different locations in the solar system they all share the need to contend with perhaps one of the most brutal environments any man made vehicle has to experience, atmospheric entry from deep space.

## 1.1. Research Context

The harsh heating environment a vehicle experiences while it enters the atmosphere makes it one of the most critical stages of a vehicle's mission. A vehicle entering the atmosphere at velocities greater than  $10\text{km s}^{-1}$  is said to be travelling in the superorbital entry regime, which is representative of velocities a vehicle will be travelling at during Lunar, Martian or asteroid return missions. It is above this velocity threshold that radiative heat transfer to the surface of the vehicle starts becoming a dominant heat transfer mechanism [14]. Convective heat transfer to the surface of a vehicle can be modelled with reasonable accuracy provided surface reactivity is known [15] but the same is not true of radiative heat transfer and calculations still have significant levels of uncertainty. This uncertainty results in potential

## 1. Introduction

overdesign of thermal protection systems of reentry vehicles, usually by means of extra mass. For a context where mass is critical, this can severely reduce the capacity and stability of a single mission.

As test flights for the purpose of collecting atmospheric entry data are extremely costly, obtaining data for the validation of numerical models is normally left to experimental facilities capable of producing conditions representative of the environment during flight. Shock tubes, tunnels and expansion tubes do this by generating flows at the same velocities a vehicle travels at and plasma tunnels and arc jet facilities produce the flow encountered behind the shock. Expansion tubes are one of the only facilities capable of recreating gas flows with the same velocities that a vehicle experiences during superorbital flight, producing optical images of the flow field around or through the model, or measurements taken on the surface of the model such as pressure or heat transfer.

One drawback of expansion tubes is that the model typically used for reentry experiments needs to be a small scaled version of the actual flight vehicle. To maintain similarity between the experimental flow and flight, the total flight enthalpy must be matched and binary scaling applied: binary scaling is the conservation of the product of density and a characteristic length,  $\rho L$ . When done correctly, binary scaling conserves Reynolds number and viscous effects, binary reactions such as nonequilibrium dissociation, convective heat transfer, and radiative heat transfer if the flow is optically thin [16]. When considering nonequilibrium radiation, the intensity of radiation is proportional to density but the relaxation zone thickness is inversely proportional to density, this has the consequence of radiative flux remaining independant of density at a given velocity [17]. Binary scaling begins to break down when considering the heat lost from the flow via radiation. Radiative heat loss from the flowfield scales with density times volume of gas,  $\rho L^3$ , and the mass of gas entering the shock layer scales by density times area,  $\rho L^2$ . Dividing the two parameters results in the heat removed from the shock layer per mass of gas, which scales with proportion to the characteristic length  $L$  [16]. This dependance on characteristic length may result in less heat being removed from the shock layer via radiation compared to the full scale vehicle and therefore potential loss of similarity from the flight condition. The severity of this dependance is determined by the level of coupling between radiation flux and the flowfield, which can be determined by the ratio of energy radiated and the total energy entering the shock layer, commonly known as the Goulard number ( $\Gamma$ ) [18]. Typically, a value of 0.01 is used to determine whether a flowfield is strongly coupled with radiative flow [19], with strongly coupled flowfields having a Goulard number greater than 0.01 [19].

Sharma and Whiting [15] also list four flow mechanisms that may reduce the nonequilibrium or equilibrium radiative load to a vehicle and violate binary scaling:

1. Truncation of the shock layer occurs when the nonequilibrium region is thicker than the shock layer.
2. Collisional limiting reduces radiation intensity at low density.
3. Radiation cooling occurs when energy loss via radiation is significant.
4. Radiative absorption in the gas.

Table 1.1.: Goulard number for some entry vehicles.

Vehicle	$\Gamma$
Titan Explorer	0.4 [20][18]
Galileo	0.1 [18]
Stardust (66km altitude)	0.022 <sup>1</sup>
Lunar Return, Fire II (peak radiation)	0.01 [20]
Hayabusa (peak radiation)	0.013[20]

<sup>1</sup> Calculated from Tauber and Sutton correlation [21].

The Goulard number for a selection of entry vehicles is shown in table 1.1 for Earth re-entry where the Goulard number at the time of peak radiation was greater than or equal to 0.01. The large Goulard numbers for the Titan Explorer and Galileo vehicles are due to the atmospheric composition and high entry velocity respectively.

The values of the Goulard number in table 1.1 suggest that for experiments where the test flow has been scaled from the trajectory of one of these vehicles that coupling is significant and the scaled flow may not accurately replicate the flight condition. This is because not enough radiative cooling would have occurred within the experimental flow. This may be avoided by selectively choosing the trajectory point to one with lower radiative coupling but this may give way to other difficulties in producing the test flow or the quality of measurements if radiation levels are lower. If one was to have access to a large enough facility, model scaling would not be necessary and the potential to perform unscaled experiments over full scale models would become possible and a unique set of data critical to our understanding of high enthalpy radiating flowfields could be obtained.

X3, a large scale expansion tube at the University of Queensland (UQ), has the potential to produce high enthalpy flows with core flow diameters on the order of several hundred millimetres, compared to the smaller X2 (also at UQ) which is limited to a maximum core flow of approximately 100mm diameter. While X2 is routinely used for various types of radiation experiments, at the beginning of this present study X3 had never been used in its upgraded configuration to produce high enthalpy test flows, with the only experiments having been performed for a Mach 10 scramjet.

## 1.2. Research Aims

This thesis predominately focusses on the facility development of X3 with the aim of producing high enthalpy test conditions to measure radiation of flow over blunt re-entry vehicle geometries. Part of the work in this thesis follows on from the work of Gildfind et al. [22] who designed a new lightweight piston for X3 and is divided into two main parts; facility development and radiation experiments. The radiation experiments section consists of the development of the final condition and matching it to a trajectory point as well as optical measurement taken over a full scale Hayabusa capsule geometry, the first time a full scale re-entry capsule has been tested at the actual flight velocity and enthalpy.

### 1.2.1. Facility Development

*Can X3 produce high enthalpy flows suitable for radiation experiments and limitations?* The upgraded configuration of X3 has never been used to produce high velocity high enthalpy flows and the new lightweight piston has never been used in an experiment that produced a test flow. In theory expansion tubes are currently the only facility that can produce high enthalpy superorbital radiating flows over a model, but there are many intricacies that can be detrimental to the quality of the test flow. As the design of X3 was completed with cost in mind, [23], and the configuration changed from dual stage to a single stage driver, it is not known how remaining features, such as internal area changes and a new nozzle, affect the flow quality and if phenomena that are not significant on smaller facilities begin to affect the flow on a larger facility. This aim includes the design of a series of driver operating conditions with the lightweight piston, a look at the relative performance of X3 compared to X2, and a study on the changing of some parameters, namely the shock tube length and the implementation of a secondary driver, to examine if they influence the flow.

### 1.2.2. Radiation Experiments

*Once the driver has been developed, can it produce a test flow that is useful for high enthalpy radiation experiments?* For a given driver, there is a limit to its performance and the type of conditions it can produce. For radiating flows the performance is typically limited by velocity or density. A target test condition is one from X2 for a 1:5 scaled Hayabusa model at peak radiation with binary scaling applied ( $\rho L$  scaling). This condition has a high velocity ( $10.5 \text{ km s}^{-1}$ ) and relatively high density ( $2.6 \times 10^{-3} \text{ kg m}^{-3}$ ) compared to other operating conditions in X2. The condition in question uses one of the stronger driver conditions available in X2 and it is unknown whether new operating conditions designed in X3 will be capable of recreating the flow condition.

*Is it possible to take time resolved spectroscopic measurements using available instrumentation?* Spectroscopic measurements of flow over a model have not previously been taken in X3 for any

configuration. Numerous experimental campaigns in X2 means that the process of setting up a spectral system is rather well established on that facility with the wealth of knowledge and refinement of the system over the years. While the principles of setting up spectroscopic systems on X3 are the same, the size of X3's test section and the size of regions of interest in the flow field introduce a unique set of considerations when designing the system. The desire to make use of X3's longer test time and obtain time resolved spectroscopy using a high speed intensifier coupled with a high speed camera, which is a new setup, comes with its own set of challenges that must be overcome. In addition, the low frequency of experiments in X3 means that a trial and error approach for fine tuning instrumentation setting, and the entire endeavour will have many obstacles that must be overcome.

## 1.3. Thesis Outline

This thesis is structured as follows:

**Chapter 2: Literature Review** This chapter gives the reader an overview of why radiating flows are important and provides a very brief introduction on the structure and features of a radiating shock layer. The development of both experimental and numerical tools are presented and the reader is left with an idea of the current state of the art when it comes to reproducing and calculating radiating flows. Finally the FIRE flight experiment and Hayabusa capsule are introduced with more detail presented about the analysis of Hayabusa and associated numerical work that has been conducted as well as experimental work performed in X2 at UQ. The chapter is concluded with an introduction to expansion tubes with a focus on X2 and X3.

**Chapter 3: X3's Driver** The details of X3's driver are outlined here and analytical models that can be used to predict the behaviour of the piston with chosen reservoir and compression tube fill pressures. A significant portion of this chapter is dedicated to creating a numerical model of the driver and reservoir using the 1D CFD code L1d and an exploration into the different object parameters that are available in the code. This chapter also includes the modification and implementation of new parameters in L1d all of which have an effect on the numerical behaviour of the piston and will be used to tailor the L1d model to be able to accurately predict experimental results. Finally, blank-off experiments are performed in X3 with a comparison to the numerical data from the L1d model.

**Chapter 4: Driver Performance** This chapter begins with the next developmental step of the L1d model, which is to include the rupturing diaphragm, identifying an operating condition where the piston is tuned, and examining how well L1d is able to reproduce the behaviour of the piston, driver and diaphragm compared to experiment. All the resulting driver conditions are presented and their relative performance is evaluated using a fixed driven tube configuration that was used in X2. The chapter is concluded with an examination of the effects of including a secondary driver as well as changing the length of the shock tube, and the consequence of using primary diaphragms with different material properties.

**Chapter 5: Radiation Experiments** The development of the final operating condition is outlined in this chapter. Pressure measurements taken before and after the nozzle were compared to analytical calculations, with the potential variation in operating condition determined by varying key parameters within the analytical formulation. The final analytical condition, based on experiment, is compared to the trajectory of Hayabusa. Details of the optical setup, high speed two-dimensional imaging and time resolved spectroscopy are presented. Sample images and an overview of the analysis performed are included. The final results include features identified within the measurements and a comparison of shock stand-off with literature.

**Chapter 6: Conclusion** This chapter summarises the important results and discoveries from the preceding chapters and relates them to the goals listed in section 1.2. A list of recommendations for future work is included; the list is primarily based on lessons learnt and difficulties encountered during the thesis, and suggests potential improvements to the facility and experimental campaigns that would extend the work in this thesis.

# 2

---

## Literature Review

### 2.1. Radiating Flows

When a vehicle enters the atmosphere, either for direct entry or aerocapture manouevres, it experiences the harshest heating environment of its entire journey. During such manouevres, a shock forms in front of the vehicle which converts the kinetic energy of incoming particles to thermal energy as they collide with particles in the high density shock layer. There is a sudden increase in translational energy before further inter particle collisions then increase the rotational, vibrational and electronic energy levels. Once the vibrational energy levels reach a high enough state, the bonds within the particles break and dissociation occurs. Additional collisions further elevate the energy of bound electrons to higher states, and the particles emit electromagnetic radiation when the excited electrons fall to less energetic states [24]. The excitation and de-excitation processes occurring at different rates leads to a nonequilibrium region after the shock where dissociation is still occurring [25]. Early studies done by Wilson [26] found that at shock speeds below approximately  $10\text{km s}^{-1}$  radiation was strongest in the narrow nonequilibrium region immediately downstream of the shock, whereas for higher speeds, the nonequilibrium radiation was not as strong as radiation further downstream in the shock layer. Given sufficient energy, ionisation can also occur in the shock layer, which leads to radiation from free-bound transition and bremsstrahlung radiation. For the case of air, ionisation begins with the formation of  $\text{NO}^+$  which is the only significant ionised species in air below shock speeds of around  $8\text{km s}^{-1}$  [25]. At higher speeds,  $\text{N}_2^+$ ,  $\text{N}^+$  and  $\text{O}^+$  form, although the production of free electrons is still mostly due to the formation of  $\text{NO}^+$ . The presence of ions contributes significantly to the overall radiative heating, with different ions having a more predominant effect depending on the flight speed [25]. To calculate the radiation within the shock layer, the gaseous emissivity within the equilibrium region,  $\varepsilon$ , can be defined by

$$\varepsilon = 1 - e^{-aKx} = 1 - e^{-a\sigma Nx} \quad (2.1)$$

where  $K$  is the linear absorption coefficient, given by the product of the cross section of absorption  $\sigma$  and the density of the absorbing particles  $N$ , and  $x$  is the number of units of gas the radiation travels

through. Typically  $a$  is set to unity but Breene and Nardone [27] found that  $a = 1.8$  approximates the angular integration better for smaller path lengths. The radiant intensity can then be defined as

$$I_v = \epsilon_v B_v dv = B_v (1 - e^{-a\sigma N_x}) dv \quad (2.2)$$

where  $B_v$  is the Planck blackbody curve defined by

$$B_v = \frac{2hv^3}{c^2} \frac{1}{e^{\frac{hv}{k_B T}} - 1} \quad (2.3)$$

where  $h$  is Planck's constant,  $c$  is the speed of light,  $k_B$  is the Boltzmann constant and  $T$  is the absolute temperature, for a given frequency  $v$ . Difficulties in calculating intensity arise once the absorption is considered; cross sections and absorption coefficients must be known for high temperature gasses present behind a shock as well as other radiation processes that exist at high temperatures. In the early 60s several radiative models were devised and used as a reference for experimental validation, examples of such models were presented by Breene and Nardone [27], Nardone et al. [28], Meyerott et al. [29], and Kivel and Bailey [30].

### 2.1.1. Early Experiments

Some early attempts to measure radiating flows were conducted in a non-reflected shock tube at the AVCO Everett Research Laboratories [31–33] where radiation emission from shock heated nitrogen was measured. In these experiments the authors were able to observe radiation emissions for the first positive band of  $N_2$  and the first negative band of  $N_2^+$  over a range of shock speeds. The spectral intensity at equilibrium was measured using monochromators coupled with photomultipliers to measure intensity in narrow wavelength bands for shock speeds ranging from  $4 - 7 \text{ km s}^{-1}$ . A schematic of the experimental setup is shown in fig. 2.1. In studies performed by Allen [33], an electric arc driven shock tube was used to generate a  $6.9 \text{ km s}^{-1}$  shock and the rotational, vibrational and electronic temperatures were calculated for the nonequilibrium region using spectral distributions relative to the equilibrium state. In addition to shock tubes, experiments were conducted in ballistic ranges [34, 35] which launched a blunt projectile into a hypersonic counterflow resulting in relative speeds up to  $12.4 \text{ km s}^{-1}$ . Models of different material were tested at different flow velocities, and it was found that for the spectral range of the radiometer, the experimental measurements of equilibrium radiation agreed well with theoretical results, but theory and experiment started to diverge at low densities. Figure 2.2 shows sample data obtained in [35] for various materials with a comparison to a theoretical model used at the time for a  $6.46 \text{ km s}^{-1}$  flow condition. The authors found that as the density was lowered the experimental results deviated from theory and excess radiation was measured compared to predictions from equilibrium theory which was attributed to the development of significant nonequilibrium regions

## 2. Literature Review

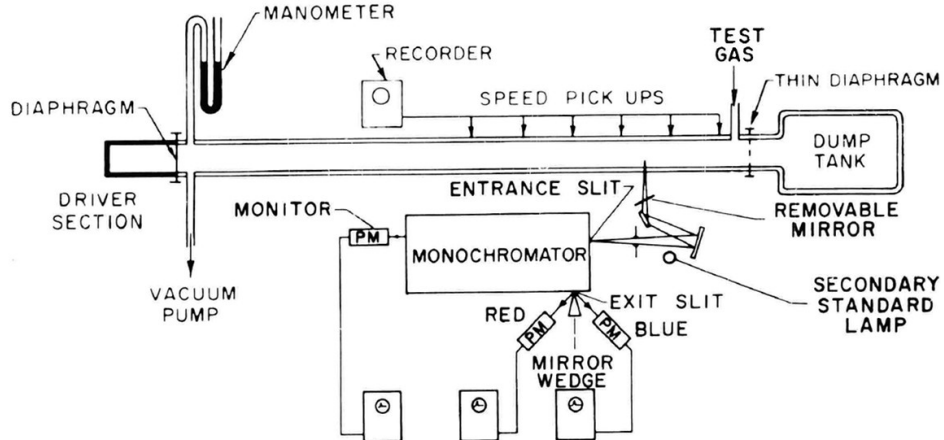


Figure 2.1.: Experimental arrangement at AVCO Everett Research Laboratories used in [31] and [32].

when the density is lowered. The authors in [35] also found that as density was further reduced, the radiation measured continued to decrease rather than asymptote to a constant value. This behaviour was said to be due to the truncation of the nonequilibrium region by the presence of the model as the time for the gas to reach equilibrium is larger than the residence time of the gas in the shock layer.

### 2.1.2. Facility and Measurement Developments

As optical technology advanced so that spectral and temporal resolution increased, more facilities were developed along with methods to generate high shock speeds to recreate the high temperature phenomena that occur at hypersonic speeds. The shock speed produced is essentially driven by the sound speed of the driver gas, which can be increased by reducing the molecular weight of the gas or increasing its temperature. Some methods used to heat the driver gas involve: External heating [36], combustion of hydrogen in the driver [37, 38], isentropically compressing the gas with a piston [39, 40], or discharging an electrical current through the driver gas [41, 42]. X3, the experimental facility used in this thesis, utilises free-piston compression to isentropically compress the driver gas and is more thoroughly described in later sections.

Measurements taken by Sharma and Walter [17] in the electric arc driven shock tube (EAST) at the NASA Ames Research Center obtained spectra over the 300 – 430nm range behind a 6.2km shock in pure nitrogen. Spectroscopic measurements were taken using a multichannel photoelectric sensor which allowed the full spectral region to be captured in a single experiment and mitigated the requirement of shot to shot consistency required by previous measurement devices [17]. Similar measurements were taken in EAST by Grinstead et al. [43], for a condition designed to predict radiative heating for the Orion re-entry vehicle, see fig. 2.3. The experiments performed by Grinstead et al. [43] allowed analysis of the nonequilibrium region of the shock and relaxation mechanics

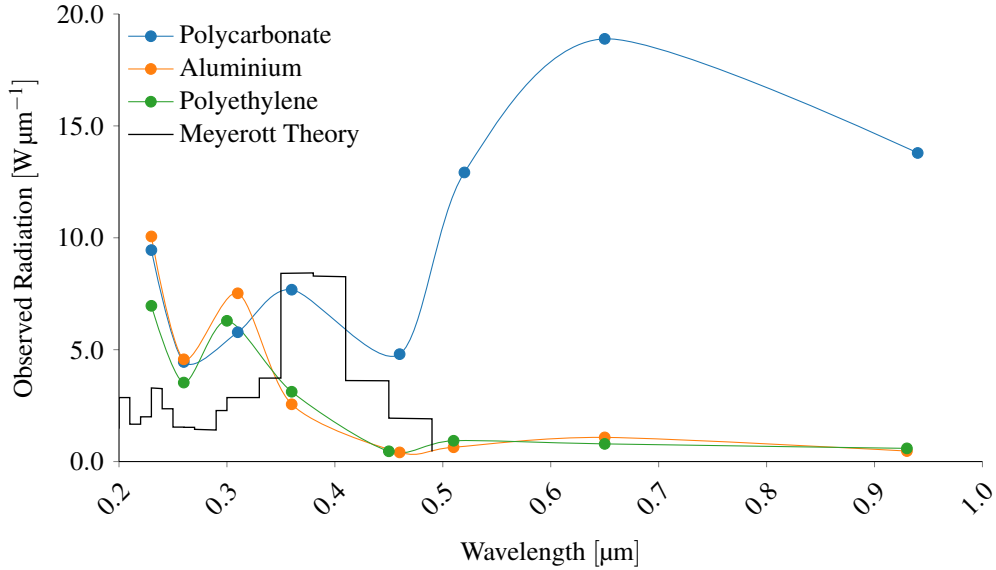


Figure 2.2.: Comparison of experimental results from ballistic range experiments at a velocity of  $6.46 \text{ km s}^{-1}$  with theoretical model by Meyerott et al. [29]; plot reproduced from [35]. The freestream density used was 1.9% of the density at sea level and the equilibrium shock temperature was 7760K.

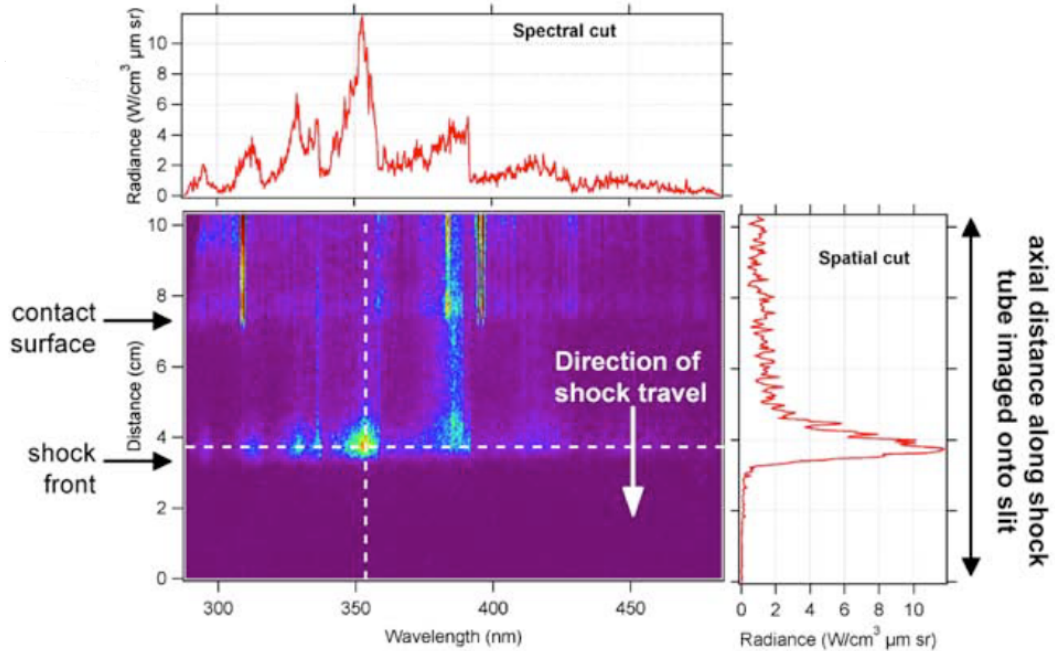


Figure 2.3.: Example of spectrograph image with spectral and spatial cuts, taken from [43].

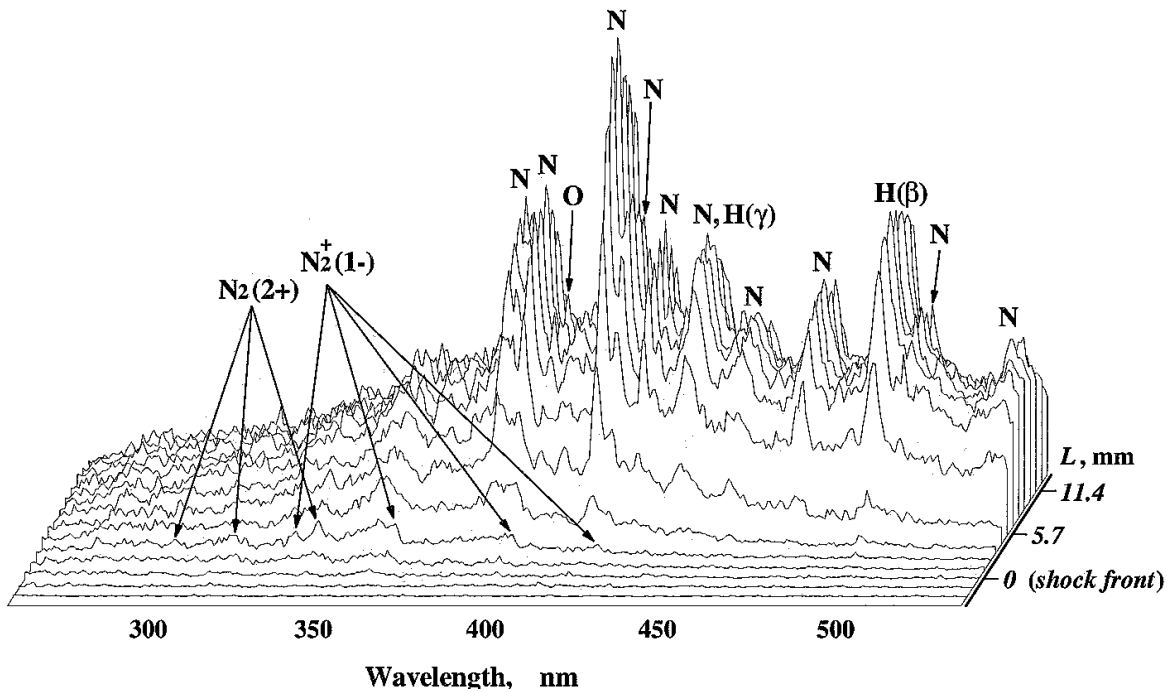


Figure 2.4.: Spatial variation of spectra in relation to location of the shock front for a  $11.9 \text{ km s}^{-1}$  shock [45].

of spectral features, similar to that performed by Johnston [44] who compared the experimental results with NASA's nonequilibrium radiation code HARA and found that they could predict radiative measurements within 15% for the 0.3Torr condition and within 40% for the 0.1Torr condition.

Similar experiments were performed in a free-piston double-diaphragm shock tube at the Institute of Space and Astronautical Science [45] in Kanagawa, Japan. Using a spatially resolved spectrometer aligned along the axis of the shock tube flow, the authors were able to achieve a spatial resolution of 1.1mm and measure the emission spectrum from air behind an  $11.9 \text{ km s}^{-1}$  shock with the observed spatial variation shown in fig. 2.4. Molecular spectra of  $\text{N}_2(2+)$  and  $\text{N}_2^+(1-)$  were found to be present immediately after the shock, whereas atomic line spectra of N and O become prominent at a greater distance from the shock front.

In addition to improved optical technology being used, other visualisation methods were also being employed, Miller [46] used schlieren and shadowgraph techniques to measure the shock shape in front of spheres and hemispheres for a range of density ratios and made comparisons with a selection of shock-shape predictions. Hornung [47] used optical interferometry to confirm theoretical methods of calculating shock stand-off and density field in the shock layer in front of a blunt body using a reaction rate parameter as a correlation factor. Laufer and McKenzie [48] used Laser-Induced Fluorescence to excite rotation lines of  $\text{O}_2$  at 193nm and measurements confirmed that the model they developed to predict fluorescence from the excitation of rotational transitions in molecular oxygen to be sufficiently accurate. Wilkes et al. [49] developed a portable fluorescence imaging system for use in NASA's

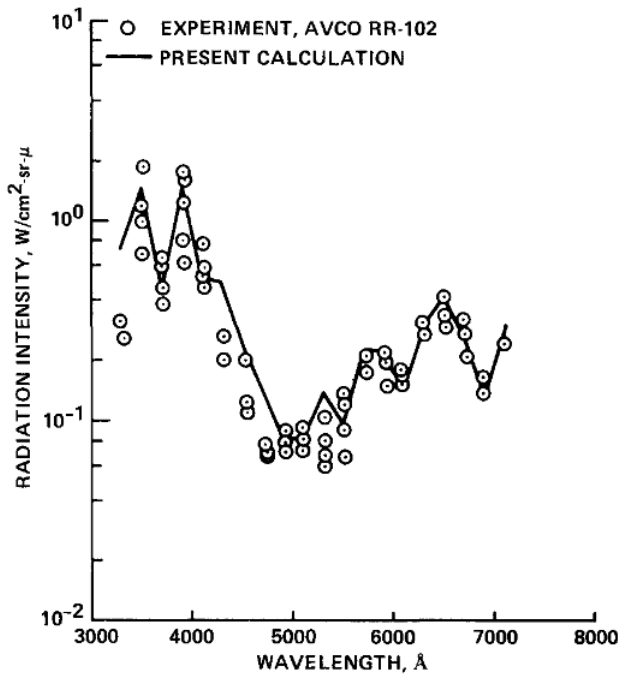


Figure 2.5.: Comparison between experimental data [31] and theoretical model [51] of spectra in the equilibrium region behind a shock wave travelling at  $4.8 \text{ km s}^{-1}$  into nitrogen with density of  $1.498 \times 10^{-5} \text{ g cm}^{-3}$ .

hypersonic facilities with demonstrations in NO-seeded free-jet flow and while no references could be found of this technique being used for radiating flows, Planar Laser-Induced Fluorescence tuned to the transition of NO was demonstrated in an Argon-NO gas mixture with flow over a two-dimensional blunt body [50].

### 2.1.3. Theoretical Models

While experimental investigations were being undertaken, theoretical models to predict radiation intensity were also being developed. One of the early models was developed by Park [51, 52], which uses two temperatures: one temperature to characterise translational energy of atoms and molecules and rotational energy of molecules, and a second temperature to characterise the vibrational energy of molecules, translational energy of electrons and electronic excitation energy of atoms and molecules. Once the reaction rates and species behind the shock were known, NEQAIR [53] was used by Park [51, 52] to calculate the theoretical radiative emissions. At the time of development, the only available experimental results for validation were those taken 20 years prior and comparisons were made with the data obtained in the AVCO Everett Research Laboratories [31, 33].

A comparison between the theoretical model and experimental results is shown in fig. 2.5 for pure nitrogen at  $4.8 \text{ km s}^{-1}$  with a density of  $1.498 \times 10^{-5} \text{ g cm}^{-3}$  with both experiment and theoretical

## 2. Literature Review

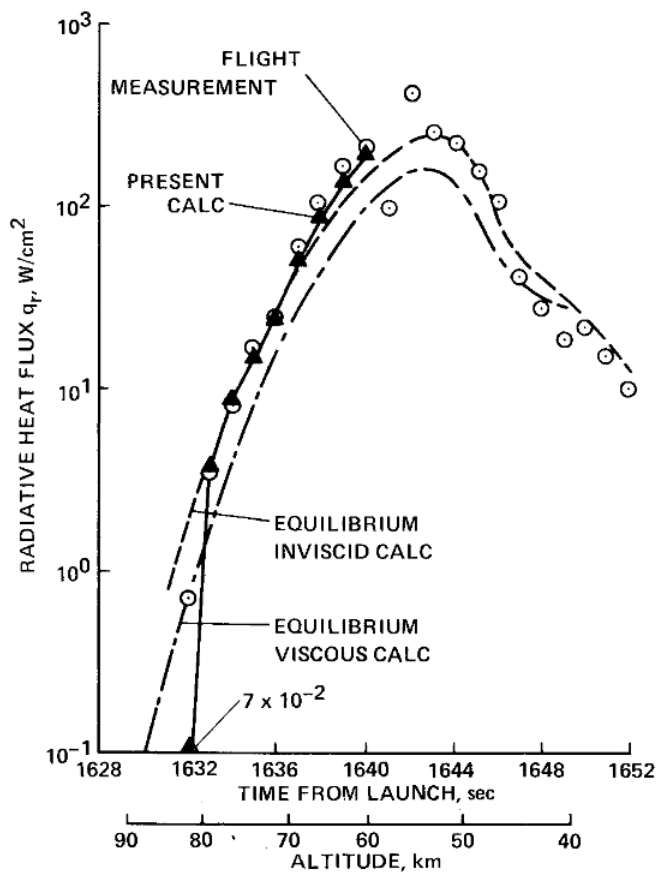


Figure 2.6.: Comparison between measured and theoretical stagnation point heat transfer for Fire II vehicle. "Present calc" is that performed by Park in [52], the equilibrium inviscid calculation is from [54], and the equilibrium viscous calculation is from [55]. Figure taken from [52].

calculation using a spectral bandwidth of 200nm and measurements taken every 200nm, and good agreement between theory and experiment was found. In [52], the same methodology was applied to air and comparisons with experiments and flight data were made. While good agreement was found the author concluded that further work was required for spectral calculations due to the assumptions made with assigning vibrational temperatures and the effect this has on calculating species concentrations. A comparison is shown for the Fire II vehicle for altitudes above 60km and with other model comparisons in fig. 2.6, the data agrees well between altitudes of 60–81km but underestimates the radiative flux at higher altitudes, which is attributed to the finite thickness of the shock wave that was neglected in the continuum at the time.

Feldick et al. [57] compared two nonequilibrium radiation tools by evaluating flows from Fire II and the Stardust capsule reentry: the Langley Aerothermodynamic Upwind Radiation Algorithm (LAURA) [58], which has the High-Temperature Aerothermodynamic Radiation code (HARA) [59] incorporated, and the Data-Parallel Line Radiation Method (DPLR) [60]. Although the codes handle the nonequilibrium energies differently, the predicted convective fluxes agreed within 5% but the

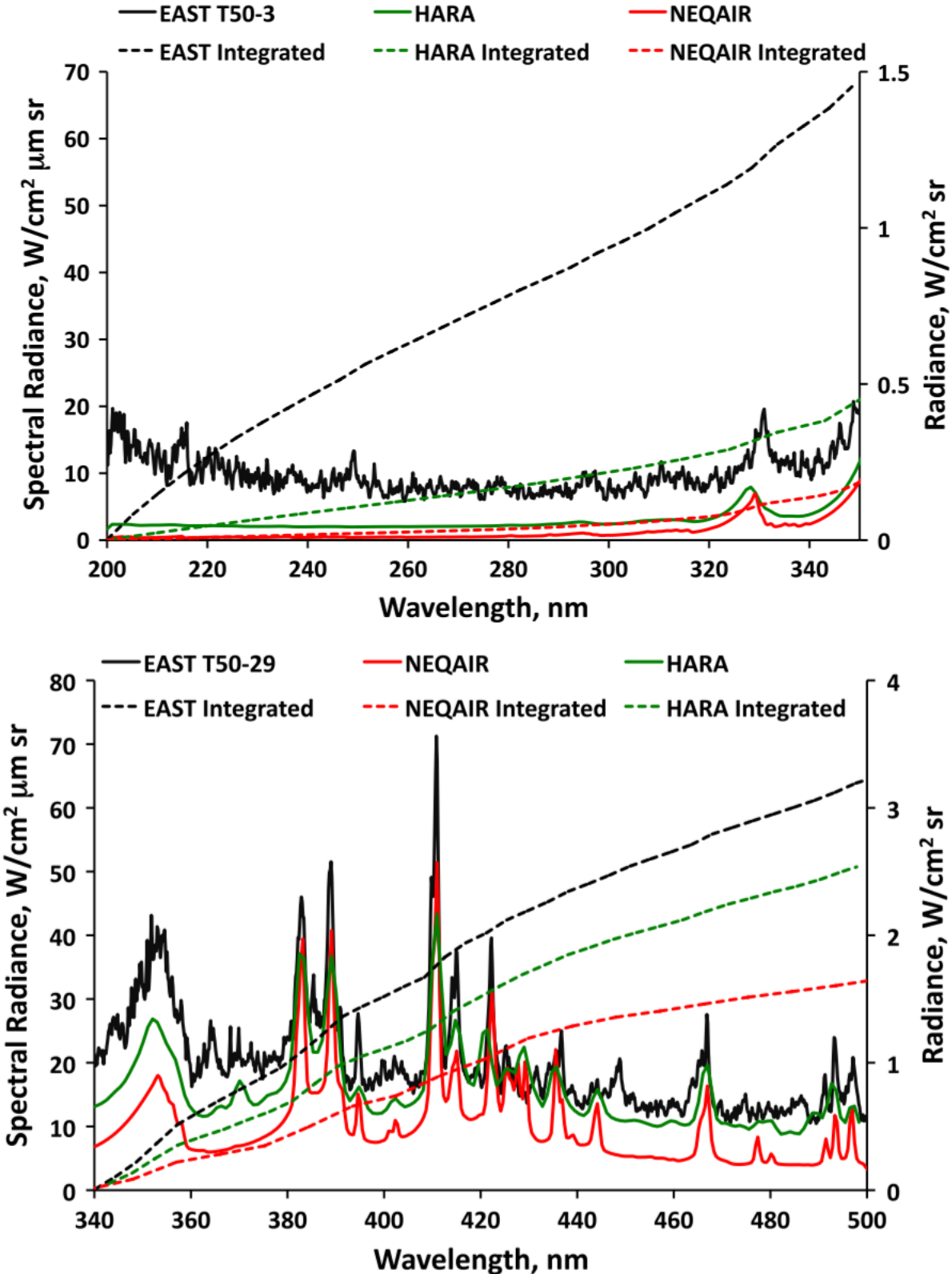


Figure 2.7.: EAST measurements taken behind a moving shock compared with NEQAIR and HARA codes in UV and visible regions for shock speeds of  $9.65 \text{ km s}^{-1}$  (top) and  $10.29 \text{ km s}^{-1}$  (bottom) [56].

## 2. Literature Review

energy distribution models had a considerable effect on radiative transport properties [57]. Brandis et al. [56] performed a detailed uncertainty analysis comparing NEQAIR and HARA with measurements taken in EAST in the VUV, UV/Vis, Vis/NIR and IR regions. Brandis et al. found that both codes predicted radiance within 20% of the experiments for all regions except in the UV/Vis, where the codes underestimated intensity by approximately 85% due to significant background continuum, or possible nonequilibrium flow effects in the experiment. The comparison of NEQAIR, HARA and EAST is shown in fig. 2.7 with the top plot for a shock speed of  $9.65\text{km s}^{-1}$  through air and the bottom plot for a shock speed of  $10.29\text{km s}^{-1}$  and a different wavelength range. The top plot shows 85% disagreement between EAST and the two codes, whereas the bottom plot, although a faster condition and different spectral region, shows a much better agreement. As a summary, Brandis et al. [56] mention that it is still not clear how nonequilibrium flow effects influence the flow and cause disparity between experiments and the theoretical models, and that temporal effects behind the shock need to be considered. In addition to the aforementioned models, other radiation codes that have been developed include; SPRADIAN, developed at the Institute of Space and Astronautical Science, Kanagawa, Japan [61], Photaura, developed at the University of Queensland, Brisbane, Australia [62], PARADE [63] and URANUS [64], but they will not be discussed here.

### 2.1.4. Flight Data

#### Fire I & II

As a precursor to the Apollo missions, two early flight experiments were the Fire I and Fire II (Flight Investigation Reentry Environment) vehicles which were launched to measure actual convective and radiative heat transfer during flight [65, 66]. While Fire I deviated from its intended trajectory and did not achieve the planned flight speed, Fire II was able to maintain its trajectory and resulted in a full set of convective and radiative data. The vehicle was equipped with radiometers to measure total radiation and spectral radiometers to measure radiation within a specific wavelength region. A calorimeter experiment was performed with the heat shield with the aim to estimate total heat transfer. Calorimeter and radiative heat transfer rates were obtained during the flight test, and the data was used to estimate radiative heating in the vacuum ultraviolet region ( $\lambda < 200\text{nm}$ ). Some results of heating measurements from Fire II are shown in fig. 2.8 and the method used to estimate the ultra violet radiation heat transfer to the vehicle is also illustrated.

The total heat transfer measured by the calorimeter is shown by the orange line in fig. 2.8 and is the addition of convective heating and radiative heating. The convective heating was assumed to be accurately predicted by theory and is represented by the green line, therefore the difference between the total measured heating and theoretical convective heating was determined to be the radiative heating. The red line in fig. 2.8 is the sum of theoretical convective heating and measured radiative heating, the measured heating is indicated at 1642.6s, Cauchon [66] estimates the vacuum ultraviolet radiation,

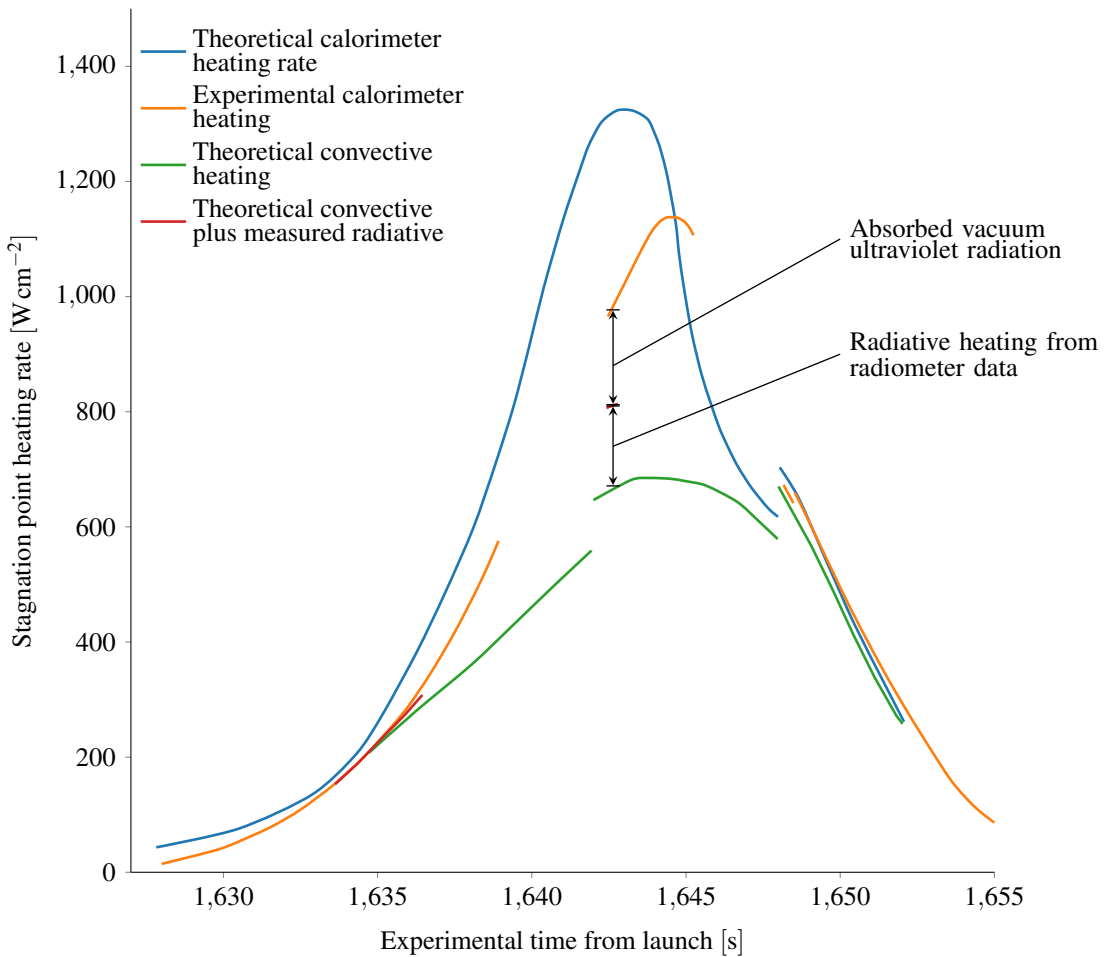


Figure 2.8.: Heating rates and estimation of vacuum ultraviolet radiation for Fire II, taken from [66]

which was unable to be measured and not included in calculations, as the difference between the orange (total experimental heating) and the red line (theoretical convective plus measured radiative). Following the Fire missions the Apollo 4 flight vehicle was tested at lunar return velocities [67] and was instrumented with pressure transducers, calorimeters and radiometers with the instrumentation layout shown in fig. 2.9. Radiation measurements made at the stagnation point agreed well with the theoretical models used at the time, with the calculations including nonadiabatic and cooling effects, and nonequilibrium radiation predictions were made using empirical data from ground testing.

### 2.1.5. Hayabusa

In more recent times, atmospheric entry observation missions have been conducted for the Hayabusa [68–70], Stardust [71, 72] and ATV-1 [73] capsules. Each observation involved using various spectroscopic instrumentation to measure radiative intensities of the shock layer in front of each vehicle. An ICCD image of the Hayabusa capsule taken by Buttsworth et al. [68] by the *Australian Ultraviolet Spectrograph* is shown in fig. 2.10. The vertical axis is the spatial dimension with the direction of flight going from top to bottom, and the horizontal axis is the wavelength axis with higher wavelength being

## 2. Literature Review

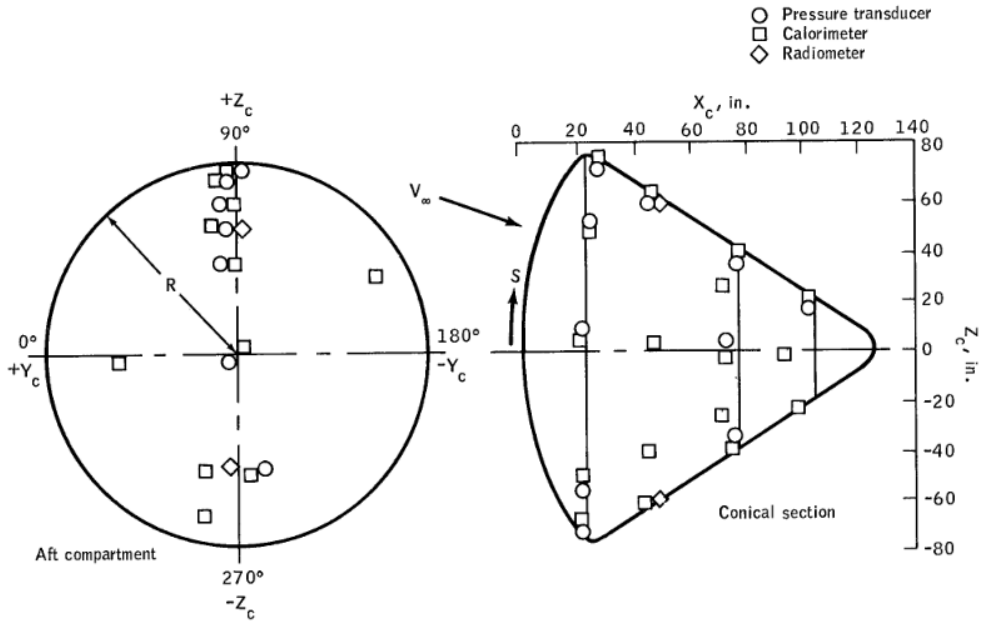


Figure 2.9.: Instrumentation layout of the Apollo 4 vehicle [67].

on the right. Figure 2.10 shows the location of the capsule, the disintegrating main bus and a reference region used for background subtraction. The measurements taken by Buttsworth et al. were in the near ultraviolet region, and by fitting a Planck irradiance value to the data at 455–460nm and assuming an emissivity of 0.9, the authors calculated a peak body temperature of approximately 3050K.

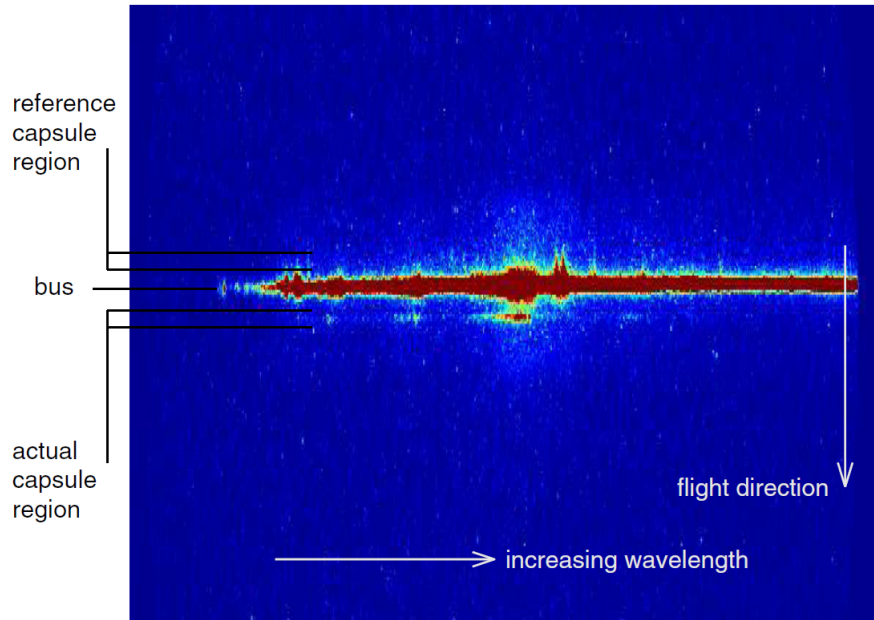


Figure 2.10.: ICCD image acquired during Hayabusa reentry showing locations of the capsule, bus and reference region. The spatial dimension has been expanded from the original image [68].

Spectral data of Hayabusa's reentry obtained by Jenniskens et al. [74] predicted a variation of 200K

from the calculation of Buttsworth et al. [68], which is attributed to different methodology in selecting the Planck fit and the spectral region. McIntyre et al. [70] took ground measurements of visible and near infrared regions throughout Hayabusa's reentry, and the surface temperature calculated from the spectral measurements was found to be  $3100\text{K} \pm 100\text{K}$  which is in good agreement with the results from Buttsworth et al. McIntyre et al. also used spectral features to calculate the shock layer temperature by matching lines with a simulated temperature in SPECAIR, and found that a temperature of  $7400\text{K} \pm 400\text{K}$  provided a good fit to the oxygen line at 777nm and nitrogen line at 820nm. Prior to the Hayabusa reentry, Buttsworth et al. [75] performed experiments of a 1:10 scale Hayabusa model in the X2 expansion tube. Models used were plain steel and an epoxy-coated steel model to simulate ablation, spectral measurements were taken in the same spectral region as those taken during the airborne observations. The results from the experimental campaign showed that major emissions in the UV region are due to CN, which was greatly reduced for the uncoated model.

To expand on the campaign by Buttsworth et al. [75], Fahy [76] and Fahy et al. [77] performed experiments in X2 with a 1:5 scale Hayabusa model, combining the experimental results with numerical calculations in an attempt to reconstruct the measurements taken during flight. Fahy found that the spectral intensities in the infrared region agreed within 30%, whereas the instensities in the ultraviolet region agreed within 50%. Numerical calculations have also been conducted by Kihara et al. [78], Suzuki et al. [79] and Winter et al. [80], in adition to the aforementioned studies by Fahy [77]. Results from these simulation will be used for comparative purposes later in this thesis and as such a brief overview of their respective modelling strategies is presented below.

**Kihara et al. [78]** The flow field was calculated using Navier-Stokes equations extended to include thermo-chemical nonequilibrium flow. The freestream gas was 11 species air and the ablation gas consisted of 9 species ( $\text{H}_2$ ,  $\text{C}_2$ ,  $\text{C}_3$ , CN, CO, H, C,  $\text{H}^+$ ,  $\text{C}^+$ ) with a total of 153 reactions included across all species. The model used four temperatures, translational, rotational, vibrational, and electronic, to calculate thermal nonequilibrium and the flow field was coupled with radiative emissions.

**Suzuki et al. [79]** The flow field was calculated using Navier-Stokes equations with vibrational-electron-electronic energy conservation equations. The freestream gas comprised 11 species air and the ablation gas consisted of 10 species, with the addition of  $\text{C}_2\text{H}$  compared to Kihara et al. [78]. Park's two-temperature model was used to calculate thermal nonequilibrium. Preferential dissociation was not used and the flow field was radiatively coupled.

**Winter et al. [80]** The flow field was calculated with DPLR2D, a two dimensional axisymmetric form of DPLR (Data Parallel Line Relaxation [60]) which solves reacting Navier-Stokes equations and models finite-rate chemistry and nonequilibrium. Air was modelled with Park's 1990 11 species 19-reaction air model [25], with the flow assumed to be in thermal nonequilibrium using Park's two-temperature model. A catalytic boundary condition was used with an emissivity of 0.85, and NEQAIR was used to calculate plasma radiation.

## 2. Literature Review

**Fahy [77]** The flow field comprised 11 species air calculated in Eilmer3, which utilises the integral form of the Navier-Stokes equations and includes vibrational-electron-electronic energy conservation equations [81]. Both a catalytic and non-catalytic boundary condition were tested with a wall emissivity of 0.9. With the inclusion of a mass flux boundary for the model, a total of 20 gas species were included and Park's 24-reaction scheme [82] was used.

## 2.2. Expansion Tubes

### 2.2.1. Development

The idea of the expansion tube was first proposed by Resler and Boxsom [83], who suggested that the stagnation process and steady expansion could be replaced with an unsteady expansion, which adds energy to the flow without the dissociation which occurs if a shock alone was used [84]. Trimpli [85] performed a theoretical analysis on expansion tubes and found that the Mach number in the test section in the expansion tube far exceeded the Mach number of reflected and non-reflected shock tunnels for the same ratios of  $p_2/p_1$  and  $p_1/p_7$ . The subscripts are explained in fig. 2.11 which is an idealised distance-time diagram for a free piston expansion tube [86]. In fig. 2.11 a shock is driven into the shock tube by the high pressure driver gas after the rupture of the primary diaphragm. This shock adds energy to the test gas until it reaches the secondary diaphragm where, after the diaphragm bursts, the shock processed test gas expands into the acceleration tube, through a nozzle (not shown in fig. 2.11) and into the test section. The useful test time of the facility starts at the arrival of the test gas (subscript 7) and is terminated by either the unsteady expansion arising at the secondary diaphragm or the  $u+a$  characteristic wave, depending on the length of the acceleration tube. Other limitations to useful test time are discussed in this section.

Some early versions of expansion tubes were constructed by NASA at Langley Research Center [87] and NASA Ames Research Center [88]. Jones [87] evaluated the conversion of a shock tunnel into an expansion tube with an unheated hydrogen driver and found that differences between experiment and theory due to viscous effects, diaphragm rupture, finite chemical reaction rates and three-dimensional flow effects were not severe enough to subtract from the performance of the facility. Givens et al. [88] conducted experiments on a combustion-driven expansion tube and was able to generate test times of  $100\mu\text{s}$  at velocities of  $7.5\text{km s}^{-1}$ . The authors identified the test to have unsteady properties, which they attributed to oblique disturbances that arose at the secondary diaphragm (separating the test gas and expansion section). Miller [89] performed experiments in the Langley expansion tube, a 15.24cm diameter tube divided into three section by two diaphragms: the intermediate section (shock tube) 4.66m long and acceleration section (acceleration tube) 16.98m long, and found an acceleration tube fill pressure of 3.2Pa provided the longest test time duration. The optimum shock tube fill pressure was found to be 3.45kPa. Miller also suggested that the range of achievable operating conditions was not

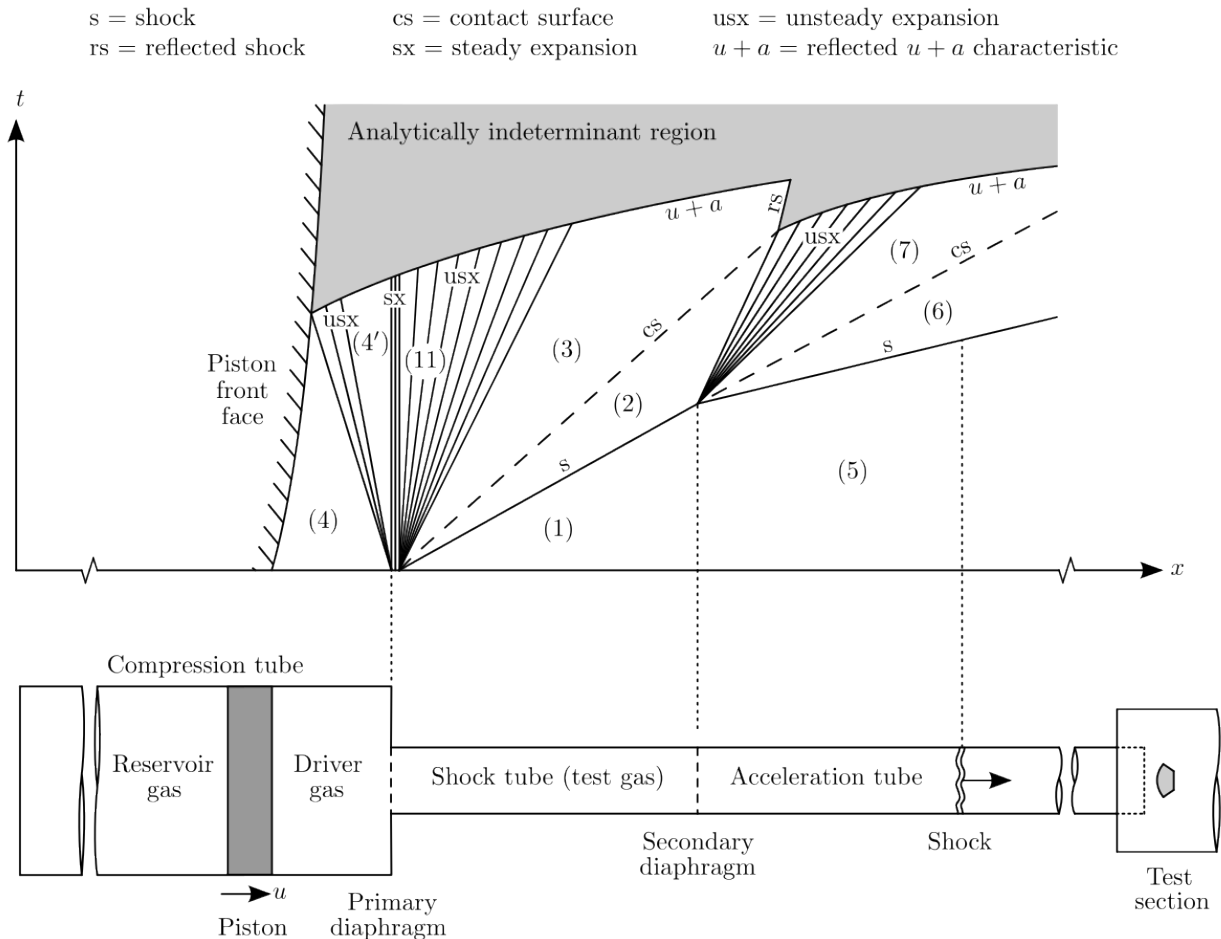


Figure 2.11.: Idealised distance-time diagram of free piston driven expansion tube (taken from [86]).

A nozzle at the end of the acceleration tube is often not used and thus not shown here.

## 2. Literature Review

as large as theoretical analysis suggested, although test times of 200–300 $\mu$ s were sufficient to establish steady flow around blunt test models.

Paull et al. [90] developed a free-piston driven expansion tube at UQ, TQ, and qualitatively compared pitot pressure measurements to those obtained from the Langley expansion tube, and similar features in the pitot pressure trace observed at Langley were repeated at UQ. Paull et al. also explored the use of different driver gases —air, argon and helium—which produced a range of acceptably steady flow conditions with steady test times ranging from 70 $\mu$ s, with an enthalpy of 42MJkg $^{-1}$ , to 200 $\mu$ s, with a test flow enthalpy of 11MJkg $^{-1}$ , although the tested conditions had varying levels of pressure steadiness. Neely et al. [91] further expanded the operational capabilities of the aforementioned expansion tube and measured static wall pressure, pitot pressure and heat transfer to a flat plate. An investigation into test flow disturbances was performed by Paull and Stalker [92] who showed that the test time in expansion tubes could be limited by the expansion wave at the secondary diaphragm, or by disturbances in the driver gas and suggested that driver conditions should be chosen so there is sufficient increase in sound speed from the expanded driver gas to the test gas which serves to inhibit the propagation of acoustic waves into the test gas.

Another deviation from theory is mass entrainment in the boundary layer which was shown by Mirels [93] to reduce the distance between the shock and gas interface in a given section of tube. The phenomena was first observed by Duff [94] in a low pressure shock tube, and contrary to a higher pressure shock tube where the distance between shock and contact surface continually increases, it was found that the distance between shock and contact surface reaches a limiting value and remains constant. The consequence of boundary layer development is a reduction in test time from the ideal case due to the effective shortening of the test gas slug length. Contrary to theory, which states that the gas slug reaches maximum length and remains constant, simulations performed by Gildfind et al. [95] with an extended acceleration tube resulted in the boundary layer engulfing the test gas. Experiments by Toniato [96] with a shortened shock tube in X3 (i.e. longer acceleration tube) obtained results that suggested the boundary layer had completely engulfed the core flow, as pressure measurements were significantly different from those using a shorter shock tube. Ultimately, the effect of mass entrainment in the shock layer serves to reduce the shock speed and the total test gas time.

### 2.2.2. Use of a Secondary Driver

To further increase the performance of expansion tubes, Morgan and Stalker [97] added an extra section of helium gas between the driver tube and shock tube to act as a shock heated secondary driver. Using a secondary driver, Morgan and Stalker were able to operate the tunnel close to its maximum enthalpy simulation and obtain shock speeds up to 18.7km s $^{-1}$  in the acceleration tube. Theoretical work by Paull and Stalker [92] examined the propagation of acoustic waves originating in the driver gas into the test gas and corrupting the quality test flow. They concluded that the transmission of waves into

the test gas could be inhibited if the sound speed of the test gas was higher than the sound speed of the expanded driver gas which required the expanded driver gas to have a higher Mach number. The authors then implied that expansion tubes may only be useful at the high velocity end of its range of operation. For low enthalpy conditions (i.e. scramjet conditions) the sound speed of the test gas is typically lower than the expanded driver gas sound speed [98] which according to Paull and Stalker [92] promotes noise propagation. The implementation of the secondary driver by Morgan and Stalker [97] was done with an increase in sound speed from driver gas to secondary driver gas, and in theory, the inclusion of a secondary driver may inhibit the propagation of acoustic noise originating in the driver gas.

Gildfind et al. [98] conducted a survey of the use of a secondary driver across a wide range of operating conditions in X2 using air as the test gas. Apart from finding that the secondary driver could be used to increase performance, Gildfind et al. also discovered that by adjusting the secondary driver fill pressure they could vary the static of the test gas, effectively increasing the variety of test flows achievable. Additionally, if a reflected shock occurred at the secondary diaphragm (between the secondary driver and shock tube) the performance of the expansion tube would decrease. While they did not purposely examine the use of the secondary driver as an acoustic buffer, they did find that test flows with the secondary driver did have less noise, but the pressure was constantly rising throughout the test time. Toniato [96] performed condition development experiments with and without a secondary driver in X3 and found that the inclusion of a secondary driver provided no improvement and postulated that due to the interface of the secondary driver gas and test gas being under-tailored (test gas sound speed lower than secondary driver gas sound speed), a new source of noise may arise at the secondary diaphragm, which in a large facility like X3 still has significant mass, and massless diaphragm assumptions may no longer be valid.

### 2.2.3. X2

X2, described by Doolan and Morgan [99], originally was designed as a two-stage free-piston driver and two superorbital test flows with air were presented with test times up to  $100\mu\text{s}$ . Typically a free-piston driver employs a large area change at the primary diaphragm which allows for stronger shocks to be driven compared to the driver strength [99] but the cost compared to having a constant area at the primary diaphragm is significantly larger due to the much larger stresses that arise at the area change. Constant area at the primary diaphragm can reduce costs and complexity but the compressed driver gas slug needs to be sufficiently long to delay unsteady expansion waves arriving at the test section and according to Morgan [100] the facility would end up being 3–4 times longer than if an area change was present at the primary diaphragm. Doolan and Morgan [99] compressed the driver gas in two stages: firstly through a larger diameter tube with a compound piston (aluminium carrier with a heavier steel inner piston) before the inner piston completed the compression of the driver gas in a section of tube with smaller diameter. An illustration of the operation of the two-stage

## 2. Literature Review

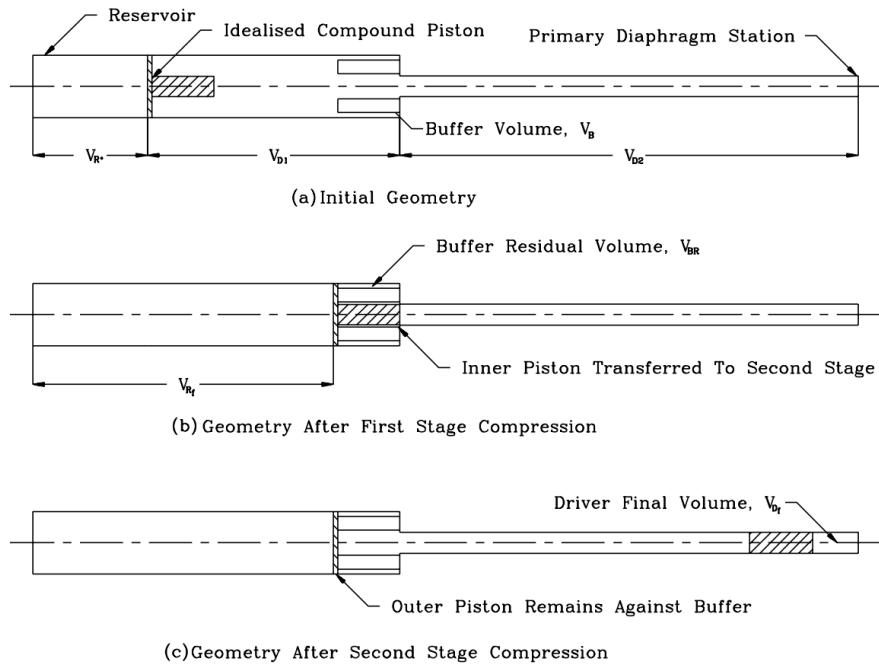


Figure 2.12.: Diagram of the two-stage piston initially used on X2. (a) Initial geometry. (b) After first stage compression in the larger section of compression tube. (c) After second stage compression in the smaller diameter tube.

driver is presented in fig. 2.12: the compound piston travels along the larger diameter tube (volume  $V_{D1}$ ) before the inner piston is transferred to the smaller diameter tube (volume  $V_{D2}$ ) and completes the compression until the driver gas reaches its final compressed volume ( $V_{D_f}$ ).

Early attempts to measure radiation in X2 were performed by Palmer [101], who developed a thin-skin calorimeter heat flux sensor and found there were significant differences between experimental results and theoretical models for the flow conditions used. Palmer et al. [102] measured heat flux using thin-skin calorimeters on a 1:10 scale MUSES-C (Hayabusa) model for two flow conditions with equivalent velocities of  $7\text{km s}^{-1}$  and  $9\text{km s}^{-1}$  with a sufficient level of agreement with numerical models. X2's two-stage free-piston driver was initially a prototype for the much larger X3 facility, and after X3 was commissioned in 2001 [103], X2's free-piston driver was upgraded to a single-stage free-piston driver [104] employing an area change at the primary diaphragm and a 35kg piston. A diagram of X2 and X3 is shown in fig. 2.13 which compares the relative size of the two facilities.

Gildfind [105] further upgraded X2's driver by reducing the weight of the 35kg piston to a mere 10kg to obtain tuned (see chapter 3) operation of the piston and design high Mach number, high total pressure scramjet flow conditions. The result of designing tuned conditions for the 10kg piston was a range of driver operating conditions which have been supplemented with higher sound speed conditions but remain in use today. X2 is now the prominent facility for experimental and measurement techniques and condition development in the Xlabs at UQ, as it is easily operated and has a relatively quick turnaround between experiments. It has lead to the development of a selection of standard operating

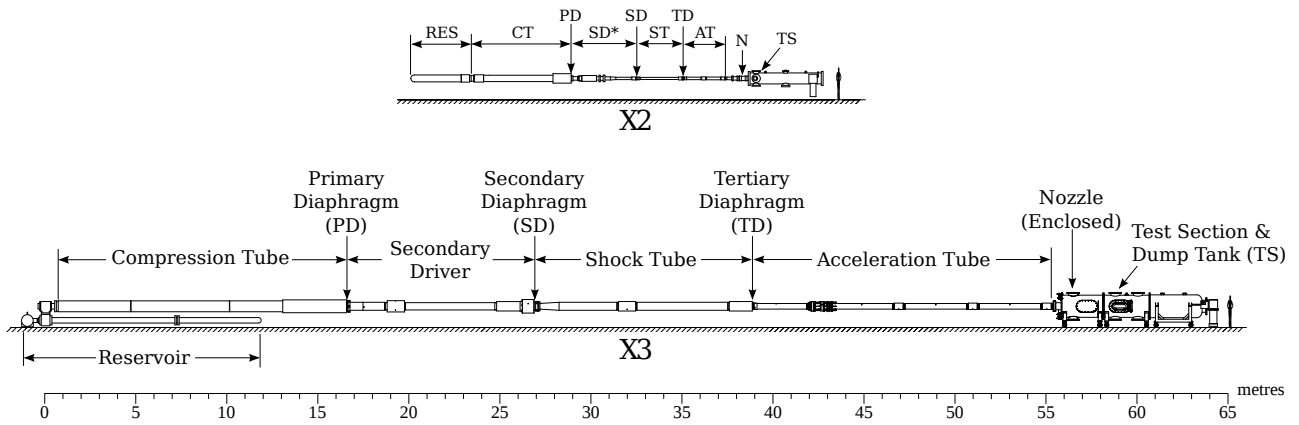


Figure 2.13.: Diagram of X2 and X3 showing relative size and locations of important features.

conditions and significant progress was made in understanding the strengths and limitations of those operating conditions [106, 107]. New conditions can be developed with simple analytical theory [108].

Recent work in X2 has seen the development of conditions to replicate multiple atmospheres in addition to air operating conditions: Mars [109, 110] (work done in [110] was performed by replacing the free-piston driven driver with an unheated fixed-volume driver), Venus [111], Saturn/Uranus [112], Jupiter [113] and Titan [114, 115]. In addition to a variety of operating conditions, a variety of experimental techniques has also been developed: capacity to take vacuum ultraviolet spectra [116], simulating expanding flows [117], heated carbon models to simulate ablations [118, 119], and thermography measurements [120]. Eichmann [121] used the optical setup in fig. 2.14 which is representative of most optical setups used on X2 with experimental and optical considerations being the main cause of optical variation.

## 2.2.4. X3

X3 is the larger of two expansion tubes currently in the Xlabs at UQ and has seen significantly less experimental use when compared to X2, mainly due to the difficulties and cost that come with the operation of a large facility; for example, the need for heavy machinery to perform turnarounds and move sections of the tube. The first experiments performed in X3 were aerodynamic measurements of a model of the Mars Pathfinder [122] and experiments using a radiation gauge on a Fire II and Titan Explorer model [123, 124] were also performed.

Like X2, X3 was originally driven by a two-stage free-piston driver [23] (in fact X2's driver was a prototype for X3's driver) and, like X2, was upgraded to a single-stage free-piston driver (again using X2 as a prototype) with a piston mass of 200kg, an upgrade that made room for an additional diaphragm station [125]. Additionally, other upgrades listed in [125] include the addition of an expansion nozzle to the end of the acceleration tube, which is observed to increase steady test time,

## 2. Literature Review

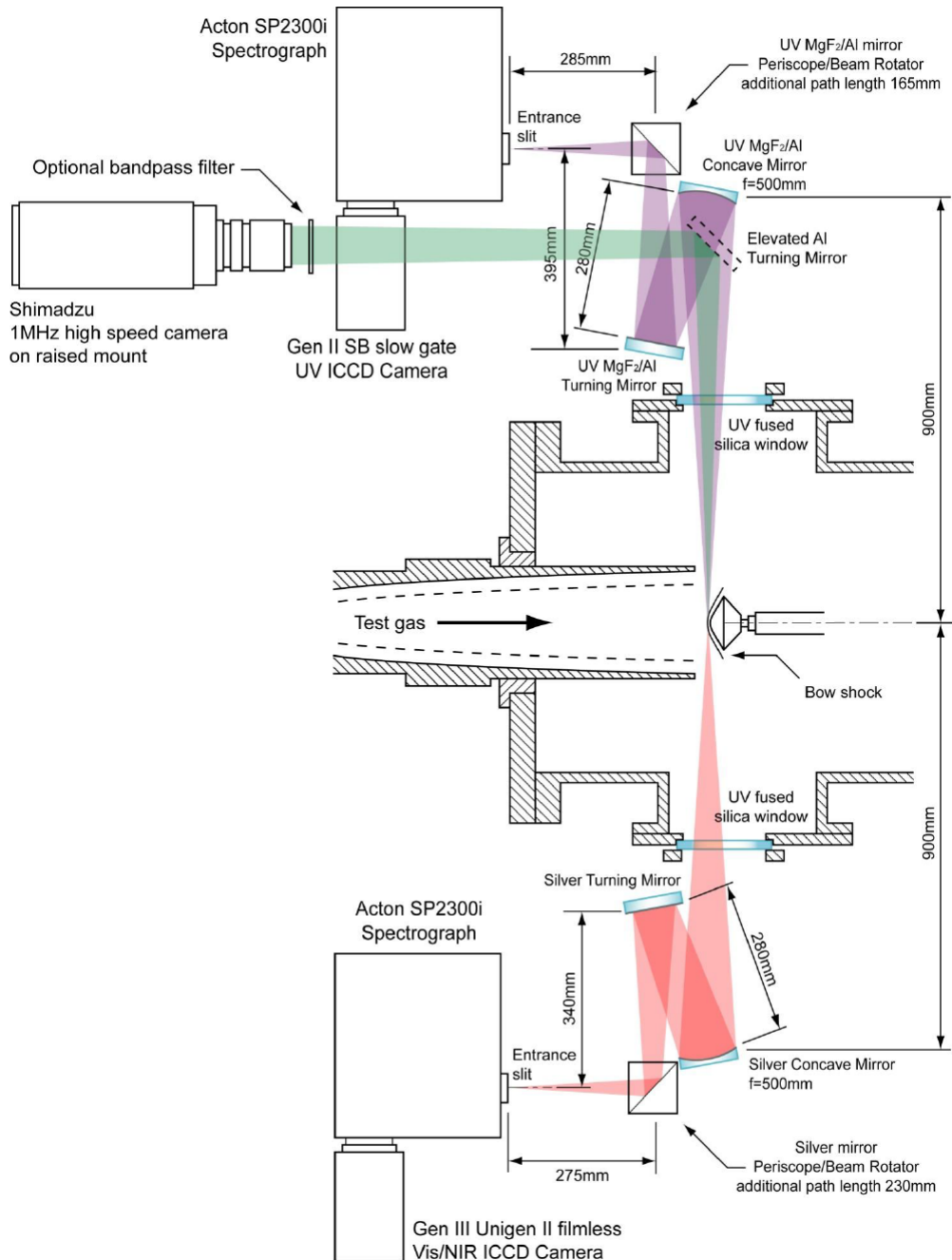


Figure 2.14.: Optical setup used by Eichmann [121] on X2 for a test gas to simulate the Martian atmosphere, which contains typical optical setups used on X2. For this case UV and Vis/NIR spectra are taken through the side windows and high speed video is taken via turning mirror through a window on top of the dump tank.

increases core flow diameter, and mitigates viscous “corruption” of the test gas for low enthalpy true flight scramjet conditions [125]; the addition of the expansion nozzle does come at a cost, reducing density-length scaling capability and a reduction in total pressure/enthalpy multiplication across the unsteady expansion for set Mach number conditions. The first iteration of hypersonic nozzle was a Mach 10 nozzle for X2 designed by Scott [126]. A scaled version of the X2 nozzle was installed on X3 by Davey [127], it was constructed by winding glass fibre coated with an epoxy resin around a mandrel shaped to the nozzle contour, a technique previously used by Jacobs and Stalker [128] for a nozzle on the T4 reflected shock tunnel. A larger test section was also implemented to accommodate the new expansion nozzle and also allows for larger models with increased instrumentation capacity. Recently, Toniato [96] designed a Mach 12 hypersonic nozzle to produce test flows for a Mach 12 scramjet, constructed using a similar method to Davey [127].

After the implementation of the upgrades mentioned in the previous paragraph, a Mach 10 scramjet condition was developed by Gildfind et al. [129] and subsequent Mach 10 scramjet experiments were performed by Sancho [130]. Using the operating conditions and scramjet model from [130], Wheatley [131] applied tunable diode laser absorption spectroscopy to the scramjet nozzle in an attempt to measure water vapour after the combustion process, but although combustion products were detected, the measurements were unable to be used to calculate temperature but with improvements listed by the author it could be used to measure temperature and other flow properties. In the meantime, Gildfind et al. [22] designed a 100kg lightweight piston for X3 with the goal of developing tuned high sound speed driver conditions and performed preliminary blanked off shots and concluded that an extension to the reservoir volume was required to achieve the desired performance of the compression tube. The work performed by Gildfind et al. in [22] leads directly into the contents of chapters 3 and 4 which detail work done towards designing tuned operating conditions for the 100kg lightweight piston with two thicknesses of diaphragm and the performance capabilities of the newly designed driver, which is essential for increasing the capabilities of X3 and obtaining test conditions that can be used for high enthalpy radiating flow experiments.

# 3

---

## X3's Driver

### 3.1. Chapter Overview

This chapter details the analysis and preliminary work performed to arrive at new driver operating conditions that utilise the new lightweight piston and reservoir extension mentioned in section 2.2.4. An overview of the preliminary condition design of the lightweight piston conducted by Gildfind et al. [22] is discussed and used as the baseline for the development of new operating conditions; it is noted that the analysis performed by Gildfind did not include the reservoir extension. For the present analysis, analytical methods were used to scope out a potential operating range. While these methods do not result in final parameters, they present a good first estimate of important parameters used in numerical simulations of the driver. Numerical caluclations were performed in L1d, a one-dimensional Lagrangian solver for simulating unsteady impulse facilities [132]. Initial simulations were run with a blank-off plate (i.e. a non-rupturing diaphragm) installed at the primary diaphragm location and compared to experimental results of the same arrangement, in order to tune and validate the L1d model. After several iterations, numerical calculations arrived at an acceptable reproduction of the pressure trace measured in the compression tube, and the resulting L1d model was used to simulate rupturing diaphragm experiments in chapter 4.

### 3.2. Expansion Tube Layout

A generic layout of the expansion tube is shown in fig. 3.1: high pressure air in the reservoir propels a piston along the compression tube compressing the driver gas until the primary diaphragm (PD) ruptures. The high pressure driver gas drives a shock through the next section of tube, in the case of fig. 3.1 through the secondary driver. Once the shock reaches the secondary diaphragm (SD), the secondary diaphragm bursts and the secondary driver gas drives a shock through the test gas in the shock tube. This process is repeated at the tertiary diaphragm (TD) but the shock processed test gas is expanded into the low pressure acceleration tube via an unsteady expansion, with a further expansion through the nozzle into the test section.

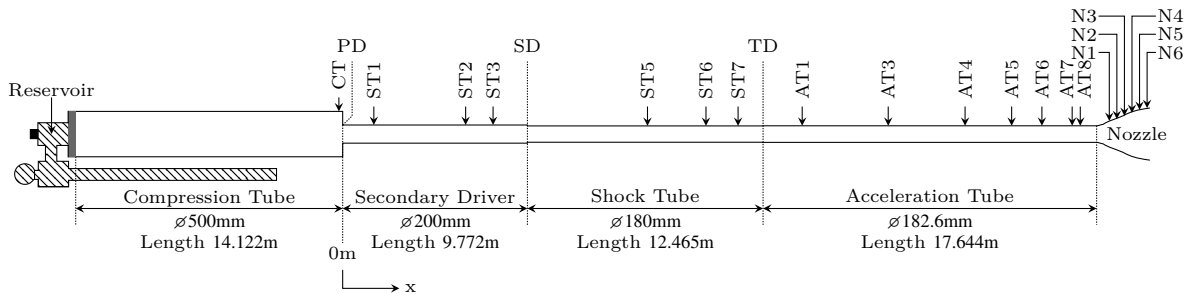


Figure 3.1.: Generic layout of X3 with all current sensors and diaphragm locations at relative positions, the primary diaphragm is located at 0m.

Table 3.1.: Sensor locations

Sensor	Location [m]
CT	-0.201

A common configuration for X3 operation is to remove SD and operate with a shock tube from PD to TD in fig. 3.1. While this chapter does not involve experiments with a rupturing primary diaphragm, explanations of expansion tube processes generally use “shock tube” as the term describing the next section of tube after the compression tube. Analysis in this chapter mostly concerns the reservoir, compression tube and primary diaphragm (or blank-off plate). The primary diaphragm/blank-off plate is said to be at 0m and other features of the tunnel are references from the location of the primary diaphragm. The location of wall pressure sensors used in this chapter is presented in table 3.1 which only consists of CT for this chapter.

### 3.3. X3 Driver Introduction

X3 uses a single-stage free-piston driver to isentropically compress a driver gas, typically a mixture of helium and argon until the gas reaches a high enough pressure to burst the primary diaphragm, driving a shock wave through the next section of tube. The piston itself is driven by a high pressure reservoir of air, which is filled to the order of 1–10 megapascals, and in the case of X3 is operationally limited to 14MPa. One of the challenges of implementing a free-piston driver is ability to maintain quasi-constant driver gas pressure after diaphragm rupture [133], a situation that can be achieved by having a sufficiently high piston velocity at the time of diaphragm rupture (depending on the specific driver condition). With the piston still in motion and if the area ratio between compression tube and driven tube is large [133], the driver gas venting from the compression tube can be compensated by the reduction of volume of the compression tube due to the motion of the piston, thereby maintaining an

### 3. X3's Driver

approximately constant driver gas supply pressure for a longer duration. Additionally, the trajectory of the piston must be designed so it does not strike the end of the compression tube with significant velocity, as with maximum speeds on the order of  $200\text{m s}^{-1}$ , the impact has potential to cause catastrophic damage.

The previous configuration of X3 used a 200kg piston and a reservoir with a volume of 270L (plus the volume of manifolds and connections). Tuning of the 200kg piston was achieved by adding argon to the helium driver and introducing an orifice plate at the driver-shock tube area change [22]. The addition of argon reduced the sound speed of the driver gas, and the orifice plate introduced a steady expansion at the compression tube exit, both of which reduced the performance of the driver. Achieving tuned piston operation with a driver gas with higher sound speed requires faster piston velocities, which in turn requires a lighter piston. This led Gildfind et al. [22] to design a lightweight 100.8kg piston for X3, expanding the potential of X3 and allowing for increased performance and holding times post-rupture. Preliminary blank-off shots found that additional capacity of the reservoir was required, as the maximum pressure rating was not enough to propel the piston to the required speeds, with the previously smaller volume. A reservoir extension was manufactured with a nominal volume of 300L which approximately doubled the total reservoir volume.

A lighter piston allows the reservoir gas to accelerate the piston to higher speeds within the same length of compression tube and allows the compressed driver gas to bring the piston to rest at the end of the compression tube from a higher velocity compared to a heavier piston. The addition of the reservoir extension means the reservoir gas sees a smaller incremental expansion into the volume behind the piston as it is propelled along the compression tube, thereby increasing the pressure behind the piston. The result is that lower reservoir fill pressures are required to match a given condition, effectively expanding the operating envelope of the driver. The inclusion of the new hardware allows for higher concentrations of helium and higher compression ratios (ratio of rupture density to initial density), whilst maintaining tuned operation and a soft landing, which both result in a stronger shock in the driven tube and an increase to the overall performance of the facility.

## 3.4. Previous 200kg Piston

Before exploring the analysis of the lightweight piston, a summary of the 200kg piston used for the Mach 10 scramjet experiments conducted by Sancho [130] and the performance that could be achieved by the 200kg piston are presented. The most commonly used configuration of X3's driver is summarised in table 3.2, which powered the flow conditions for a Mach 10,  $3.5\text{km s}^{-1}$  experiment.

In his work to numerically reproduce the test flow, Gildfind et al. [134] performed L1d simulations of the 200kg piston with the results shown in fig. 3.2. From the pressure traces, it is evident that the diaphragm ruptures at 17.5MPa, which is represented by the change in gradient of the rising

Table 3.2.: Operating parameters for X3's driver using the 200kg piston [130].

Parameter	Value	Units
Reservoir pressure	3.8	MPa
Driver pressure	30	kPa
Helium partial pressure	18	kPa
Argon partial pressure	12	kPa
Rupture pressure	17.5	MPa
Orifice plate diameter	149	mm

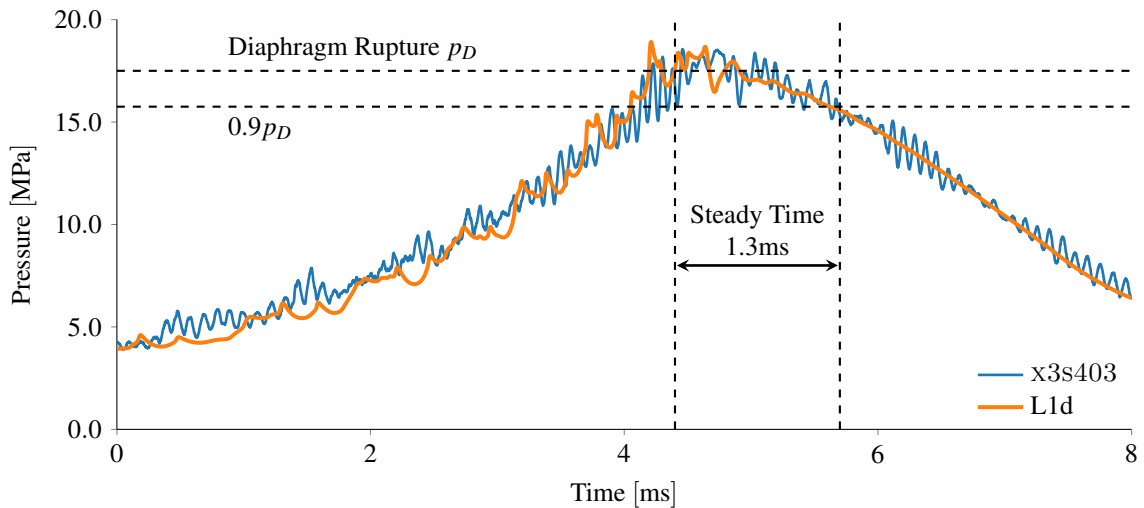


Figure 3.2.: Comparison of experimental driver pressure trace with L1d simulation for the 200kg piston with operating conditions from table 3.2, plot adapted from Gildfind et al. [134]. The Steady Time is said to end once the pressure drops to 90% of the rupture pressure.

pressure. For this case, the driver gas pressure remains approximately constant for a short duration, approximately 1.3ms, before dropping rapidly. According to Itoh et al. [135], one challenge with using a free-piston driver is the reduction in shock tube performance and decrease in test time because of the short duration of the driver condition. By tuning the piston, the driver condition can be help approximately constant for a longer duration mitigating the reduction in shock tube performance. L1d simulations of X2 performed by Gildfind [86] indicated that shock attenuation was due to a reduction in driver pressure. While shock speed attenuation was not an issue for the Mach 10 condition in X3, with the shock speed in the secondary driver only dropping by 5% (approximately  $3150\text{--}3000\text{ m s}^{-1}$  over 10m) [130], the duration of steady pressure in fig. 3.2 could theoretically be increased and potentially improve the overall condition.

The purpose of the L1d simulations done by Gildfind et al. [134] was to characterise test flows downstream of the driver, observing that L1d typically overestimates shock speed, Gildfind reduced

### 3. X3's Driver

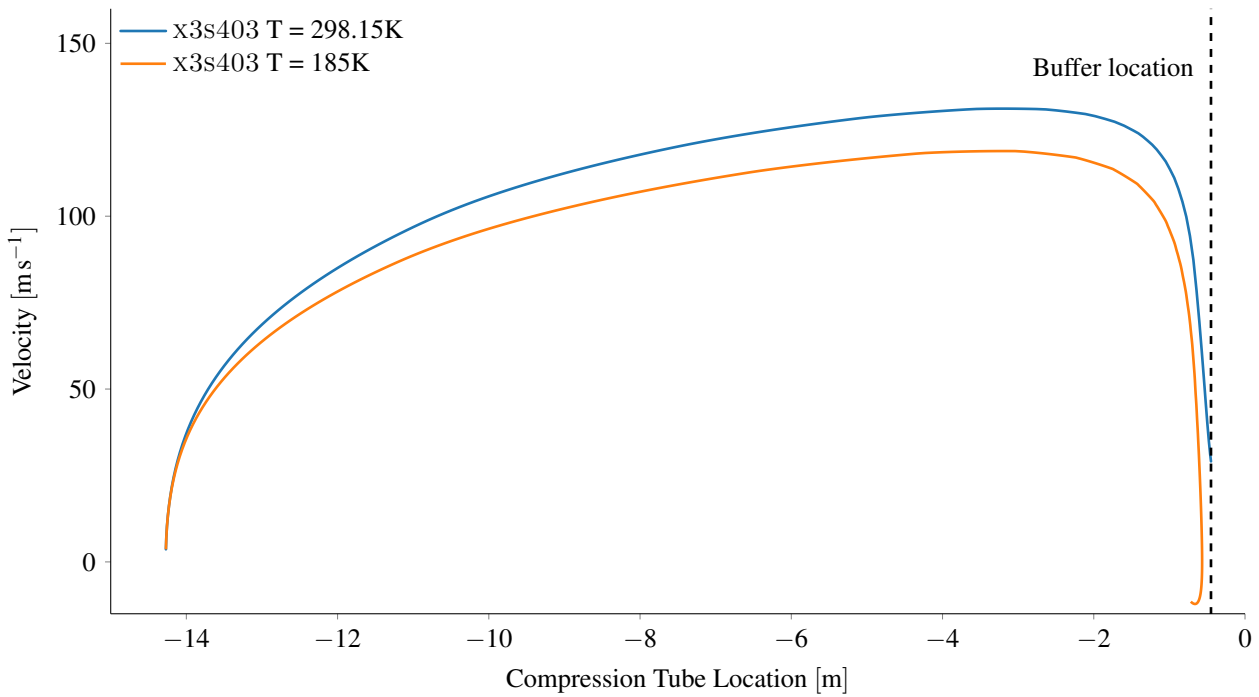


Figure 3.3.: Velocity of the 200kg piston along the length of the compression tube. The piston starts at -14.1m and travels towards the primary diaphragm which is located at 0m, with the nylon buffers to catch the piston, which are indicated by the black dashed line, located at -0.2m. Piston trajectories are taken from work done by Gildfind et al. [134].

the driver gas fill temperature from 298.15K to 185K (effectively scaling sound speed at diaphragm rupture) and in this case was able to match shock speeds and pressures in the shock tube (the condition uses a secondary driver before the shock tube and the comparison of wall sensors in the secondary driver was not presented). While this method worked well for downstream processes, it changes the piston dynamics, as the lower temperatures in the simulation results in a lower piston speed. The piston trajectories of both simulations are shown in fig. 3.3. Considering both initial driver gas temperatures, neither results in a soft landing at the buffers, although the downstream analytical results show good agreement with the experimental measurements presented in [134]. The 185K driver gas trajectory shows the piston beginning to rebound due to the driver gas not venting out of the compression tube fast enough, whereas the 298.15K has the piston striking the buffers. However, during experiments there was no apparent damage to the buffers, so the results of either L1d are most likely not capturing the true trajectory. During the rework of the L1d model (section 3.7), it was found that the reservoir geometry used by Gildfind et al. [134] was incorrectly specified but didn't affect the study as the application of a loss factor at the piston launcher compensated for the extra volume of the reservoir. The application of a loss factor allowed the driver pressure to be reproduced, fig. 3.2, but not the piston trajectory, fig. 3.3. The present study, there is a need for the L1d model to accurately predict the piston trajectory which requires the geometry of the X3's reservoir to be carefully specified.

## 3.5. Analytical Methods

Several analytical methods have been developed to calculate the operation and performance of the free-piston driver. Two methods are covered within this section, one developed by Stalker [133] and the other developed by Hornung [136]. While neither method can completely and accurately predict the entire trajectory of the piston due to necessary simplifying assumptions, both give useful information of parameters and general trends which can be considered when performing the numerical calculations and can be sufficient for design purposes. Stalker [133] equated the work required to expel the driver gas to the kinetic energy of the piston at the moment of diaphragm rupture under the assumption of constant conditions in the driver, before arriving at a pressure trace for the driver gas. Hornung [136] calculates transiently the pressure acting on both faces of the piston with a method that can be iterated over time resulting in piston trajectory and transient driver pressure.

### 3.5.1. Stalker's Method

This section will outline the methodology developed by Stalker [133] to estimate the trajectory of the piston and performance of the driver. Stalker starts by equating the mass flow out of the compression tube with the volume change in the compression tube due to the motion of the piston, both at the time of diaphragm rupture, see eq. (3.1). Here  $\rho$  and  $V$  are the density and volume of the gas in the compression tube;  $\rho_*$  and  $a_*$  are the density and speed of sound of the gas flowing out of the compression tube and  $A_*$  is the cross-sectional area of the driven tube (i.e. shock tube);  $U$  is the velocity of the piston to match the gas venting out of the compression tube and  $A$  is the area of the compression tube respectively.

$$\frac{d(\rho V)}{dt} = -\rho_* a_* A_* = -\rho U A \quad (3.1)$$

The analysis Stalker performs is concerned with the period of time where the driver conditions are approximately constant and an approximate solution to eq. (3.1) can be found by setting the piston speed such that the mass of gas swept by the piston matches the driver gas mass loss from the compression tube ( $U = U_r$ ). The rate of change of piston velocity  $du/dt$  can be defined by the pressure difference across the two piston faces

$$\frac{du}{dt} = -\frac{P_r - P_b}{\sigma} \quad (3.2)$$

where  $P_r$  is the driver pressure at rupture acting on the front piston face,  $P_b$  is the reservoir pressure acting on the rear face and  $\sigma$  is the piston mass per area. Stalker uses the equality in eq. (3.3) which equates the work done to the piston as it expels the remainder of the driver gas assuming it is at constant

### 3. X3's Driver

pressure, with the kinetic energy of the piston at the moment of diaphragm rupture factored by by “ $k$ ”. For values of  $k > 0.5$  he finds the result in eq. (3.4).

$$(p_r - p_b)V_r = k\sigma A u_r^2 \quad (3.3)$$

$$\frac{\rho}{\rho_r} = \frac{1}{(1-z+0.5kz^2)} \times \exp \left[ \frac{-2}{\sqrt{2k-1}} \left( \arctan \left( \frac{kz-1}{\sqrt{2k-1}} \right) - \arctan \left( \frac{-1}{\sqrt{2k-1}} \right) \right) \right] \quad (3.4)$$

Equation (3.4) defines the density of the compression tube gas normalised by the gas density at the point of diaphragm rupture as a function of  $k$  and  $z$ , where

$$z = tA \frac{u_r}{V_r} = \frac{u_r}{x_r} t \quad (3.5)$$

$$\frac{x}{x_r} = \frac{k}{2} z^2 - z + 1 \quad (3.6)$$

$$\frac{u}{U_r} = 1 - kz \quad (3.7)$$

In eq. (3.5), eq. (3.6) and eq. (3.7) subscript  $r$  refers to the conditions at diaphragm rupture,  $u$  is piston velocity,  $V$  is driver gas volume and  $x$  is location of the piston’s front face. Stalker determined that by selecting values of  $k > 1$ , and ensuring the piston velocity matches the mass flow out of the compression tube, the piston should not strike the end of the compression tube [133]. For the case when the piston velocity is faster than required to match the flow out of the compression tube ( $u_r > U_r$ ), the piston will not strike the end of the compression tube since at the point in time when the piston velocity matches the gas flow (i.e  $u = U_r$ ), the solution requires that the work done by the piston to the remainder of the driver gas equals the pistons kinetic energy factored by  $k$  (i.e. the left side of eq. (3.3) is greater than the right side). Performing a similar analysis to Gildfind [86], setting  $k$  equal to 1, the pressure in the compression tube normalized by the maximum pressure is plotted against the dimensionless variable  $z$  in fig. 3.4. The condition where the density is a maximum is set at nondimensional time  $z = 0$  and denominated by the subscript  $r$ . As this is the maximum pressure, diaphragm rupture must occur either at  $z = 0$  or at some point in time prior to this,  $z < 0$ .

Itoh et al. [135] introduce an overdrive parameter  $\beta$  which is the ratio of piston velocity at diaphragm rupture and required piston velocity to match gas out flow (i.e.  $\beta = 1$  means the piston velocity matches the gas outflow at the time of diaphragm rupture). Itoh suggests that the permissible pressure variation of the driver gas after diaphragm rupture should be limited to  $\pm 10\%$  and values of  $\beta$  with this limitation are typically in the range 1.2–1.6. Figure 3.4 has been annotated to show the 10% pressure increase by selecting the point of diaphragm rupture to occur at  $z \approx -0.4$  and the duration of useful driver pressure lasts until  $z \approx 0.45$  where the pressure drops to 10% below the rupture pressure. The velocity of the piston at the “rupture” condition can be solved via a mass balance at the exit of the compression tube for a given diaphragm rupture pressure and compression ratio  $\lambda$ , which is defined as the ratio of driver

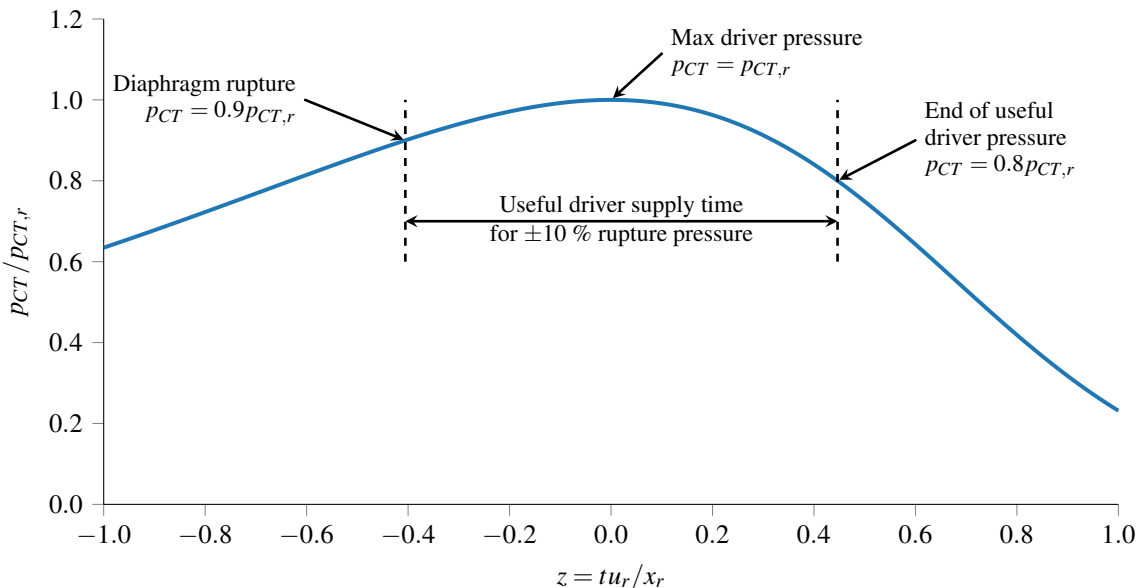


Figure 3.4.: Compression tube (CT) pressure normalised by the “rupture” condition pressure plotted against nondimensional time  $z$ , a result of the Stalker methodology.

gas density at diaphragm rupture to initial driver gas density. The actual piston velocity at rupture can be found by solving eq. (3.7) at the desired nondimensional time  $z$ . Once the target piston speed at rupture is known, the trajectory of the piston can be iterated with time, assuming a steady expansion of the reservoir gas acts on the piston’s back face and the driver gas pressure increases isentropically as the compression tube volume decreases. The piston trajectory can be solved for multiple piston masses until the velocity at diaphragm rupture for a given compression ratio matches the velocity calculated from eq. (3.4).

For this process, the driver dimensions, driver gas composition and diaphragm rtpure pressure have been specified, and the compression ratio varied across a range of values. The results of solving Stalker’s methodology are shown in fig. 3.5, with numerical values in table 3.3 for helium concentrations of 0%, 75%, 85%, 100% for the driver gas, the balance of the driver gas being argon, and for the rupture pressures of diaphragms available at the time of analysis. The grey lines indicate usable compression ratios for the lightweight piston based on the analysis. The 100% argon (0% helium) case results in the largest variation of compression ratio across rupture pressures with a compression ratio of 67 for the 35MPa rupture pressure and 43 for the 17.5MPa rupture pressure. The range of compression ratios decrease as helium is added to the driver gas mixture, with compression ratios of 13 and 15 respectively for the 26.3MPa and 35MPa rupture pressures for 100% helium (the compression ratio for a rupture pressure of 17.5MPa would be even lower). These compression ratios are low enough that increase in sound speed of the compressed driver gas from the additional helium concentration is counteracted by the small compression ratio. By using an orifice plate at the exit of the compression tube, the concentration of helium in the driver gas can be increased without a reduction in compression ratio because of the orifice reduced the compression tube exit area and throttles the mass flow of the gas leaving the compression tube. The effect of increasing helium concentration with and without

### 3. X3's Driver

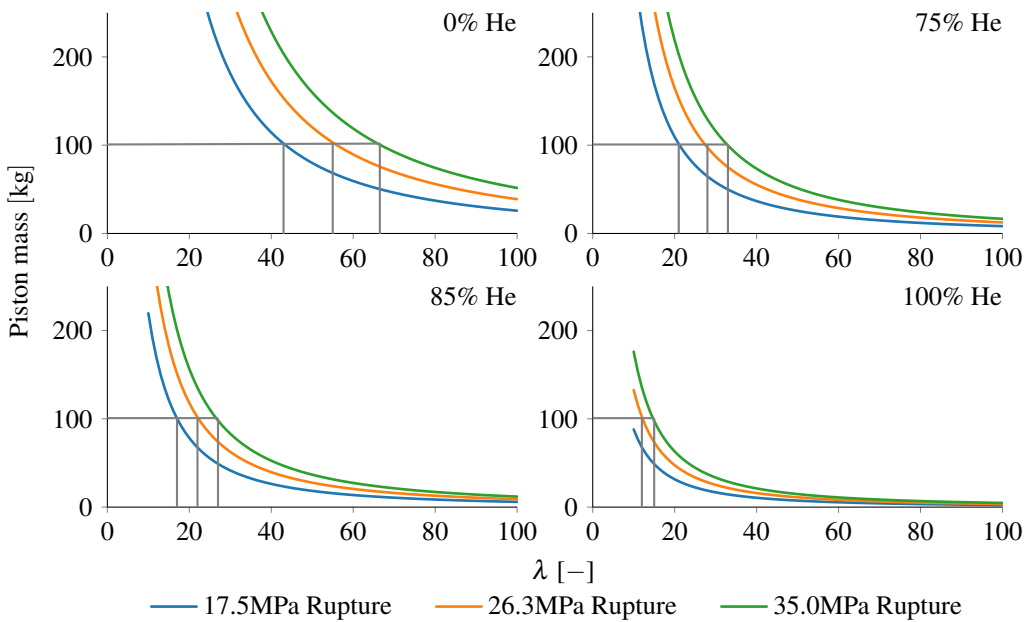


Figure 3.5.: Compression ratio for the nominal rupture pressures of available diaphragms for X3's lightweight piston mass of 100.8kg.

Table 3.3.: Compression ratios for tuned piston operation for nominal rupture pressures dervied from Stalker's method.

Helium Concentration [%]	Rupture Pressure		
	17.5MPa	26.3MPa	35.0MPa
0	43	55	66
75	21	28	33
85	17	22	27
100	—	15	12

an orifice plate is examined in more detail using Hornung's method in section 3.5.2. Regardless, the results from Stalker's methodology still present a reasonable estimate to the final operating conditions of the lightweight piston in X3's compression tube.

#### 3.5.2. Hornung's Method

As with the Stalker analysis, the methodology outlined by Hornung [136] provides a simple analytical method to calculate the piston trajectory. Unlike the Stalker methodology which equates the piston's energy with the work required to expel the driver gas from the compression tube, Hornung's method involves calculating full piston dynamics. The application of Hornung's method used here is the same as that used by Gildfind [86], which takes equations of motion derived during the formulation

of Hornung's method and iterating over the stroke of the piston. The equations used in the iterative application of Hornung's method are discussed in this section. Assumptions made by Hornung [136] in the formation of his methodology are as follows:

- The seals on the piston are perfect and it moves along the tube without friction.
- For helium as a driver gas, a piston speed of  $300\text{ms}^{-1}$  is still relatively subsonic and no waves are formed due to the piston motion, although this assumption is less valid for high levels of argon in the driver gas.
- Flow effects arising from the interaction between the piston and the tube wall are ignored.
- An infinite length inline reservoir is assumed so expansion waves generated by the piston acceleration are not reflected back to the piston.
- The piston deceleration after diaphragm rupture is significant such that an upstream-running reflected shock forms off the rear face of the piston assuming it stops instantaneously.
- The diaphragm rupture occurs instantaneously.
- An inertial reference frame is assumed, so any potential recoil of the compression tube is ignored.

The model developed by Hornung divides the trajectory into two parts, before and after diaphragm rupture and this section will cover the analysis of each separately.

### Before Diaphragm Rupture

Throughout this analysis, the subscripts  $D$ ,  $R$  and  $0$  correspond to the driver gas, reservoir gas and the initial gas conditions before piston launch. The pressure acting on the upstream side of the piston can be calculated via an unsteady expansion in eq. (3.8), where  $u$  is the velocity of the piston

$$p_R = p_{R0} \left( 1 - \frac{\gamma_R - 1}{2} \frac{u}{a_{R0}} \right)^{\frac{2\gamma_R}{\gamma_R - 1}} \quad (3.8)$$

The pressure acting on the downstream face of the piston is calculated in eq. (3.9) by performing an isentropic compression of the driver gas, where  $L$  is the length of the compression tube and  $x$  is the distance between the piston and diaphragm

$$p_D = p_{D0} \left( \frac{x}{L} \right)^{-\gamma_D} \quad (3.9)$$

Equation (3.8) and eq. (3.9) can be used to formulate an equation of motion of the piston in eq. (3.10).  $M$  is the mass of the piston and  $D$  is the diameter of the compression tube.

$$-M \frac{d^2x}{dt^2} = \frac{\pi D^2}{4} \left[ p_{R0} \left( 1 - \frac{\gamma_R - 1}{2} \frac{u}{a_{R0}} \right)^{\frac{2\gamma_R}{\gamma_R - 1}} - p_{D0} \left( \frac{L}{x} \right)^{\gamma_D} \right] \quad (3.10)$$

### After Diaphragm Rupture

Hornung [136] calculates the pressure on the upstream side of the piston after diaphragm rupture by assuming that the deceleration of the piston is instantaneous and a shock forms, the piston is then exposed to the shock processed reservoir gas. If the piston acceleration and the reservoir sound speed are known, the distance the shock forms behind the piston can be calculated [136]. Using the conditions at diaphragm rupture and knowledge of the initial sound speed, the Mach number ( $M_r$ ) of the shock behind the piston can be calculated by solving eq. (3.11).

$$M_r^2 - \frac{(\gamma_R + 1)u_r/a_{R_0}}{2 + (\gamma_R - 1)u_r/a_{R_0}} M_r - 1 = 0 \quad (3.11)$$

The normal shock relation in eq. (3.12) can be used with the Mach number calculated in eq. (3.11) to find the pressure acting on the upstream face of the piston,  $u_r$  is the velocity of the piston at diaphragm rupture.

$$p_R = p_{R_0} \left[ 1 - \left( \frac{\gamma_R - 1}{2} \right) \frac{u_r}{a_{R_0}} \right]^{\frac{2\gamma_R}{\gamma_R - 1}} \left[ 1 + \frac{2\gamma_R}{\gamma_R + 1} (M_r^2 - 1) \right] \quad (3.12)$$

For the downstream face of the piston, the flow of driver gas out of the compression tube needs to be considered. It is assumed that the exit of the compression tube acts as a sonic throat for the gas. The mass flow rate of driver gas still contained in the driver can be calculated in eq. (3.13) where  $m$  is the mass of driver gas in the compression tube and  $d$  is the diameter of the compression tube exit.

$$\frac{dm}{dt} = -\rho_D \sqrt{\gamma_D p_D / \rho_D} \left( \frac{2}{\gamma_D + 1} \right)^{\frac{\gamma_D + 1}{2(\gamma_D + 1)}} \frac{\pi d^2}{4} \quad (3.13)$$

Isentropic relations can be used to relate the driver gas density to the initial pressure and the remaining volume in the compression tube. The density of the driver gas can be found using eq. (3.14), and isentropic relations can be used to find the driver gas pressure relative to the pressure at diaphragm rupture, in eq. (3.15) subscript  $r$  refers to the gas conditions when the diaphragm ruptures. The substitution of eq. (3.15) into eq. (3.13) results in a relation to calculate the rate of change of the driver gas mass in eq. (3.16).

$$\rho_D = \frac{4m}{\pi D^2 x} \quad (3.14)$$

$$\frac{p_D}{p_{D_r}} = \left( \frac{x_r}{m_r} \right)^{\gamma_D} \left( \frac{m}{x} \right)^{\gamma_D} \quad (3.15)$$

$$\frac{dm}{dt} = -\frac{\sqrt{\pi\gamma_D}}{2} \left( \frac{2}{\gamma_D + 1} \right)^{\frac{\gamma_D + 1}{2(\gamma_D - 1)}} \frac{d^2}{D^2} \sqrt{p_{D_r}} \left( \frac{x_r}{m_r} \right)^{\frac{\gamma_D}{2}} \left( \frac{m}{x} \right)^{\frac{\gamma_D + 1}{2}} \quad (3.16)$$

The change of driver gas mass in eq. (3.16) can update the mass term in eq. (3.15) which can be rearranged to obtain a pressure acting on the downstream face of the piston. Finding the pressure difference across the piston using eq. (3.12) and eq. (3.15), the acceleration of the piston after diaphragm ruptures can be determined from eq. (3.17).

$$\frac{d^2x}{dt^2} = \left[ p_{D_r} \left( \frac{x_r}{m_r} \right)^{\gamma_D} \left( \frac{m}{x} \right)^{\gamma_D} - p_R \right] \frac{\pi D^2}{4M} \quad (3.17)$$

## Summary

Using eq. (3.10) and eq. (3.17), the entire trajectory of the piston can be calculated by iterating with time. The nature of the assumptions made by Hornung [136] means results from the analysis are limited in their use, especially regarding reservoir properties, and to a lesser extent, early stages of the piston trajectory. What Hornung's analysis does reasonably well, is predict the trajectory after diaphragm rupture; at this point the pressure in the compression tube is at least an order of magnitude higher than the pressure acting on the upstream face of the piston, so any error in the reservoir gas processing will not result in significant error for the calculation of the remaining trajectory. A detailed overview of the results obtained from using Hornung's methodology is presented in section 3.6.1.

## 3.6. Lightweight Piston - Analytical Results

This section looks in more detail at the analytical results from Hornung's methodology. A result of the analysis will be a range of the potential operating conditions and an idea of the trends that arise as different parameters are varied. As the piston mass and tube dimensions are fixed, this leaves reservoir pressure, compression tube pressure, driver gas composition and orifice plate diameter as the remaining variables. While the goal of this chapter is to design a driver that can produce high enthalpy radiation flows, the output of the analysis was the development of a large range of potential driver conditions.

### 3.6.1. Analytical Analysis

The result of Stalker's analysis was that for the mass of the lightweight piston, compression ratios were found for a range of diaphragm rupture pressures and different helium compositions, see table 3.4. Using the compression ratios determined in fig. 3.5, the piston velocity at diaphragm rupture as well as initial compression tube fill pressure can also be calculated. Figure 3.6 shows the velocity the piston

### 3. X3's Driver

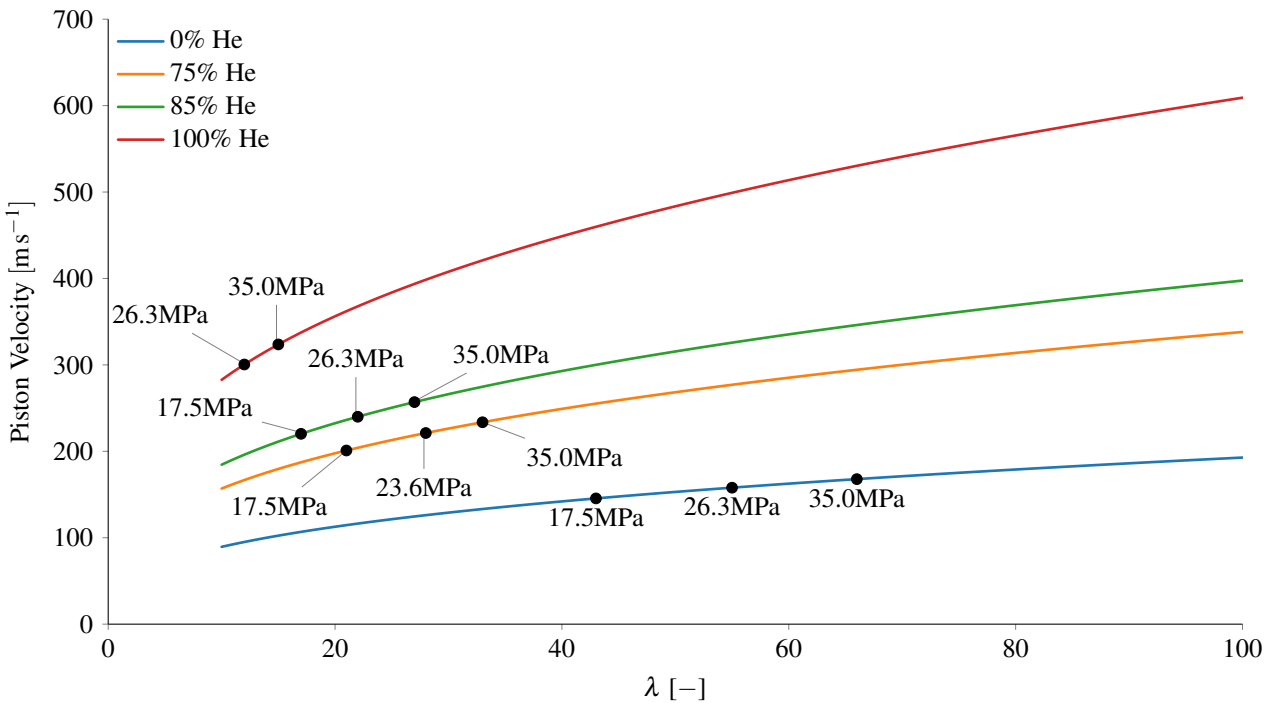


Figure 3.6.: Piston velocity at rupture to match the gas outflow from the compression tube for various helium concentration of the driver gas. The black marks correspond to the compression ratios found in fig. 3.5 for the mass of the lightweight piston. The corresponding rupture pressure of each point is labelled.

must be travelling at the moment of diaphragm rupture to satisfy the Stalker condition for different helium concentration in the compression tube. The marked compression ratios from each subplot in fig. 3.5 are shown in fig. 3.6 and the piston velocities for each rupture pressure along with the driver gas initial fill pressures are shown in table 3.4. The general trend is that for higher concentrations of helium, the driver gas fill pressure increases (significantly at high concentrations) and the compression ratio decreases, to conserve the soft landing condition of the piston. Interestingly, the driver fill pressures do not change much as the diaphragm rupture pressure increases for constant levels of helium; rather the compression ratio increases.

A study of the piston's trajectory was performed using Hornung's methodology [136], which is outlined in section 3.5.2. The analysis was performed to obtain a range of driver operating conditions for the three rupture pressures: the level of pressure overdrive after rupture was varied, as were the concentrations of helium and argon in the driver gas. As alluded to earlier, the reservoir pressure output from Hornung's methodology is not representative of the actual value and will be ignored, but the initial driver pressure and the piston dynamics after diaphragm rupture are comparable to more detailed numerical methods. The analysis process for a rupture pressure of 17.5MPa will be explained in this section but the final results will include data for rupture pressure of 26.3MPa and 35.0MPa (2, 3 and 4mm thick diaphragm thicknesses respectively).

Table 3.4.: Summary of results from Stalker analysis

Helium %	17.5MPa			26.3MPa			35.0MPa		
	$\lambda$	$p_{D_0}$ [kPa]	$u_r$ $[m s^{-1}]$	$\lambda$	$p_{D_0}$ [kPa]	$u_r$ $[m s^{-1}]$	$\lambda$	$p_{D_0}$ [kPa]	$u_r$ $[m s^{-1}]$
	[-]	[–]	[–]	[-]	[–]	[–]	[-]	[–]	[–]
0	43	33.2	145.5	55	33.1	157.9	66	32.5	167.8
75	21	109.5	201.0	28	102.1	221.2	33	103.1	233.6
85	17	155.7	220.2	22	152.6	240.0	27	144.0	256.0
100	—	—	—	15	288.9	323.7	12	556.5	300.5

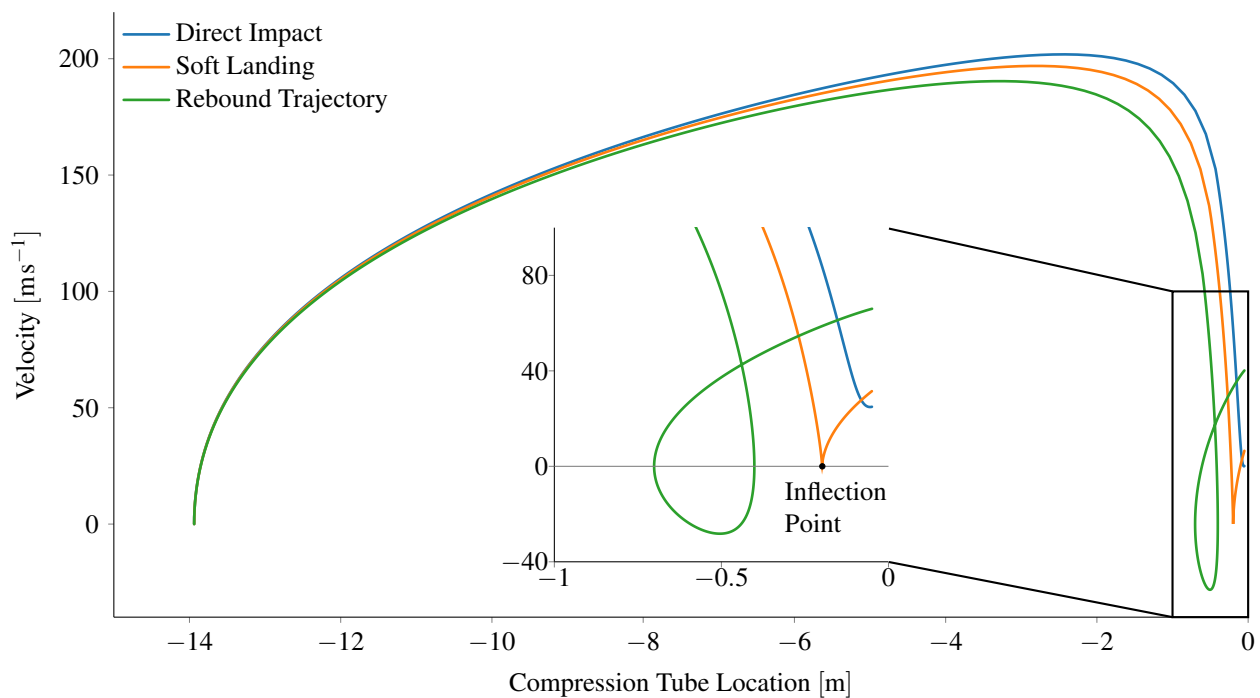


Figure 3.7.: Example of the three possible piston trajectories. The inflection point for the soft landing trajectory has been indicated.

As the main output of this part of the analysis is the piston trajectory, constraints must be applied to determine a suitable trajectory. The constraints were set such that the piston's trajectory has an inflection point, a point after diaphragm rupture where both the piston's velocity and acceleration are zero; this concept is explained in further detail by Gildfind [86] and Itoh et al. [135]. For this to occur, the parameters of the model must be set such that once the high pressure driver gas brings the piston to rest, it is not so high that it pushes the piston back upstream, but rather the reservoir gas behind the piston pushes the piston downstream again. If an inflection point is achieved, buffers (typically constructed of nylon in X2 and X3), can be sized so the piston comes to rest against the buffers at the inflection point. If the piston does not have an inflection point, the consequences are either a direct impact with the end of the tube, or the piston rebounding before accelerating downstream into the

### 3. X3's Driver

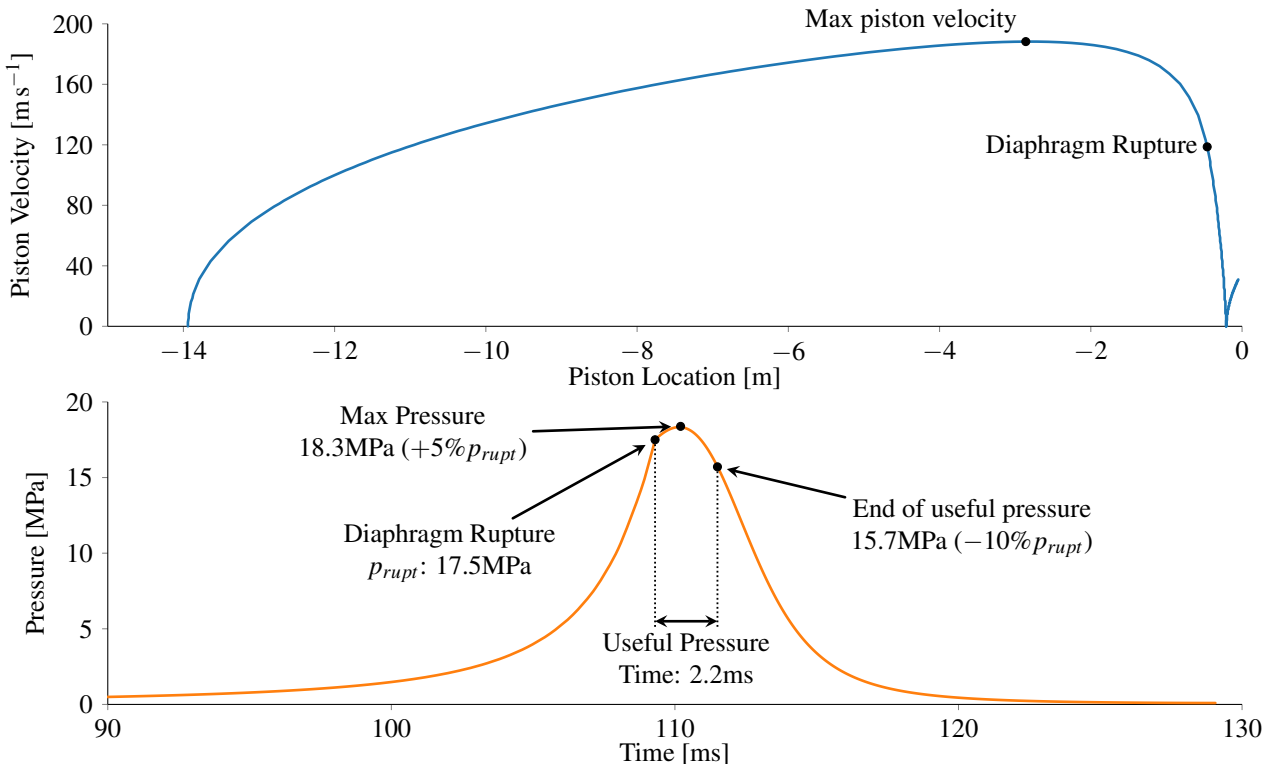


Figure 3.8.: Top: Piston trajectory satisfying the soft landing condition calculated using Hornung's methodology [136] for a diaphragm that ruptures at 17.5MPa. Bottom: Corresponding driver gas pressure for this condition. Also indicated is the maximum pressure and the minimum pressure to satisfy the  $\pm 10\%$  pressure variation threshold, with the time of useful driver pressure totalling 2.3ms.

end of the compression tube. The different piston trajectories are shown in fig. 3.7; although the soft landing trajectory continues after the inflection point, buffers sized to the distance of the inflection point can be implemented.

To obtain trajectories with inflection points, the minimum velocity of the piston after diaphragm rupture must be constrained to zero. A second constraint applied was the degree of pressure overdrive which also has feedback effects on the piston trajectory and therefore the initial fill conditions. An example of a piston trajectory and pressure trace in the compression tube is presented in fig. 3.8 for a diaphragm that ruptures at 17.5MPa. For this case the pressure overdrive is 5% and the total supply time at a useful driver pressure is approximately 2.3ms. The compression tube fill pressure is 59.6kPa of argon and the top image in fig. 3.8 shows that for a reservoir pressure of 1.85MPa, the piston will have a soft landing. Realistically, a reservoir pressure of 1.85MPa will not be appropriate, as it does not account for the finite volume of the reservoir and losses throughout the system, but the driver gas fill pressure itself can be used as an approximate reliable solution.

The preliminary Hornung analysis results for a rupture pressure of 17.5MPa are shown in fig. 3.9 for a range of parameters: each result represents a driver operating condition with a diaphragm burst pressure

of 17.5MPa, specified pressure overdrive and a soft piston landing using X3's 100.8kg lightweight piston. The general trends show that for high helium concentrations the required initial pressure of the driver gas increases exponentially, which agrees with the analysis using Stalker's methodology. The piston velocity at diaphragm rupture also steadily increases with increasing helium concentration, although the overall change is not significant. The time of useful driver supply pressure increases as expected with increasing overdrive, but also increases at high helium concentrations due to the constraints applied to the model which result in lower compression ratios and physically move driver gas volume at the time of daphram rupture. One feature regarding facility performance is that with increased overdrive, the shock speed and thus performance of the driver decreases, again a factor of the reduced compression ratio. The effect of compression ratio is also seen by the small shock speed increase with increased amounts of helium in the driver gas, as the increase in sound speed by having a lighter gas is mitigated by the reduction in temperature due to less compression of the driver gas. This is further illustrated by the decrease in shock speed in fig. 3.9 (d) for 80% helium; thus decrease is suspected to be due to the performance dropping due to reduced compression ratio outweighing the benefit of increasing the helium concentration. At helium concentrations higher than 80%, the piston trajectory found with Hornung's methodology that satisfied the soft landing and overdrive requirements were not feasible solutions (e.g. compression tube was filled to near rupture pressure), and are therefore not shown in fig. 3.9.

While there is some variance in the results between the anaylsis using Stalker's methodology and Hornung's methodology, the overall trends are the same. Both sets of results show a reduction in pressure ratio with increased helium, but the decrease in compression ratio negates the benefit of increased helium concentration. The analysis so far has assumed that the area of the compression tube reduced down to that of the shock tube; an alternative configuration involves using an orifice plate at the compression tube exit to further limit the mass flow rate of driver gas [137] and is typically used to assist in achieving a soft landing for driver gases with higher sound speed. If the volumetric flow rate of the gas exiting the compression tube is considered, it is the product of area and speed of sound of the gas assuming the flow is sonic at the exit. If the ratio of specific heats and gas temperature remain constant, the volumetric flow rate is dependant on the product of exit area and square root of the gas constant, see eq. (3.18).

$$\frac{dV}{dt} = \frac{\dot{m}}{\rho} = A^* u^* = \sqrt{\gamma T} \times A^* \sqrt{R} \quad (3.18)$$

$$\left( \frac{D_2}{D_1} \right)^2 = \frac{A_2}{A_1} = \sqrt{\frac{R_{D,1}}{R_{D,2}}} \quad (3.19)$$

Argon and helium have the same ratio of specific heats, thus adding helium to the driver gas mixture requires the exit area of the compression tube to be scaled by the ratio displayed in eq. (3.19), which allows the same reservoir and compression tube fill pressures to be used for multiple gas mixtures, as

### 3. X3's Driver

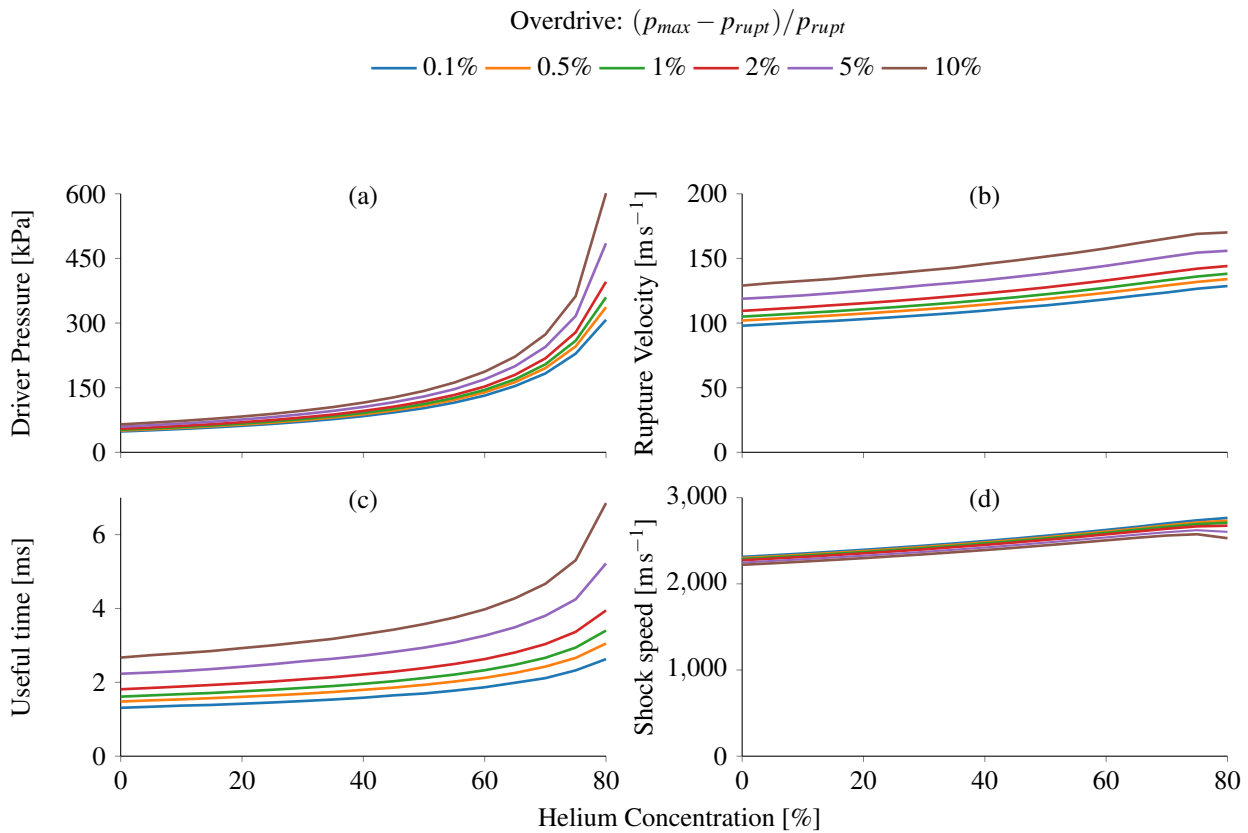


Figure 3.9.: Results from applying Hornung's methodology to a range of helium concentrations and compression tube overdrive percentages (which is defined as the ratio of the instantaneous driver pressure above the rupture pressure) and obtaining facility operation parameters for soft landing operation. The plots show the variation in; (a) required driver gas fill pressure, (b) piston velocity at diaphragm rupture, (c) the duration of useful driver time, (d) shock speed in 13.5kPa air estimated using PITOT [108]. Piston trajectories for more than 80% helium are not shown.

long as the correctly sized orifice plate is available. If a soft landing condition is obtained for a driver gas with a low gas constant (such as 100% argon), helium which has the same ratio of specific heats can be added to the gas mixture, thereby increasing the gas constant, and the orifice plate area must be scaled downward according to the square root of the inverse ratio of gas constants (i.e. higher gas constant needs more area throttling).

From the perspective of achieving a piston trajectory with a soft landing, the addition of the orifice plate serves as a simple way to scale the amount of helium in the driver tube. Applying this to Hornung's methodology and taking the computed trajectories with 100% argon as the driver gas, the helium concentration can be increased, the driver area ratio reduced and predicted shock speeds change as shown in fig. 3.10. Each band of shock speeds show the variation in overdrive for the three diaphragm rupture pressures available, and contrary to fig. 3.9, the shock speed increase from the addition of helium using an orifice plate far outweighs the shock speed increase when not using an orifice plate.

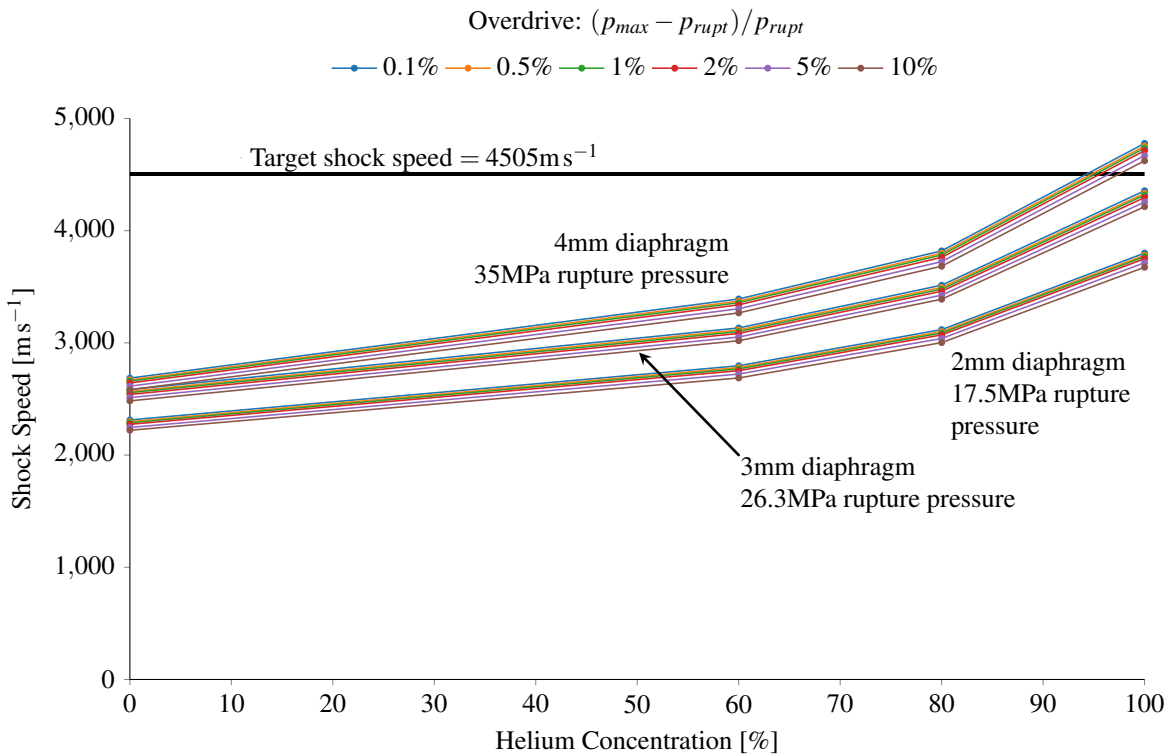


Figure 3.10.: Shock speeds in 13.5kPa air with orifice plates sized according to eq. (3.19). Each group of lines are associated with the same thickness of diaphragm: 2mm, 3mm and 4mm, for an air shock tube filled to 13.5kPa. The black solid line is the target shock speed for an X2 crossover condition that was used by Fahy et al. [76].

The target shock speed of  $4505 \text{ m s}^{-1}$  is the theoretical shock speed target by Fahy et al. [76] (Fahy's measured shock speed ended up being  $4738 \text{ m s}^{-1}$ ) and from the theoretical results this shock speed may be achievable using a rupture pressure of 35MPa and 100% helium as the driver gas.

The conclusion from the analysis of X3's driver is that there are many combinations of reservoir fill pressure, compression tube fill pressure, orifice plate diameter and driver gas mixture that will result in a lightweight piston trajectory with a soft landing. While a working reservoir fill pressure is not obtained from this section, a good estimate has been obtained for the other parameters to achieve working compression tube conditions and, while it does not capture all effects in the actual facility (e.g. diaphragm rupture time, buffer location, etc) the behavior of the piston after diaphragm rupture can be predicted with some level of accuracy .

## 3.7. Numerical Model

While the previous section looks at X3's driver from a theoretical perspective, this section will cover the development of a numerical model in L1d that will be used for the final design of the actual

### 3. X3's Driver

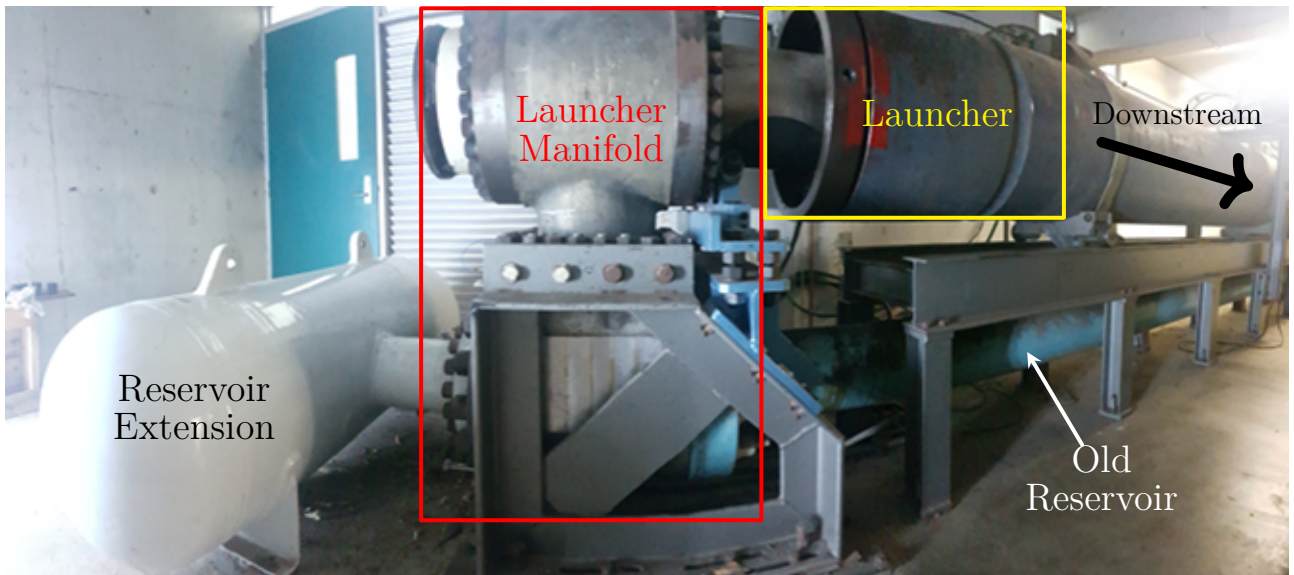


Figure 3.11.: X3 reservoir and piston launcher arrangement with sections of the assembly identified.  
(note: image is distorted to increase field of view)

operating conditions. L1d is a code “for the quasi-one-dimensional modelling of the gas-dynamic processes within transient-flow facilities”, Jacobs [132]. The code has objects for gas slugs, pistons and diaphragms and uses engineering correlations and equations to model flow effects such as viscosity, heat loss, etc. and has the capacity to model other features and configurations commonly found in hypersonic facilities [132]. This section covers the main development process in producing an L1d model capable of predicting the behaviour of the lightweight piston in X3’s compression tube.

#### 3.7.1. X3 Geometry

The first step in developing a usable model in L1d is to represent the geometry in the axial direction in a way that it is able to reproduce the gas flow behaviour of the actual geometry. An image of X3’s reservoir and launcher hardware divided into distinct sections is presented in fig. 3.11 with each of the main sections identified.

The launcher manifold (identified by the red box in fig. 3.11) has complex inner geometry that needs to be accounted for in L1d. Figure 3.12 shows a CAD model of the launcher assembly which illustrates some of the complexities present in X3. The lower part of the launcher manifold is assembled from the casing of a previously used component on another facility and the flow path of the lower section of the launcher manifold is connected to the upper section of the launcher manifold through a series of holes which are illustrated in the blue circles in fig. 3.12. The piston launcher (identified by the yellow box in fig. 3.11) is able to move freely with respect to the launcher manifold and the flow path into the launcher tube is a series of slotted holes around the circumference of the tube as identified by the red

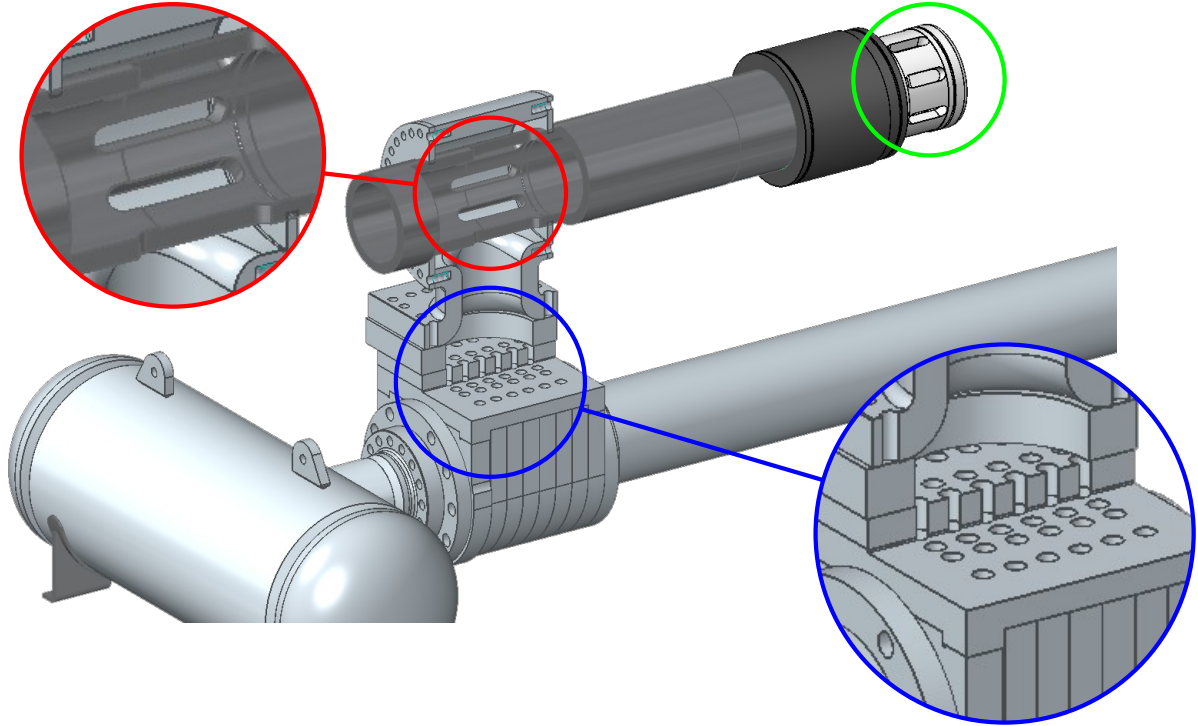


Figure 3.12.: CAD model with cutaway showing the internals of X3's launcher assembly. The complex geometry of the flow path in the launcher manifold is highlighted by the red and blue circles and the geometry of the piston launcher is highlighted by the green circle.

circles of fig. 3.12, a similar arrangement is also used where the piston is seated before it is launched along the compression tube, see green circle in fig. 3.12.

The process used to model the reservoir in the axial direction was to place each section of the reservoir at a location representative of the geometric flow path distance from the back face of the piston in the model while matching the diameter of the flow path according to the geometry of each section. If the axial distribution of volume along the flow path is correct, the gas losses due to the obstructions along the flow path can be accounted for with the addition of a loss factor at the end of the launcher in L1d. The loss factor acts as a momentum sink similar to minor losses when analysing pipe flow problems [138] and by varying the magnitude of the loss factor the losses throughout the reservoir can be captured within the model. The equation driving momentum losses determined by the loss factor is presented in eq. (3.20), where  $F_{loss}$  is removed from the momentum of the flow,  $k$  is the loss factor,  $\rho$  is the gas density,  $U_{cell}$  is the velocity of the cell,  $U_{abs}$  is the absolute velocity of the gas within the cell,  $A_{cell}$  is the area of the cell and  $L_{cell}$  is the width of the cell, where the centre of the cell is within the designated loss region.

$$F_{loss} = -k \times \frac{1}{2} \rho U_{cell} U_{abs} \times A_{cell} \times L_{cell} \quad (3.20)$$

The final geometrical model of X3's reservoir and launcher assembly is presented in fig. 3.13 with each

### 3. X3's Driver

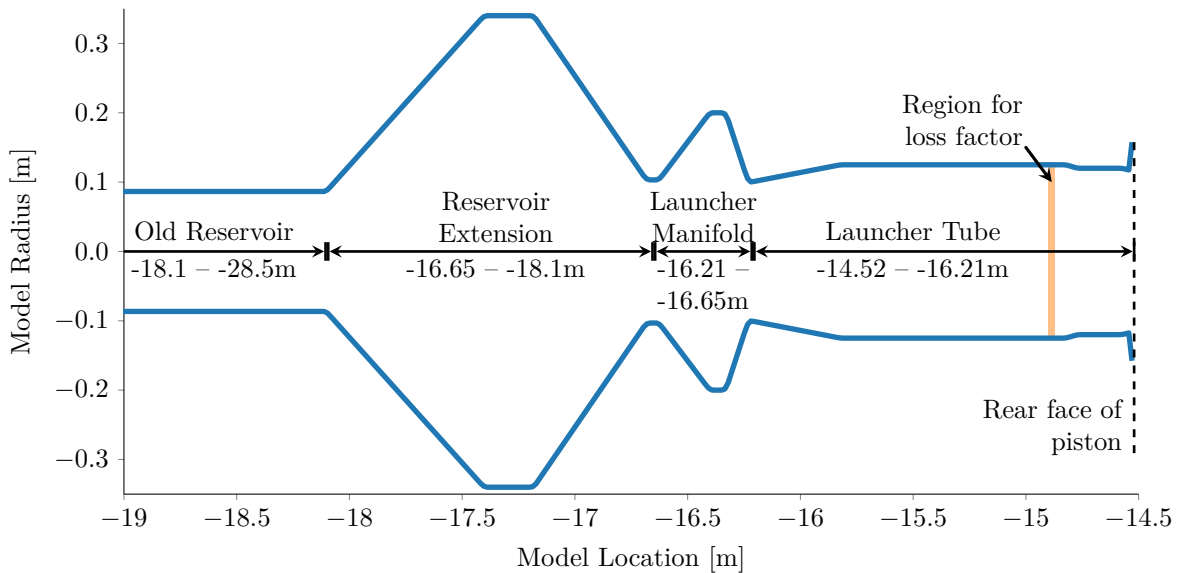


Figure 3.13.: Geometry used for the model of X3's reservoir and launcher assembly in L1d. The rear face of the piston is located at -14.52m and the old reservoir extends to -28.5m in the model. The radius of each section is as follows; old reservoir, 0.0865m, reservoir extension, 0.34m, launcher manifold, 0.2m, and launcher tube, 0.125m.

section labelled and the lengths in the model shown. The orange highlighted region is the location of the applied loss factor, which is placed slightly upstream of the radius reduction which itself accounts for the slots of the piston launcher, with a loss factor of 0.5 being applied over that length. Due to the fact that the gas slug cells in L1d change in width (i.e. in the axial direction) as the gas expands or compresses, the magnitude of the rate of change of radius in the L1d model cannot be too high: gas cells may miss geometrical features as their location is determined by their centroid as they move along the axial direction. An example of the gradual change in radius can be observed in fig. 3.13 in the axial range -18.1– -17.4m where the radius changes from  $\pm 0.0865\text{m}$  to  $\pm 0.34\text{m}$  rather than follow the actual geometric shape of the reservoir which has a more sudden change.

### 3.7.2. Piston

As the main goal of the L1d model was to design operating conditions with concern for the piston trajectory, the behaviour of the piston within the L1d model must also be considered. The piston itself has friction factors that can be modified, the purpose of which is to model the friction produced from the piston seals on each face when the pressure of the gas on each side of the piston pushes the seal outwards into the wall of the compression tube. A cutaway schematic is presented in fig. 3.14, where the yellow piece is the seal and the dark grey piece is the load ring which has interspersed holes to allow the driver gas access to the seal (orange surface). The lightweight piston does not have a rear seal but the L1d model has the capacity for seal friction on both the upstream and downstream sides of the

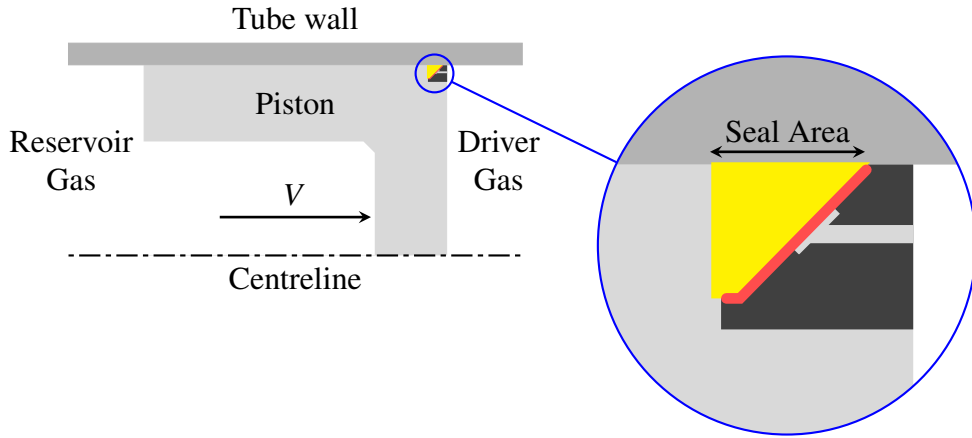


Figure 3.14.: Axisymmetric schematic of the chevron seal (yellow) on the front of X3's lightweight piston. The driver gas is able to flow through holes in the brass load ring (dark grey piece) and act on the surface of the chevron seal (highlighted in orange), pushing the seal outwards towards the tube wall. The seal area is defined as the width of the seal multiplied by the circumference of the piston.

piston. The magnitude of the frictional force contributed by each seal is defined by equation eq. (3.21) where  $F_{loss}$  is the drop in effective force on the piston,  $\langle \text{Friction Coefficient} \rangle$  is the friction coefficient entered into L1d,  $\langle \text{Seal Area} \rangle$  is the area of the seals contacting the wall of the compression tube ( $0.0324\text{m}^2$ ) and  $\langle \text{Pressure} \rangle$  is the pressure acting on the corresponding face of the piston. The piston geometry allows the pressure on each side of the piston to act on the seal in a radial direction towards the wall of the compression tube which makes the form of eq. (3.21) the same as the equation for calculating normal friction force,  $f_{friction} = \mu N$ .

$$F_{loss} = \langle \text{Friction Coefficient} \rangle \times \langle \text{Seal Area} \rangle \times \langle \text{Pressure} \rangle \quad (3.21)$$

The value of  $F_{loss}$  is subtracted from the calculation of the total force acting on the piston when its change in velocity is calculated each time step. The friction factor for the downstream and upstream seals can be changed independently. As each source of friction uses the pressure acting on the corresponding face, the variation of each friction factor has different effects on the trajectory of the piston and the pressure trace in the compression tube. The only measurement taken during blank-off experiments is the pressure measured in the compression tube so that only the effect of friction on the calculated compression tube pressure will be examined in more detail here.

In fig. 3.15, the effect of friction factor variations on the compression tube pressure trace is illustrated. The general trend of both plots in fig. 3.15 is that a larger value for friction factor reduces the maximum pressure and increases the time from the start of the simulation to the time of maximum pressure. If attention is paid to the first pressure rise in each plot of fig. 3.15 at approximately 0.95ms, it is evident that variation of the upstream friction factor has already had some effect on the pressure trace whereas

### 3. X3's Driver

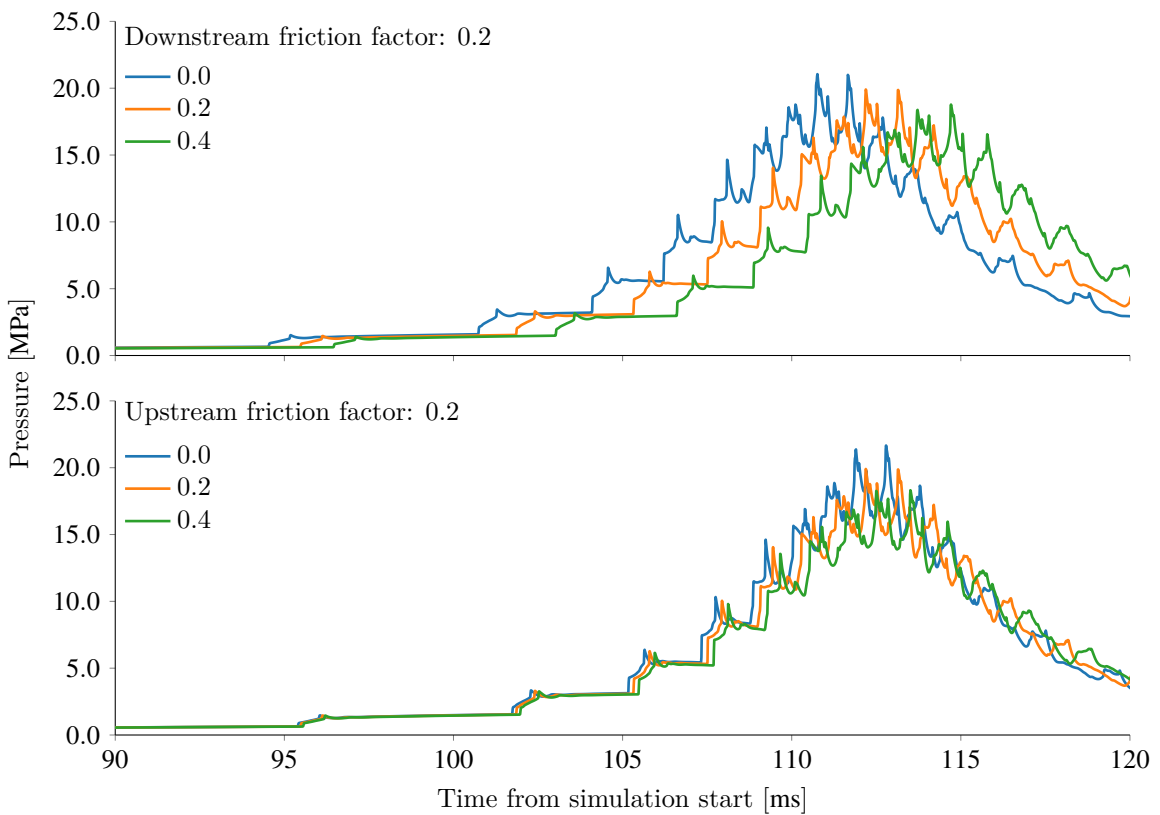
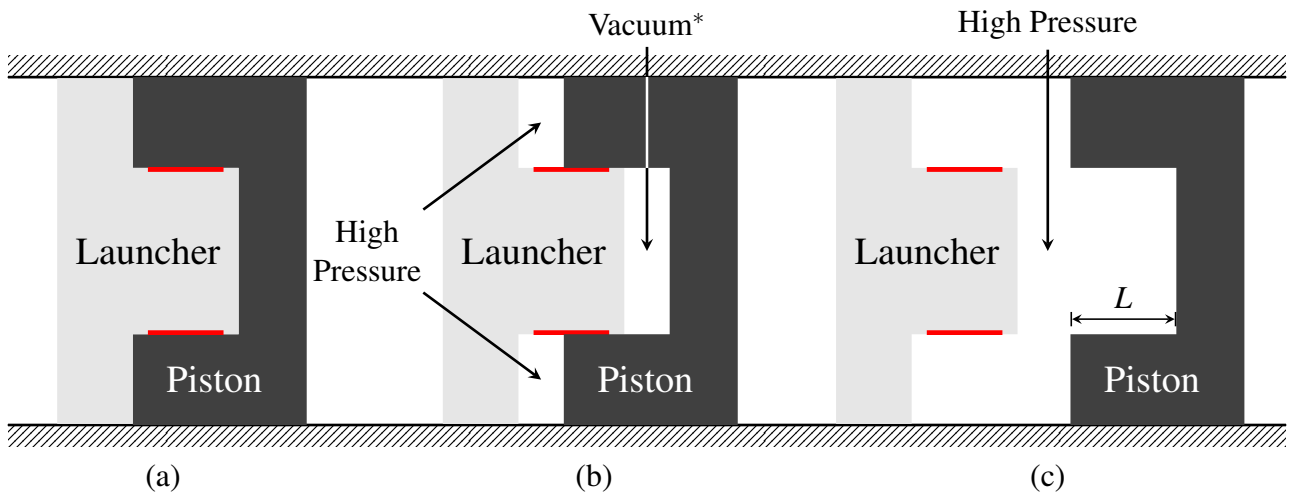


Figure 3.15.: Effects of varying the friction factor for upstream (upper plot) and downstream (lower plot) of the piston on the compression tube pressure calculated in L1d for simulations with a 100% argon driver gas. In both plots the friction coefficient for the side of the piston not being varied is set to 0.2 meaning the two orange plots are identical (i.e. in the upper plot the downstream friction factor is set to 0.2 and in the lower plot the upstream friction factor is set to 0.2).

the influence of the downstream friction factor does not occur until later in the piston's trajectory. This is due to the upstream face of the piston being exposed to the high reservoir pressure from the beginning of the trajectory and it is not until approximately 100ms after the simulation starts where the pressures on both faces are comparable. As the driver gas is compressed further, the effects of the downstream friction factor become more evident and begin to outweigh the effects of the upstream friction factor, although both friction factors are additional in nature. Each friction factor affects one feature of the driver gas pressure more than the other, from fig. 3.15, the upstream friction factor has a larger influence of the timing on the pressure trace whereas the downstream friction factor affects the maximum pressure more severely than the upstream friction factor.

While the friction factors give some element of control to the piston's motion, they are limited by the fact that they depend on the pressure on either side of the piston. A final consideration implemented into L1d for the analysis of X3's piston was the effect of the launcher on the trajectory. The fit of the lightweight piston over the launcher is not smooth and machinery is required to locate the piston on the launcher after each shot; potential causes are slight misalignments or non-concentricities, but that



\*The reservoir gas can access this region via a small hole from the High Pressure region.

Figure 3.16.: Illustration of the piston coming off the launcher, which has a length  $L$ , at the beginning of the piston's trajectory at the beginning of an experiment. The high pressure reservoir gas flows through slots in the launcher indicated by the red lines. (a) Before the shot the piston rests on the launcher with the space between the piston and launcher kept at vacuum, (b) Reservoir gas is allowed between the piston and launcher into the regions labelled “High Pressure” and “Vacuum” (see note) and the piston is pushed off the launcher, (c) once the piston leaves the launcher the reservoir gas continues to flow through the launcher pushing the piston downstream (to the right).

is not the focus here. The reality is that the lightweight piston does not easily slide off the launcher<sup>1</sup> and this may affect the piston trajectory and pressure trace in the compression tube.

The effect of the launcher was modelled by reducing the area the reservoir gas could push on the piston for length  $L$  at the beginning of the piston's stroke (see fig. 3.16). This effectively models the region labelled “Vacuum” in fig. 3.16 (b) as a vacuum although it is likely the actual pressure in this region is similar to the region labelled “High Pressure”. Once the piston travels a distance  $L$ , the reservoir gas is allowed to push on the full rear face of the piston for the remainder of its trajectory (fig. 3.16 (c)). While the effects of the launcher on the piston's trajectory are most likely small, varying the length  $L$  in L1d has a considerable effect on the timing of the pressure waves, presented in fig. 3.17 where the peak pressure in the compression tube is delayed by 10ms for a launcher length  $L$  of 2m. The launcher lengths in fig. 3.17 are not realistic (the launcher's length is only 0.3m) but for the purpose of matching the piston's trajectory and compression tube pressure trace, the addition of the launcher to the L1d model allows for an extra control in the timing of the pressure waves without too much loss in peak pressure.

<sup>1</sup>The most recent check found that up to 2MPa of reservoir gas was required to launch the piston.

### 3. X3's Driver

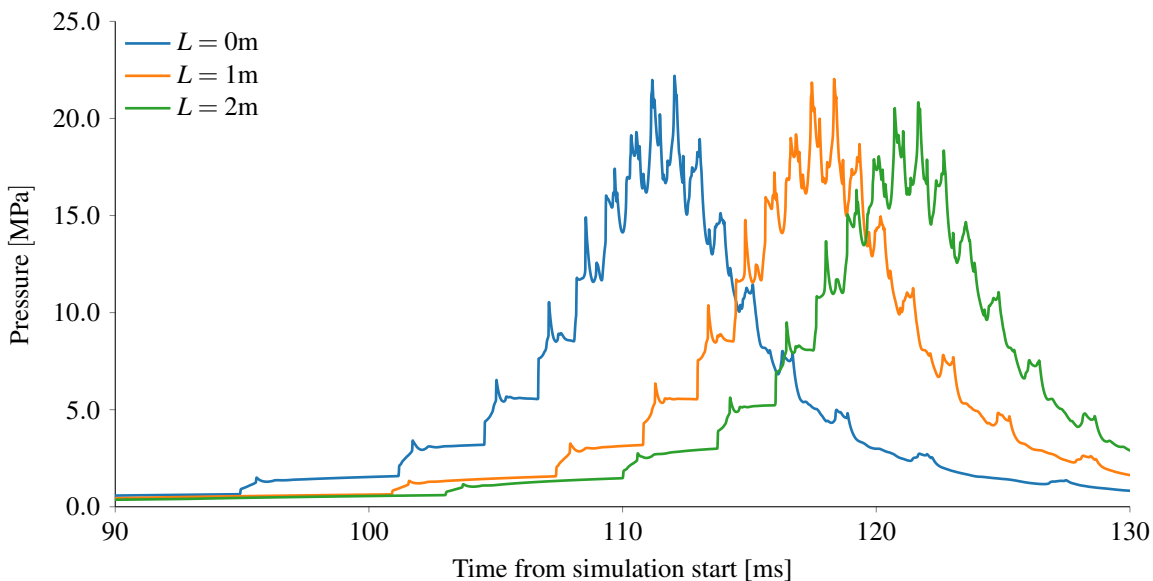


Figure 3.17.: Effect of changing the launcher length  $L$  on compression tube pressure, the actual length of the launcher is 0.3m.

Table 3.5.: Final values of parameters used in the L1d model. All parameters are dimensionless except for launcher length which has effective units of metres.

Feature	L1d Parameter	Value
Flow physics	Adiabatic Flow	0
Flow physics	Viscous Effects	1
Geometry	Loss Factor	0.5
Piston	Downstream Friction Factor	0.0
Piston	Upstream Friction Factor	0.1
Piston	Launcher Length $L$	1.0

### 3.7.3. Final Model Parameters

The final values for the piston friction factors, loss factor and effective launcher length are presented in table 3.5; the values remain unchanged for the model validation in section 3.8.2 and throughout the condition development in chapter 4. Not discussed previously are the L1d options to model adiabatic flow and viscous effects. The adiabatic flag was left off for all simulations, and heat losses using pipe flow correlations were used to adjust the temperature of the flow within the code using a wall temperature of 300K. L1d's default friction source terms were left on for the reservoir and compression tube which, based on another pipe flow correlation, model effects of friction through shear stress along cell boundaries resisting their motion.

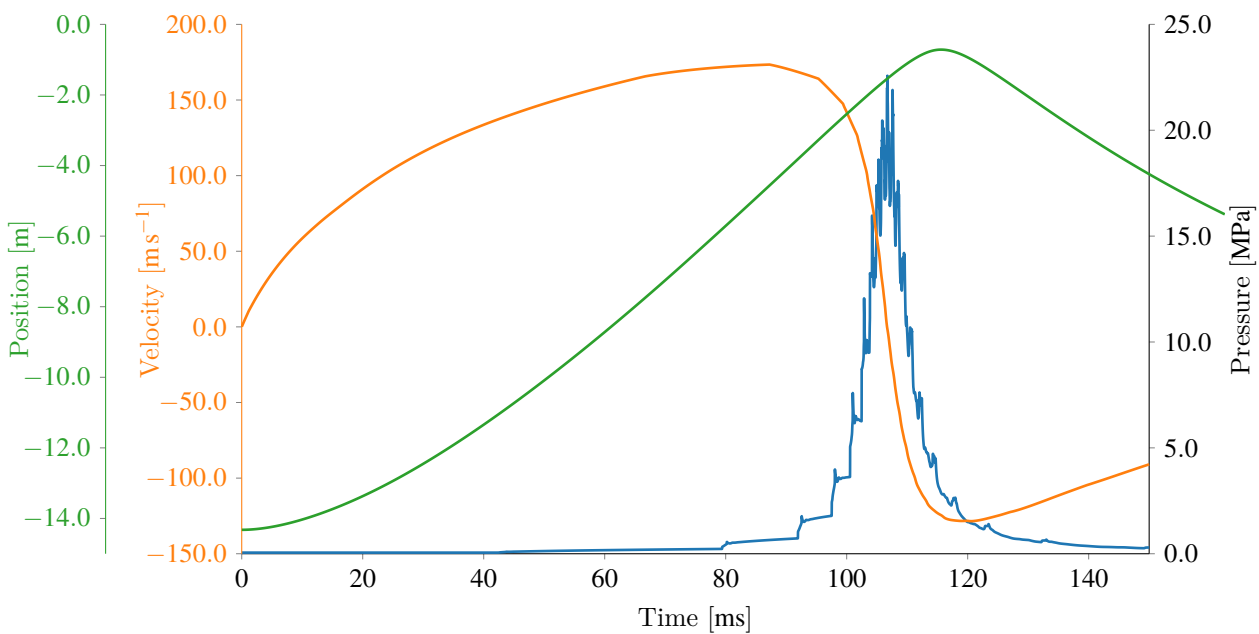


Figure 3.18.: Example of simulated data for a blank-off shot. The centre of the piston has an initial location of -14.122m and the blank-off plate is located at the primary diaphragm station at 0m.

## 3.8. Blank-off Shots and Model Validation

While the actual development of the L1d model and the blank-off shots are an iterative process, only the final results of the L1d model will be presented in this section. An example of the data that can be obtained or simulated during a blank-off shot is shown in fig. 3.18, where the blue curve is the compression tube pressure which can be compared between experiment and simulation. The piston location and velocity were not directly measured but the final location of the piston during the blank-off shots could be located by the use of weld rods which is discussed in section 3.8.2. Gildfind et al. [139] has developed an accelerometer package that can be mounted to the front face of the piston in X3, but it was not available at the time the blank-off shots were conducted and only has a structural limit of 2000g, which is unsuitable for the lightweight piston.

### 3.8.1. Reservoir Extension

The first blank-off shots conducted with the lightweight piston were undertaken purely to reproduce the compression tube pressure traces obtained by Gildfind et al. [22] during the initial lightweight piston commissioning. The experiments performed by Gildfind were conducted before the installation of the reservoir extension and the purpose of this blank-off shot was to determine the effect of the addition of the reservoir extension on the performance of the facility.

### 3. X3's Driver

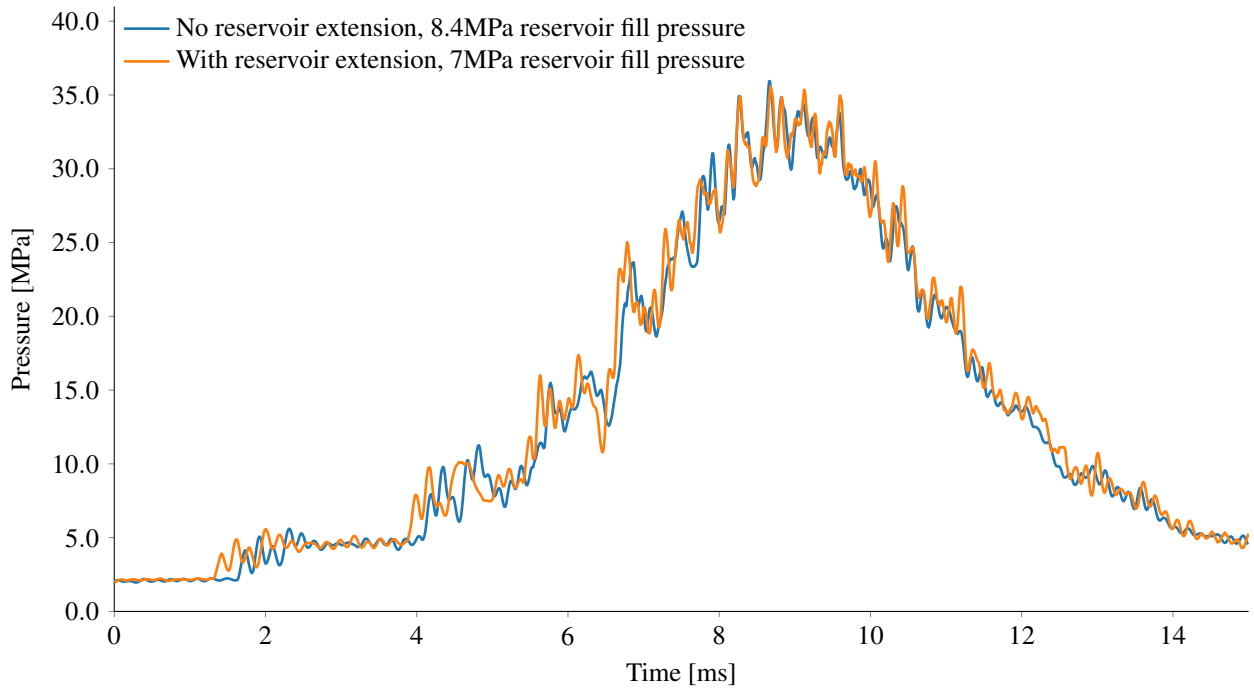


Figure 3.19.: Comparison of the compression tube pressure for both equivalent blanked-off shots. The blue line was presented in [22] without the reservoir extension. The orange line was conducted using the reservoir extension before the slots in the launcher were enlarged.

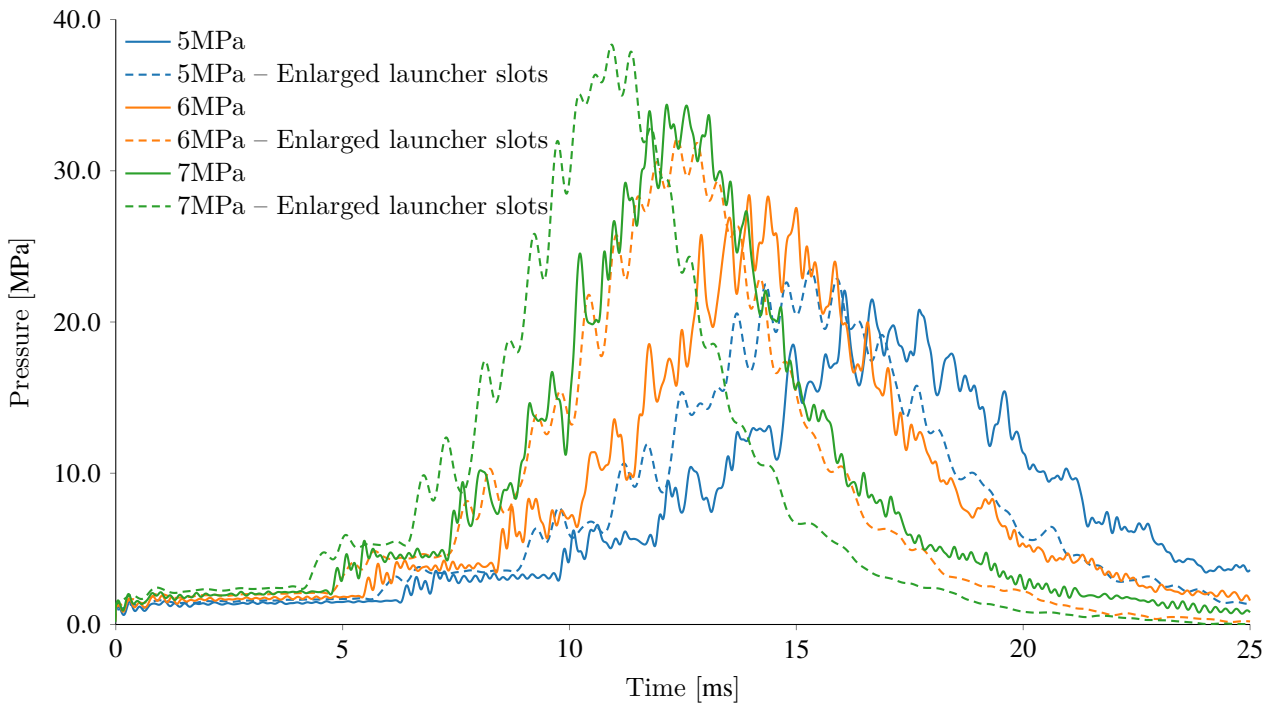


Figure 3.20.: Compression tube pressure comparison of identical fill pressure in the reservoir and compression tube before and after the launcher slots were enlarged. The compression tube was filled with 53kPa argon. The dotted lines are the shots performed after the launcher slots were enlarged.

The comparison in fig. 3.19 shows that a reservoir pressure of 7MPa was required to match the compression tube pressure measured by Gildfind et al. [22], who used a reservoir pressure of 8.4MPa for a compression tube filled with 53kPa of argon. Although this reduction of reservoir pressure was not as large as hoped, it still shows the merit of installing the extension. After the blank-off shots in fig. 3.19 were performed, the area of the slots in the launcher manifold and the piston launcher were increased to reduce pressure losses and potentially reduce the required reservoir pressure even further. Figure 3.20 illustrates the performance increase after the launcher slots were enlarged. The dotted pressure traces for each pressure show an increase in peak pressure and the measurement of the peak pressure occurs earlier compared to the pressure traces taken before the launcher slots were enlarged. This indicates that the piston is travelling with a higher velocity because of the stronger push it gets from the reservoir gas. An increase of approximately 20% for the peak pressure in the compression tube was observed across the three different reservoir pressures in fig. 3.23.

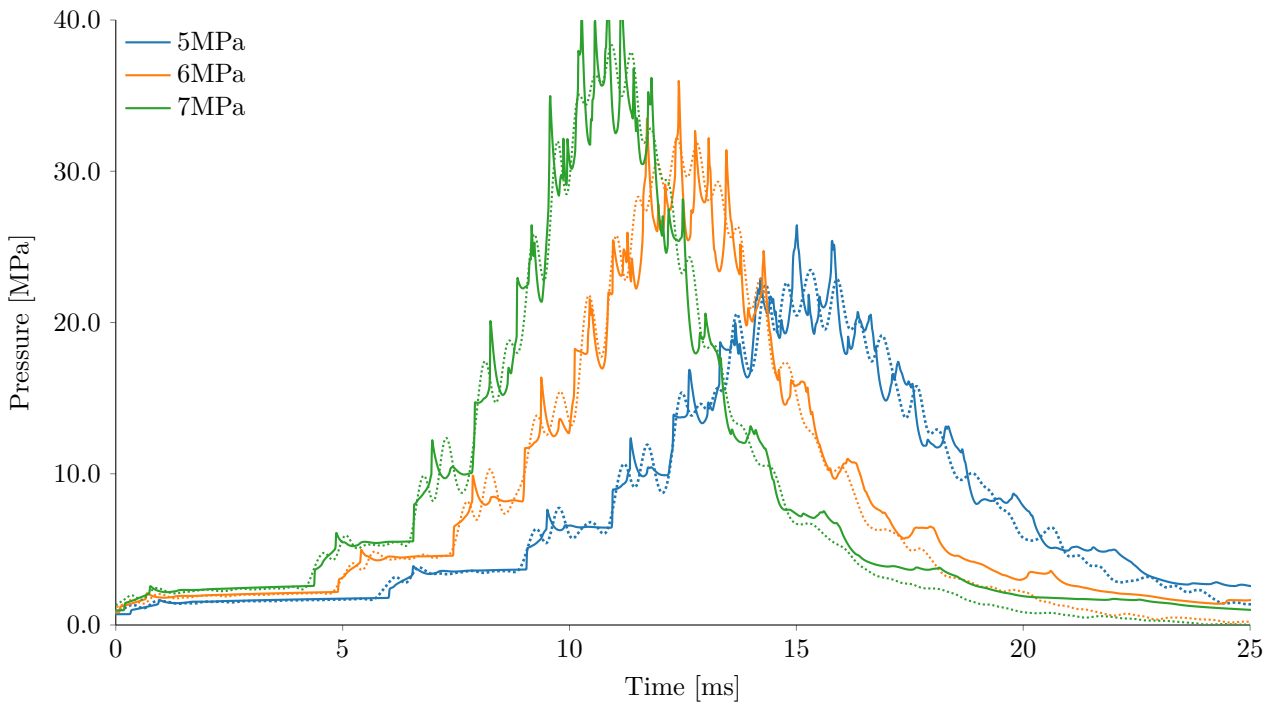


Figure 3.21.: Comparison of the compression tube pressure trace between blank-off shots (dotted lines) and L1d simulations (solid lines) for three different reservoir pressures. Shots were performed after the launcher slots were enlarged.

### 3.8.2. L1d Validation

Blank-off shots used to validate the L1d model were performed after the area of the slots in the launcher manifold and on the piston launcher were increased. The blank-off shots were performed with an argon driver gas filled to 53kPa and the reservoir was varied to 5MPa, 6MPa and 7MPa. The comparison of compression tube pressure traces in fig. 3.21 shows a very good agreement between the L1d model and experimental measurements, with no variation in the L1d model or parameters being required

### 3. X3's Driver

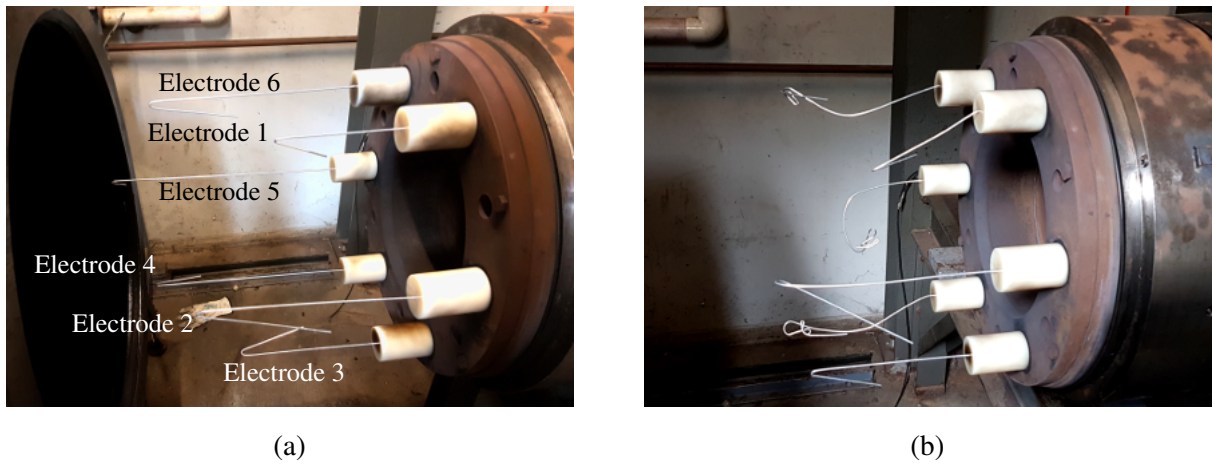


Figure 3.22.: Welding electrode arrangement for the 5MPa blanked off shot; (a) before shot (b) after shot, deformed rods indicate distance the piston has travelled

when varying the reservoir fill pressure. It is important to note that the model not only matches the maximum pressure, but also the timing of the waves in the driver gas, which suggests that the location of the piston is correct within the model, as the arrival of the compression waves at the pressure sensor depend on the sound speed of the driver gas and the location of the piston.

The location of the piston at the end of its stroke can be measured using welding electrodes mounted on the nylon buffers, similar to that done by Gildfind [86]. As the mass of each individual electrode is small compared to the piston, the welding electrodes will be deflected out of the way once the piston makes contact, without any transfer of energy with the piston. By varying the lengths of the electrodes, the longest undeformed electrode gives a lower limit of how far the piston travels down the compression tube and similarly the shortest deformed electrode gives the upper limit. Images of the welding electrodes before and after a blank-off shot are shown in fig. 3.22 for a 5MPa reservoir fill pressure. In fig. 3.22b, Electrode 2 which had a starting length of 25.2cm has suffered a small deflection, but Electrode 3 (20.7cm) has not been deflected. In this example the resolution of the electrodes is on the order of 5cm and it was decided that the piston ended its stroke at 25cm from the end of the buffers, rather than taking the length of the longest undeformed electrode which is 20.7cm.

In fig. 3.22b, Electrode 1 has been deformed where the electrode meets the buffer. This occurred for each blank-off shot where weld rods were employed but as Electrode 1 was always the shortest and measurements were taken with other electrodes this was not an issue but it is still unclear why the deformation kept happening, possibly due to the hole in the buffer not being normal to the surface. The measurements taken using the welding electrodes were compared with the numerical simulation and the results are displayed in fig. 3.23. The L1d results are presented as position-velocity curves and the welding electrodes as vertical dashed lines. The prediction of the 5MPa shot was within 20mm of the measured value whereas for the 6MPa and 7MPa shots, the predicted values were within 40mm of the measured value. Considering the limitations of the model and the fact the piston travels approximately 14m along the compression tube, the error was deemed to be acceptable and the L1d

model successfully able to predict the location of the piston. The error observed in fig. 3.22 means that buffers should be sized shorter than what is calculated in L1d, with the inflection point of the piston's trajectory occurring slightly upstream of the buffers (see section 4.3.2).

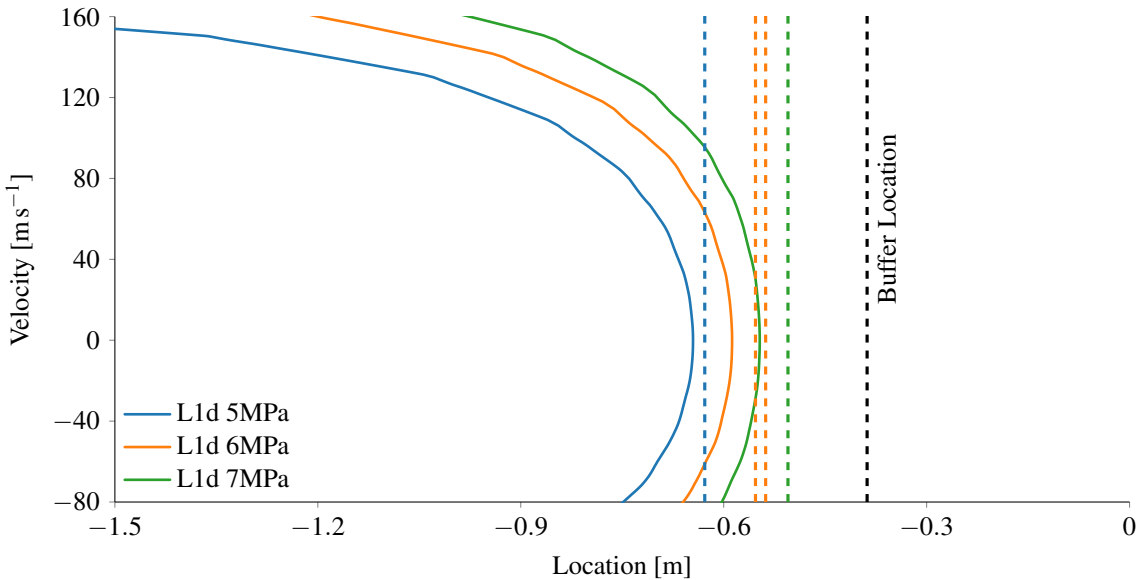


Figure 3.23.: The simulated piston stroke (solid lines) compared with the experimental maximum distance from the weld rods (dashed vertical lines). The buffer location is indicated by the black vertical dashed line and the primary diaphragm is located at 0m.

## 3.9. Chapter Conclusion

This chapter has seen the development of an L1d model that will be used in the next chapter to design compression tube operating conditions which are essential to the rest of this thesis. Experimental validation has shown that it is capable of accurately predicting the compression tube pressure and piston trajectory during blank-off shots with various reservoir fill pressures without any modification or re-tuning of the L1d model between conditions required. It is expected that for changes in hardware (e.g. a different piston) minor modifications of the L1d model will be required, mostly piston parameters, to accurately reproduce the piston trajectory and compression tube pressure. For the stated reasons, it is believed that the L1d model can now be used as a tool to reliably predict the behaviour of the reservoir and compression tube for a range of fill pressures. Part of the experimental validation involved the commissioning of a new reservoir extension and lightweight piston, two essential pieces of hardware required to increase the performance of X3 and make radiating, high enthalpy test flows achievable. The results presented in this chapter will be used in the next chapter as the L1d model is expanded to include a rupturing diaphragm and shock tube as fully operational drivers for X3 are developed and tested.

# 4

---

## Driver Performance

### 4.1. Chapter Overview

In the previous chapter, it was shown that the L1d model could reproduce the experimental performance of X3's compression tube and reservoir, with the compression tube pressure being recreated and the location of the piston being calculated to within 50mm. This chapter will look at the introduction of a rupturing diaphragm object in L1d and the sizing of new buffers for use with the lightweight piston, and the process involved with arriving at working operating conditions. Two thicknesses of diaphragm were initially available for use on X3: a 2mm thick diaphragm that nominally ruptured at 17.5MPa and a 3mm thick diaphragm that nominally ruptured at 26.3MPa. In earlier experiments by Sancho [130] two 2mm diaphragms were combined to create 4mm total diaphragm thickness that ruptured at 35MPa. Since the 4mm diaphragm was not used due to the 3mm diaphragm rupturing at higher than expected pressures, and expected reservoir pressures for 4mm conditions being higher than 10MPa (the max capacity of the reservoir), conditions were developed for a 100% argon driver gas for the 2mm and 3mm diaphragm, and increased helium concentrations were achieved by then incorporating orifice plates. This chapter concludes with an overview of experimental shock speeds and pressures from a range of different helium concentrations in the compression tube for both diaphragm thicknesses, with the overall goal of reproducing the Hayabusa flow condition used in X2 by Fahy et al. [76]. The potential use of a secondary driver for performance enhancement is briefly examined and the flow properties in the test section are presented for the experiments which were available.

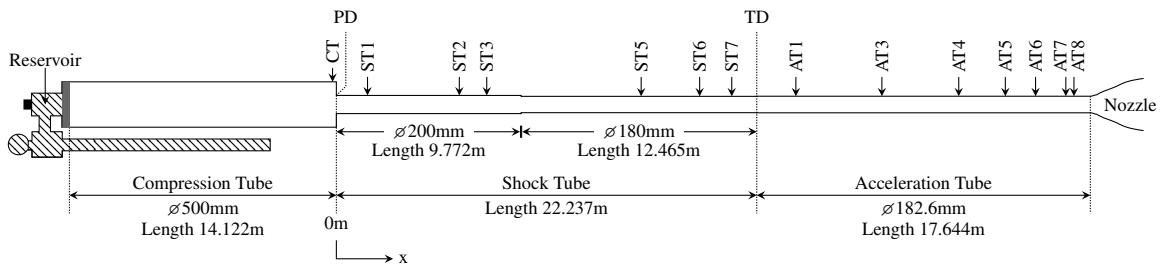


Figure 4.1.: Standard configuration of X3.

Table 4.1.: Tube wall static sensor locations

Compression Tube		Shock Tube		Acceleration Tube	
Sensor	Location [m]	Sensor	Location [m]	Sensor	Location [m]
CT	-0.201	ST1	1.649	AT1	24.307
		ST2	6.504	AT3	28.857
		ST3	7.955	AT4	32.922
		ST5	16.123	AT5	35.386
		ST6	19.217	AT6	36.986
		ST7	20.915	AT7	38.587
				AT8	39.016

## 4.2. Expansion Tube Layout

Most of the analysis in this chapter uses a configuration of X3 with a shock tube of length 22.237m (from the primary diaphragm station to the tertiary diaphragm station), as described by the schematic in fig. 4.1. This configuration does introduce a diameter change in the middle of the shock tube which is expected to have some influence on the flow, but the extent is not determined. The locations of sensors in the shock tube and acceleration tube are shown in table 4.1. For all shots in this chapter the tertiary diaphragm (TD in fig. 4.1) consisted of 12.5 $\mu$ m thick mylar, with the shock and acceleration tube nominally being filled with air to 13.5kPa and 17Pa respectively, this matched the initial state of X2 for the Hayabusa condition developed by Fahy [77]. A summary of all the experiments performed in this chapter is presented in appendix A. The schematic of the operating mode will be updated throughout this chapter as required.

## 4.3. The Diaphragm in L1d

For the condition to be developed with a rupturing diaphragm, a target operating condition had to be decided upon. From fig. 3.9 (d) and fig. 3.10 it is evident that faster shock speeds can be obtained with lower piston overdrive ratios at the expense of steady driver pressure time. For the purpose of high enthalpy radiation test conditions, the steady driver time is not as critical as it would be for a reflected shock tunnel or scramjet conditions, thus a target overdrive of 0.1% was chosen and a 49kPa driver fill pressure (for the purpose of designing operating fill pressures the driver gas was 100% argon) was used for the 2mm diaphragms. To arrive at a tuned condition within L1d, an iterative process was required. Each iteration required a series of simulations run with varying reservoir pressures, where one of the reservoir pressures would produce an inflection point in the piston motion.

In fig. 3.7 it is apparent that the inflection point will not necessarily be located at the end of the tube, and buffers need to be sized to catch the piston at the location of the inflection point. The introduction of buffers in the compression tube removes volume and the location of the piston when the diaphragm ruptures moves upstream. Each time the buffer length is increased in the L1d model, the piston's inflection point is pushed upstream and buffers must continually be lengthened until the inflection point is at the end of the buffers.

### 4.3.1. Diaphragm Object Adjustments

The diaphragm object in L1d is used to separate two gas slugs until it registers a pressure difference across the diaphragm greater than the specified rupture pressure. Once the rupture conditions are satisfied, the two gas slug objects can interact and the diaphragm is removed. Although the code has the capability to include diaphragm inertia by treating it as a piston with decaying mass, this feature was not used in this study. By default, the diaphragm object uses adjacent cells to calculate the pressure difference, or has the capability to average the pressure of a range of cells within a specified distance of the diaphragm. One drawback of using the adjacent cell is the nature by which L1d handles waves when they reach the diaphragm and reflect back up the tube. In fig. 3.17, after the pressure wave passes the sensor in the compression tube, there is a pressure increase shortly after the wave before it settles at the higher pressure. When the wave reaches each end of the compression tube (diaphragm or piston) the gas dynamics equations in the code result in an artificially high pressure at the end of the tube, which may cause the diaphragm to spuriously rupture if the region of high pressure is not accounted for correctly. This is demonstrated in fig. 4.3, where the highest pressure occurs near the primary diaphragm (located at 0m) for the 0.07–0.15m curve. Similarly, the same phenomena can be observed for the 0.07–0.50m curve at approximately -0.5m, which is the location of the downstream face of the piston.

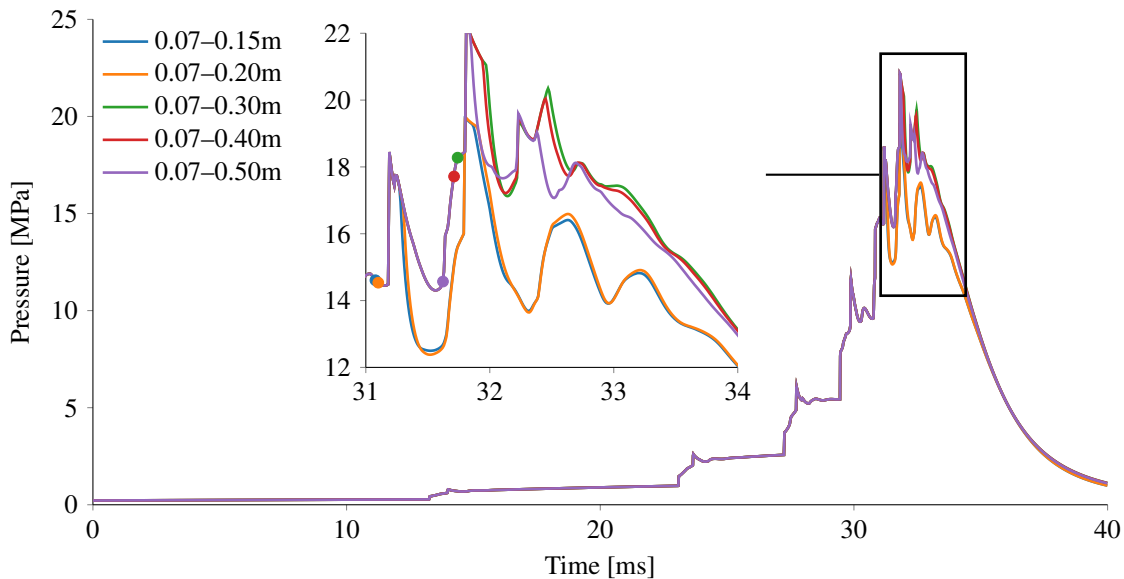


Figure 4.2.: Difference in rupture timing when the length of the averaging region is varied. The distances of the averaging region is an absolute distance from the diaphragm object

To counter this issue the cell pressure averaging code was modified to average a region of cells between two distances not adjacent to the diaphragm object. By averaging the pressure in cells not adjacent to the diaphragm the effect of artificially high pressure in the cells at the end of the tube was removed and the diaphragm ruptured in a manner that seemed more reasonable when comparing the rupture time with the pressure in the compression tube. By varying the averaging width that is considered for rupturing the diaphragm, and the addition of a diaphragm hold time (i.e. a delay between rupture conditions being met and actual rupture) the timing of the diaphragm rupture can be controlled. An example of the variation in rupture timing is shown in fig. 4.2 which is a series of pressure traces measured at the compression tube pressure sensor, and the time of diaphragm rupture is represented by the markers of the same colour. For the case in fig. 4.2 the rupture times appear to separate into two groups depending on the length of the averaging region, most likely based on the timing of the pressure wave.

Examples of how the pressure wave affects the average pressures in the averaging regions are shown in fig. 4.3. For the cases of 0.07m–0.15m and 0.07m–0.2m as the averaging region upstream of the diaphragm, the pressure wave is moving right to left. For the remaining cases the pressure wave is moving left to right, which explains why the 0.07m–0.5m case ruptures earlier than the 0.07m–0.3m and 0.07m–0.4m case. For the simulations in fig. 4.2 and fig. 4.3 the diaphragm has a rupture delay of 20 $\mu$ s so the diaphragm object actually ruptures 20 $\mu$ s after the times identified in fig. 4.3.

As the averaging schemes in fig. 4.2 do not have significant variation, an averaging region of 0.07m–0.5m was chosen for the final L1d model and was used to find solutions to tune the piston. After performing experiments, the rupture pressures were slightly higher than predicted so the delay time was changed to 100 $\mu$ s as it improved the similarity of compression tube pressure traces between L1d and experiment after diaphragm rupture, although the effect on piston trajectory was insignificant.

## 4. Driver Performance

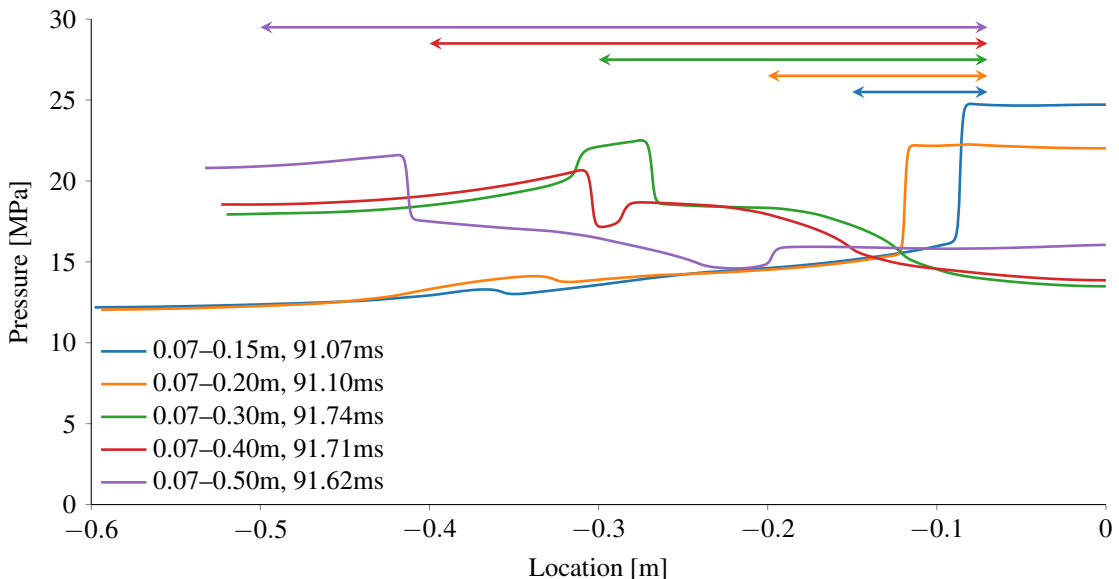


Figure 4.3.: Pressure distribution in compression tube at the time of diaphragm rupture for different averaging regions. The simulation time for each region is presented in the legend and the coloured arrows graphically represent the region that is averaged when calculating diaphragm rupture.

### 4.3.2. A Tuned Piston Condition

Once the diaphragm object within L1d had been configured, simulations in L1d could be performed in an iterative manner to arrive at operating conditions where the piston would be tuned. As the goal of this exercise was purely to arrive at conditions for tuned piston operation, the driver fill pressure was not varied and the change in performance due to varying driver fill pressure was not examined. The 49kPa fill pressure used was found from performing the piston analysis using Hornung's methodology (section 3.5.2) and choosing a low overdrive ratio. While the theoretical results allow little room to vary the fill pressure, it is possible to use orifice plates to obtain a new set of reservoir and driver fill pressures. A consequence of using orifice plates is that they effectively reduce the performance of the driver. For a certain driver condition, an area reduction with an orifice plate introduces a steady expansion due to the area change between the orifice plate and shock tube, which produces a weaker condition than if the same driver had no orifice plate. While the direct effect of an orifice plate is a reduction in pressure, but not necessarily shock speed, it does enable a wider range of operating conditions to be reached and results in a net gain in performance.

By varying the reservoir pressure and adjusting the buffer lengths accordingly, a final reservoir fill pressure of 6.7MPa and buffer length of 120mm was found to provide a tuned solution. The piston trajectories from a range of reservoir fill pressures with 120mm buffers calculated in L1d are shown in fig. 4.4, including the final condition with a reservoir fill pressure of 6.7MPa. The inflection point occurs approximately 40mm upstream of the buffers in L1d and this is representative of the error in

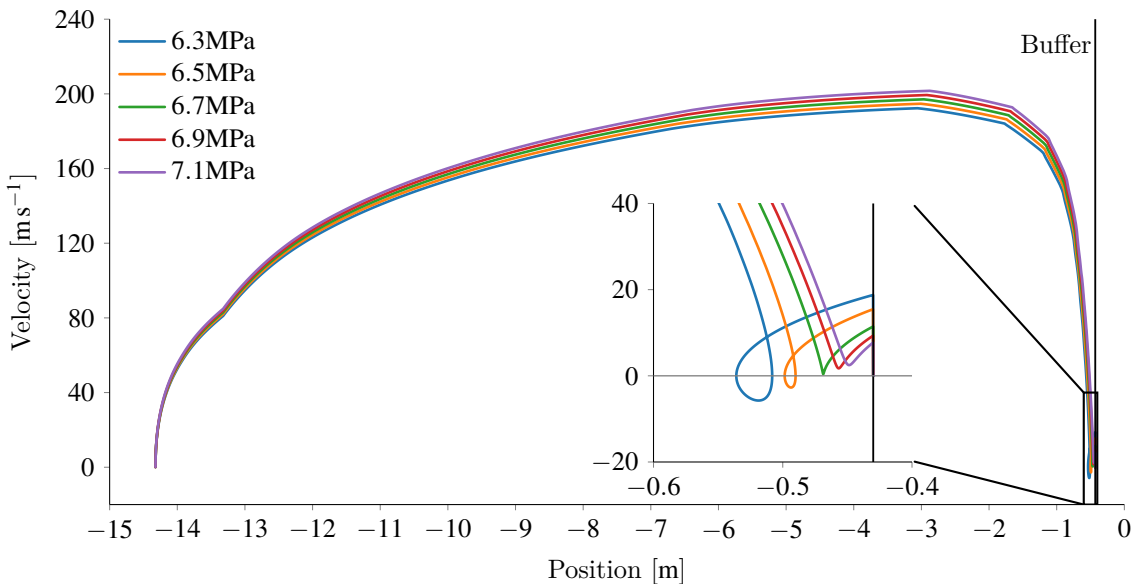


Figure 4.4.: Pitson trajectory calculated in L1d for a range of reservoir pressures. For a reservoir pressure of 6.7MPa (green line), an inflection point occurs just upstream of the buffers.

piston stroke present in the measurements in fig. 3.23. In fig. 4.4, it should be pointed out that the piston's change in velocity with respect to position is of larger magnitude before the inflection point than it is after. Thus it is better for the piston to strike the buffers after the inflection point as the piston will be travelling at a lower velocity than if it was to strike the buffers before the inflection point (while it is still decellerating).

## 4.4. Experiments with a Rupturing Diaphragm

As a new driver fill pressure was going to be used for the rupturing diaphragm shots, blank-off shots were repeated with the new buffer arrangement and fill pressures to confirm that L1d was not sensitive to the change in fill pressure and the new buffer arrangement. The 200kg piston used 6 buffers with 50mm diameter whereas the new buffer configuration employed 12 buffers at 80mm diameter, six with a length of 120mm and six with a length of 100mm (to reduce impact forces should the piston strike the buffers at high velocity). The buffers are threaded into an annular plate attached to the end of the diaphragm holder which forms the end of the compression tube when the sections are connected together. The initial design of the buffers comprised of a single piece of nylon, with the nylon directly screwing into the annular plate as in fig. 4.5a. Interestingly, the buffers are dense enough that a pressure differential builds up across the buffers and the first blank-off shot with the new buffers resulted in them being totally destroyed without being struck by the piston. A redesign in fig. 4.5b has each buffer bolted into a steel adapter and the subsequent blank-off shot saw no damage occurring to the buffers.

Two blank-off experiments were performed and although the first saw the buffers get destroyed, the

#### 4. Driver Performance

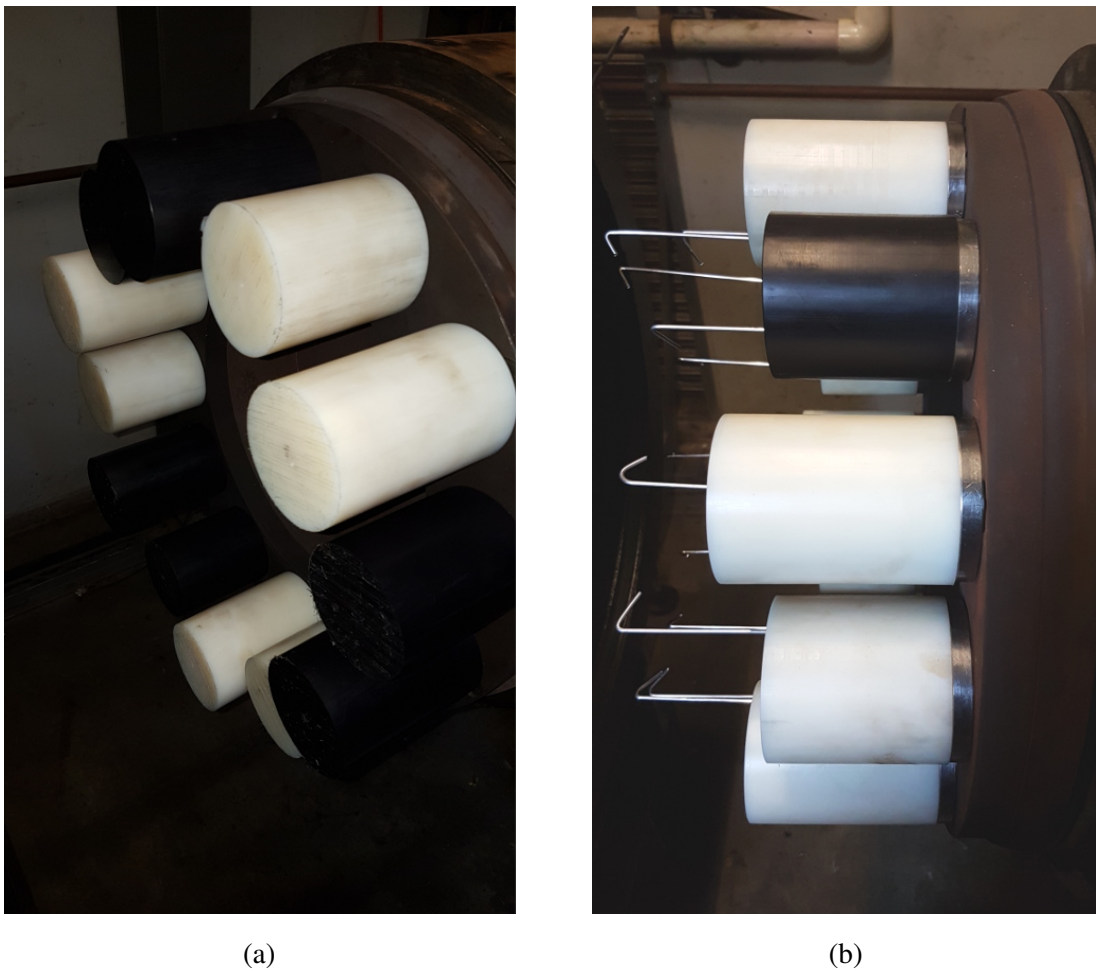


Figure 4.5.: (a), The initial buffer design, where each buffer consists of a single piece of nylon which is threaded into an annular plate. (b), The final buffer design, where each buffer is bolted to a steel adapter which is threaded into the annular plate; welding electrodes are present from before a blank-off shot.

pressure calculated in L1d agreed well with the measured pressure in the compression tube. The compression tube pressure traces from the two blank-off shots are shown in fig. 4.6, and include comparison with the pressure trace from L1d which shows a close agreement. As the L1d model was able to reproduce the data accurately after implementing the changes, a series of experiments with rupturing diaphragms were performed. The reference condition used a 100% argon driver gas filled to 49kPa with a 6.7MPa reservoir, and the helium concentration was then increased by restricting the compression tube exit area via orifice plates following the sizing in table 4.2.

As a proof of concept, the compression tube traces calculated in L1d for each helium concentration is shown in fig. 4.7, which illustrates that the use of an appropriately sized orifice plate for different percentages of helium results in the same pressure trace for different gas compositions. In fig. 4.7 both numerical and experimental data is presented for the same series of experiments, with both showing no significant deviation in compression tube pressure, and the main difference being the magnitude and frequency of the pressure waves. If no orifice plate was used for the same fill conditions, the

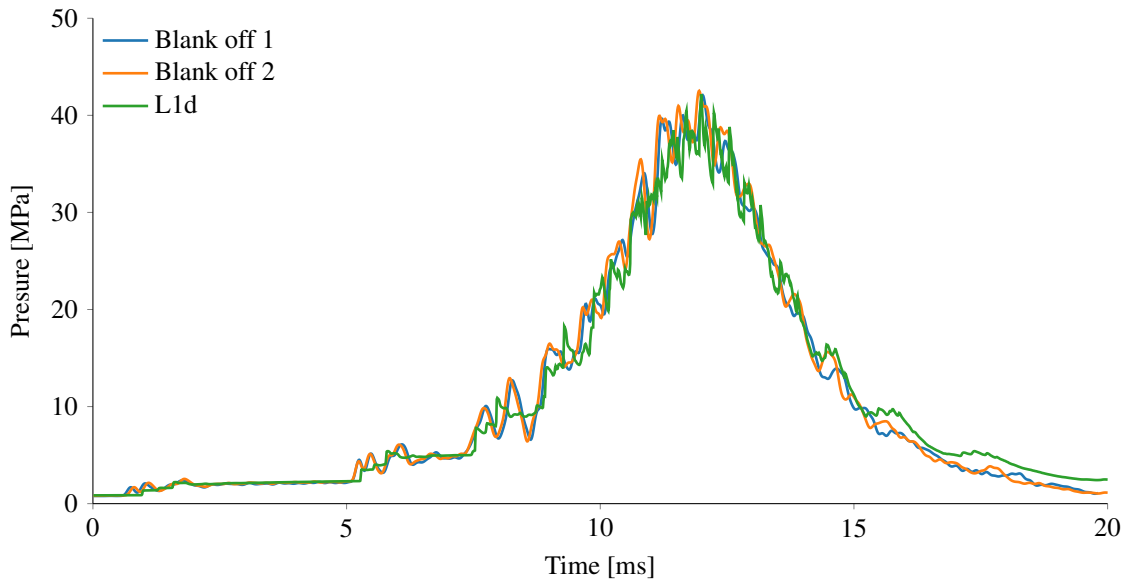


Figure 4.6.: Blank off shots performed with the same fill pressures at the rupturing diaphragm shot with comparison with L1d. The data from the blank-off shot has been filtered with a 5<sup>th</sup> order Butterworth filter with 100kHz cutoff.

Table 4.2.: Area restriction required and orifice plate size for different concentrations of helium in the driver gas; the shock tube diameter is 200mm and the area ratio is the ratio of shock tube area to orifice plate area.

Gas Concentration		Orifice Plate Diameter	Area Ratio	Expanded Mach Number
He %	Ar %	mm	—	—
0	100	200.0	1	1.00
60	40	164.7	0.678	1.95
75	25	149.0	0.555	2.25
85	15	139.2	0.484	2.45
100	0	112.5	0.316	3.08

#### 4. Driver Performance

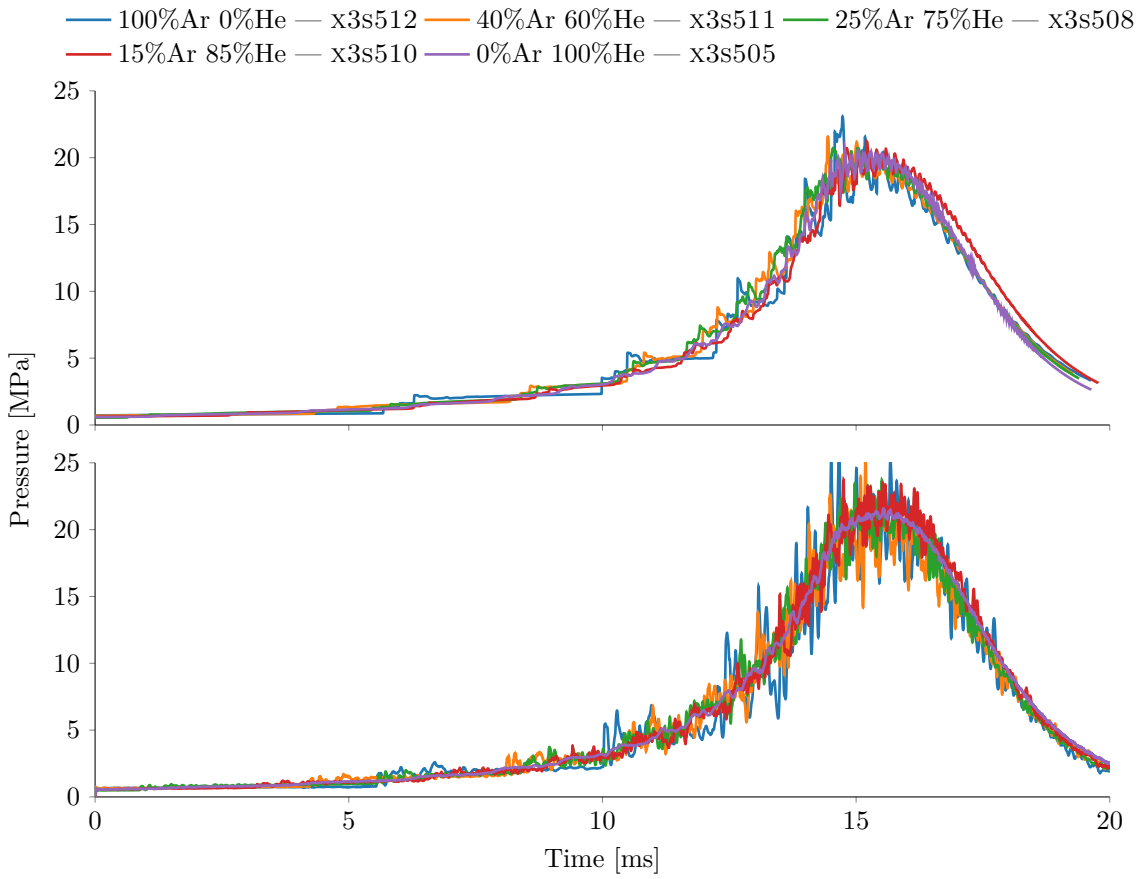


Figure 4.7.: Compression tube pressure traces for a range of driver gas compositions dictated by orifice plate sizes outlined in table 4.2. The top plot is data from the L1d simulation and the bottom plot is the corresponding experimental data. The experimental data has been filtered with a 5<sup>th</sup> order Butterworth filter with a 100kHz cutoff.

consequence would be a drop in compression tube pressure after diaphragm rupture due to the gas venting with a higher sound speed and a large (and potentially disastrous) deviation from the nominal piston trajectory.

For the orifice plates and driver gas compositions in table 4.2, and the two diaphragm thicknesses, experiments were performed with shock and acceleration tube fill pressures of 13.5kPa air and 17Pa air respectively, with the aim to match the conditions achieved by Fahy et al. in X2 [76]. The apparent rupture pressures observed in the experiments were higher than the nominal rupture pressures quoted so far, with the 2mm diaphragm rupturing at around 19.5MPa rather than 17.5MPa, and the 3mm diaphragm rupturing around 29MPa rather than 26.3MPa. This discrepancy in rupture pressures was accounted for by increasing the diaphragm hold time in L1d to 100 $\mu$ s and modifying the rupture pressure for the case of the 3mm diaphragm. Ultimately, these modifications did not result in any major change in the piston trajectory and considering some of the difficulties in operating X3 —mainly leaks into the compression tube, as well as lack of any damage or deformation to the nylon buffers —further modifications to the operating condition were not made. A direct comparison of the compression

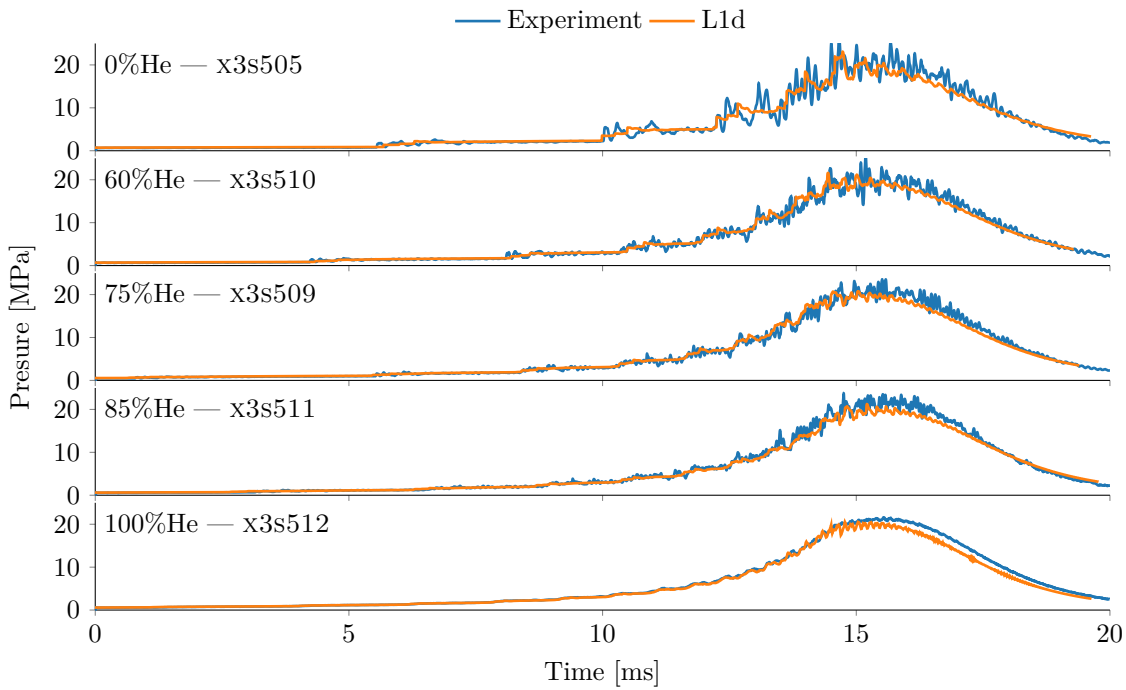


Figure 4.8.: Compression tube pressures for all driver gas compositions for the 2mm diaphragm.  
Experimental data has been filtered with a 5<sup>th</sup> order Butterworth filter with 100kHz cutoff.

tube pressure in L1d and that obtained experimentally is shown in fig. 4.8 for the 2mm diaphragm and in fig. 4.9 for the 3mm diaphragm. Generally, the rise in driver gas pressure and rupture pressure of the diaphragm is reproduced, but after diaphragm rupture L1d underpredicts the pressure in the compression tube and this is the case for all driver gas compositions and both diaphragms.

## 4.5. Driver Performance

Ultimately, the goal of X3's driver upgrade is to match the conditions used by Fahy et al. [76] to perform 1:5 scaled Hayabusa experiments in X2. Furthermore, if X3's driver can match that condition, it acts as a high benchmark for testing at whole range of enthalpies up to this benchmark. In theory, filling X3's shock tube and acceleration tube to the same pressures used by Fahy should result in the same test flow condition if the driver performs well enough to produce the required shock speeds. The driver for the scaled Hayabusa experiments in X2 used a 2mm thick cold rolled steel diaphragm with an estimated rupture pressure of 27.9MPa, a compression tube fill pressure of 92.8kPa of 100% helium, and an orifice plate that produced a Mach 2.2 flow after the steady expansion [76]. Comparatively, the driver used on X3 is similar and it was expected that shock speeds similar to those obtained on X2 could be achieved with the 3mm diaphragm and 100% helium driver gas, and the higher compression ratio of X3's driver (46kPa fill compared to 92.8kPa) would somewhat counteract the higher expanded Mach number due to the orifice plate (3.08 compared to 2.2).

#### 4. Driver Performance

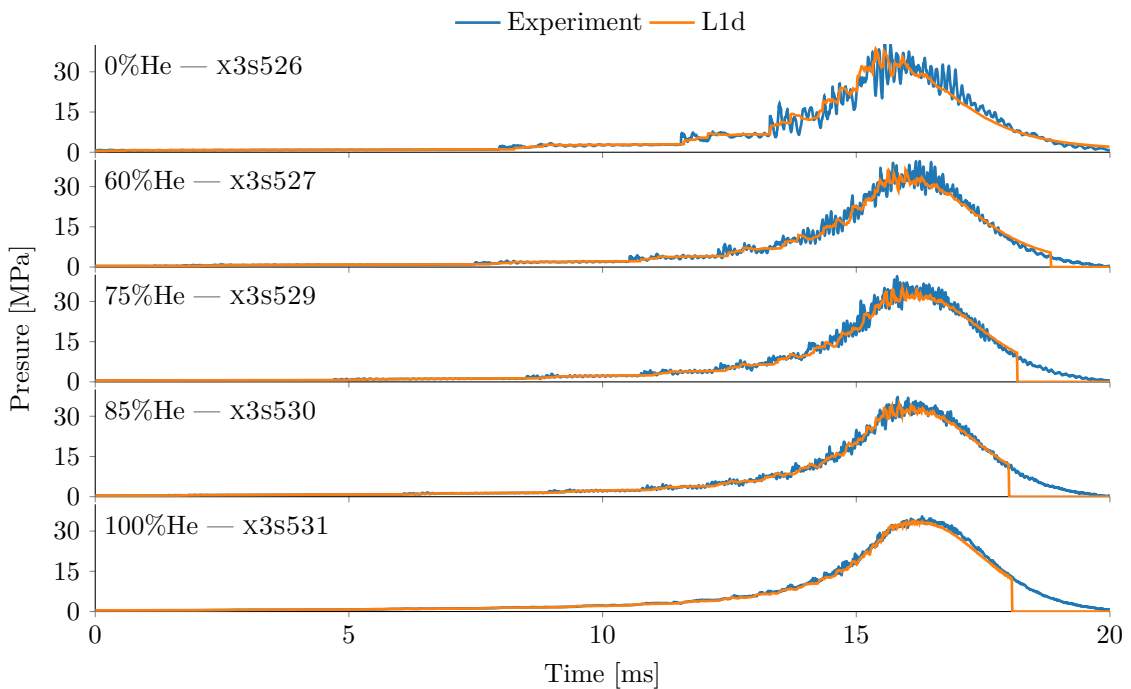


Figure 4.9.: Compression tube pressures for all driver gas compositions for the 3mm diaphragm. Experimental data has been filtered with a 5<sup>th</sup> order Butterworth filter with 100kHz cutoff.

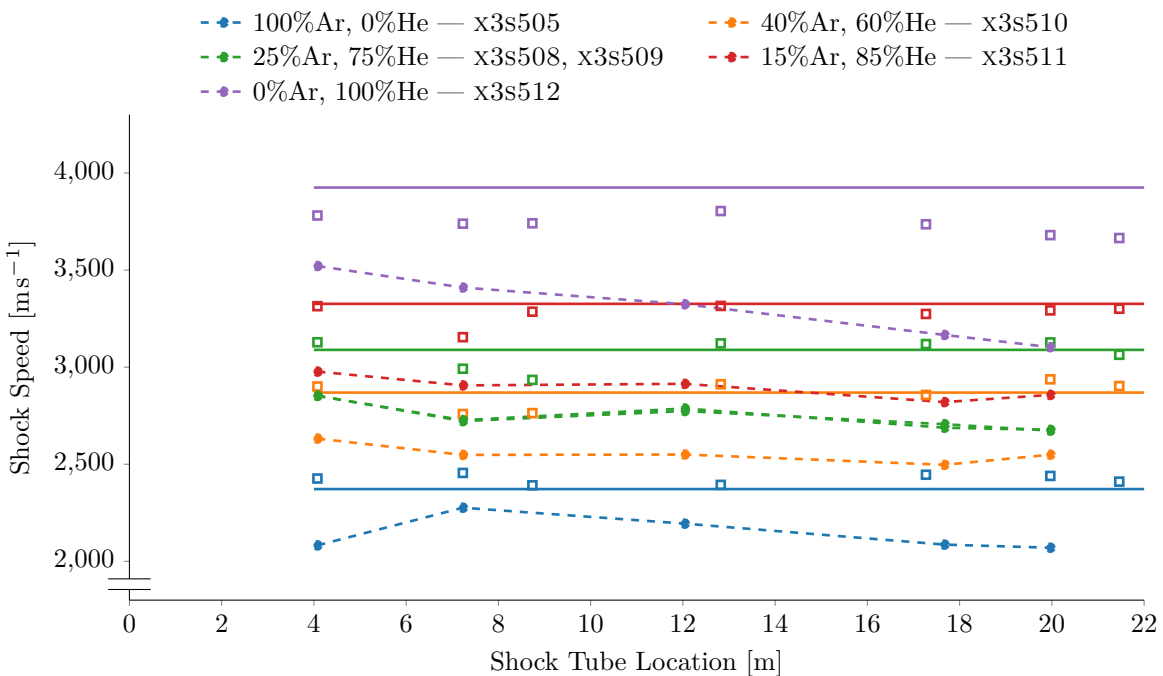


Figure 4.10.: Shock speed along the shock tube for 2mm thick diaphragms with different driver gas compositions. The horizontal line is the theoretical shock speed calculated in PITOT, the hollow square markers are the numerical results obtained in L1d and the circular markers are the experimentally measured shock speeds. The experimental data points are connected with a dashed line.

The brief comparison above does not account for other effects that can reduce the performance of X3's driver such as three dimensional flow features through the driver area change and the influence of the primary diaphragm. A comparison between analytical, numerical and experimental shocks speeds in the shock tube for the 2mm diaphragm is presented in fig. 4.10 and similar results for the 3mm diaphragm in fig. 4.11. In both of these figures, the horizontal line is the shock speed calculated in PITOT. Shock speeds calculated in L1d and those measured experimentally represented by square and circular markers respectively. In fig. 4.10, the 25%Ar, 75%He driver composition is represented twice, by shots x3s508 and x3s509. Similarly in fig. 4.11, x3s528 and x3s529 both use a 25%Ar, 75%He driver composition and x3s531 and x3s532 both use a 100%He driver composition.

In fig. 4.10 and fig. 4.11, the shock speeds calculated in L1d generally agree well with the shock speeds calculated with PITOT. Counter to this, the experimental shock speeds throughout the shock tube are consistently 15% slower for all driver gas compositions and diaphragm thicknesses. It has been speculated that there is a feature of the diaphragm opening mechanism that restricts the flow of driver gas into the shock tube and thus reduces the effective performance of the driver; this also explains the discrepancies in compression tube traces in fig. 4.8 and fig. 4.9 where the experimental pressure remains higher after diaphragm rupture than in L1d.

Wall pressure traces for x3s505 and x3s526, which use a 100% argon driver and 2mm and 3mm diaphragms respectively, are shown in fig. 4.12 and fig. 4.13. Despite the discrepancy in shock speeds for all the driver conditions, L1d does a reasonable job at predicting the initial pressure behind the shock, although it does start to deviate from experimental measurements when the driver gas arrives at the wall sensor, as shown by the experimental pressure increase at ST2 and ST3 in fig. 4.12. This reinforces the theory that L1d does not accurately capture a phenomena (e.g. oblique shocks) that occurs through primary diaphragm and this reduces the similarity between simulation and experiment.

Static wall pressures measured for the remaining shots are presented in appendix B along with static wall pressures calculated in L1d. Overall, L1d matches the post-shock pressure well except for x3s531 in fig. B.10 and x3s532 in fig. B.11, where L1d over predicts the post-shock pressure at the end of the shock tube by approximately 30%. Additionally, for shots with a 100% helium driver (x3s512, x3s531 and x3s532), L1d simulations result in an upstream facing shock just behind the contact surface which processes the expanded driver gas to match the gas properties at the contact surface, suggesting a flow process of the driver gas is not captured in L1d. As the experimental shock speeds are slower than those calculated by L1d, it is expected that L1d should also predict higher static pressures, which it does not except for the mentioned cases. The target shock speed of  $4505\text{m s}^{-1}$  which was obtained by Fahy et al. [76] using the same shock tube fill pressure was not obtained with the newly developed driver operating conditions although theoretical predictions suggested that the condition was achievable.

#### 4. Driver Performance

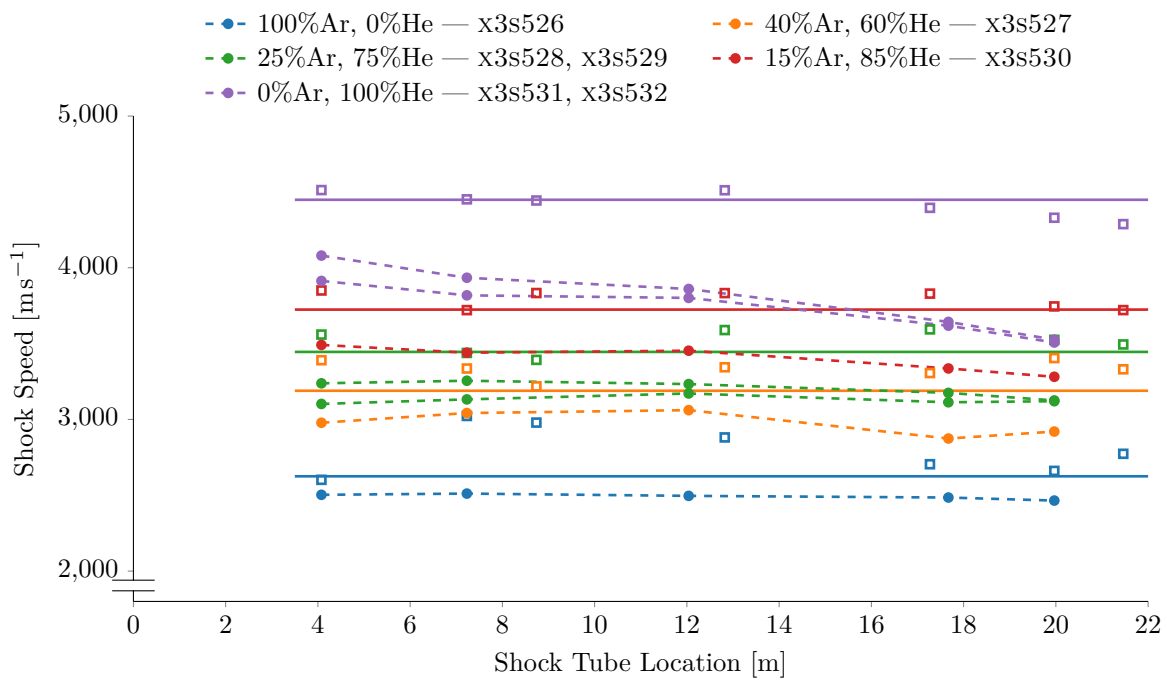


Figure 4.11.: Shock speed along the shock tube for 3mm thick diaphragms with different driver gas compositions. The horizontal line is the theoretical shock speed calculated in PITOT, the hollow square markers are the numerical results obtained in L1d and the circular markers are the experimentally measured shock speeds.

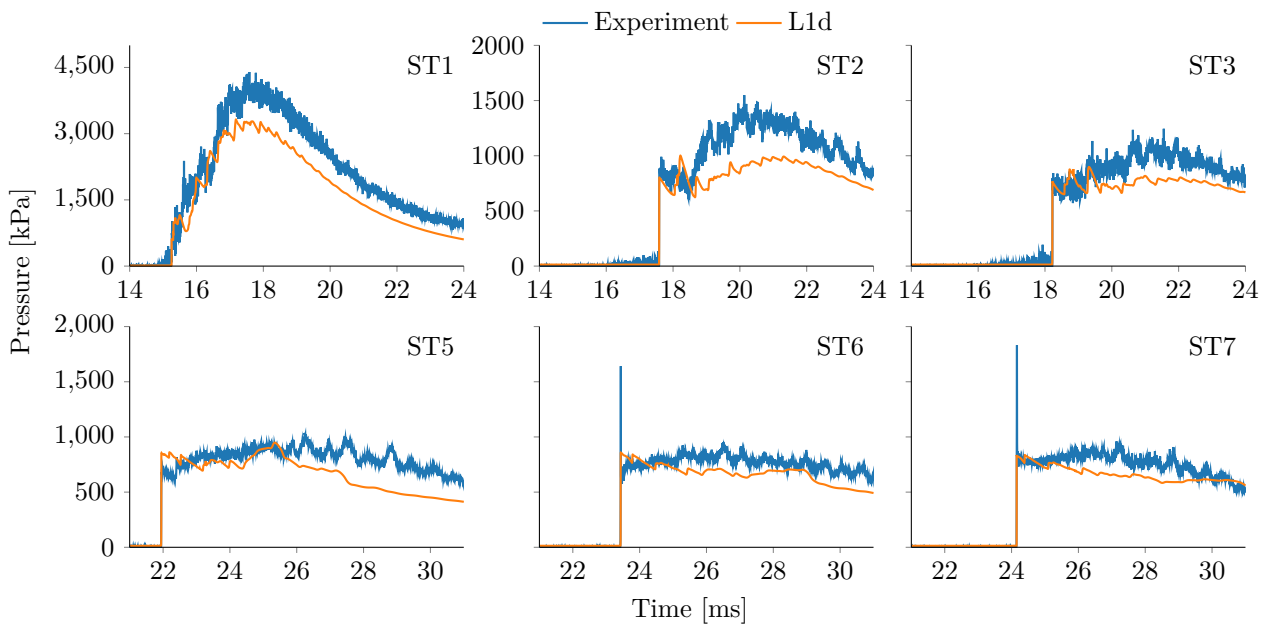


Figure 4.12.: Wall pressure traces along the shock tube for x3s505 which uses a 100% argon driver and 2mm diaphragm. The experimental data has been filtered with a 5<sup>th</sup> order Butterworth filter with a 250kHz cutoff.

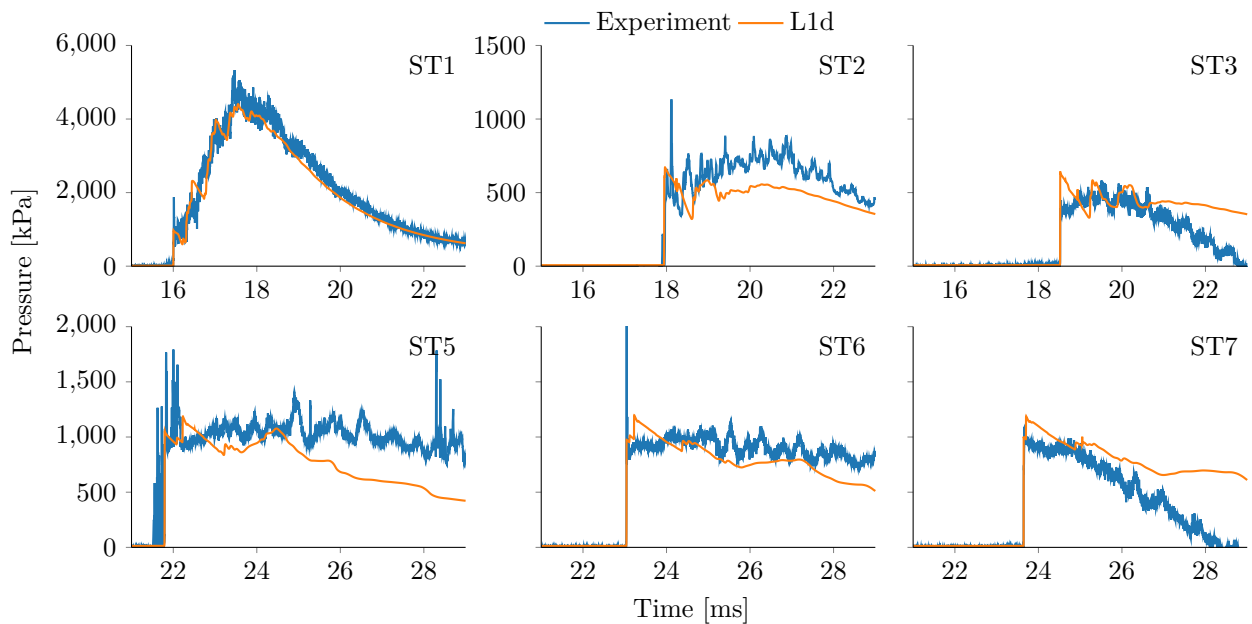


Figure 4.13.: Wall pressure traces along the shock tube for x3s526 which uses a 100% argon driver and 3mm diaphragm. The experimental data has been filtered with a 5<sup>th</sup> order Butterworth filter with a 250kHz cutoff. A median filter with a window of 100 data points has been applied to the sensor of ST2 as it was showing erratic values at the maximum voltage. The sensors at ST3 and ST7 were beginning to fail and the sudden drop in pressure is a feature of the sensor, not the gas pressure.

## 4.6. Acceleration Tube

The shock speeds in the acceleration tube for all shots with both diaphragms are presented in fig. 4.14 and fig. 4.15. L1d simulations of the acceleration tube are not included as they significantly overpredicted the shock speed along the acceleration tube, similar to the analytical calculation. At the time the shots with 2mm diaphragms were performed, there were issues with the pumping system which meant the target pressure of 17Pa could not be obtained and it becomes difficult to identify trends in the shock speeds. The performance in the acceleration tube can still roughly be quantified as deviations from the target pressure were not substantial except for x3s512. Generally, the shock speeds are much lower than the analytical predictions and the experimental shock speed attenuates by approximately  $1000\text{ m s}^{-1}$  over the length of the acceleration tube for both diaphragms, a significant reduction from the expected performance. The shock speeds for the 3mm diaphragm in fig. 4.15 were measured with acceleration tube fill pressures close to 17Pa and more consistent trends can be observed. As with the 2mm diaphragm, the experimental shock speeds are significantly lower than the analytical predictions but the same relative increases can be observed, e.g. the relative shock speed increase from x3s526 and x3s527 compared to the shock speed increase from x3s527 and x3s528 appear to be the same experimentally and theoretically. The first sensors used to measure the shock speed are AT3 and AT4 which find the first shock speed measurement 9m from the tertiary diaphragm, so the exact level of

#### 4. Driver Performance

shock attenuation is unknown. It is also noted that sensor AT1 was susceptible to vibrations and could not be reliably used to identify shock arrival.

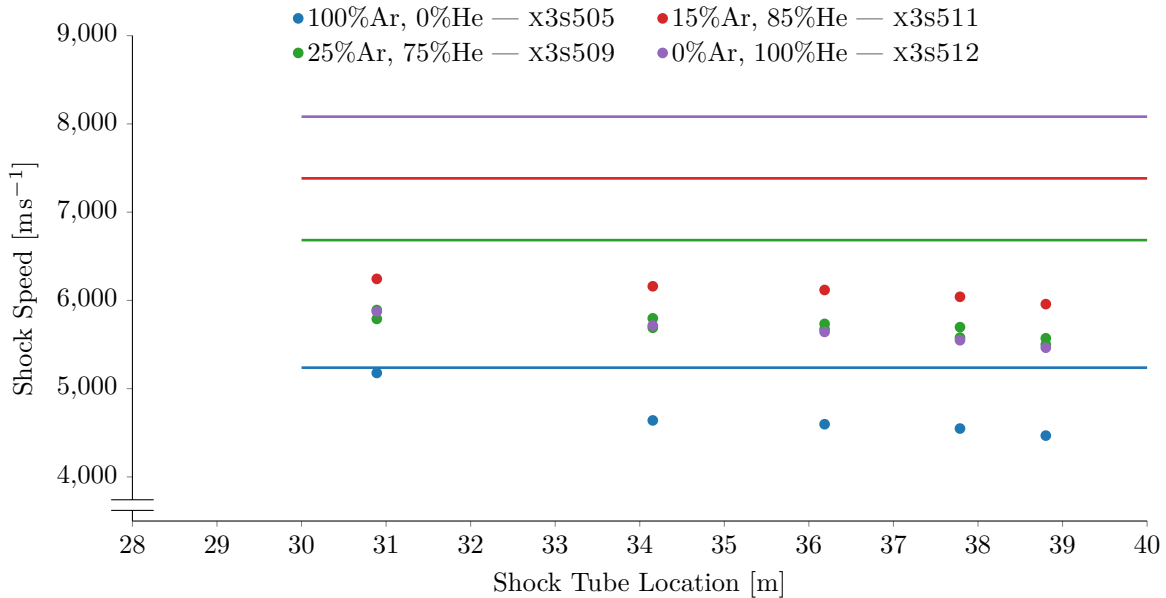


Figure 4.14.: Shock speeds in the acceleration tube for different driver gas compositions using a 2mm thick diaphragm. Difficulties with leaks and pump rates meant that the target acceleration tube pressure of 17Pa was not achieved for several shots. Actual acceleration tube pressures are as follows; x3s505 - 21Pa, x3s508 - 28Pa, x3s509 - 25Pa, x3s511 - 17Pa, x3s512 - 40Pa

Figure 4.16 and fig. 4.17 contain the wall pressure traces along the acceleration tube for shots x3s505 and x3s526 respectively. The orange line in the plots for AT6, AT7 and AT8 is the theoretically calculated test gas pressure entering the nozzle. For all cases the theoretical prediction underestimates the static pressure, which is consistent with the slower experimental shock speeds and indicates the test gas is not fully expanded. In addition to the discrepancy in pressures, there is a pressure gradient in the test gas static pressure, which is attributed to the boundary layer impeding the unsteady expansion [95]. The increase in noise in the pressure trace is likely to be due to the downstream end of the expansion at the tertiary diaphragm arriving at the pressure sensor, or according to Jacobs [140] who found a reduction of noise when performing laminar simulations of an expansion tube, the increase in noise may be due to the boundary layer transitioning to turbulent.

As with the shock tube, the effect that the mass of the tertiary diaphragm has on the performance of the acceleration tube is not quantified. Work by Roberts et al. [141] found that the diaphragm could considerably influence the quality and steady duration of the test gas and one should use the thinnest possible diaphragm. Due to X3's size, a diaphragm capable of withstanding the pressure difference due to the required fill pressures (in this case to act as a boundary between 13.5kPa and 17Pa) will need to be thicker than a diaphragm used in a smaller facility, such as X2 which, is disadvantageous for X3 and trying to achieve high enthalpy conditions.

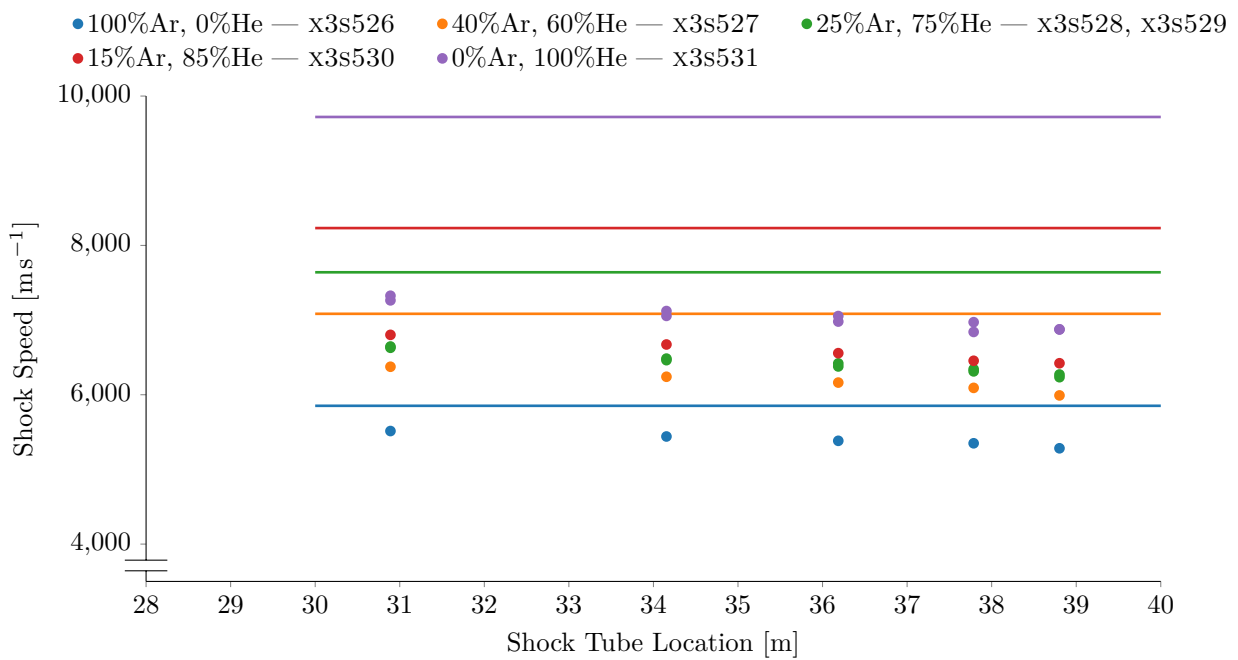


Figure 4.15.: Shock speeds in the acceleration tube for different driver gas compositions using a 3mm thick diaphragm. The difficulties in obtaining the target acceleration tube fill pressure encountered in earlier experiments had been solved, so all shots were performed at the target fill pressure, 17Pa.

## 4.7. Secondary Driver

At this point a series of driver configurations for X3 had been tested with a shock tube fill pressure of 13.5kPa and acceleration tube fill pressure of 17Pa and the resulting performance had been quantified. Unfortunately, no driver configuration produced the shock speeds required to match the 1:5 scale Hayabusa condition used by Fahy et al. in X2 [76], and as the operating conditions were limited by the driver configuration, either the hardware, or the test condition needed to be changed. This section will look at the attempts to incorporate a secondary driver in an attempt to increase performance. The configuration of X3 was changed to accommodate a secondary driver as shown in fig. 4.18.

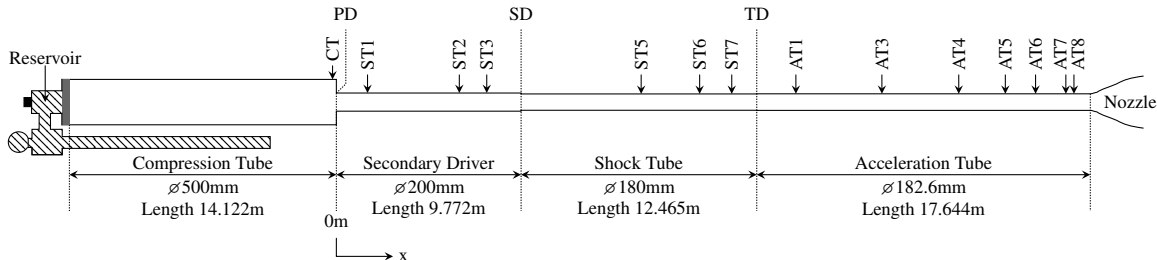


Figure 4.18.: Configuration of X3 with 3 diaphragms and the tube separated into four sections; compression tube, secondary driver, shock tube and acceleration tube.

#### 4. Driver Performance

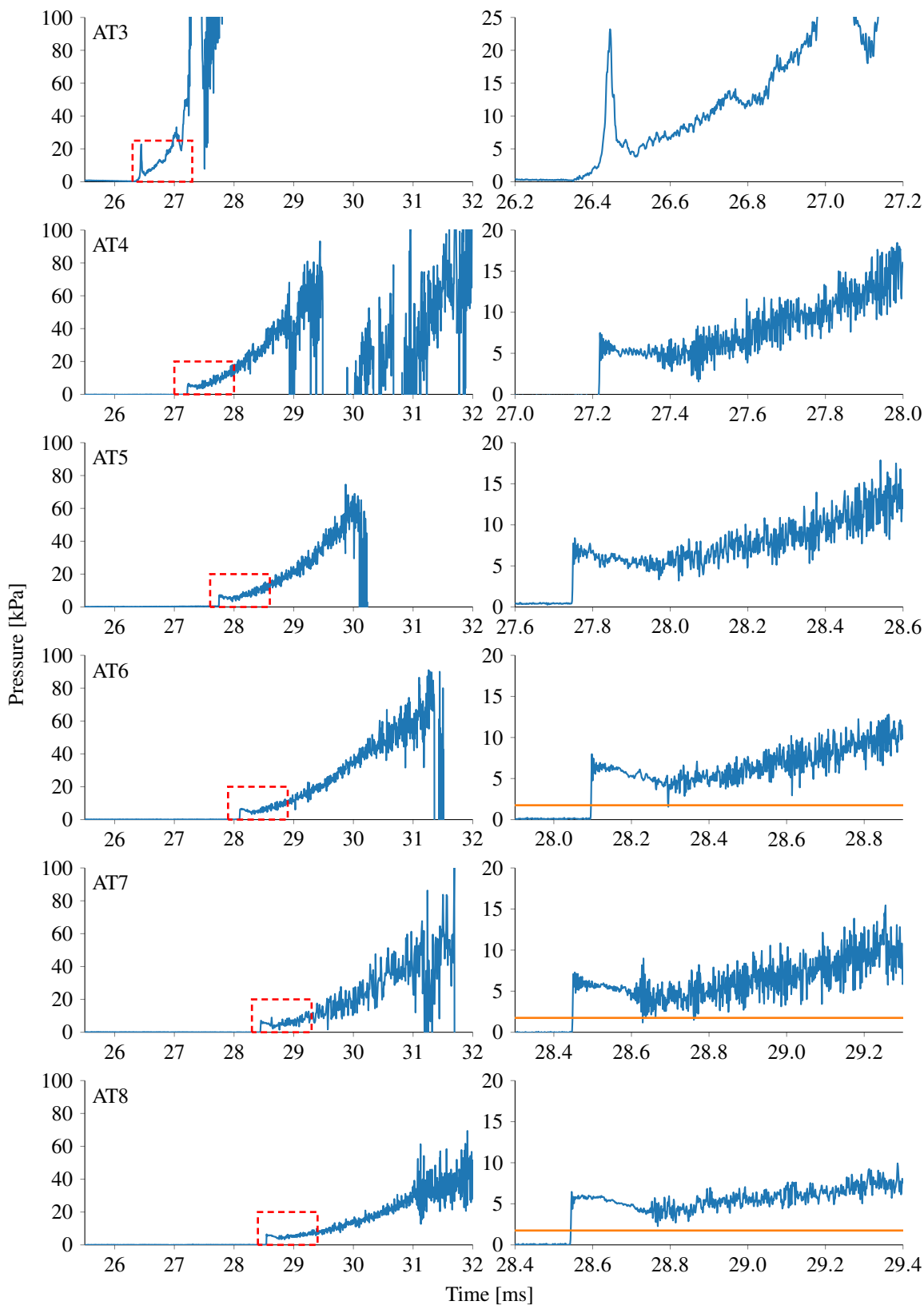


Figure 4.16.: Acceleration tube wall static pressure traces for x3s505. The plots on the right present the region outlined by the dashed red box and show the acceleration tube gas and arrival of the test gas. The horizontal orange line is the theoretical prediction calculated with PITOT. Data is filtered with a 5<sup>th</sup> order Butterworth filter with a 250kHz cutoff.

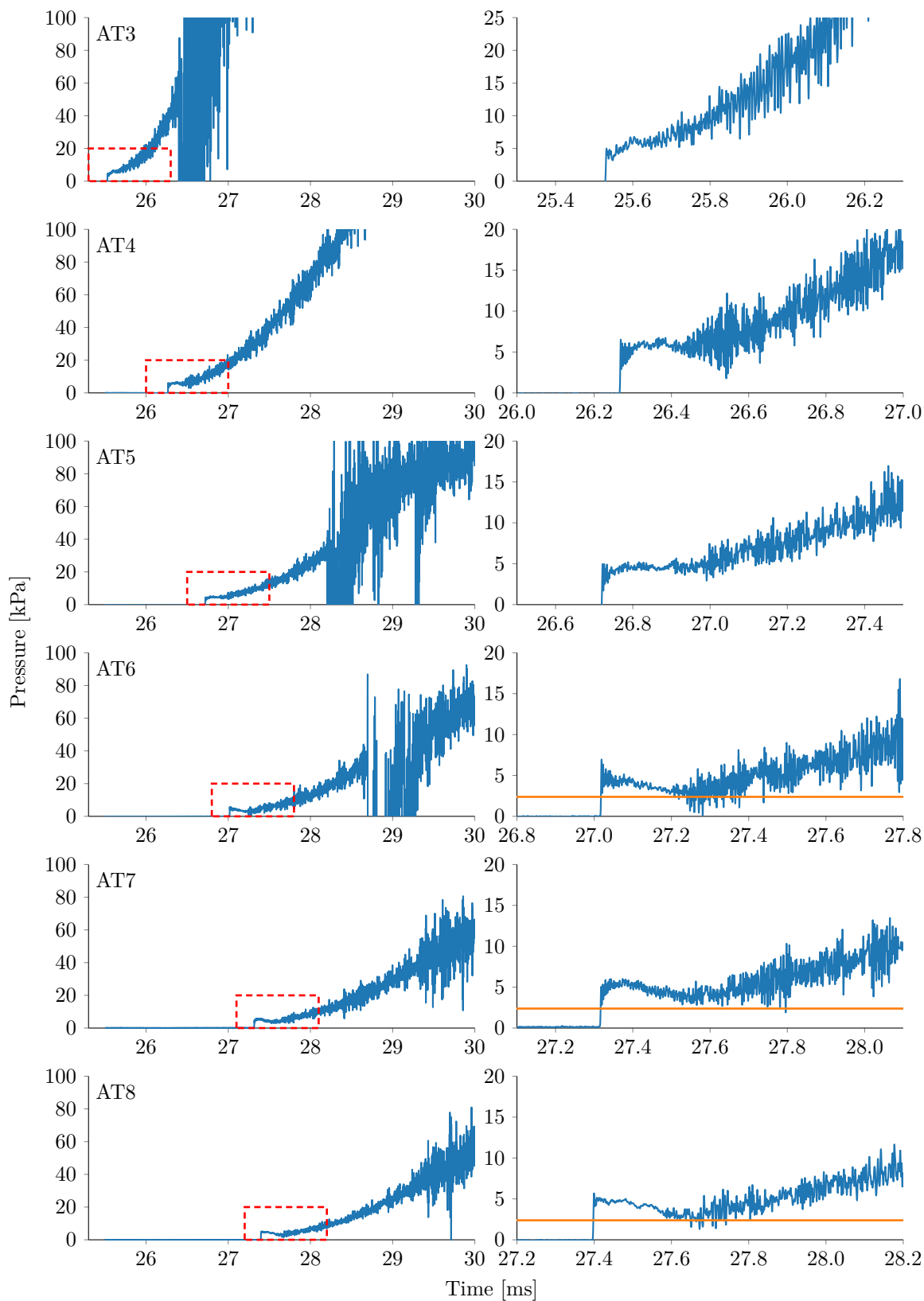


Figure 4.17.: Acceleration tube wall static pressure traces for x3s526. The plots on the right present the region outlined by the dashed red box and show the acceleration tube gas and arrival of the test gas. The horizontal orange line is the theoretical prediction calculated with PITOT. Data is filtered with a 5<sup>th</sup> order Butterworth filter with a 250kHz cutoff.

#### 4. Driver Performance

$s$  = shock  
 $rs$  = reflected shock  
 $cs$  = contact surface  
 $sx$  = steady expansion  
 $usx$  = unsteady expansion  
 $u + a$  = reflected  $u + a$  characteristic

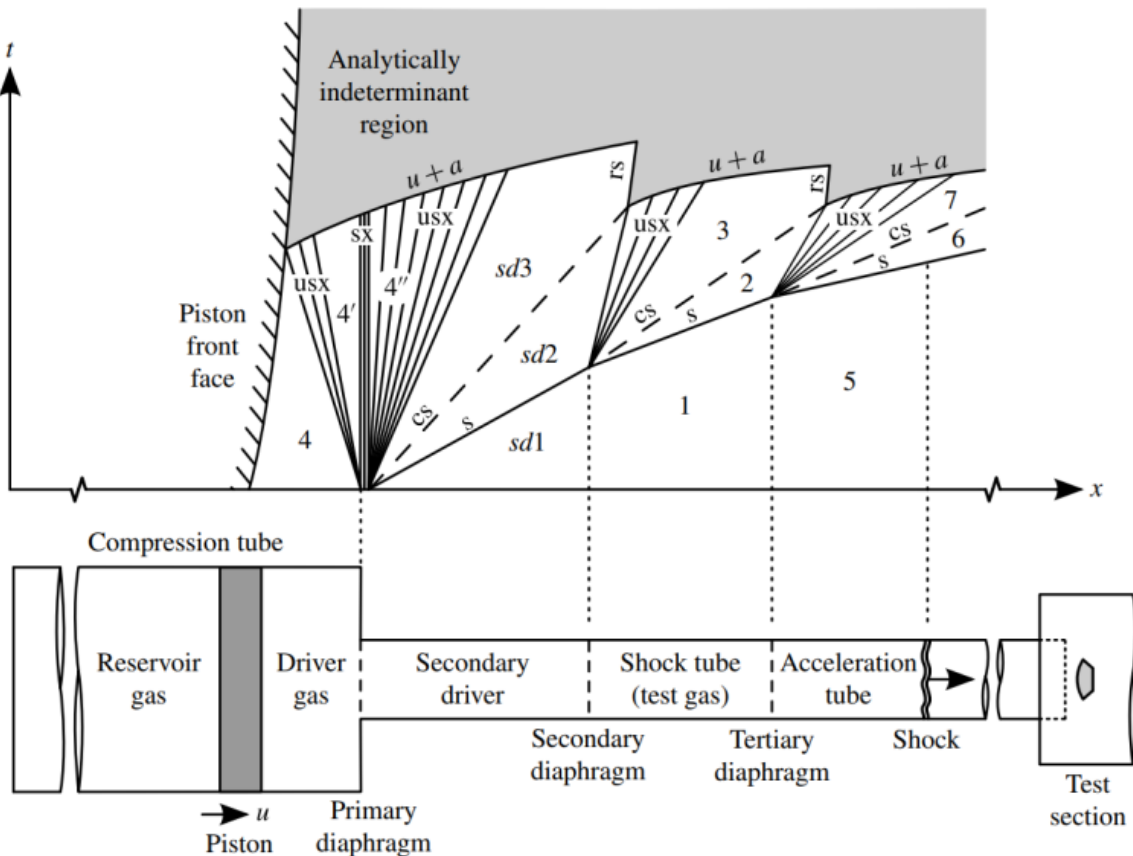


Figure 4.19.: Idealised distance-time diagram of a free piston driven expansion tube with a secondary driver (taken from [142]).

The secondary driver can be used to increase the shock strength through the test gas for high enthalpy conditions, or as a method to prevent the transmission of flow disturbances from the driver for low enthalpy conditions [142]. An idealised distance-time diagram of an expansion tube with a secondary driver is presented in fig. 4.19 which is a modified version of fig. 2.11. The secondary driver is an additional gas slug, typically helium, located between the driver gas and the test gas and essentially acts as the driver to the test gas once it has been processed by the shock produced from the driver. The shock strength through the test gas can be determined by the properties of the shock processed secondary driver gas (state  $sd2$  in fig. 4.19), and considering that state  $sd2$  and state  $sd3$  have the same pressure and velocity, as long as the sound speed of state  $sd3$  is higher than state  $sd2$ , the secondary driver will drive a stronger shock through the test gas than the primary driver would do by itself.

If a reflected shock arises at the secondary diaphragm, the performance increase from the addition of the secondary driver will be lost [142]. For a given secondary driver fill pressure, there is some shock tube fill pressures where the unsteady expansion of the shock processed secondary driver gas (state  $sd2$ ) will lose its strength, and for higher pressures a reflected shock will form at the interface. Using ideal gas assumptions, Gildfind et al. [142] found that the density of the secondary driver gas should be

greater than 0.9 times the density of the test gas, i.e.  $\rho_{sd1} > 0.9\rho_1$ , and for the current case where the shock tube is filled to 13.5kPa, a helium secondary driver should be filled to at least 87.9kPa to avoid a reflected shock. For a select condition, Gildfind et al. [142] also found that the addition of a secondary driver for performance increase has diminishing returns as the test gas density is increased. For the 100% helium driver on X3 and the fill conditions used so far, PITOT was used to calculate the shock speed through the test gas when a helium secondary driver was added and the results are displayed in fig. 4.20. Included in fig. 4.20, are the secondary driver fill pressures for which a reflected shock will occur at the gas interface, and on the other end of the scale, the fill pressure where a reduction of sound speed from state  $sd3$  to  $sd2$  is observed and the performance of the secondary driver drops below that of just the primary driver. For intermediate fill pressures the performance of the driver increases with the addition of the secondary driver, but the increase in shock speed is minimal due to the high density of the initial test gas fill condition.

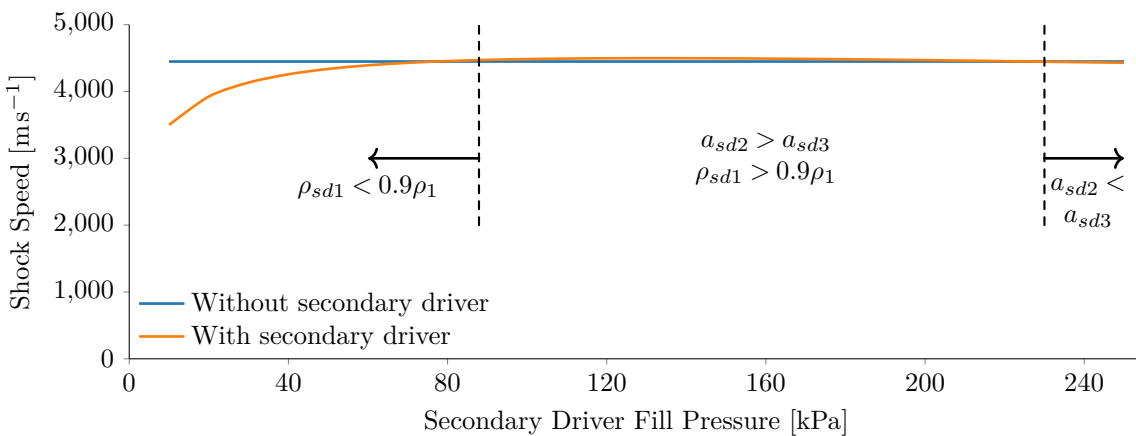


Figure 4.20.: Effect of using a helium secondary driver on shock tube shock speed for condition x3s531, which uses a 100% helium driver, 3mm diaphragm and shock tube fill pressure of 13.5kPa. The flat blue line is the shock speed with no secondary driver and the orange line is the shock speed in the shock tube with the inclusion of a helium secondary driver. The region where  $a_{sd2} > a_{sd3}$  and  $\rho_{sd1} > 0.9\rho_1$  are the secondary driver fill pressure where a performance increase is inspected.

A survey of different secondary driver fill pressures was also run in L1d. The secondary diaphragm hold time was also varied to simulate the effect of the diaphragm mass, as to satisfying the density ratio of 0.9 a relatively thick diaphragm would be required and performance losses through the diaphragm would be expected to rise. The shock speeds calculated by the L1d simulations are shown in fig. 4.21 arranged by fill pressure in the secondary driver. As suggested in fig. 4.21, for the PITOT calculation, there is not a significant variation in shock tube shock speed with increasing secondary driver fill pressure and the effect of the diaphragm hold time seems to be minimal. All the L1d simulations result in a reduction of shock speed on the order of 10–20% at the end of the shock tube with the addition of a secondary driver which is contrary to the PITOT results which result in matched or slightly improved shock speeds, and may be due to driver wave processes.

#### 4. Driver Performance

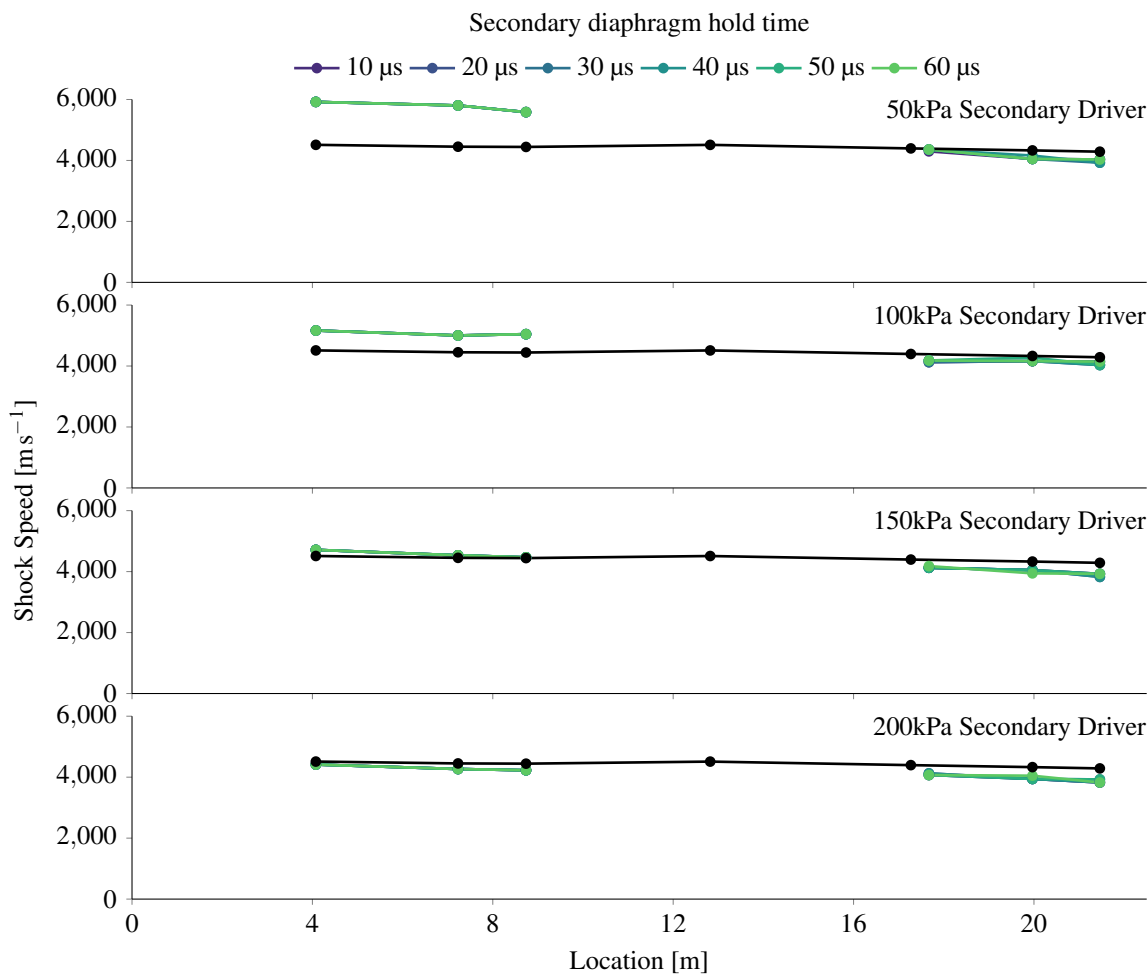


Figure 4.21.: Shock speeds calculated in L1d when a secondary driver is introduced to a driver with 100% helium and a 3mm diaphragm.

Experimentally, the thickness of the secondary diaphragm is restricted to the minimum that can withstand the pressure differential when the tubes are filled. The secondary driver fill pressures were chosen to be as close as possible to the burst pressure of the diaphragm used for a particular experiment. The shock speeds obtained with various combinations of diaphragm and fill pressure are presented in fig. 4.22, and with the exception of x3s513, there was no obvious improvement to the shock speed in the shock tube. In x3s513, the secondary driver was not filled to high enough pressure and the reduction in shock speed is assumed to be due to losses through the secondary diaphragm. In the acceleration tube, shock speeds from the experiments with 3mm diaphragms show that the shock speed is matched, or in the case of x3s535 slightly improved, but the variation is still within the usual shot to shot variation and the apparent improvement is not conclusive. The shock speed in the acceleration tube is not shown for the 2mm diaphragm driver with a secondary driver because of inconsistencies with the acceleration tube fill pressure, and thus no meaningful comparison in shock speed can be made. Additionally, leaks into the compression tube occurred for x3s535, x3s536 and x3s537 and the effect of this on shock speed is unknown.

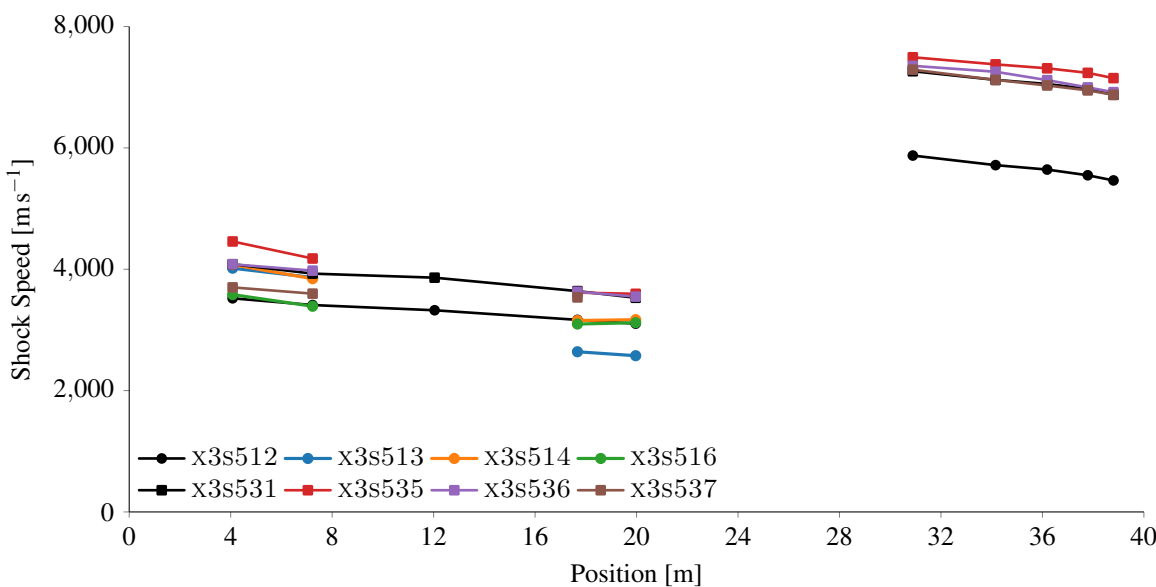


Figure 4.22.: Experimental shock speeds in the shock tube and the effect of various secondary driver configurations for the 2mm and 3mm diaphragms with 100% helium driver gas. Shock speeds in the acceleration tube for x3s513, x3s514 and x3s516 are not shown due to the experiments being conducted with different acceleration tube fill pressures.

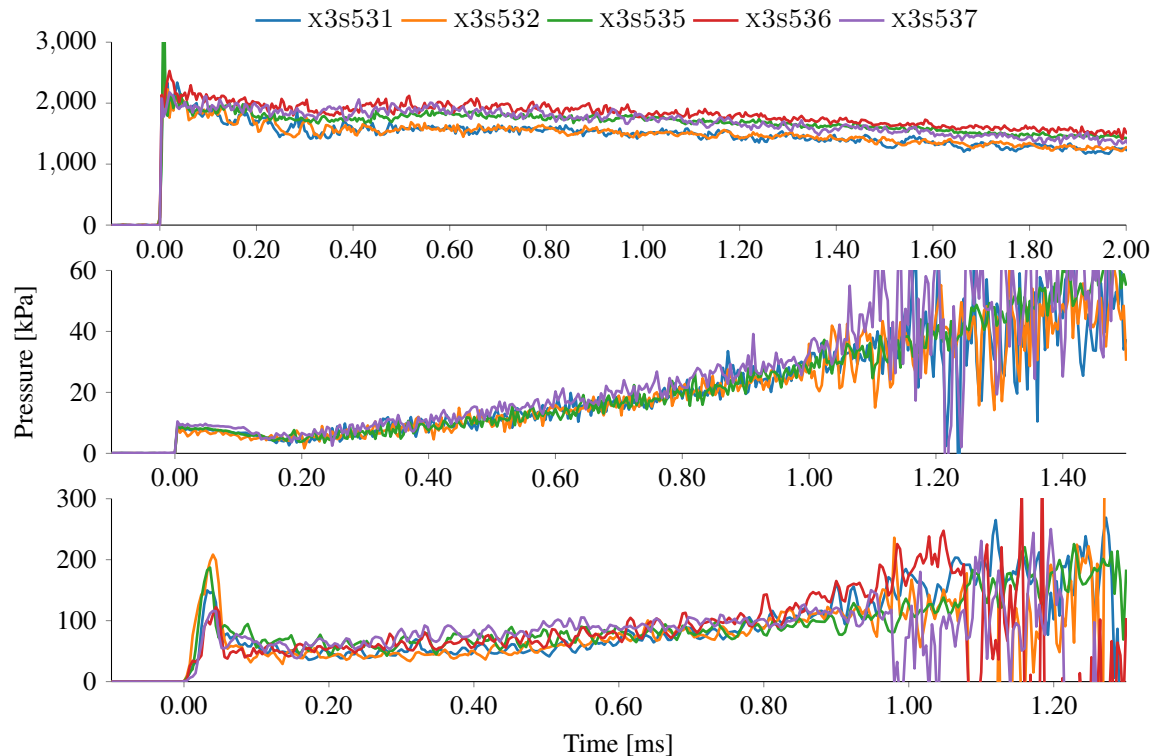


Figure 4.23.: Wall pressure traces in the shock and acceleration tubes and Pitot pressure trace taken at the exit of the nozzle. The top plot contains the wall traces at ST6, the middle plot is the wall pressure at AT8 and the bottom plot is Pitot pressure at the nozzle exit. The Pitot pressure measurement was taken with an offset from the tube centreline of 20mm. All data has been filtered with a 5<sup>th</sup> order Butterworth filter with 250kHz cutoff.

#### 4. Driver Performance

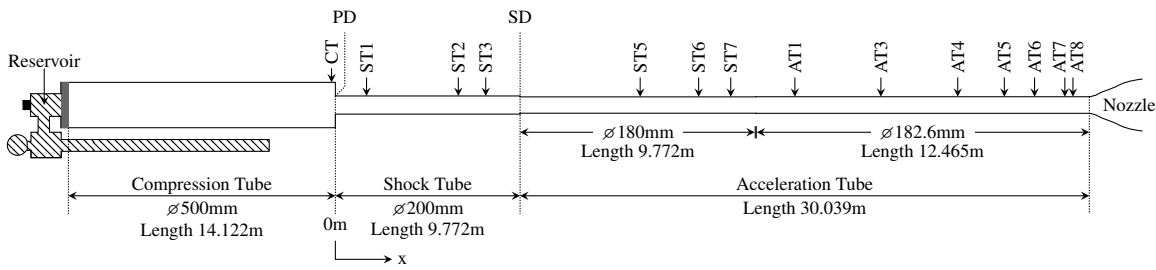


Figure 4.24.: Configuration of X3 with a short shock tube, and correspondingly lengthened acceleration tube.

Pressure traces taken at various locations in X3 are shown in fig. 4.23. The trend for the wall pressure at ST6 is that the shots with a secondary driver have a higher pressure, possibly due to the orifice plate used for a 100% driver gas which restricts the flow of driver gas behind the test gas slug. For the pressure traces taken at AT8 there is no discernible difference and at the nozzle exit it appears that the shots with a secondary driver have slightly higher pressure, although the magnitude of the noise makes it difficult to reach a concrete conclusion. Overall the added complexity to the flow process and difficulty in performing experiments with a secondary driver did not justify the small performance increase observed in fig. 4.22 and fig. 4.23.

The target condition in this section requires a relatively high pressure shock tube fill pressure, for which any performance increase with a secondary driver would be marginal. This has been confirmed experimentally, with no notable performance increase observed with the addition of a secondary driver. For operation of this driver at lower density conditions, it is expected that a secondary driver will increase the performance but it remains unknown how close to theory the secondary driver will behave and what the influence of the diaphragm is for low density conditions.

## 4.8. Shock Tube Length

In fig. 4.11 the 100% helium driver used during x3s531 provides the fastest shock speed but also has the largest shock attenuation, a reduction of  $400\text{ms}^{-1}$  throughout the shock tube compared to x3s530 which only attenuates  $230\text{ms}^{-1}$ , which may be due to the small orifice plate that was necessary to tune the piston. High speed viscous effects have not been ruled out but shock speeds calculated in L1d did not show a significant increase in shock speed attenuation (see fig. 4.11). Experiments with a shortened shock tube were performed to investigate if any improvement to the flow condition could be found. The configuration of the facility is shown in fig. 4.24. The shock speeds measured throughout the tube are shown in fig. 4.25 with the acceleration tube now beginning at the secondary diaphragm station. The shock speed measured in the new acceleration tube shows an increase in shock speed compared to the original configuration in x3s531, although the attenuation throughout the new longer acceleration

tube results in no net gain in shock speed at the entrance of the nozzle. The effect of the area change at the tertiary diaphragm station on the flow has not been quantified.

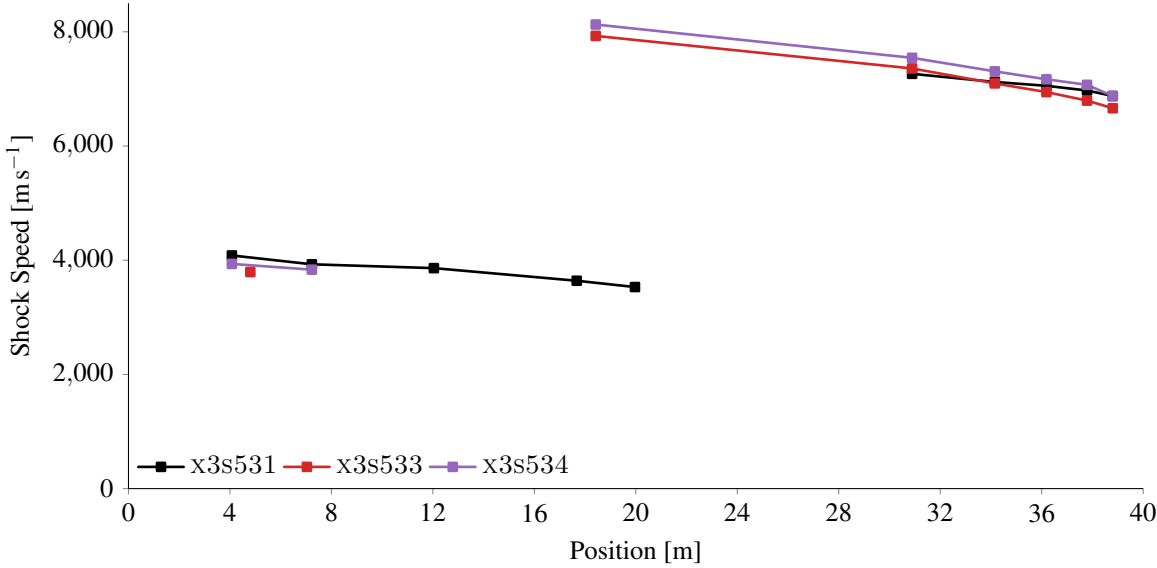


Figure 4.25.: Comparison of shock speeds measured in the shock and acceleration tubes for both configurations: long shock tube (x3s531) and short shock tube (x3s533 and x3s534).

Wall pressure traces at AT8 and Pitot pressure traces at the nozzle exit are presented in fig. 4.26 for equivalent experiments with long and short shock tubes. At AT8, the wall pressure just behind the shock exhibits the same behaviour for both shock tube configurations, but the test gas pressure rises quicker for shots with a long shock tube, x3s531 and x3s532, compared to shots with a short shock tube, x3s533 and x3s534. It also appears that using a short shock tube delays the noise arrival in the pressure traces at AT8, but as the noise arrival is not consistent across different experiments, it is difficult to conclude whether a delay in noise arrival is actually caused by the different shock tube length. The same delay in noise arrival also exists in the Pitot pressure traces in fig. 4.26.

Axisymmetric simulations of X3's acceleration tube of a Mach 10 scramjet condition performed by Gildfind et al. [95] found that pressure in the test gas slug increases as the boundary layer develops. For the case of the longer shock tube the test gas has less distance to travel before reaching AT8 and it is expected that less boundary layer will have developed compared to experiments with a short shock tube. Following the findings by Gildfind it is consistent that the less developed boundary layer that should occur with the long shock tube has the test gas having a higher pressure.

McGilvray et al. [143] observed a drop in Pitot pressure during the test time (but not a drop in static pressure) that was attributed to boundary layer transition in the acceleration tube for low enthalpy scramjet conditions in X3. Experiments with a short shock tube conducted by Toniato [96] resulted in the conclusion the boundary layer had converged at the centre of the tube by the end of the acceleration tube. The same phenomena observed by McGilvray et al. [143] was not apparent in Pitot pressure measurements at the exit of the nozzle. Analytical work by Peterson and Hanson [144] showed that a

#### 4. Driver Performance

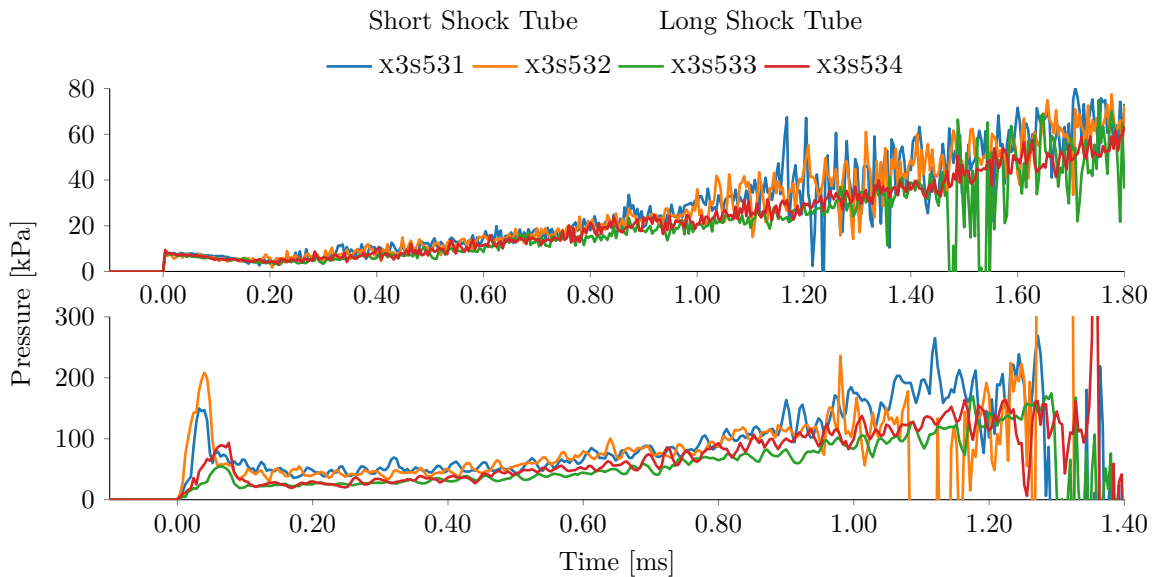


Figure 4.26.: The top figure is the wall pressure trace at AT8 in the acceleration tube just before the nozzle entrance and the bottom figure is Pitot pressure at the exit of the nozzle. The Pitot pressure measurement is offset from the tube centreline by 20mm, All data has been filtered with a 5<sup>th</sup> order Butterworth filter with a 250kHz cutoff frequency.

turbulent boundary layer is thicker than a laminar one at the same time after shock passage and that transition is more likely to occur earlier in higher pressure experiments. This suggests that the flow in the experiments conducted by Toniato [96] with a short shock tube have transitioned to turbulence wheras the acceleration tube flow for the current operating conditions do not, although further work is required to confirm this hypothesis, possibly by taking heat transfer measurements along the tube wall, similar to that done by McGilvray et al. [143].

The two different shock tube lengths tested in this section do not show any significant difference in behaviour except for the short shock tube having a slightly lower test gas pressure due to a thicker boundary layer. Pressure traces at AT8 and Pitot pressure traces at the nozzle exit also show that using a short shock tube delays the arrival of noise, but the signals are not consistent enough to make concrete conclusions that the shock tube length actually influences noise arrival times.

## 4.9. Stronger Diaphragms

The diaphragms used in the earlier sections of this chapter were inherited from experimental campaigns performed by Sancho [130] and material properties were not known. New primary diaphragms were subsequently used with a higher yield and ultimate strength which resulted in higher rupture pressures and the piston deviating from it's designed tuned trajectory. The discrepancy between the two diaphragms for the same fill conditions is shown in fig. 4.27 with the rupture pressure increasing

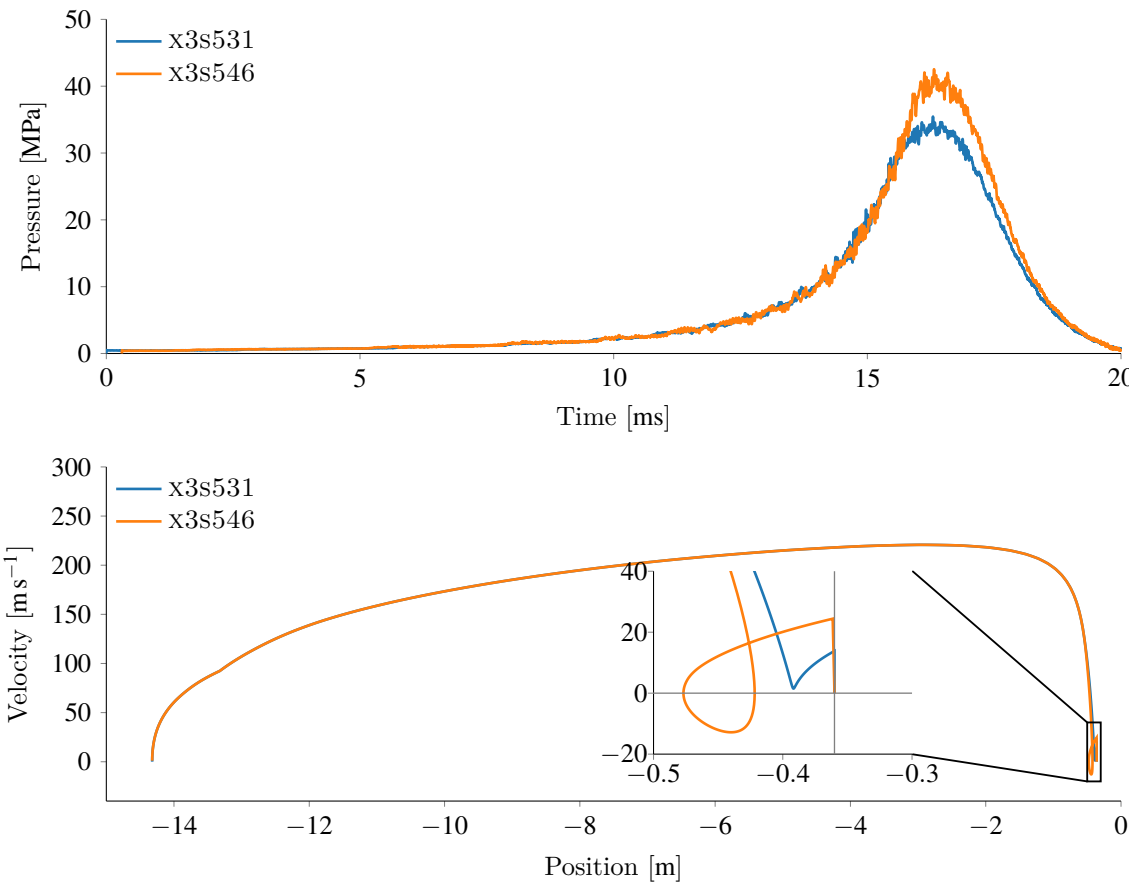


Figure 4.27.: Top: Compression tube pressure traces for two primary diaphragms of different properties: x3s531 uses the original diaphragm and x3s546 uses a stronger diaphragm. Pressure traces have been filtered with a 5<sup>th</sup> order Butterworth filter with a cutoff frequency of 250kHz. Bottom: Calculated piston trajectory in L1d using the two different rupture pressures of 29MPa and 35MPa for the original and new primary diaphragms respectively. The vertical black line is the end of the buffers in the model.

from 29MPa in x3s531 to approximately 35-37MPa in x3s546 and the maximum pressure increasing from 35MPa to 42MPa, an increase of 20–30% for both pressures. The effect on piston trajectory calculated in L1d can be seen in the bottom graph in fig. 4.27 where the orange curve is the trajectory due to the higher rupture pressure. Increasing the pressure in front of the piston causes the piston to rebound up the compression tube before accelerating downstream again as the driver gas vents and the L1d model predicting the piston hitting the end of the compression tube at  $20\text{ m s}^{-1}$ .

Attempts were made to obtain a tuned piston condition for the new diaphragms, since the extra rupture pressure would enable faster shock speeds and therefore test conditions closer to the target condition. L1d was used to find tuned conditions by increasing the reservoir pressure and reducing the driver fill pressure but the length of the compression tube and the uncertainty in piston location mentioned in section 3.8.2 meant that the calculated inflection point was too close to the end of the compression tube, (i.e. leaving a very small required buffer length) and the piston was most likely directly impacting

#### 4. Driver Performance

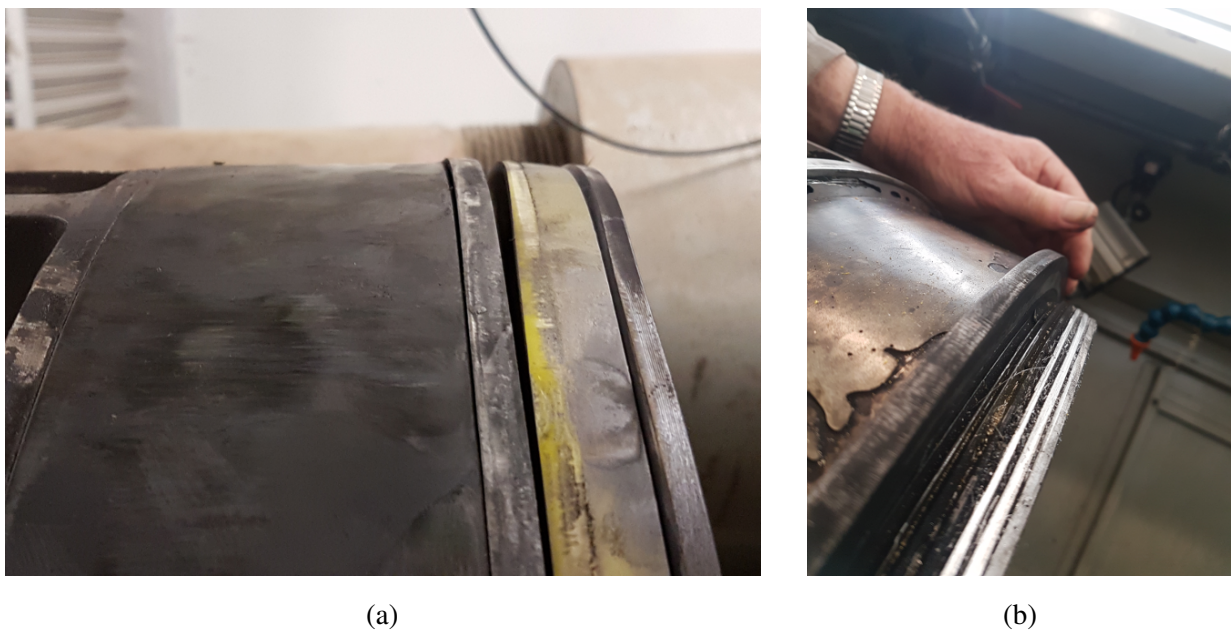


Figure 4.28.: (a), Damage to the load ring and steel locating ring. (b), Damaged piston thread after the load ring rolled over the threads.

the nylon buffers, a hypothesis that was reinforced by significant damage occurring to the buffers each shot. Additionally, the maximum deceleration of the piston with the stronger primary diaphragm increased from approximately 6000g to 8000g (+33%) which influenced the loading of the individual piston parts. The piston itself has a load ring, which threads onto the front of the piston and locates the chevron seal as well as a locating ring. During the higher deceleration of the shots with the stronger diaphragms, the inertia of the locating ring and chevron seal was sufficient enough that the load ring rolled off the piston thread, deforming the load ring and damaging the threads. Figure 4.28 (a) shows the deformation to the load ring on the front face of the piston and fig. 4.28 (b) shows the damaged thread where the load ring rolled off the piston thread. Repairs were needed to continue using the piston and alternative diaphragms were sourced that would reproduce the rupture pressure of the 3mm diaphragms used in earlier sections of this chapter.

## 4.10. Chapter Conclusion

After finalising the L1d model and confirming it was not sensitive to variations in compression tube fill pressure, it was used to simulate experiments with a rupturing diaphragm, and to design driver operating conditions with a 2mm and 3mm diaphragm. Experimental validation of the model showed that a nominally tuned piston trajectory in L1d was reproducible in X3, and damage occurred to the piston or nylon buffers during experiments. The two conditions designed used a 100% argon driver gas with compression tube and reservoir fill pressures of 49kPa and 6.7MPa respectively for the 2mm diaphragm, and 46kPa and 8.8MPa respectively for the 3mm diaphragm. Both conditions could then

have increased helium concentrations in the driver gas using an orifice plate to throttle the flow into the shock tube. For both diaphragms, L1d predicts that the driver gas vents out of the compression tube faster than what is measured in the experiment, possibly due to the duration of the diaphragm opening process and L1d's inability to capture the corresponding flow processes. L1d was shown to reasonably predict the post-shock pressure in the shock tube for both diaphragm thicknesses, but systematically over predicted the shock speed, another feature which is attributed to diaphragm effects.

Theoretical calculations of the acceleration tube flow were found to overestimate the shock speed in the acceleration tube and correspondingly underestimate the measured wall pressures. While the thinnest available mylar diaphragm was used, the size of X3 means even the thinnest diaphragm has considerable mass compared to smaller facilities. While it is thought that the size of the diaphragm reduces the performance of the unsteady expansion or can completely stagnate the gas, the extent that this affects the performance of the condition is unknown. The shock speeds driven into a 13.5kPa shock tube and 17Pa acceleration tube were not fast enough to reproduce the target conditions to perform scaled 1:5 Hayabusa experiments, and most likely a lighter piston or higher pressure operation is required to make such a condition realisable.

The influences of a secondary driver and shorter shock tube were also examined. Analytical estimates found that only a small increase in shock speed would be obtained, on the order of  $50\text{ m s}^{-1}$ , and this was experimentally verified by varying the secondary driver fill pressure and secondary diaphragm thickness. Results found that minimal variation in shock-tube shock speed was achieved and while there appeared to be some performance increase in the acceleration tube for experiments with the 3mm primary diaphragm, it is inconclusive whether this is due to the addition of the secondary driver or uncertainties in the fill pressures. Experiments with a shortened shock tube resulted in no variation in shock speed at similar locations but a slight increase in pressure in the acceleration tube and test section due to increased boundary layer development as the length of the acceleration tube was increased with reduction in shock tube length.

Primary diaphragms with higher yield and ultimate strengths were inadvertently purchased as the experiments progressed. These diaphragms ruptured at a higher pressure than the previously used diaphragms and the piston trajectory deviated from its tuned condition. Efforts to reduce the impact were not enough to prevent breaking the nylon buffers each shot and eventually the impact and/or increased inertial loads caused a brass ring on the piston used to locate the chevron seal to partially strip the piston threads and deform. As the new diaphragms ruptured at higher pressures, they could be scored to prevent shrapnel travelling down the tube. Scoring the diaphragms reduces the rupture pressure and this technique was used to reproduce the rupture pressure of the 2mm diaphragms in [96] and also in the next chapter. To accommodate diaphragm scoring, a new procedure involving testing the diaphragms in a static diaphragm test rig before use in the facility was implemented and discussed in chapter 5.

# Radiation Experiments

## 5.1. Chapter Overview

This chapter summarises the final experimental campaign, which includes the establishment of a new flow condition using the driver conditions developed in chapter 4 and optical measurements of the flow over two different size models. While only a page separates this chapter from the last, in the time between the final shot in chapter 4 and the first shot detailed in this chapter, the lightweight piston was repaired and new parts machined to replace damaged ones, different diaphragm material was purchased to change from unscored to scored diaphragms, a new Mach 12 nozzle [145] was installed, and experimental campaigns for a Mach 12 scramjet [96] and preliminary shots for a reflected shock tube condition [146] were conducted. For the aforementioned reasons the first part of this chapter will appear to repeat some aspects of the previous chapters but it is nevertheless necessary to lead into the final experimental campaign of this thesis. In chapter 4 it was discovered that, even with the piston and reservoir upgrades leading to significant increase in performance, X3 still did not have the capability to match the scaled Hayabusa condition previously used in X2 [76]. Thus a new fill condition to replicate the true flight condition at Hayabusa's peak radiation trajectory point was developed and both a 1:5 scale and full scale model of the Hayabusa capsule were used in experiments at the newly developed true flight condition. This chapter details the development of test condition, the design of the optical setup, the experimental results, and analysis of optical measurements for both model sizes.

## 5.2. Expansion Tube Layout

The development of the final operating condition, and the experiments where optical measurements were taken were performed with X3 in the configuration shown in fig. 5.1. This is the same configuration as used in most of the previous chapter with a steel diaphragm at the primary diaphragm station and  $12.5\mu\text{m}$  at the tertiary diaphragm station, resulting in a shock tube with a length of 22.237m and acceleration tube 17.644m long. The installation of the new Mach 12 nozzle [96] also introduced new sensors in the nozzle wall, originally included for comparison with CFD, but in the context of this thesis will be used for shock speed comparison. The location of all the wall static pressure

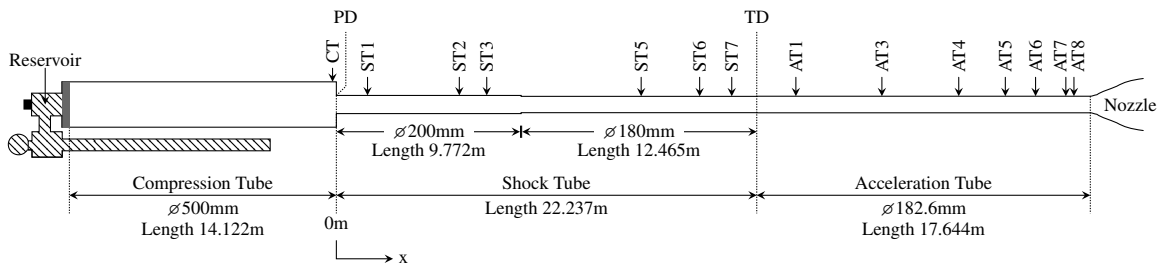


Figure 5.1.: Standard configuration of X3.

Table 5.1.: Sensor locations

Compression Tube		Shock Tube		Acceleration Tube		Nozzle	
Sensor	Location x [m]	Sensor	Location x [m]	Sensor	Location x [m]	Sensor	Location x [m]
CT	-0.201	ST1	1.649	AT1	24.307	N1	40.551
		ST2	6.504	AT3	28.857	N2	40.951
		ST3	7.955	AT4	32.922	N3	41.351
		ST5	16.123	AT5	35.386	N4	41.751
		ST6	19.217	AT6	36.986	N5	42.151
		ST7	20.915	AT7	38.587	N6	42.551
				AT8	39.016		

sensors are presented in table 5.1, the full details of the shots performed in this chapter are provided in appendix A.

## 5.3. Repeatability

After completing the shots in chapter 4, repairs had to be made to the piston, which involved the installation of a new chevron seal, wear rings, and a lighter load ring (brass to aluminium to reduce inertial loads) components that could have a substantial effect on the behaviour of the piston within the compression tube. Additionally, a stronger, thicker steel was used for the primary diaphragms which would allow them to be scored deeper yet still achieve the same high rupture pressure (29MPa) of the 3mm unscored diaphragms, but with a reduced chance of large diaphragm fragments travelling along the tube.

The development of a new static diaphragm test rig by Stennett (unpublished), shown in fig. 5.3a, meant that the static score depth and rupture pressure of the diaphragms were known to good accuracy before performing an experiment in X3 and equivalent static rupture pressures could be achieved for

## 5. Radiation Experiments



Figure 5.2.: (a), Scored diaphragm ruptured in the static test rig and (b), scored diaphragm ruptured during an experiment.

two different diaphragm configurations by adjusting score depth. The static test rig works by clamping the diaphragms in place and pressurising one side with oil until the pressure is sufficient to rupture the deformed diaphragm. The rupturing pressure in the static rig then needs to be related to the dynamic burst pressure in X3. This was calculated using the ratio of static breaking pressure to experimental bursting pressure obtained for some thinner diaphragms used in other experiments which required a multiplication of 1.3–1.7 to convert the static pressure to dynamic burst pressure (i.e. Static breaking pressure  $\times 1.5 \pm 0.2 \approx$  experimental burst pressure). An illustration of the difference between static and dynamic diaphragm rupture is presented in fig. 5.2. In fig. 5.2 (a), the diaphragm only breaks along a score line as the incompressibility of the oil means there is no stored energy to push the petals of the diaphragm outwards as in fig. 5.2 (b), where the energy stored in the driver gas pushes the diaphragm petals outwards and they conform to the shape of the shock tube. The diaphragms used in the static test rig have a smaller diameter than those used in X3, but the pressurised area is constant. Compared to the diaphragm in fig. 5.2 (a), thinner, more ductile diaphragms bulge a lot more under static load before they break.

This process allowed the specification of the primary diaphragm to change from the existing 3mm thick “mild steel” unscored diaphragm with unknown properties (most likely mild steel but the record of it was no longer available) to 4mm thick Strenx 700 (from supplied SSAB) with quoted yield and ultimate strengths of 706–768MPa and 781MPa–840MPa respectively (the variation arising because two supplied datasheets were provided with the delivery) with a score depth of 0.8mm. The quoted elongation at failure of the Strenx was also significantly lower than standard values for mild steel (18% compared to 30–40% from previous datasheets), but aside from the risk of the diaphragm not opening and conforming to the shape of the tube. It remains unknown how the change in elongation at failure affects the performance of the driver or if the diaphragm rupturing process is significantly different compared to diaphragms with larger values for elongation at failure, due to reduced ductility.

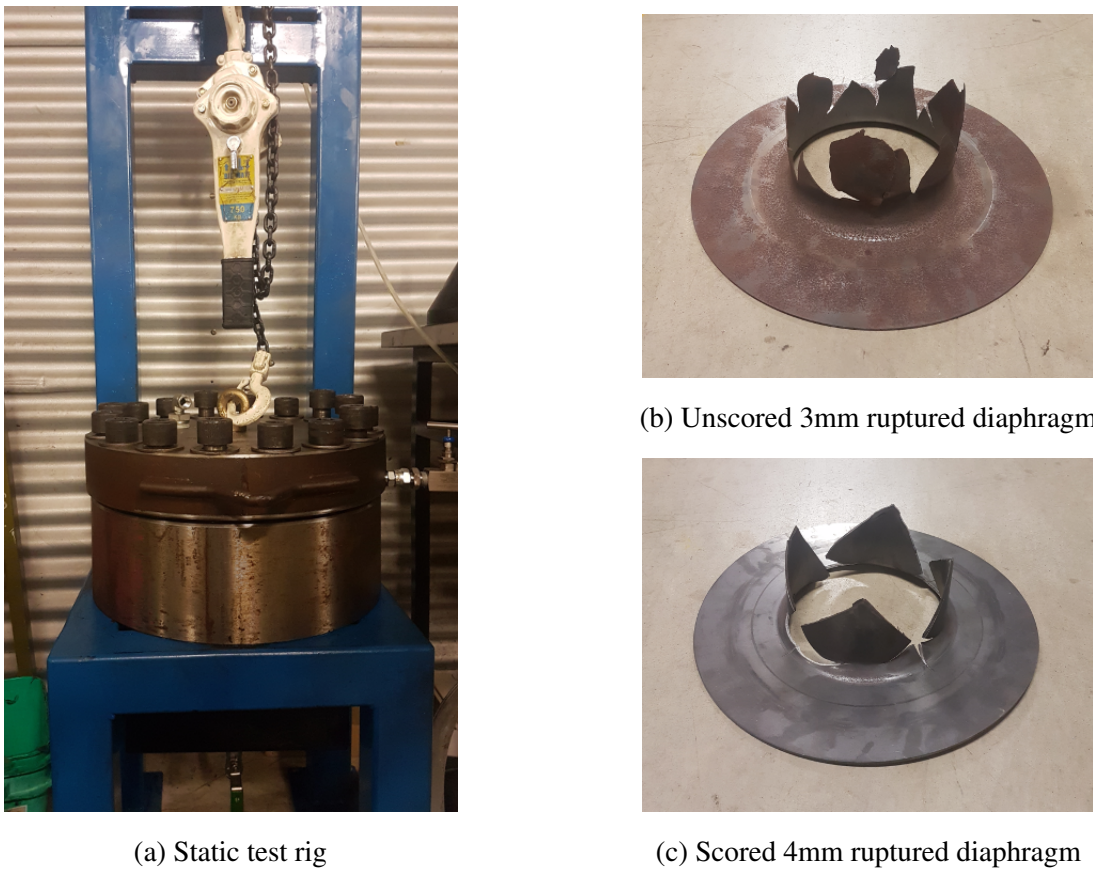


Figure 5.3.

Images of the 3mm unscored diaphragm and 4mm scored diaphragm after rupture (in X3) are shown in fig. 5.3b and fig. 5.3c. Although it is difficult to see in fig. 5.3, the 4mm diaphragm does not conform to the shape of the tube as well as the 3mm diaphragm does. A final score depth of 0.8mm was chosen for the diaphragms to be used in experiments. Based on the ratio of 1.3–1.7 (between static and dynamic rupture), a score depth of 0.8mm cause the diaphragms to statically rupture at 18MPa, which corresponds to a dynamic rupture pressure of 23.4–30.6MPa. Given the limitations in achieving an accurate score depth beyond a resolution of 0.1mm, a target rupture pressure of approximately 29MPa, and considering the repairs made to the piston, it was decided that a score depth of 0.8mm was reasonable until further information could be obtained.

The first shots with the new diaphragms and newly repaired pistons were performed for comparison with x3s530 and x3s531 (shots performed with 85% and 100% helium driver gas compositions with the 3mm diaphragm) and to determine if any of the changes to the diaphragm and piston had a significant effect on the behavior of the piston in the compression tube both before and after diaphragm rupture, and for any changes in performance in the driven tubes. Figure 5.4 shows a comparison of the compression tube pressure during the piston stroke for a 85% helium, 15% argon (by volume) driver gas. It should be noted that the 4mm scored diaphragms appear to rupture at a lower pressure than the older diaphragms which is more evident in fig. 5.5, which compares conditions with a 100% helium driver gas. Apart from the lower rupture pressure, the rest of compression process appears to be similar

## 5. Radiation Experiments

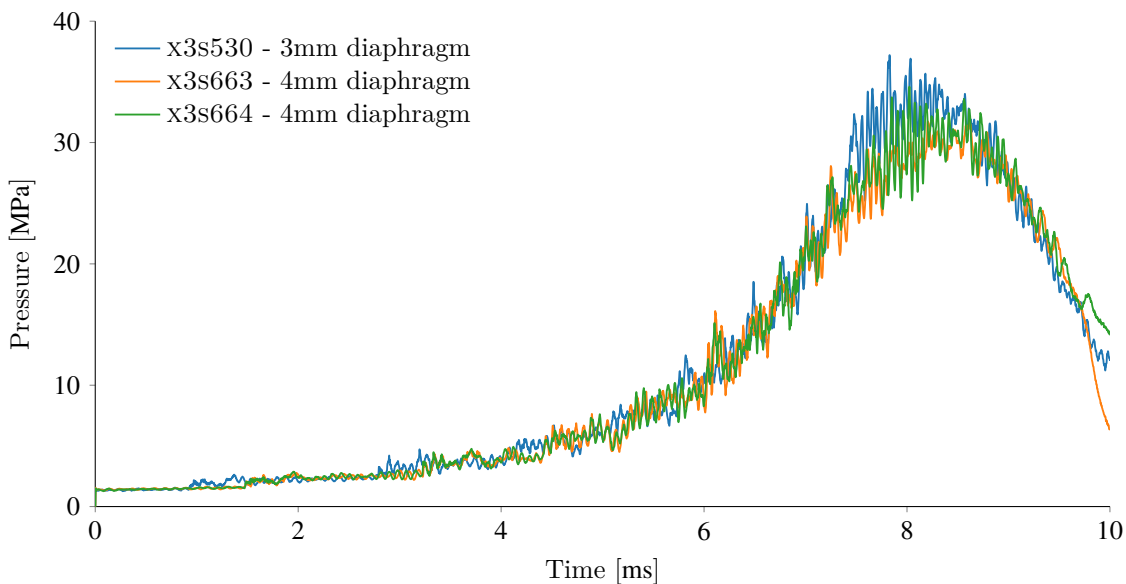


Figure 5.4.: Compression tube pressure traces comparing the 4mm diaphragms (x3s663 and x3s664) with the previous 3mm diaphragms (x3s530) with a gas mixture of 85% helium and 15% argon. Traces are filtered with a 5<sup>th</sup> order Butterworth filter with 250kHz cutoff frequency.

which suggests that the repairs to the piston have not significantly affected the piston's behavior as it travels along the tube. These closely matching results removed the need to redo blank-off shots and reassess the L1d model.

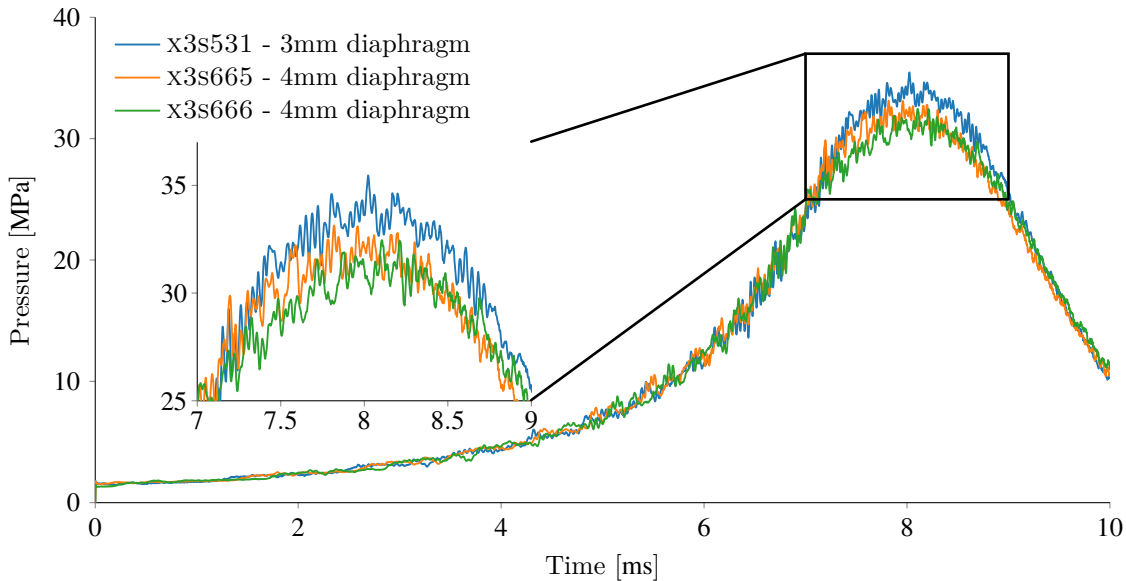


Figure 5.5.: Compression tube pressure traces comparing the 4mm diaphragms (x3s665 and x3s666) with the previous 3mm diaphragms (x3s531) with a gas mixture of 100% helium. Traces are filtered with a 5<sup>th</sup> order Butterworth filter with 250kHz cutoff frequency.

Another metric to measure the performance change of X3 using the 3mm and 4mm diaphragms is to compare the shock speeds and post shock pressure along the shock and acceleration tubes. Figure 5.6

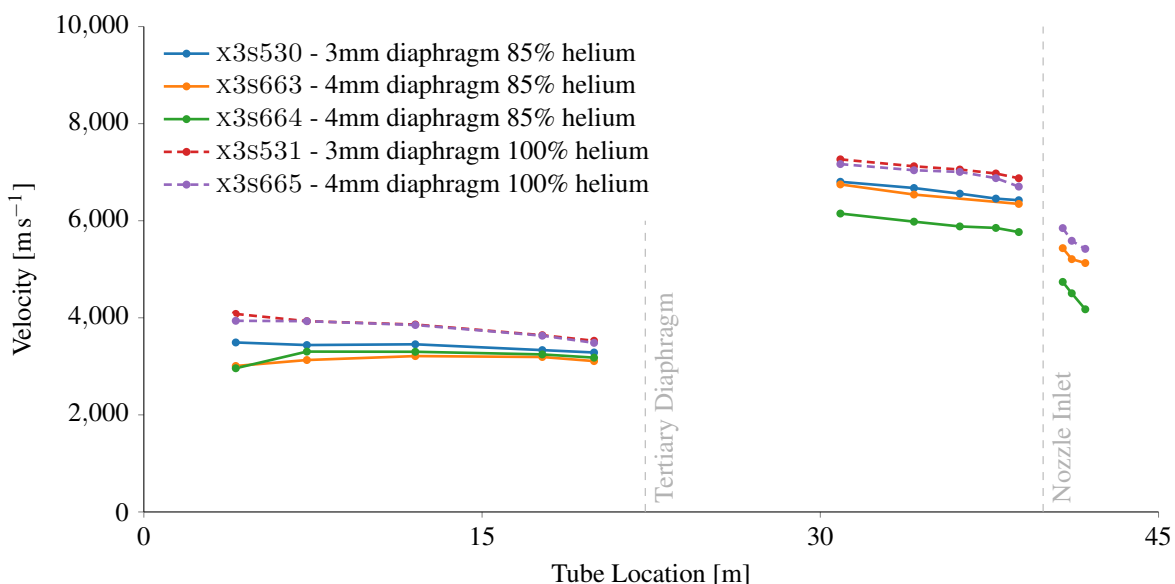


Figure 5.6.: Shock speeds along X3 for both 85% helium (solid lines) and 100% helium (dashed lines) compression tube gas compositions. Nozzle shock speeds are included for the more recent shots. The acceleration tube pressure x3s664 was higher than the nominal pressure of 17Pa, thus the reduced shock speed in the acceleration tube and nozzle.

compares the shock speeds for all the shots in figs. 5.4 and 5.5 along the length of X3, with shock speeds after the nozzle inlet available after the installation of the Mach 12 nozzle. In general, although the 4mm diaphragms appear to rupture earlier, the shock speeds along the length of the tube are comparable, especially using the 100% helium compression tube gas. The discrepancy in the shock speed in the acceleration tube for x3s664 is due to a leak in the test section and ultimately a much higher acceleration tube fill pressure being used, but this does not take away from the repeatability of shock speeds shown in the shock tube. Further comparisons can also be made by comparing wall pressure traces along the length of the tube. In figs. 5.7 and 5.8, the wall pressures at ST6, ST7, AT7 and AT8 are plotted for both 3mm and 4mm diaphragms and both compression tube gas mixtures. In both cases, the pressure traces are reproduced quite well with only a small deviation for ST6 in the compression tube gas, which arrives after the drop in pressure after the initial rise from the shock, and may be an effect of the different diaphragms. The larger deviation in pressure in ST7 is due to the PCB pressure transducer in shots x3s530 and x3s531 failing, but the repeatability after shock arrival suggests a similar comparison would have been achieved as for ST6 (for the locations of each sensor refer to fig. 5.1 and table 5.1).

## 5. Radiation Experiments

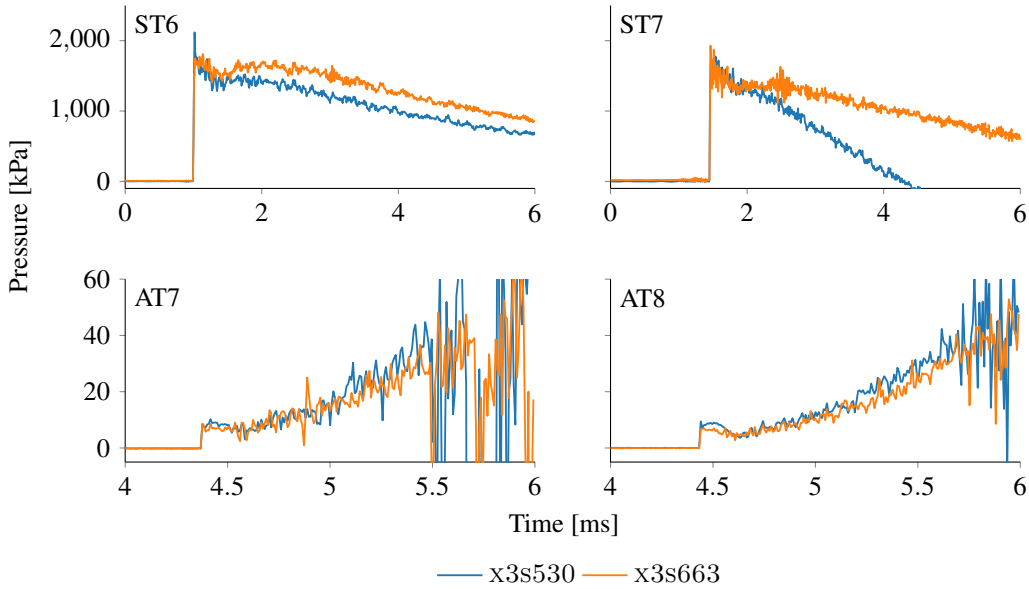


Figure 5.7.: Pressure trace comparison of ST6, ST7, AT7 and AT8 for shots x3s530 and x3s663.

Each set of data has been filtered with a 5<sup>th</sup> order Butterworth Filter with 250kHz cutoff and every 20<sup>th</sup> point has been plotted. The data for X3S663 has been aligned with the shock arrival of X3S530 for each sensor for clearer comparison.

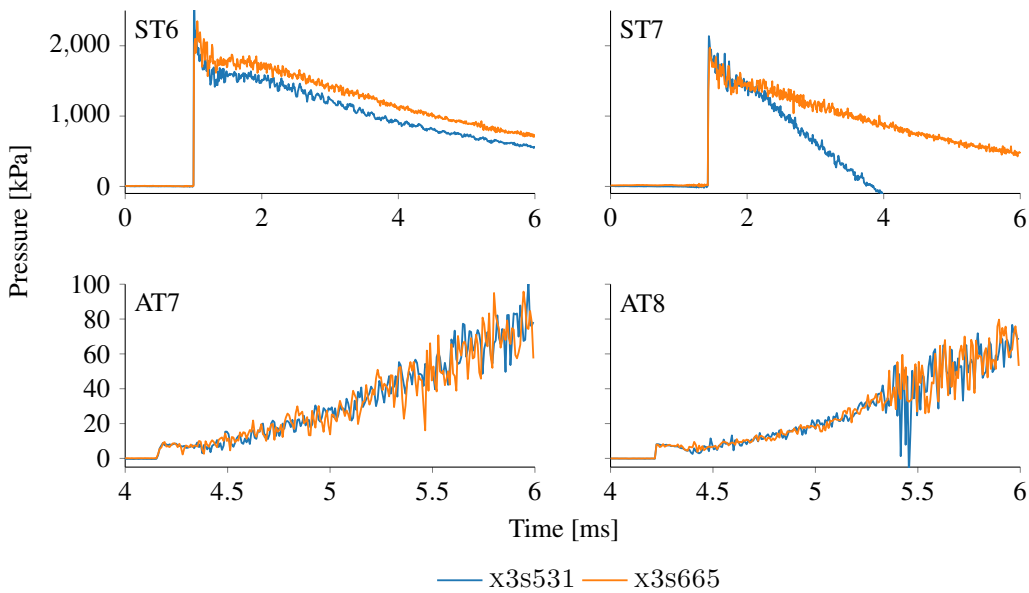


Figure 5.8.: Pressure trace comparison for ST6, ST7, AT7 and AT8 for shots x3s531 and x3s665.

Each set of data has been filtered with a 5<sup>th</sup> order Butterworth Filter with 250kHz cutoff and every 20<sup>th</sup> point has been plotted. The data for X3S665 has been aligned with the shock arrival of X3S531.

## 5.4. Developing the New Condition

At this point it has been shown that the repairs made to the lightweight piston and changes to the diaphragms did not have any adverse effect on the facility response. The next step in designing an operating condition was to change the fill pressures to effectively “undo” the density scaling that would have been present in the condition for the scaled model, if X3’s driver had been powerful enough to produce the scaled condition. To recap, the 1:5 scaled fill pressures in the shock and acceleration tubes were 13.5kPa and 17Pa respectively, and to undo scaling, the flow density in the test section needs to be five times less without any change in enthalpy. Analytical estimates suggested that the density could be reduced by a factor of five without significant change in velocity by reducing the shock and acceleration tube fill pressures by a factor of five, which suggests fill pressures of 2.7kPa for the shock tube and 3.4Pa for the acceleration tube. From the CFD analysis performed by Fahy et al. [76], the density of the scaled test flow was found to be slightly higher than the nominal condition ( $3.1 \times 10^{-3} \text{ kg m}^{-3}$  compared to  $2.6 \times 10^{-3} \text{ kg m}^{-3}$ ). The fill pressure for the shock tube was chosen to be 2.5kPa and uncertainties with the pressure gauge (the gauge was incorrectly displaying the test section pressure, underestimating pressure by approximately 1.5Pa) in X3’s acceleration tube resulted in an acceleration tube fill pressure of 3.5Pa being used for all the experiments. The only exception was x3s666 which had an acceleration tube fill pressure of 5.5Pa. Shock speeds for shots x3s665, x3s666 and x3s667 are presented in fig. 5.9 which compares the true flight operating condition with the previous attempt at a scaled condition. A comparison of wall pressure traces is also shown in fig. 5.10 for the sensors at ST6, ST7, AT7 and AT8. While the acceleration tube fill pressure dropped by approximately 40% between shots x3s666 and x3s667, the flow properties in the acceleration tube do not appear to exhibit any significant difference in pressure and shock speed.

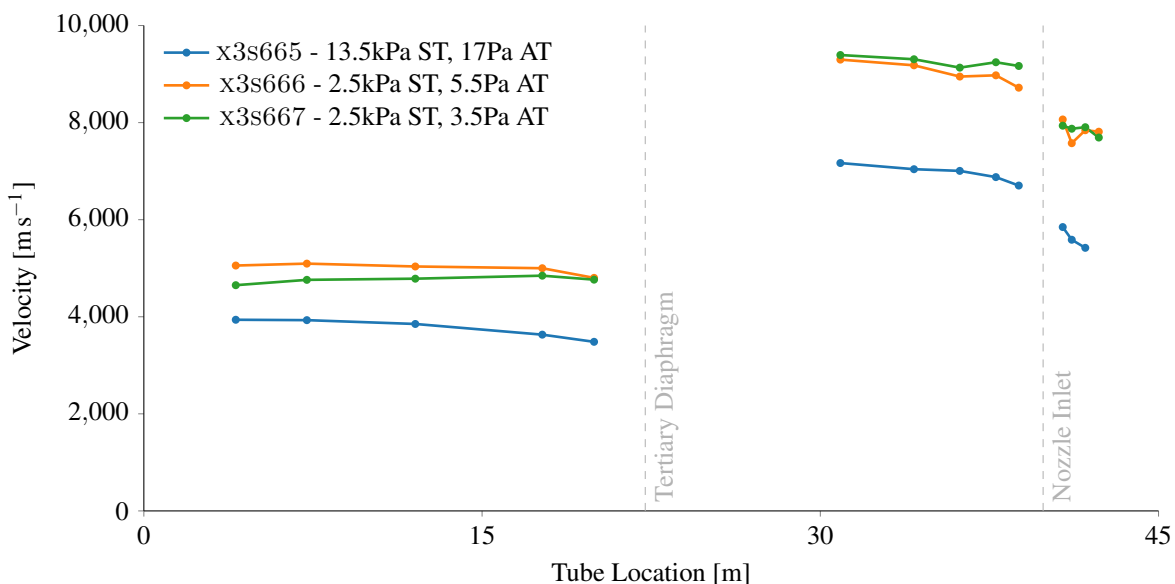


Figure 5.9.: Shock speeds for x3s665, x3s666, x3s667 which shows the iteration towards the final true flight condition (x3s667). (AT - Acceleration Tube, ST - Shock Tube)

## 5. Radiation Experiments

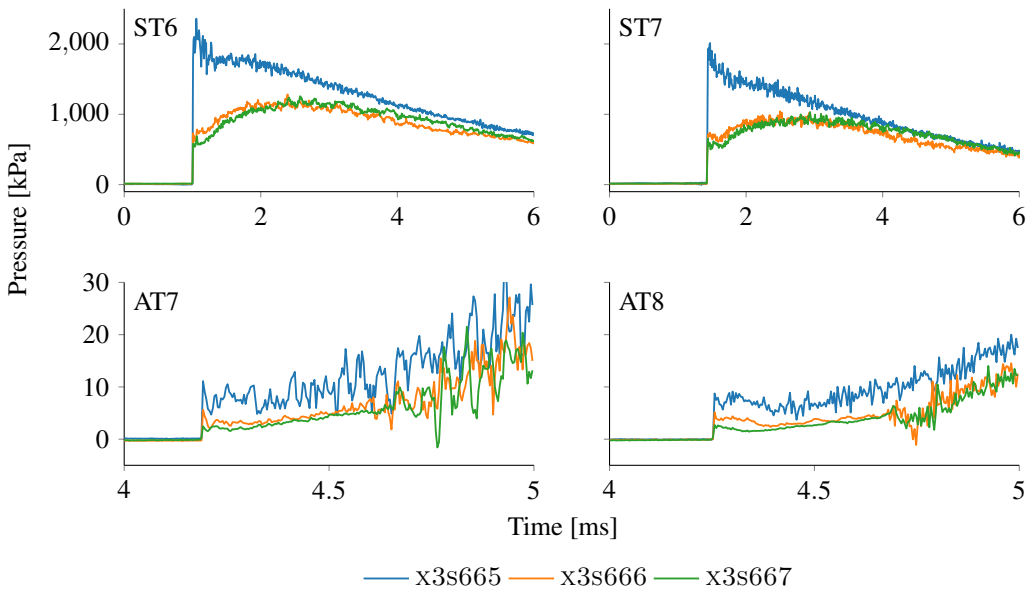


Figure 5.10.: Wall static pressures for x3s665, x3s666 and x3s667. Each set of data has been filtered with a 5<sup>th</sup> order Butterworth Filter with 250kHz cutoff and every 20<sup>th</sup> point has been plotted for ST6 and ST7 and every 10<sup>th</sup> point has been plotted for AT7 and AT8. Each pressure trace has been aligned with x3s665.

Figure 5.11 presents the average shock speeds for two groups of shots, those for condition development purposes, which include pitot rake shots with both flat and conical PCB probe caps, as well as experiments performed with the pre-nozzle inlet pitot rake (refer to probes named N# in fig. 5.1 and table 5.1), and the shots performed for the optical experiments detailed in the latter parts of this chapter. In general, there is not a lot of variation in the shock speed in the shock tube. The shot to shot variance increases in the acceleration tube and through the nozzle, where a larger magnitude of shot to shot variation was experienced, possibly due to effects of the tertiary diaphragm or inconsistencies in acceleration tube fill pressure. The pitot rake setup is shown in fig. 5.12a and both conical caps (shown) and flat caps (not shown) were used in experiments to measure the gas properties in the test section. The inlet rake in fig. 5.12b was initially designed to measure the test gas inflow at the end of the acceleration tube for verification of boundary layer thickness for the Mach 12 nozzle design [96], and can be used to provide extra data when trying to quantify a test condition.

### 5.4.1. Pitot Rake Measurements

Experiments were performed with both 15° conical probes and pitot probes: the difference being the conical probes measure pressure behind a conical shock and the pitot probes measure Pitot pressure. Figure 5.13 shows filtered data taken from two shots with the conical probe caps. It should be noted that 50psi ( $\approx 350\text{kPa}$ ) PCB sensors were used in these experiments and according to the manufacturer the lower threshold for non-linearity in the voltage response occurs at  $\leq 1\%$  of the full scale. As

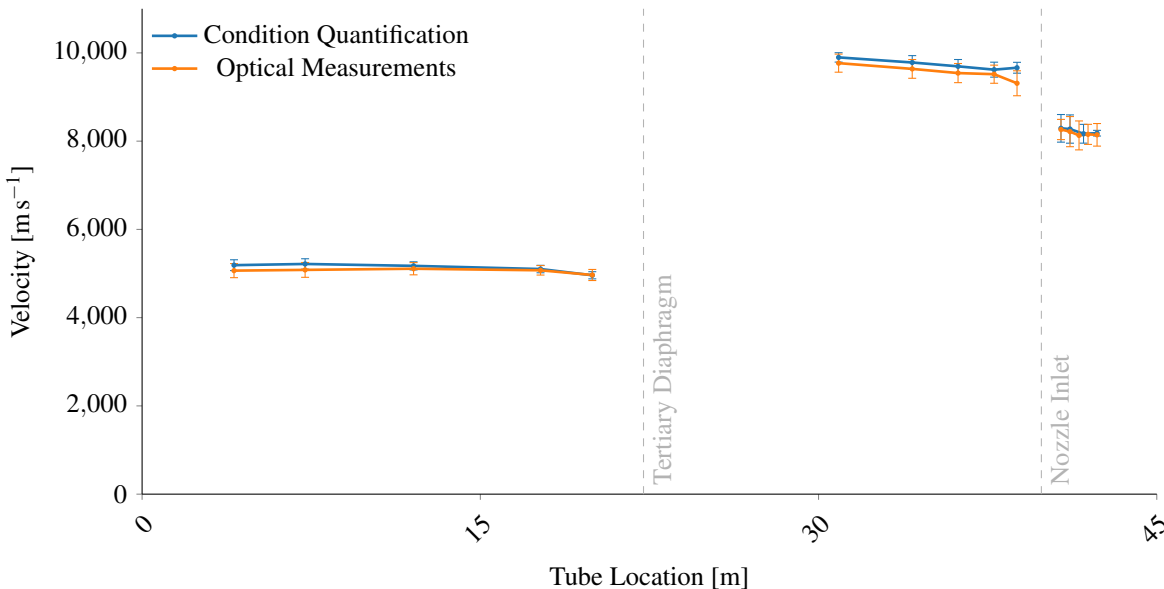


Figure 5.11.: Average shock speeds for the two groups of experiments. Pitot rake and inlet rake experiments are averages of x3s668, x3s669, x3s670, x3s673, x3s682, x3s683 while the optical experiments are averages of x3s693, x3s694, x3s696, x3s698, x3s699, x3s700, x3s701, x3s702, x3s703, x3s704 and x3s705. The standard deviation of the shock speed at each location is shown as an uncertainty bar to gauge the variance of the facility.

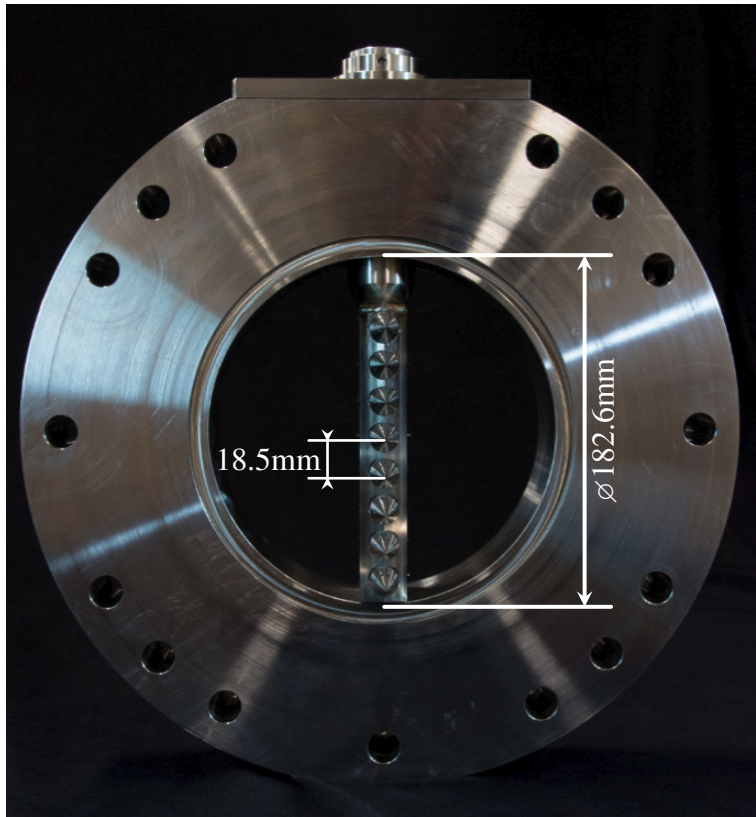
evident in fig. 5.13, where cone data is presented, a substantial quantity of the data, especially in the test time occur below 3.5kPa (1% of 350kPa) and it is unknown what the effect of the PCB's non-linearity is on the measurements. While there appears to be some agreement between x3s668 and x3s669 in fig. 5.13, a clearer comparison can be seen in fig. 5.14 which divides the test time into six equal increments of 0.1ms and compares the pressure between the two shots radially and temporally. The main discrepancy between the two shots is the sudden rise that occurs at approximately 0.6ms for x3s669 compared to the gradual rise of pressure exhibited by x3s668. This is evident in fig. 5.14 as the orange pressures of x3s669 are consistently higher than that of x3s668 in the earlier times, but the pressures appear to become much more consistent in the final time interval. It is unknown why this discrepancy occurs and it would require more experiments to know which pressure profile better represents the nominal condition.

Similarly to the experiments in fig. 5.13, experiments were performed after replacing the conical probes with pitot probes and are displayed in fig. 5.15. In fig. 5.15 it becomes evident why the test time shown in fig. 5.13 was chosen to span from 500μs – 1100μs. In experiments with pitot probes, there is an inconsistency from 0μs–500μs for which a large pressure gradient occurs across the probes and those towards the outer edge of the nozzle showing much higher pressure than the probes in the centre of the nozzle. One explanation of this phenomena is that the current operating condition (high enthalpy superorbital reentry) is significantly different from the design condition of the nozzle (Mach

## 5. Radiation Experiments



(a) Pitot rake.



(b) Nozzle inlet rake [96].

Figure 5.12.: Image (a) is X3's pitot rake assembled in the test section with conical probes, PT1 is the bottom probe and PT15 is the top probe. The laser line indicates the horizontal centre plane of the nozzle, which aligns with PT2 (the second from bottom probe). The probes are vertically spaced 20mm apart and sit approximately 60mm from the exit of the nozzle. The cylindrical device below the rake is not part of the pitot rake and relates to an independent measurement not relevant to this current study. Image (b) is the inlet rake mounted in a section of tube that is installed 660mm upstream of the nozzle inlet and, the probes are labelled P1 to P8 from top to bottom with P4 lying on the centreline. The probe spacing is 18.5mm and the assembly has the capacity to offset the probes 9mm from the centreline for increased resolution across multiple measurements. The assembly view is looking downstream along the facility.

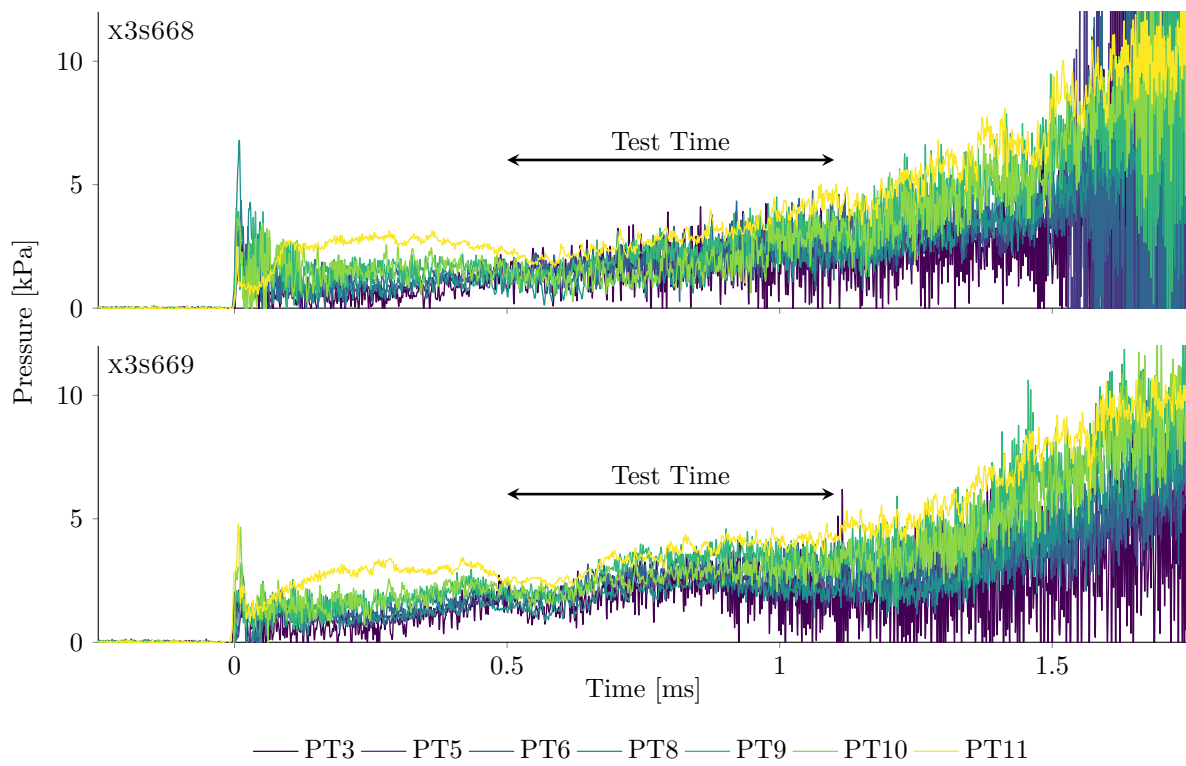


Figure 5.13.: Conical shock pressure measurements for shots x3s668 and x3s669, data is filtered with a 5<sup>th</sup> order Butterworth Filter with 250kHz cutoff. Missing probe labels are due to several PCBs failing and not obtaining useful data for either experiment.

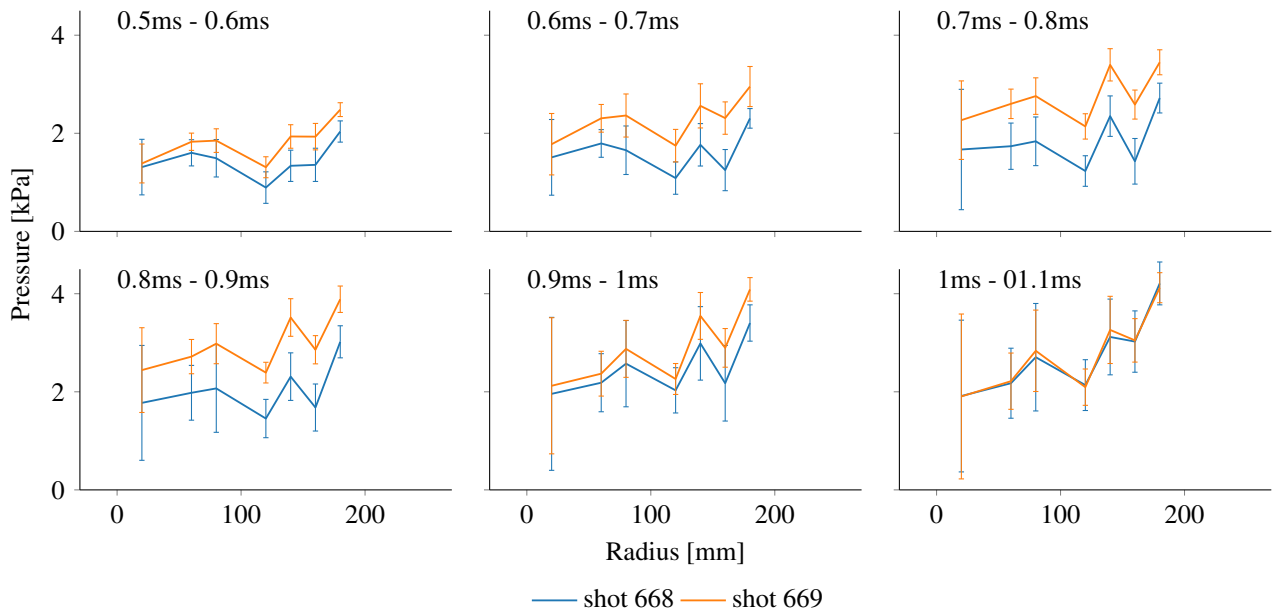


Figure 5.14.: Spatially resolved and time-averaged comparison of data from conical shock pressure plots in fig. 5.13. Each plot presents the mean pressure of each probe during the specific time interval as defined in fig. 5.13 with standard deviation shown as an indication of variance through the times indicated. The x-axis identifies the location of each 15° conical probe with 0mm being the nozzle centreline.

## 5. Radiation Experiments

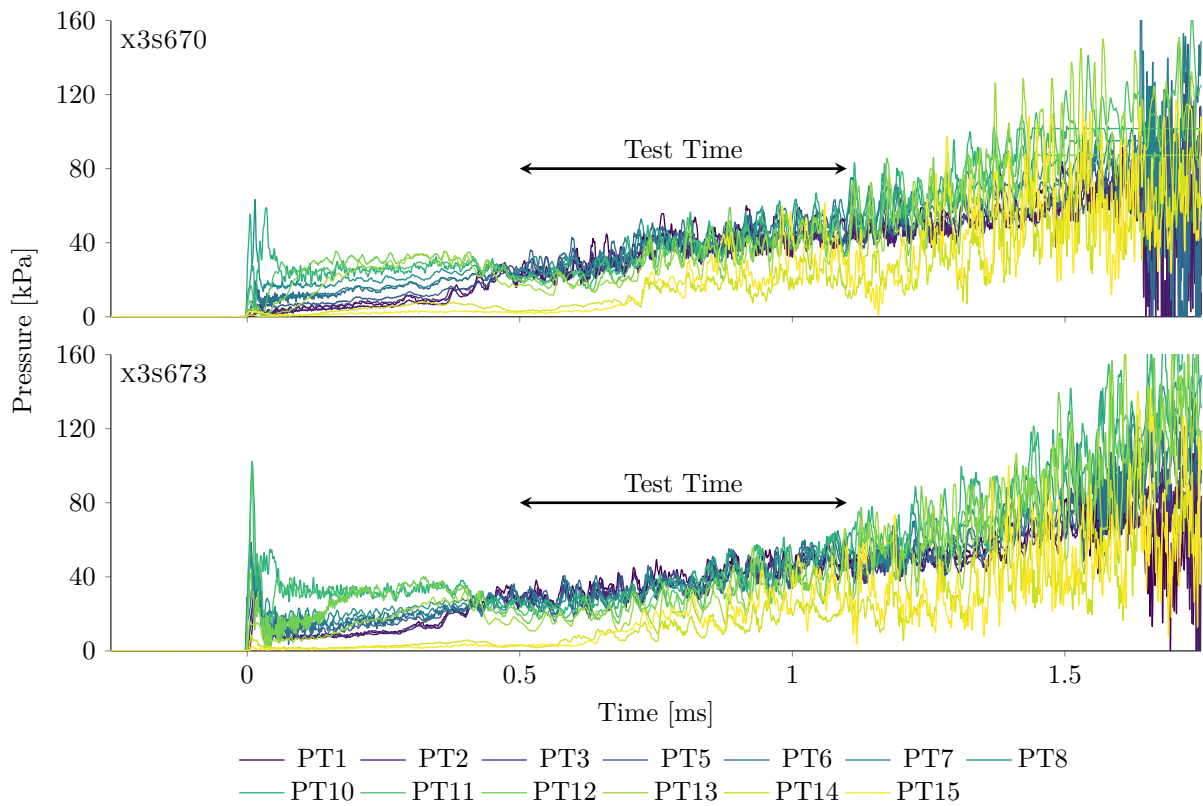


Figure 5.15.: Pitot pressure measurements for shots x3s670 and x3s673, data is filtered with a 5<sup>th</sup> order Butterworth Filter with 250kHz cutoff. PT4 and PT9 have been omitted as no useful data was obtained from those sensors.

12 scramjet [96]) and the higher Mach number at the start of the test gas arrival results in it not being processed correctly by the nozzle, until later when the Mach number has dropped sufficiently. At the time of writing this theory has not been validated and the test time is said to start when all the pitot pressure traces converge at approximately 500 $\mu$ s. Again for comparison, fig. 5.16 plots the pressure along the radius of the nozzle exit plane over multiple time intervals. It is evident that the Pitot probes are much more consistent between the two shots. An estimate of the core flow in the test section can also be made, with approximately constant Pitot pressure occurring up to a radius of 160mm (320mm diameter), or potentially up to 200mm (400mm diameter) if an approximately 30% reduction in Pitot pressure is acceptable. While the region of constant pressure in the radial direction is relatively large, the pressure is consistently rising throughout the test time and approximately doubles in pressure over the plots presented in fig. 5.16.

A comparison of the core flow measured by the Pitot probes and 15° conical probes is presented in fig. 5.17. While the Pitot probes measure a core flow from 0–160mm in the radial direction with minimal Pitot pressure variation, the conical probes measure a pressure that rises away from the centreline of the nozzle. If the potential effects of PCB non-linearity for the 15° conical probes are ignored, this suggests that there may be a flow feature present that is causing this discrepancy, although this remains speculative until additional experiments to further quantify the flow field can be conducted.

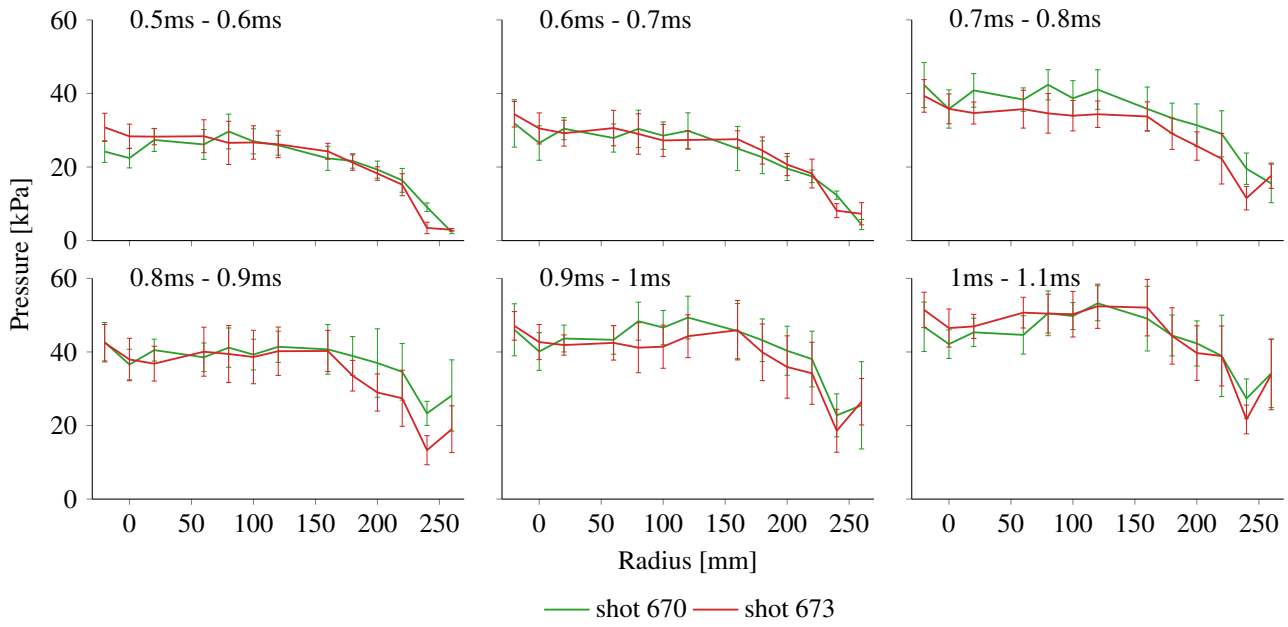


Figure 5.16.: Spatially-resolved and time-averaged comparison of data from pitot pressure plots in fig. 5.15. Each plot presents the mean pressure of each probe with standard deviation shown as an indication of variance through the times indicated. The x-axis identifies the location of each Pitot probe with 0mm being the nozzle centreline.

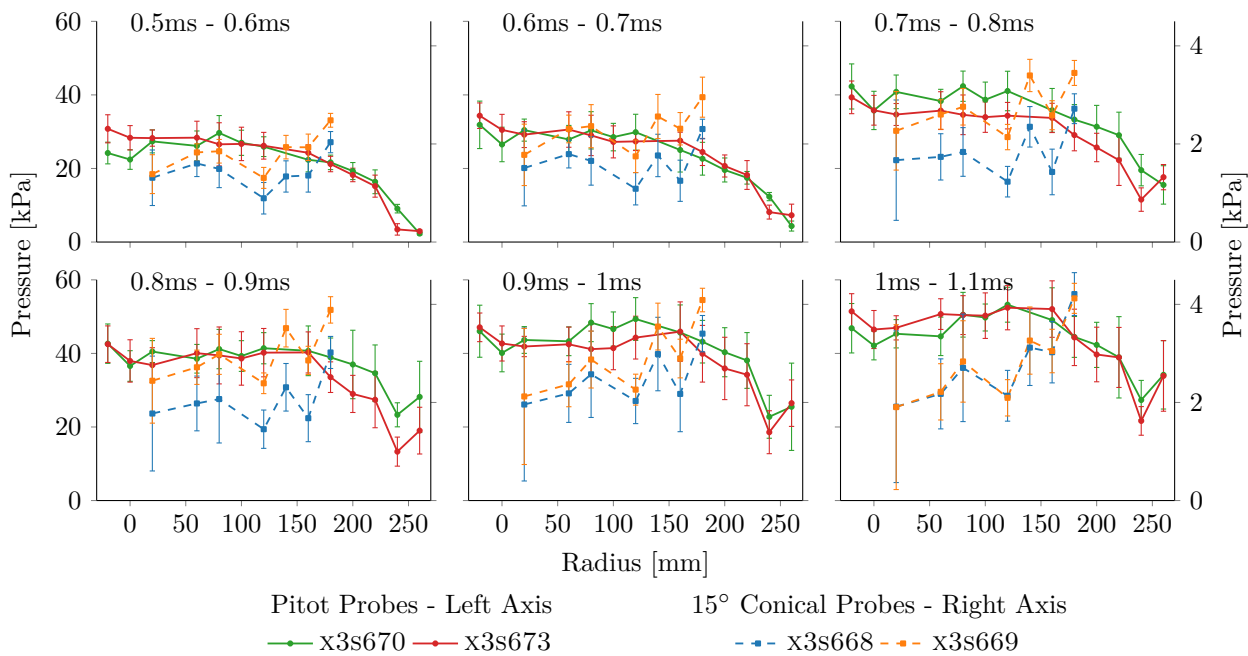


Figure 5.17.: Spatially-resolved and time-averaged comparison of data from both  $15^\circ$  conical probe and pitot pressure from fig. 5.14 and fig. 5.16. The x-axis identifies the radial location of each probe with 0mm being the location of the nozzle centreline.

## 5. Radiation Experiments

The measurements of Pitot pressure is more consistent between the two shots compared to the two measurement sets acquired by the 15° conical probes. Additionally, the data in fig. 5.17 is from four separate shots and as evident in fig. 5.11 there is some shot to shot variation in shock speeds and it is unknown how or if this translates into a variation in measured pressure at the nozzle exit.

### 5.4.2. Nozzle Inlet Rake Measurements

The initial motivation to use the pre-nozzle inlet rake (fig. 5.12b) for these conditions was to identify whether the pressure gradient that occurred before the test time mentioned in the previous paragraph was a feature of the operating condition (such as boundary layer growth in the acceleration tube) or something that developed in the nozzle. The data acquired from the inlet rake in fig. 5.18 has been aligned with the pressure trace from AT8, the most downstream tube wall static pressure sensor in the acceleration tube, similar to the methodology outlined by Sasoh et al. [147]. The beginning of the test gas has been located based on the relations derived by Mirels [93], which calculated the gas slug length with consideration to boundary layer growth between the shock layer and the contact surface. For the acceleration tube gas the calculated time for the accelerator gas to pass a fixed location was 5.2 $\mu$ s and the beginning of the test gas in fig. 5.18 has been located 5.2 $\mu$ s after shock arrival.

At the arrival of the test gas there is a drop in pressure measured at AT8 for both shots in fig. 5.18. Gildfind et al. [95] performed axisymmetric CFD of X3's acceleration tube for a Mach 10 scramjet condition and observed that the drop in pressure is due to a large bulge in the boundary layer that forms just upstream of the contact surface. The pressure traces presented by Gildfind and similar traces measured by Toniato [96] has accelerator gas slugs that are measured at AT8 for a period of time on the order of tenths of milliseconds, two orders of magnitude larger than the accelerator gas slug duration observed in fig. 5.18. The increase in pressure of the test gas measured at AT8 is due to boundary layer growth [140, 147] and the test gas has been deemed to terminate at 0.4ms in fig. 5.18 which is shortly before the arrival of flow disturbances. There is a change of gradient for AT8 at 0.33ms and it is unknown if this is due to flow disturbances or a change in behavior of the boundary layer.

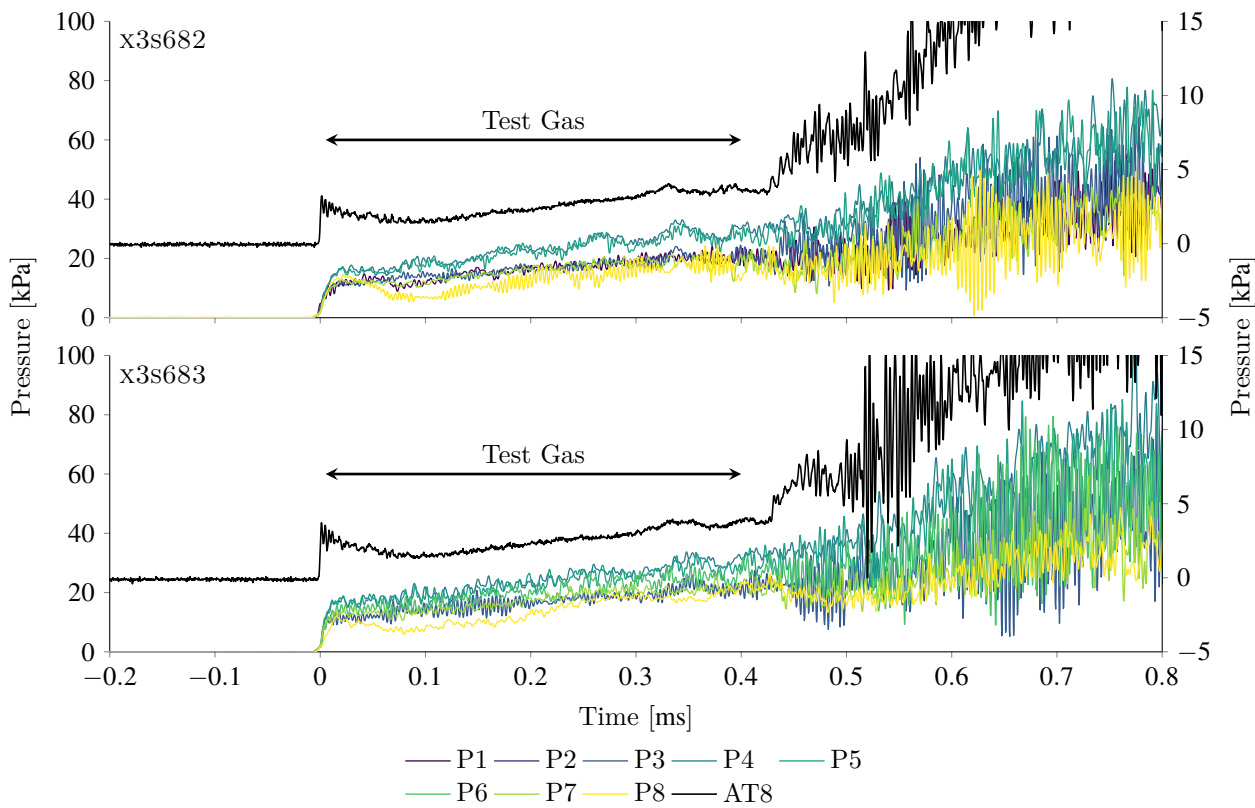


Figure 5.18.: Inlet pressure measurements for X3S682 and X3S683, data has been filtered with a 5<sup>th</sup> order Butterworth Filter with 250kHz cutoff frequency. The AT8 pressure trace is taken from the same shots and is referenced to the right vertical axis. During x3s682 probes P2 and P6 failed and during x3s683 probes P1 and P2 failed.

As with the 15° conical probes and Pitot probes at the nozzle exit, the test gas passing over the probes in the inlet rake has been divided into six equal time periods, beginning at 0.1ms in fig. 5.18 (the start of the increasing gradient) and ending at 0.4ms. The pressure for each probe has been averaged and is presented in fig. 5.19. For both shots X3S682 and X3S683, sensor P4 was aligned with the centreline of the acceleration tube and is located at a radius of 0mm in fig. 5.19 with the spacing between probes being 18.5mm. From the radial shape of the flow, it appears that P3 had been incorrectly calibrated, (also evident in measurements taken by Toniato [96] but at P6) and the low pressures compared to P5 (at the same radial location as P6) are taken to be erroneous as the flow is generally axisymmetric. Disregarding P3, probes P4 (0mm) and P5 (18.5mm) measure similar pressures for both shots from 0.1–0.25ms while constantly rising while P6 (37mm) is consistently around 40% lower. This suggests that the core flow at the nozzle exit has a radius of at least 18.5mm (diameter 37mm) for the first 0.15ms before the boundary layer grows and P5 (18.5mm) is consumed by the boundary layer.

### 5.4.3. Summary

Experiments were performed to measure pressure before and after the nozzle for the condition that was designed to produce test flows representative of the peak radiation trajectory point for the Hayabusa

## 5. Radiation Experiments

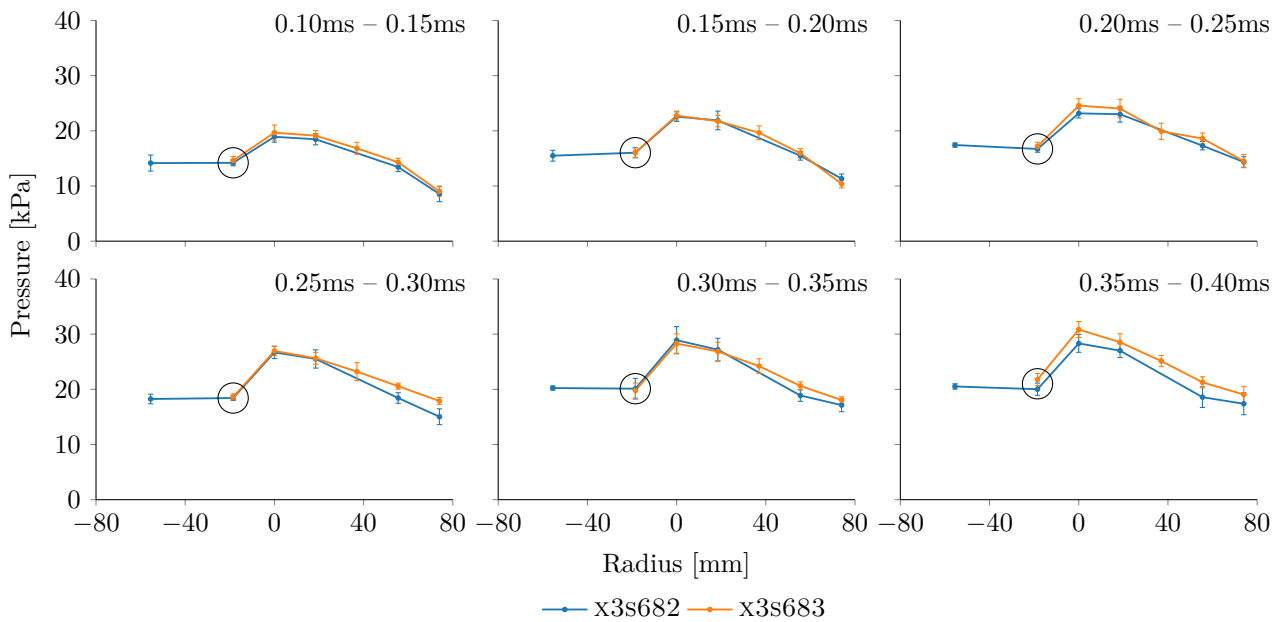


Figure 5.19.: Average pressure of each probe in fig. 5.18, error is standard deviation. Radius values is distance from the centreline with negative values the upwards direction. Missing markers error bars signify where a probe has failed and data was not obtained. The circled data point represents the PCB that is believed to give erroneous measurements.

capsule. The pressure behind a conical shock produced by  $15^\circ$  cones was measured at the entrance and exit of the nozzle as well as wall pressure at the entrance and Pitot pressure at the nozzle's exit. From the pressure measurements, the core flow diameter upstream and downstream of the nozzle can be approximated as 40mm and 320mm respectively, although the core flow diameters upstream and downstream of the nozzle can be revised to 75mm and 400mm if a reduction of approximately 30% of the core flow pressure is acceptable. The magnitude of the measured pressures can now be used with analytical calculations to infer the actual flow condition.

## 5.5. Quantifying the Condition

At this point the anticipated working condition has been tested with  $15^\circ$  conical and Pitot impact pressure probes at the nozzle exit, and with  $15^\circ$  conical impact pressure probes and wall static pressure measurements at the inlet to the nozzle. So while there is a good scope of pressure measurements for the condition, it is necessary to be able to estimate other flow properties in the test section since this determines if the condition is appropriate. At UQ, an analytical tool called PITOT [108] is typically used to evaluate flow properties generated by expansion tubes (although the majority of work using the code has been tailored to and focused on X2 due to comparatively more frequent usage of the facility). PITOT uses an analytical model of expansion tube flow processes coupled with NASA's CEA code [148, 149] to handle high temperature gas effects, with the code assuming that each flow

state is in equilibrium. The shocked test gas is most likely at equilibrium due to the high post shock pressure [24], however, in X2, thermal nonequilibrium has been shown to occur in the nozzle [150]. X3 is a much larger facility than X2, and the gas has a longer residence time in the acceleration tube and nozzle and is likely to be closer to equilibrium than in X2. PITOT can model the gas as frozen as it expands through the acceleration tube and nozzle, conserving the mass fractions of the shocked test gas and modelling it as a perfect gas. The remainder of this chapter assumed the gas is in equilibrium, although comparative results from the frozen gas model are presented in tables 5.2 and 5.4 and figs. 5.25 and 5.35. Results in table 5.4 show that the predicted shock stand-off using both assumptions only varies by approximately 5% suggesting that the equilibrium assumption was appropriate for the purpose of taking shock stand-off measurements.

PITOT has an “experiment mode”, which allows the user to input the shock tube and acceleration tube fill pressures, and measured shock speeds, and the code then calculates the gas properties behind the shock. In this mode, the shock processed test gas is expanded to the velocity of either the shock in the acceleration tube if Mirels effects are assumed, or the velocity of the accelerator gas where viscous effects on shock speed is neglected. The expanded test gas is further expanded through a nozzle based on an area ratio determined by the user. Geometrically, the nozzle has an area ration of 9.8 (nominally an inlet radius of 0.091m and an exit radius of 0.287m [96]) but from the flow profiles in fig. 5.16 and fig. 5.19, it can be argued that the area ratio of the core flow itself is on the order of 10–15 depending on how one interprets the core flow areas, and the use of this effective area ratio is common practise.

Before expanding the test gas through the nozzle, an expansion factor can be applied to the test gas allowing the user to effectively expand the test gas to a velocity faster than the shock in the acceleration tube. The expansion factor is simply a scalar value that multiplies with the secondary shock speed to calculate a modified velocity to unsteadily expand the test gas to; essentially it works in a way that the following two examples, the test gas is expanded to  $10.45\text{km s}^{-1}$ . An expansion factor of one is common as the code is able to expand the test gas to the shock speed in the acceleration tube to simulate the Mirels’ effect.

$$\underbrace{9.5\text{km s}^{-1}}_{\text{shock velocity}} \times \underbrace{1.1}_{\text{expansion factor}} \equiv \underbrace{10.0\text{km s}^{-1}}_{\text{shock velocity}} \times \underbrace{1.045}_{\text{expansion factor}} = \underbrace{10.45\text{km s}^{-1}}_{\text{expanded test gas velocity}} \quad (5.1)$$

Using the expansion factor in PITOT, the test gas can be expanded into the acceleration tube to a velocity greater than the secondary shock speed, which can be achieved by setting an expansion factor greater than one. Once the post-shock pressure of the test gas is estimated in PITOT, the expansion into the acceleration tube can be controlled via the expansion factor, likewise the expansion through the nozzle controlled by the area ratio. Ultimately, this allows the test gas to be expanded to velocities larger than the secondary shock speed, but without additional experimental measurements the implications of this have not been investigated. For the purpose of this study, the expansion factor

## 5. Radiation Experiments

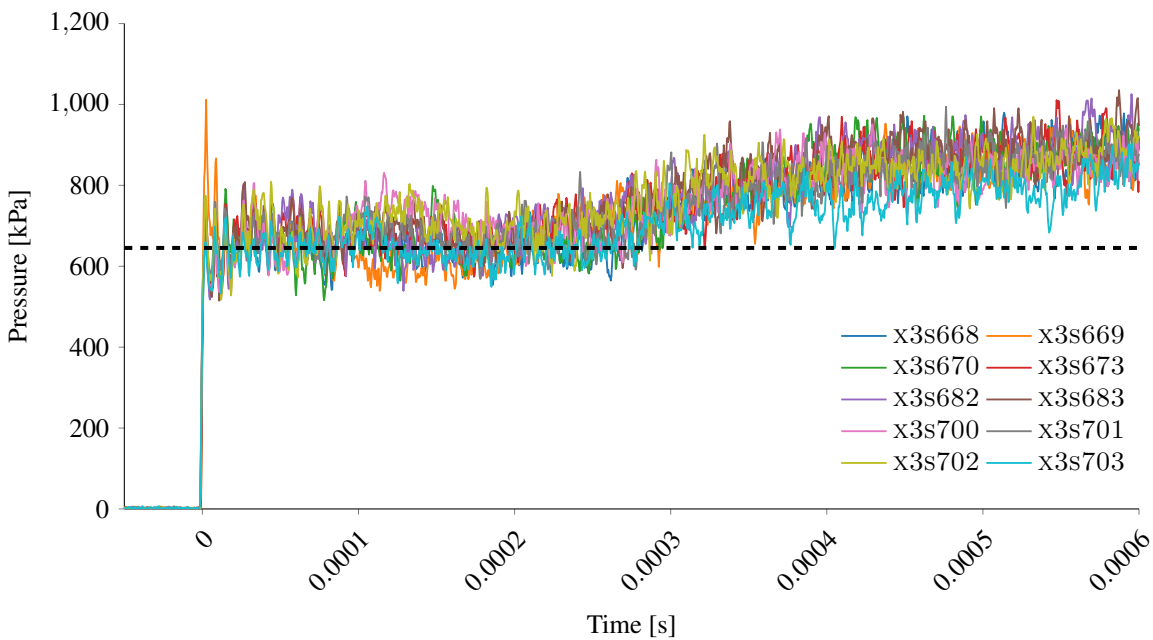


Figure 5.20.: Comparison of analytical post shock pressure, the black dashed line, against a range of experimental wall pressure traces taken from ST7.

is kept below 1.1 and it is assumed that the estimated flow properties do not deviate too much from the actual facility flow properties. As a start, fig. 5.20 shows the analytical post shock pressure for the test gas in the shock tube and compares it against a range of wall pressure traces taken at the end of the shock tube. The analytical value was calculated based on a shock speed of  $4950\text{ms}^{-1}$  (see fig. 5.11) through air at 2.5kPa, which gives a reasonable analytical estimate of post shock pressure in fig. 5.20.

Once the post shock test gas properties are established the expansion factor was varied to establish the test gas properties before the nozzle. As conical probes were used at the inlet of the nozzle there are two measurements to use to iterate the expanded test gas pressure to. Varying the expansion factor from 1.0 to 1.1, the analytical static pressure and analytical pressure after being processed by a conical shock can be compared with the experimental measurements in fig. 5.21 and fig. 5.22. In fig. 5.21, the test gas region of AT8 has been averaged with the minimum and maximum pressure displayed as error bars for a series of experiments and the pressure calculated with various expansion factors are shown as a comparison with the experimental values. The horizontal location of each shot's data in fig. 5.21 has no significance to the data and each shot should be individually compared to the theoretical curve with the same graphical arrangement being used for subsequent plots.

For clarity, a brief interpretation of fig. 5.21 will be provided here. The rising pressure from 0.1–0.4ms in fig. 5.18 measured at AT8 has been averaged with the total range of measured pressure represented by the error bars in fig. 5.21. For the five shots identified on the bottom x-axis in fig. 5.21, the pressure at AT8 measured for each shot can be read from the right vertical axis. The dark blue curve represents a variation of expansion factors using a shock speed of  $9500\text{ms}^{-1}$  (i.e.  $9500 \times 1.05 = 9975\text{ms}^{-1}$

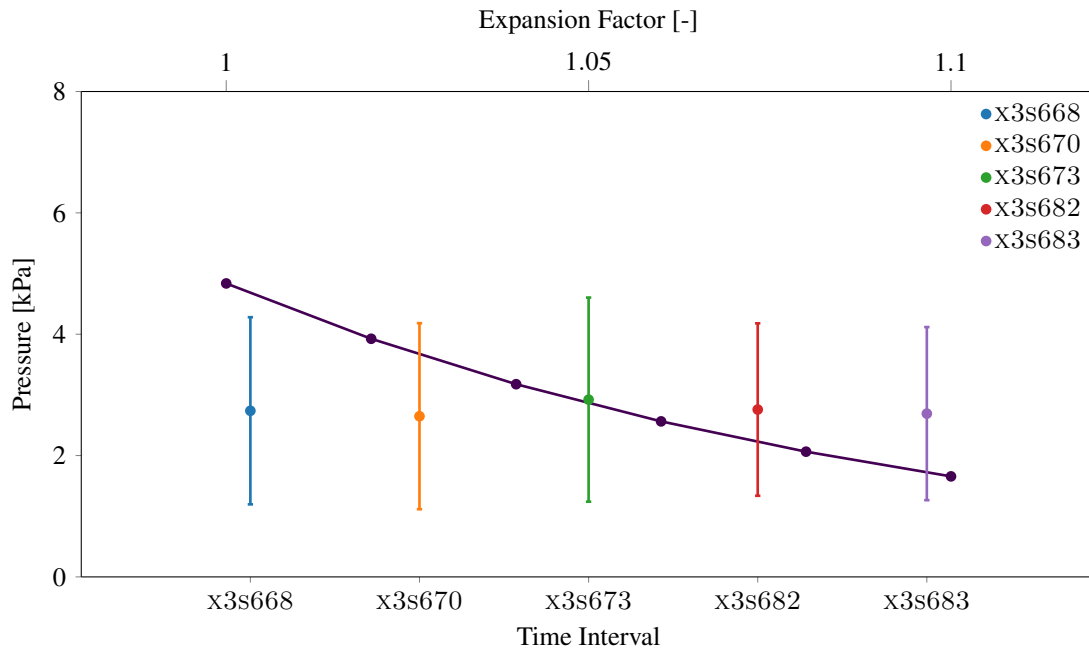


Figure 5.21.: Average wall pressure of the test gas at sensor AT8 from a selection of shots used to perform the condition analysis identified by labels on the bottom axis and legend. The error bars represent the maximum and minimum values as the pressure is constantly rising (see fig. 5.18). Analytical pressures are represented by the dark blue line and the corresponding expansion factor is identified by the top horizontal axis.

theoretical shock speed in the acceleration tube) with the expansion factors being read off the top horizontal axis and corresponding theoretical pressure read off the left axis. For this example, it can be concluded that expansion factors of 1.04–1.10 give the best agreement between experimentally measured wall pressure and theoretical calculation. The described process will also be applied to fig. 5.22, fig. 5.23 and fig. 5.24.

As with fig. 5.21, fig. 5.22 compares the analytical post conical shock pressure over a 15° degree cone against the measured experimental value. The experimental values are presented in the same time intervals as in fig. 5.19 and each plotted value is the average value of the centre probes (i.e. P4, P5, and P6). It is evident that an expansion factor of 1.06 – 1.1 best represents the operating condition up the inlet of the nozzle, but for completeness all expansion factors will be considered for comparison with the conical and Pitot probes in the test section in fig. 5.24 and fig. 5.23.

As with the properties upstream of the nozzle, a similar analysis can be performed at the nozzle exit with the conical in pitot probes. Figure 5.23 presents the comparison between analytical and experimental pressures for the conical probes and fig. 5.24 displays a similar plot for the pitot probes. As with fig. 5.19, the time intervals for the test time used in fig. 5.14 and fig. 5.16, with the mean value being the mean of a range of sensors and error calculated by summing the standard deviations as variances. The probes used for the experimental analysis was limited to those that appeared to be

## 5. Radiation Experiments

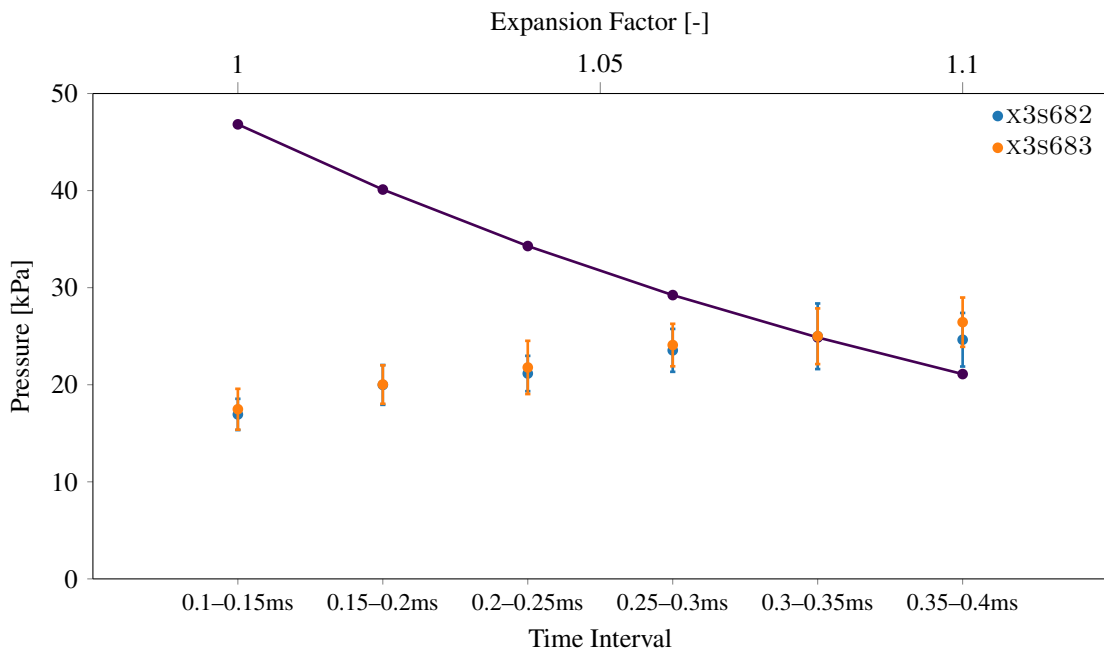


Figure 5.22.: Average conical probe pressure before the nozzle inlet for the time intervals shown in fig. 5.19. Each value is the average of P4, P5 and P6 (0mm – 37mm from centreline), error is calculated by adding the standard deviations as variances. Analytical pressures are represented by the dark blue line and the corresponding expansion factor is identified by the top horizontal axis.

representative of the core flow. For the conical probes a maximum radius of 120mm was used and for the pitot probes a maximum radius of 180mm was used. The resulting plot are presented in fig. 5.23 for the conical probes and fig. 5.24 for the pitot probes. Although all expansion factors are shown, it is evident that if only expansion factors of 1.06–1.1 are used, that a nozzle area ratio of 9–11.8 complies the best with the experimental data for both probe types.

Once the analytical comparison of the experimental flow condition is completed, the remainder of the test section flow properties can be calculated based on the selection. As the concluded parameters involve a range of options (expansion factor of 1.06–1.1 and nozzle area ratio of 9.0–11.8) the resulting flow condition presents a range of values for each property rather than a single distinct solution. Figure 5.25 shows the trajectory of the Hayabusa capsule when it landed in Woomera in 2012 [151] and the peak radiation heating along the trajectory as identified by several authors is also located [68, 70, 151]. Also included in fig. 5.25 is the conclusion of the condition analysis, the red shaded area highlights the calculated flow conditions in the test section of X3. Overall it is close to the location of peak radiative heating. While it would be desirable to increase the density slightly, at the time of writing that task has been left as a recommendation for future work. A more concise summary of the flow properties is shown in table 5.2 with a comparison to the scaled condition used in X2 experiments. Table 5.2 also contains the analytical test flow properties when the frozen model is applied to PITOT, with the main difference being drop in temperature and increase in density. The equivalent flight

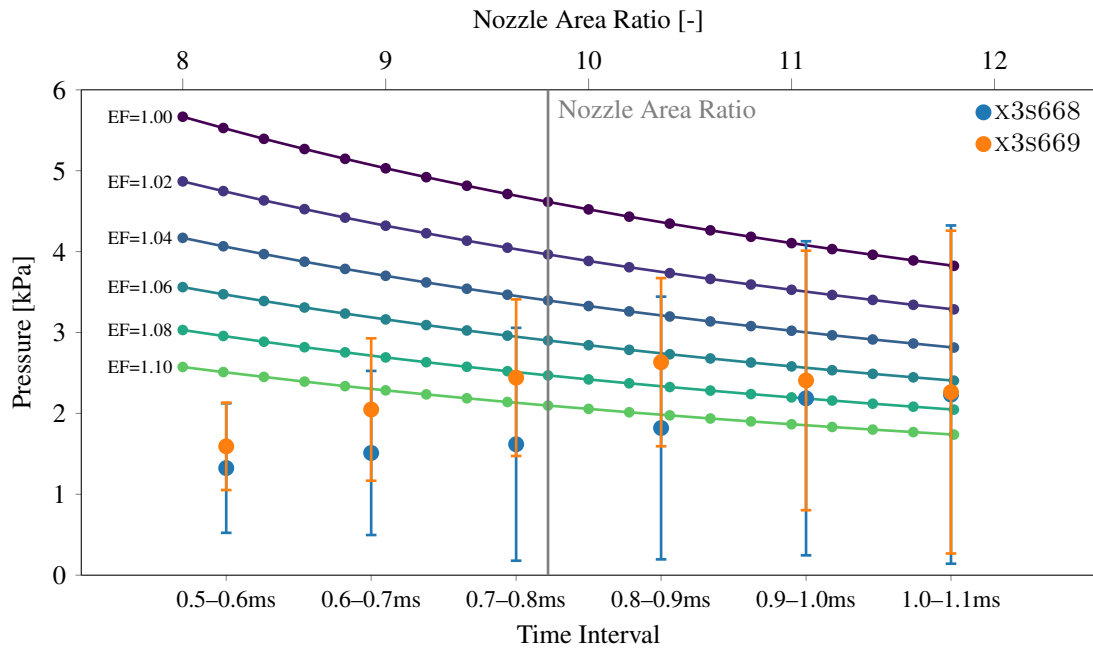


Figure 5.23.: Combined mean pressure for PT3, PT5, PT6 and PT8 for the time intervals indicated in fig. 5.14, the error is the total standard deviation across the four probes by summing the variance. The analytical data is shown by contours of expansion factor, and the corresponding nozzle area ratio can be read for the top horizontal axis.

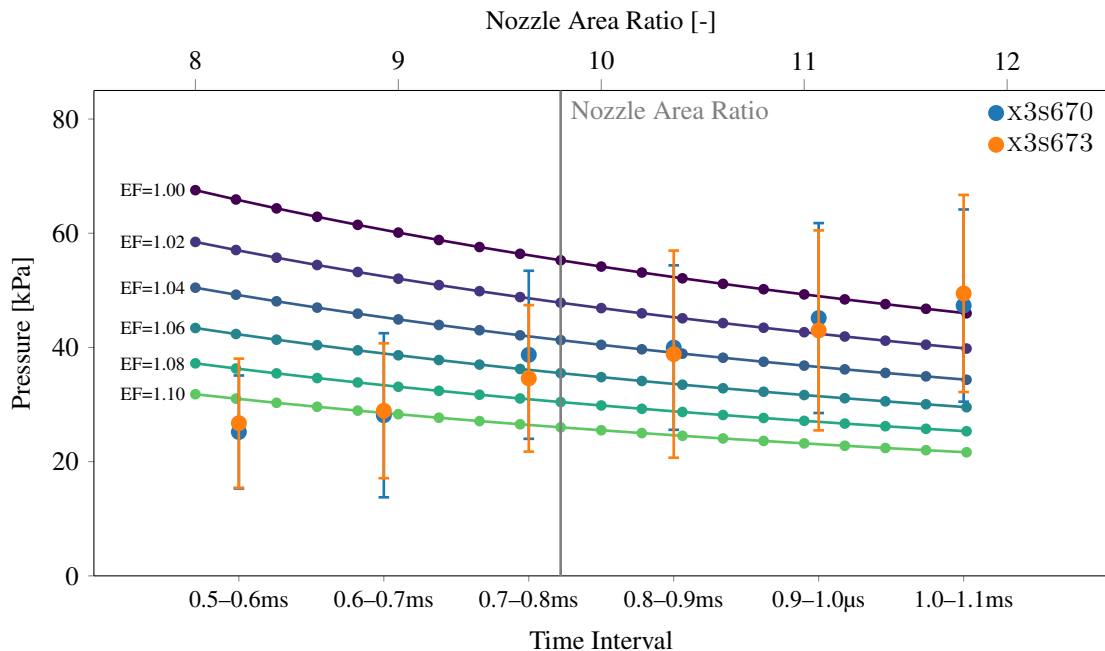


Figure 5.24.: Combined mean pressure for PT1, PT2, PT3, PT5, PT6, PT7, PT8, PT10 and PT11 for the time intervals indicated in fig. 5.16, the error is the total standard deviation across the four probes by summing the variance. The analytical data is shown by contours of expansion factor, and the corresponding nozzle area ratio can be read for the top horizontal axis.

## 5. Radiation Experiments

Table 5.2.: Analytically determined test flow properties in X3 with comparison to the 1:5 scaled X2 condition and nominal flight properties. The X2 condition is a 1:5 scaled condition of the nominal flight condition which is a trajectory point shortly after Hayabusa's peak radiation trajectory point. Calculations using a frozen test gas are presented in red.

	Minimum	Maximum	Nominal [77]	X2 Condition [77]	Units
Velocity	10.28 <b>10.27</b>	10.66 <b>10.65</b>	10.44	10.22 <sup>1</sup>	$\text{km s}^{-1}$
Temperature	2128 <b>1670</b>	2324 <b>1870</b>	258	3087 <sup>1</sup>	K
Density ( $\times 10^{-3}$ )	0.22 <b>0.25</b>	0.43 <b>0.47</b>	0.52	3.1 <sup>1,3</sup>	$\text{kg m}^{-3}$
Enthalpy	55.6 <b>55.4</b>	59.4 <b>59.1</b>	55	53.4 <sup>2</sup>	$\text{MJ kg}^{-1}$
Pitot Pressure	23.8 <b>26.6</b>	47.4 <b>46.3</b>	—	345 <sup>2</sup>	kPa
Cone Pressure	1.92 <b>2.69</b>	3.90 <b>4.78</b>	—	27.5 <sup>2</sup>	kPa
Equivalent Flight Velocity <sup>4</sup>	10.59 <b>10.53</b>	10.92 <b>11.87</b>	10.44	10.4	$\text{km s}^{-1}$

<sup>1</sup> Properties calculated from Eilmer3 simulations

<sup>2</sup> Properties calculated from PITOT

<sup>3</sup> Nominal scaled density is  $2.6 \times 10^{-3}$

<sup>4</sup> Specific heat of the calculated condition leaving the nozzle was used

velocity can be calculated by matching the enthalpy of the experimental flow and the flight condition as shown in eq. (5.2), where  $U_{exp}$  and  $T_{exp}$  are the experimental flow velocity and temperature,  $C_p$  is the specific heat of the test gas (in this case air), and  $U_{flight}$  is the equivalent flight velocity. Overall, the newly developed experimental condition in X3 is a better representation of the peak radiation trajectory point, which is evident from comparing the densities and equivalent flight velocities with the scaled condition used in X2 (table 5.2) and the peak radiation trajectory point (fig. 5.25).

$$\frac{U_{exp}^2}{2} + C_p T_{exp} = \frac{U_{flight}^2}{2} \quad (5.2)$$

The X2 condition in table 5.2 is a  $5 \times$  scaled condition of the trajectory point of peak radiation heating for Hayabusa, thus the aim of the condition development was to conserve enthalpy and achieve a density of one fifth the value used in X2. It should be pointed out that the density used in X2 in table 5.2 is higher than the nominal scaled value, and the analytical densities calculated for X3 results in a scaling factor between the two facilities of 6.5–14 rather than the nominal 5. Overall the density of the flow in X3 is slightly lower than what would be ideal and this has an effect of the equivalent

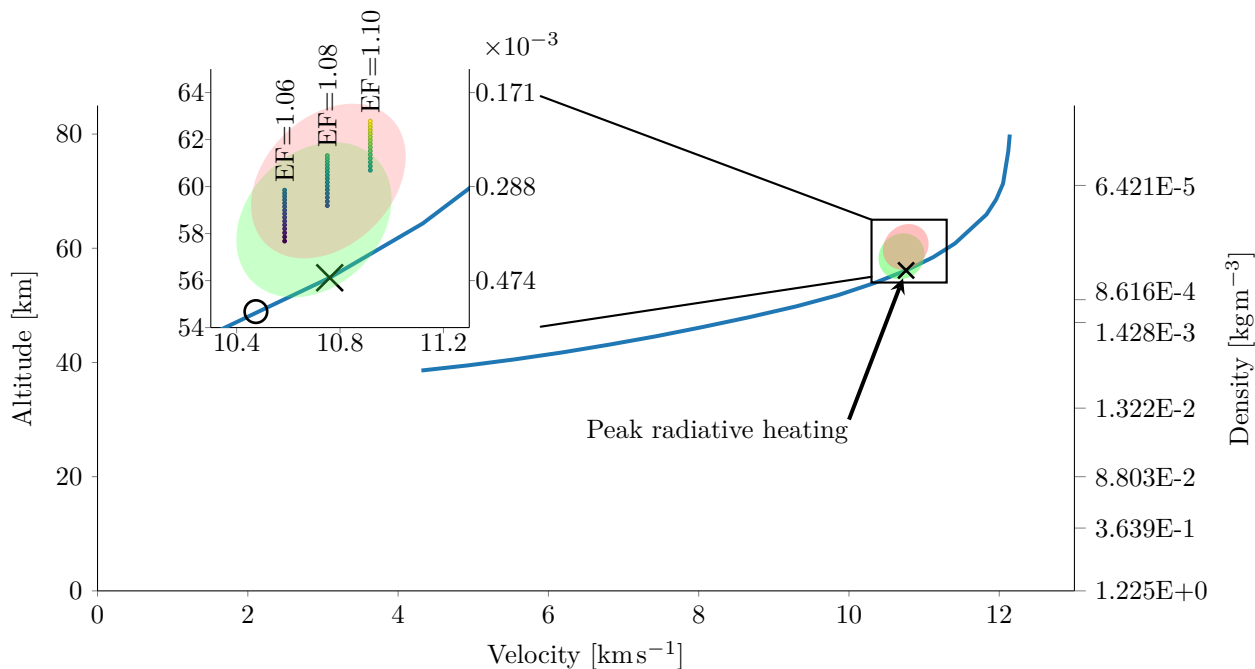


Figure 5.25.: Hayabusa trajectory with location of peak radiative heating identified and possible locations of the experimental flow condition (red area). Each point within the red area identifies the equivalent flight velocity and density of the analytical calculations completed in PITOT for expansion factors of 1.06, 1.08 and 1.10. The green area was calculated using the frozen gas model. A higher density (thus lower on the plot) signifies a smaller nozzle area ratio. Hayabusa trajectory is from Ohnishi et al. [151], the peak radiation trajectory point (cross marker) according to Ohnishi et al. [151], Buttsworth et al. [68] and McIntyre et al. [70], and the equivalent flight condition used by Fahy [77] (circle marker) in scaled experiments performed in X2. Densities shown on the right axis are the reference densities used when applying the barometric formula [152].

altitude of the condition and the location of the condition in X3 compared to the altitude-velocity trajectory plot of Hayabusa as shown in fig. 5.25.

## 5.6. Experimental Models

For the experiments conducted in the remainder of this thesis, two different models of Hayabusa were used: a 1:5 scale model similar to that used in X2 experiments by Fahy et al. [76] and a full scale model. The geometry of Hayabusa comprises the blending of a sphere with radius 200mm and a 45° cone which ends at a diameter of 400mm. The dimensions are illustrated in fig. 5.27 (b) and the 1:5 scale model conserves the geometric features. To reduce mass and ease the installation process the full scale model was constructed of multiple parts: a spherical centre steel section and the conical flared aluminium section.

## 5. Radiation Experiments

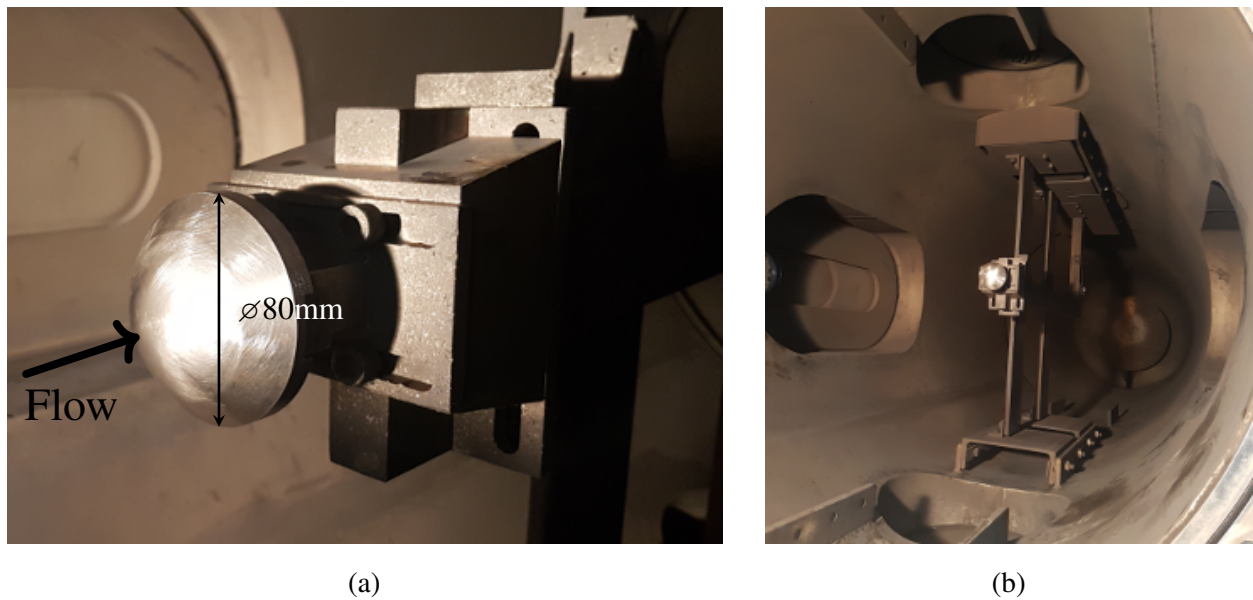


Figure 5.26.: The 1:5 scale Hayabusa model mounted in X3's test section. (a) a close up view of the model, (b) the model with the size of the test section as a reference.

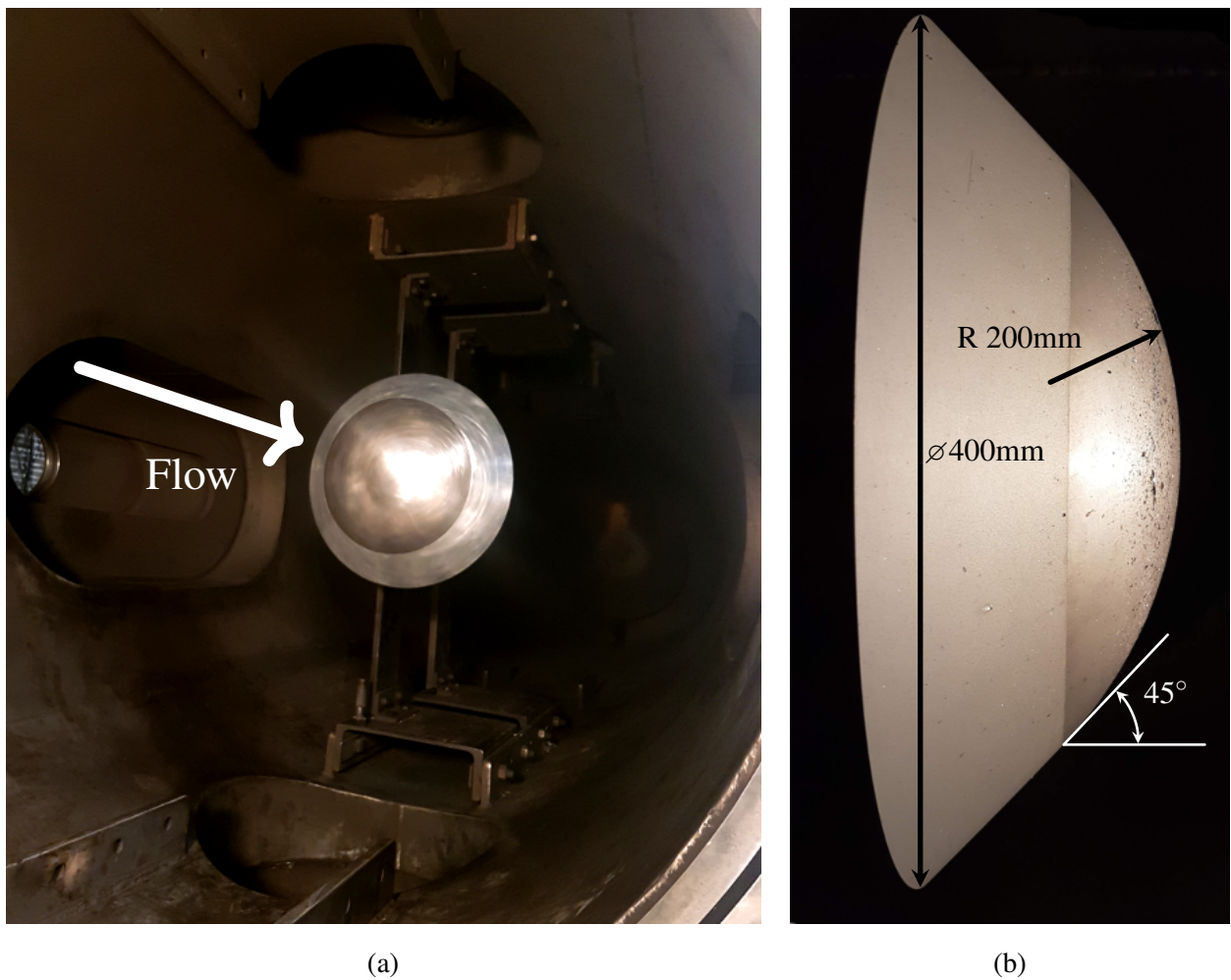


Figure 5.27.: (a) The full scale Hayabusa model mounted in X3's test section and (b) the main dimensions of the model.

## 5.7. Optics Experiments

The ultimate goal of the experimental campaign was to perform time resolved spectroscopic measurements on different scale Hayabusa models. While many difficulties were counted throughout this study, final result still yielded an experimental test flow performed at a flight condition close to peak radiation with a full size model. Typically, since experiments in X2 required small scale models, the flow condition density is increased to conserve binary scaling. The experiments performed in X3 can examine two models with no binary scaling applied; this means that binary scaling is not conserved for the scale model, but is conserved for the full scale model. Therefore a crossover exists between the full scale model in X3 and the 1:5 scale model in X2.

### 5.7.1. Optical Setup

The optical layout, which is shown in fig. 5.28, comprises a Shimadzu HPV-1 [153] used for filtered 2D imaging and the recording device for the spectral images, itself a combination of a HiCATT high speed image intensifier [154] coupled with Phantom v611 high speed camera [155]. The main difference in this setup compared to a typical optical setup for X2 (see [76] for an X2 setup) is the use of the intensifier and Phantom high speed camera instead of an ICCD camera. This arrangement allows multiple spectral images to be taken during a single test time as opposed to only one spectral image per experiment, something that is usually limited by low test times and slow frame rates on the available ICCDs.

In fig. 5.28, the first focusing mirror has a focal length of 2000mm and diameter of 20cm; all other mirrors and the lens at the exit of the spectrometer (see red circle) have a diameter of 50.8mm. Considering the exit of the spectrometer, a diverging lens with a focal length of  $f=-100\text{mm}$  was required so that the spectrometer focused on the sensor of the intensifier (coloured light brown in the red circle). This nominally magnifies the image of the entrance slit by 2.27. To account for this magnification, the size of the full scale model, and expected shock stand-off, the optics between the model and spectrometer have a nominal system magnification of 0.333, which results in the entire optical system having a nominal magnification of 0.76. When the optics were set up, the measured system magnification was found to be 0.81.

To better understand the timing of the optical instrumentation, fig. 5.29 shows the exposure scheme for the intensifier, the Phantom, and HPV-1 in x3s705. For all three instruments a high signal indicates exposure (i.e an open shutter or gate) whereas a low signal indicates no exposure (i.e. a closed shutter or gate). For the case of x3s705 the HPV-1 has a fairly straightforward exposure scheme — an  $8\mu\text{s}$  exposure every  $16\mu\text{s}$  — although the exposure arrangement for the Phantom and the intensifier is slightly more complex, with the intensifier exposing multiple times for each Phantom exposure. Initial experiments (not detailed in this thesis) showed some effects similar to haloing in image intensifiers

## 5. Radiation Experiments

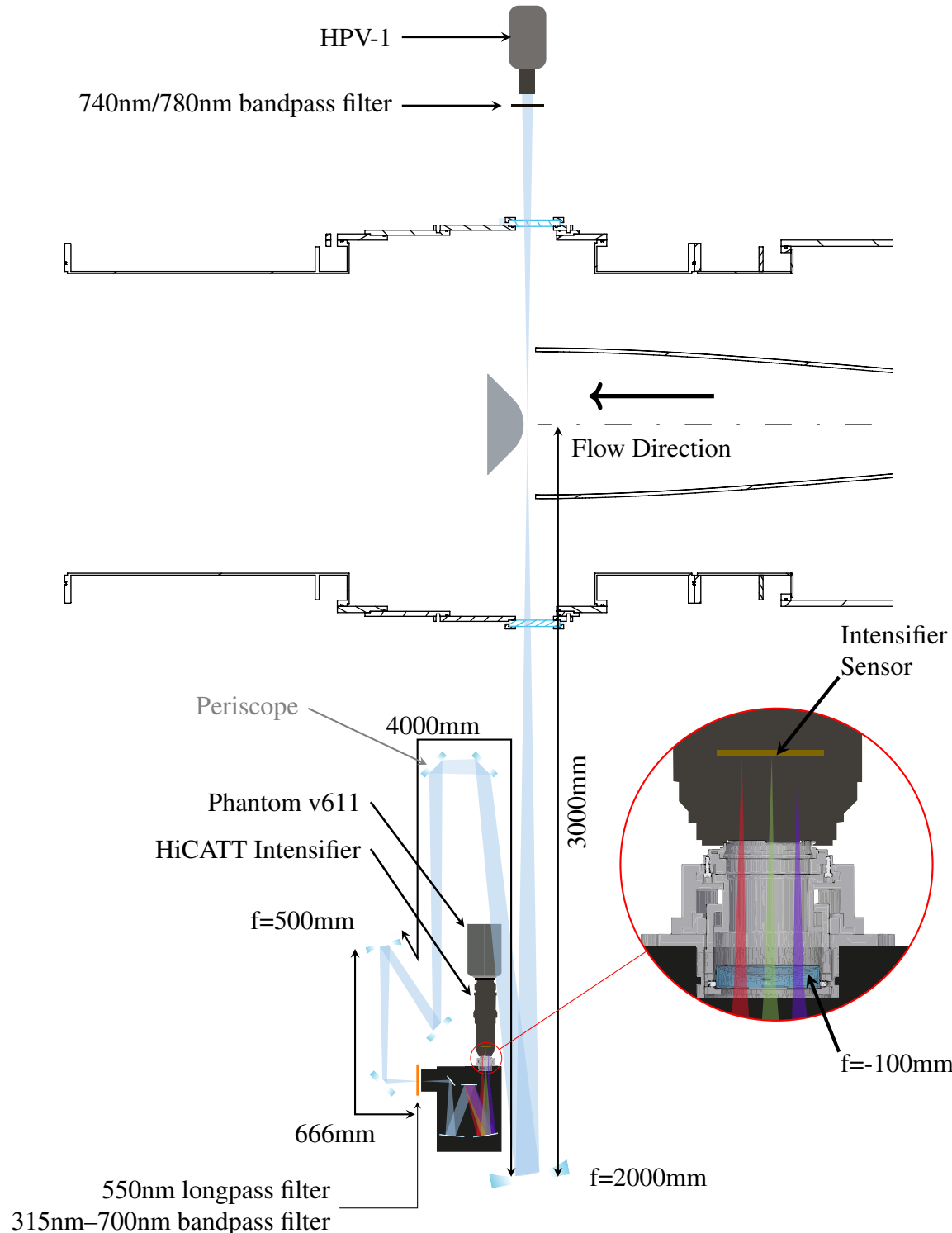


Figure 5.28.: Optical layout used for experiments with both the 1:5 scale model and full scale model.

The mirror indicated as a periscope consists of two mirrors aligned vertically which serve to change the height of the beam and rotate the image to align with the entry slit of the spectrometer. Distances are nominal and the location and size of optical components are not to scale.

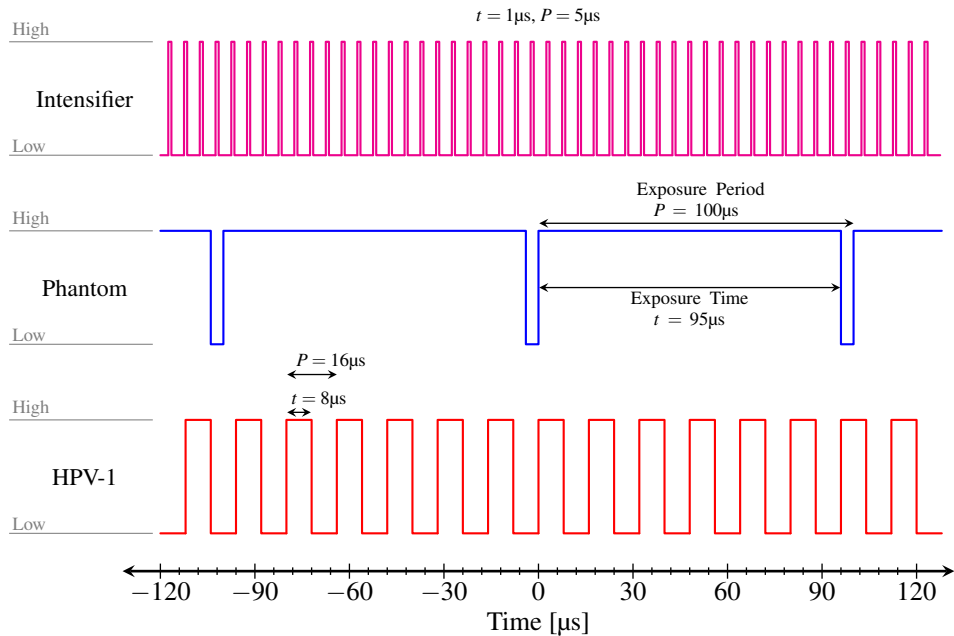


Figure 5.29.: Layout of optics timing scheme; sample values are given for X3s705. Phantom and HSP are time referenced to 0μs for simplicity

when longer exposure times and higher gains were used on the intensifier. An apparent solution at the time was to reduce the gain and increase the intensifier exposure time by open exposing multiple times per exposure of the Phantom as shown in fig. 5.29. At the time this seemed to be a reasonable solution, but some sample images taken at the end of the campaign suggest that this was merely coincidental. Nevertheless, all the shots presented in this section with spectroscopic images follow a timing scheme similar to that shown in fig. 5.29 with the values for the exposure period and exposure time for each shot detailed in table 5.3, and it should be noted that an intensifier exposure occurs while the Phantom is not exposing.

## 5.7.2. High Speed Imaging

The 2D filtered imaging was used to visualise the flow field around the model but more importantly, it can also be used to measure the shock stand-off around the model. The leading surface of Hayabusa is spherical so the model and shock shape can be approximated as locally spherical and overlayed with a circle similar to that done by Zander et al. [156] for spherical models to validate CFD, and James et al. [106] using a cylindrical model to better quantify test times. Once the geometric centre and radius of the model are known, the location of the shock front need to be detected and the result of two different methods have been shown in fig. 5.30. The two methods used were thresholding with a lower intensity limit of zero and Canny edge detection [157]. The left image in fig. 5.30 shows the shock location as calculated using the two edge detection methods and the model boundary.

## 5. Radiation Experiments

Table 5.3.: Exposure schemes based on fig. 5.29 for all shots. Each entry containing “—” means no useful data was acquired and is not included in analysis.

	HPV-1	Phantom		Intensifier	
		P	t	P	t
1:5 Scale Model	x3s693	—	—	100	95
	x3s694	—	—	100	96
	x3s696	—	—	100	95
	x3s698	16	8	—	—
	x3s699	16	8	50	45
	x3s700	16	8	50	45
1:1 Scale Model	x3s701	16	8	100	95
	x3s702	16	8	100	95
	x3s703	16	8	100	95
	x3s704	16	8	100	95
	x3s705	16	8	100	95

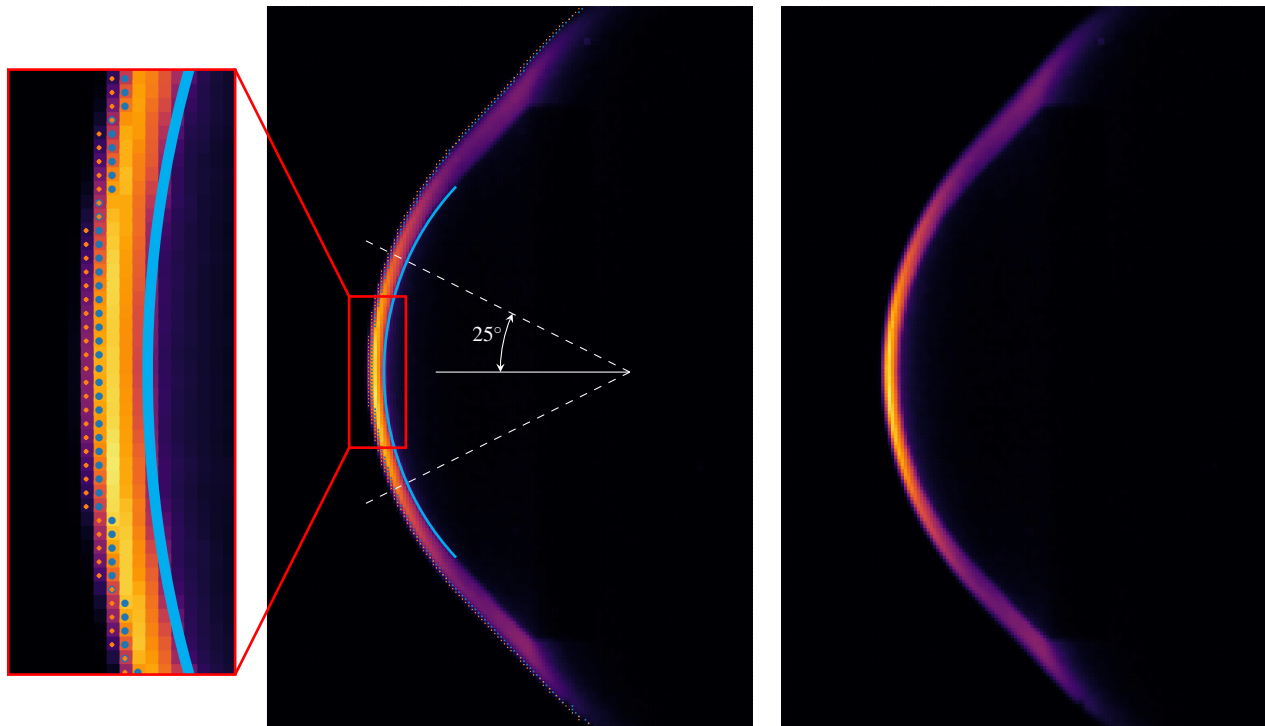


Figure 5.30.: Sample image from x3s698 taken with high speed camera with 740nm bandpass filter.

Right image shows the raw image from the high speed camera and left image has edge detection and model boundary (solid blue line). In the zoomed-in section, the blue dots identify the shock edge as identified by the Canny method and the orange dots show the shock edge using threshold detection.

Once the shock edge has been located the shock stand-off can be calculated by fitting a circle (centered at the centre of circle that located the edge of the model) to the shock and comparing the radii of the two. As the camera divides the image into discontinuous pixels the location of the shock edge is not continuous, so the effective radius of each pixel (from the centre point) varies over a region, in this case  $\pm 25^\circ$  from the stagnation streamline (see fig. 5.30), which according to Billig [158] gives an error of 2% at the edges for a perfect gas shock fit. The effective radius of each shock location was calculated and averaged with the following equation taken from [159].

$$R = \sum_{i=1}^n \frac{\sqrt{(x_i + a)^2 + (y_i + b)^2}}{n} \quad (5.3)$$

Here,  $n$  is the number of shock locations,  $x_i$  and  $y_i$  correspond to the x and y coordinates of the shock location, and  $a$  and  $b$  are the coordinates of the centre of the circle used to fit the model, which should be the same as for the shock (i.e. centre of the blue line in fig. 5.30 which is indicated where the dashed white lines converge). In fig. 5.30, the left most image provides an example of two different methods of edge detection commonly used in image processing. The blue dots denote the shock location found using Canny edge detection [157] on the raw image and the orange dots denote the shock location found by threshold detection (i.e. the left most pixel that records an intensity higher than zero). It is evident there is some discrepancy between the two methods in fig. 5.30, with Canny edge detection measuring a smaller shock stand-off, and by visual inspection it appears that the actual shock shape is located somewhere between the two methods.

It was found that for this application, using the Canny edge detection algorithm gave more consistent results when applied across the hundreds of images acquired during the experimental campaign although it was susceptible to omitting pixels with low intensity at the start of the shock (see left image in fig. 5.30). When James et al. [106] performed shock fitting, they first binarised the image before applying edge detection. This method was suitable for their application which was to measure the consistency of shock stand-off, but the shot to shot variation of shock stand-off was not discussed. The application in this thesis is to measure absolute shock stand-off for the purpose of shot to shot comparison between two model sizes and for the 1:5 scale model; here, Canny edge detection was found to vary by 30% between shots.

To improve the consistency of measuring the shock stand-off, an extra step was performed after Canny edge detection. Referring back to fig. 5.30 it is evident that there are pixels that are illuminated and to the left of the shock edge (the blue markers). By taking the intensity of the pixel where the shock edge was detected a threshold process was used on that row of pixels, with the new shock edge location being defined as the left most pixel with at least 20% the intensity of the pixel identified by Canny edge detection. This method is similar to using threshold edge detection but it accounts for the intensity in at the edge of the shock layer using a more rigorous edge detection method, examples of results of this methodology are shown in fig. 5.31.

## 5. Radiation Experiments

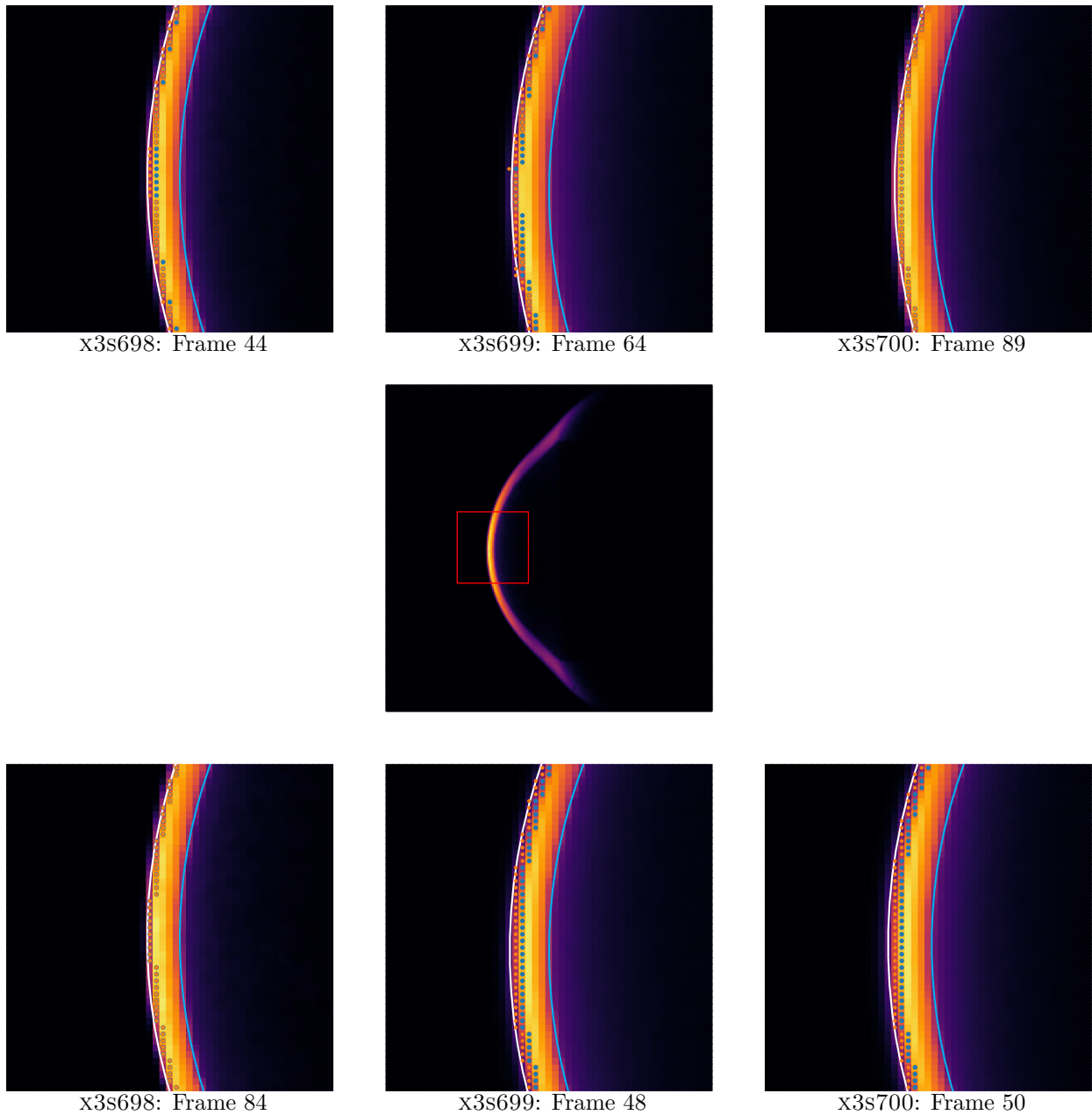


Figure 5.31.: Examples of shock fitting for two random frames for each experiment performed with the 1:5 scale model. The cyan arc shows the model edge, the white arc shows the estimated shock shape, the blue and orange points show the location of the Canny edge and the threshold edge respectively. The centre image indicates the location of the flowfield of the outside images.

By visual inspection of fig. 5.31, it appears that using an adaptive threshold detection method locates the shock boundary quite well (the white arc) and as such this method has been used to process all images for all the relevant shots. For each pixel where the shock edge is located, there is an error of half a pixel as the detection is essentially a discrete measurement with one pixel being the measurement interval, the same error can be applied to the measured radius of the model in the images. When considering the error in these measurements the following relation which defines the ratio between the shock stand-off  $\delta$  and the diameter of the spherical section of the model ( $D$ ) can be defined as per eq. (5.4).

$$\frac{\delta}{D} \pm \Delta \frac{\delta}{D} = \frac{R_S - R_M}{2 \times R_M} \pm \frac{R_S - R_M}{2 \times R_M} \sqrt{\left( \frac{\sqrt{(\Delta R_S)^2 + (\Delta R_M)^2}}{R_S - R_M} \right)^2 + \left( \frac{(\Delta R_M)}{R_M} \right)^2} \quad (5.4)$$

$R$  is radius with subscripts  $S$  and  $M$  signifying shock layer and model respectively. This gives an effective shock stand-off ratio for each pixel identified as the shock edge in each frame. The pixels can be averaged in each frame to calculate the shock stand-off ratio against time during each shot with the pixel to pixel variation being carried through as a variance of the measurement as shown in eqs. (5.5) and (5.6).

$$\sigma_{\frac{\delta}{D}}^2 \equiv \left\langle \frac{\delta^2}{D} \right\rangle - \left\langle \frac{\delta}{D} \right\rangle^2 \quad (5.5)$$

$$\left\langle \frac{\delta}{D} \right\rangle = \frac{1}{n} \sum_{i=1}^n \left( \frac{\delta}{D} \right)_i \quad \left\langle \frac{\delta^2}{D} \right\rangle = \frac{1}{n} \sum_{i=1}^n \left( \left( \frac{\delta}{D} \right)_i^2 + \left( \Delta \frac{\delta}{D} \right)_i^2 \right) \quad (5.6)$$

$\sigma^2$  is the variance of the data set and  $n$  is the number of pixels that make up the shock layer in each frame. The resulting measured shock stand-off for the 1:5 scale model is shown in fig. 5.32. The three shots generally show agreement in that the shock stand-off normalised by model diameter is close to 0.035 throughout the test time. However, considerable error is present in the measurements due to the shock layer comprising a small number of pixels and there is a variation in the measurement for the first half of the test time, but this variation is effectively less than one pixel. The three experiments agree within experimental and measurement error, repeat experiments with higher magnification would need to be performed to improve the accuracy the measurements. High speed video of the full scale models was also recorded for each shot with the same magnification settings as the 1:5 scale model, which meant each image only captured the nose of the model, therefore a greater resolution of the shock layer was achieved compared to the 1:5 scale model. This does raise an additional consideration, the greater resolution of the image also means any unsteadiness in the flow is also captured in the high speed video, which increases the difficulty of running a generic algorithm to accurately calculated shock stand-off.

## 5. Radiation Experiments

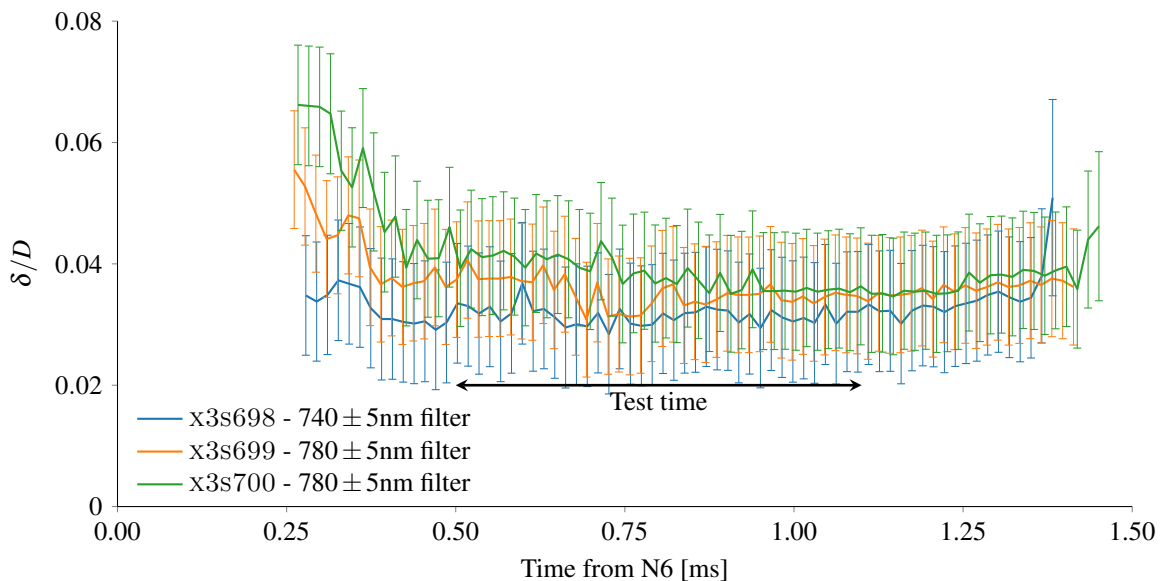


Figure 5.32.: Shock stand-off for 1:5 scale model along the stagnation line recorded with the HPV-1 high speed camera using two different bandpass filters, one for atomic nitrogen, the other for atomic oxygen. The large relative error is due to the small pixel number that the shock layer spans over for the smaller model.

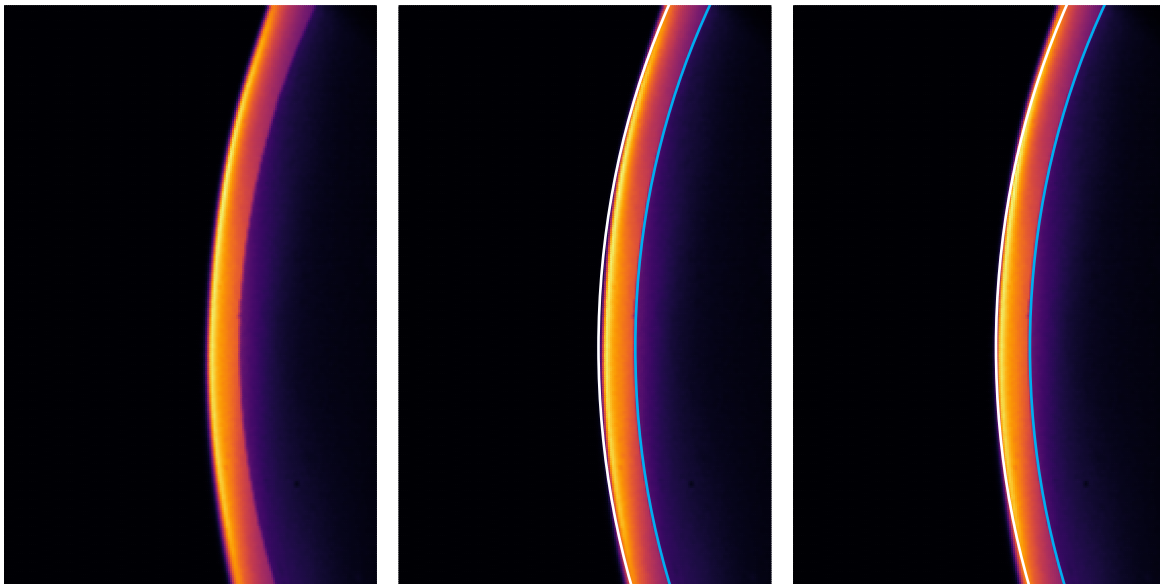


Figure 5.33.: Circle fitting for the full scale model in frame 57 of x3s705. The left image is the raw image taken from the camera. The cyan line is the model boundary and the white line is the circle fit for the shock shape using all points (centre image) and the bottom quartile in shock stand-off distances (right image).

As a general rule, any identified unsteadiness in the flow was observed to cause the localised shock layer thickness to increase, so one way to increase the reliability of the shock fitting method was to use the lowest quartile of shock stand-offs for each image for shock calculations. An example of how using the bottom quartile for shock fitting for the full scale model is shown in fig. 5.33, the centre

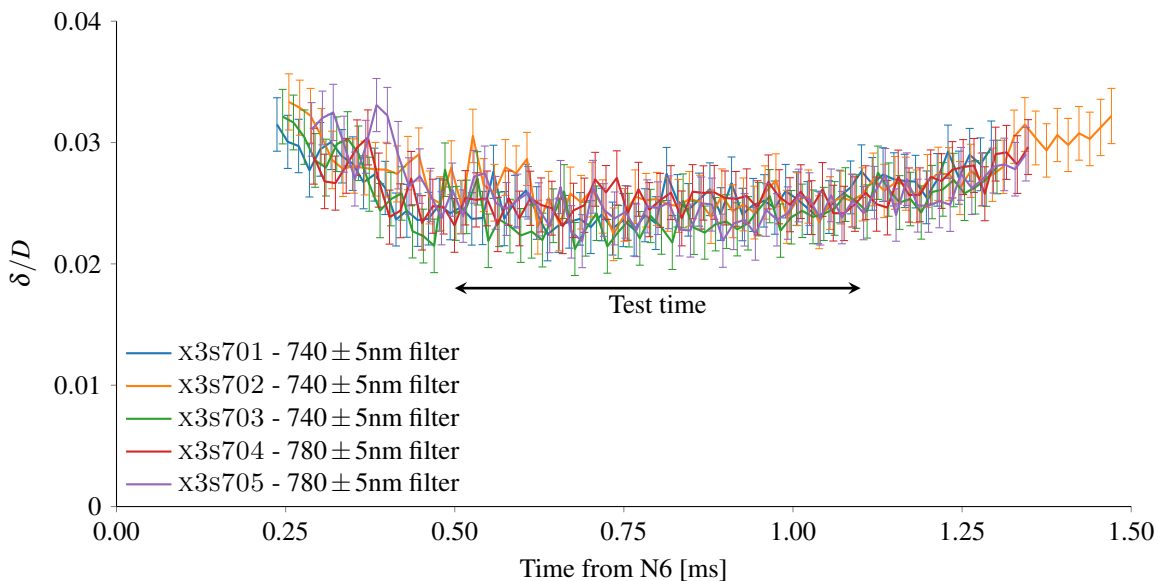


Figure 5.34.: Shock stand-off for full scale model along that stagnation line recorded with the HPV-1 high speed camera using two different bandpass filters, one for atomic nitrogen, the other for atomic oxygen.

image shows the predicted shock shape (white) when all the points are used to calculate the average, and the right image uses only shock stand-off measurements in the bottom quartile. It is evident in the middle image that the circle fit conforms more with the edges of the image and appears to inaccurately represent the shock at the stagnation line, the right image presents a much better fit in the stagnation area although there is more error at the extremes of the image. The circle fitting is constrained by the centre of the spherical section of the model and using a larger radius for the shock shape centered further to the right results in a poor circle fit for the model boundary. The resulting shock stand-off measured by the high speed camera across all shots using the full scale model is shown in fig. 5.34.

When compared with the shock stand-off of the 1:5 scale model the stand-off ratio for the full scale model is smaller due to high temperature effects. According to Hornung and Wen [160] the non-dimensional shock stand-off is dependant on the average density across the shock layer which is determined by the reaction rate. Generally, the shock stand-off is determined by the inverse ratio of densities across the shock and the shock thickness can be determined by performing a mass balance with an approximation derived by Lobb [161] as

$$\frac{\delta}{D} = 0.41 \frac{\rho_{\infty}}{\rho_2} \quad (5.7)$$

$\rho_{\infty}$  is the freestream density and  $\rho_2$  is the density behind the normal shock, and while the relation works well for high Mach number flows, it begins to break down at lower Mach numbers as the density ratio approaches unity. When considering a reacting flow, the effect that the reaction rate has on the

## 5. Radiation Experiments

flow field behind the shock needs to be considered as it will affect the average density (effectively  $\rho_2$ ) in the shock layer, which in turn affects the shock stand-off. It is expected that the ratio  $\delta/D$  will vary across the two model sizes as the freestream properties are the same, but the distance over which reactions occur and the flow reaches equilibrium will be similar. As the nonequilibrium region does not change between the two model sizes, it is expected that the 1:5 scale model will have a larger relative shock stand-off ( $\delta/D$ ) as the nonequilibrium region constitutes a larger proportion of the shock layer, resulting in a lower average post-shock density compared to the full scale model, which has a smaller proportion of the shock layer taken up by the nonequilibrium region.

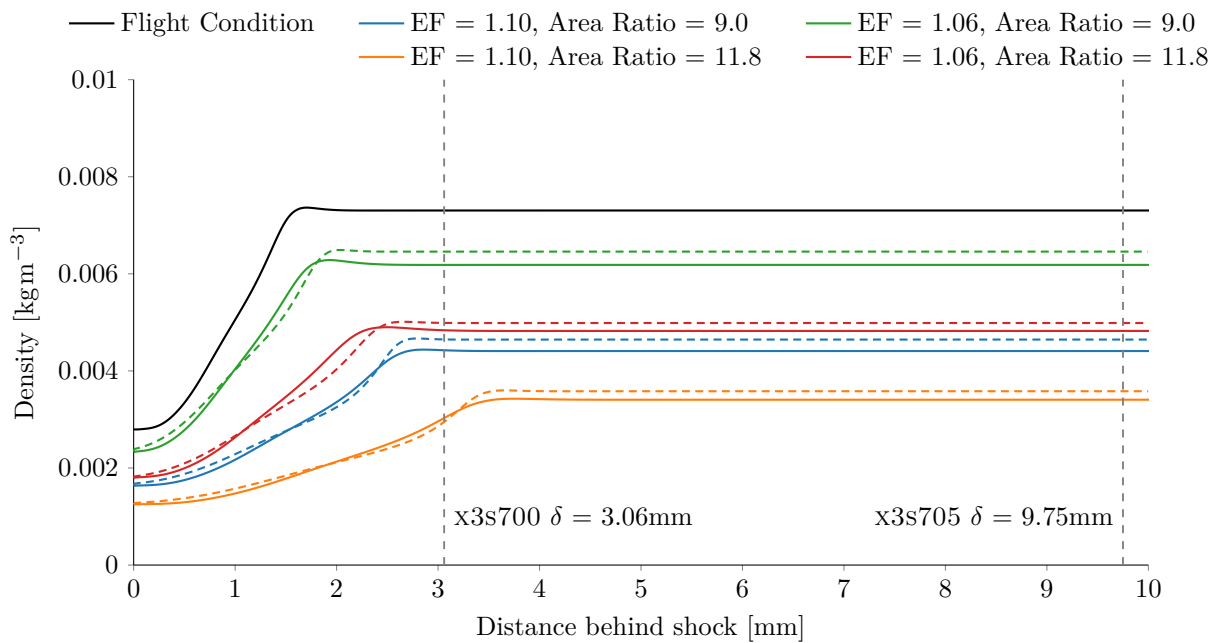


Figure 5.35.: Post shock density profile calculated using Poshax [162]. Density profile is calculated for a moving shock and presence of the model in the post shock region is not accounted for. 11-species air was used for all calculations with the reaction scheme taken from [163]. The dashed lines are the density profile behind the shock when the test gas is calculated using the frozen gas model in PITOT.

An example of how the average density in the shock layer varies with shock stand-off is demonstrated for the full scale condition used in X3 with Poshax [162] in fig. 5.35 which also shows the average shock layer thickness throughout the test time for x3s700 and x3s705. The average post-shock density for both model sizes and different possible conditions in fig. 5.35 is presented in table 5.4, along with the estimated freestream properties and estimated shock stand-off using eq. (5.7). The shock layer for the 1:5 scale model is predominately occupied by the nonequilibrium region, whereas the full scale model's shock layer has a significantly larger region at equilibrium relative to the smaller model. Both of the density profiles are for that behind a normal shock, and therefore does not include any density changes due to the presence of the model, which would have an effect on average density and shock stand-off. The average densities indicated in fig. 5.35 suggest an increase of approximately

20% to 55% of the normalised shock stand-off ( $\delta/D$ ) for the 1:5 scale model, and the measured data in fig. 5.32 and fig. 5.34 suggest an increase in  $\delta/D$  of approximately 40%, which tends towards the analytical results with larger expansion factors and nozzle area ratios, i.e. estimates that expand the test gas more. The measured shock stand-off in fig. 5.34, which is for the full scale model, is approximately 0.025 for the majority of the test time compared to the estimate of 0.032 using eq. (5.7) and the data in table 5.4. When considering the shock stand-off calculated using the frozen gas model in PITOT (red in table 5.4), the predicted shock stand-off for the full scale model only increases by approximately 5% for each case.

Table 5.4.: Average density  $\rho_2$  in the shock layer calculated using the results from Poshax in fig. 5.35.

Densities have been calculated for two shock stand-off measurements of the 1:5 scale and full scale model presented in fig. 5.35. The conditions analysed are the bounding analytical conditions (see fig. 5.25) which are the flow conditions with the highest and lowest velocity and density. The flight condition included is Hayabusa's peak radiative heating trajectory point. The red values are analytical calculation using the frozen gas model in PITOT.

	Expansion Factor	1.06	1.06	1.10	1.10	Flight Condition
	Nozzle Area Ratio	9.0	11.8	9.0	11.8	
Density ( $\times 10^{-3}$ )	$\text{kg m}^{-3}$	0.43 0.47	0.32 0.36	0.29 0.33	0.22 0.25	0.46
Temperature	K	2324 1870	2245 1781	2214 1754	2128 1670	256
Velocity	$\text{km s}^{-1}$	10.27 10.28	10.29 10.30	10.63 10.64	10.65 10.66	10.76
Pressure	Pa	291 310	212 225	189 203	137 147	34.5
x3s700	$\delta$ [mm]			3.06		
	$\rho_2$ [ $\text{kg m}^{-3}$ ] $(\times 10^{-3})$	4.87 4.95	3.31 3.43	2.89 2.97	1.89 1.90	5.87
x3s705	$\delta$ [mm]			9.75		
	$\rho_2$ [ $\text{kg m}^{-3}$ ] $(\times 10^{-3})$	5.77 5.99	4.16 4.49	3.74 3.98	2.92 3.04	6.84
$\rho_{2,\text{x3s705}}/\rho_{2,\text{x3s700}}$		1.18 1.21	1.26 1.31	1.29 1.34	1.54 1.60	1.17
$\delta/D$ for x3s705 (EQ5)		0.031 0.032	0.032 0.033	0.032 0.034	0.031 0.034	0.028

## 5. Radiation Experiments

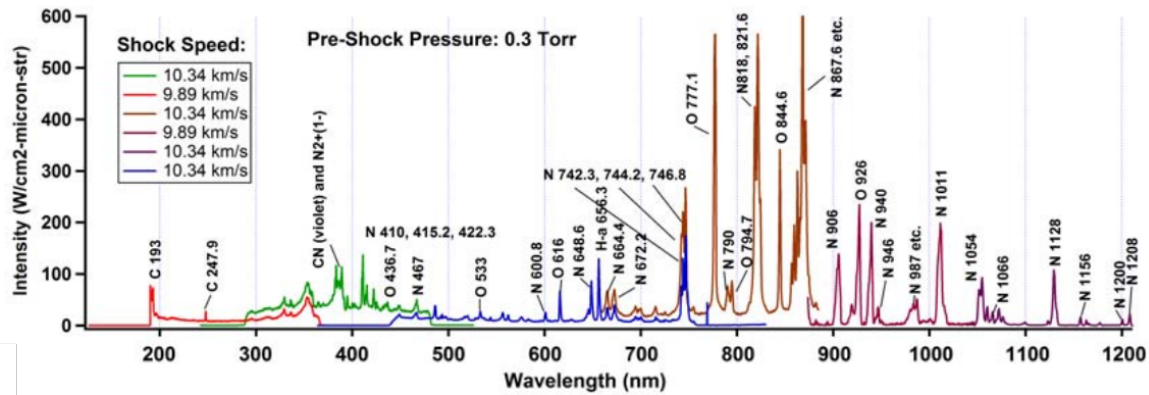


Figure 5.36.: Qualitative overview of EAST spectral measurements in air.

### 5.7.3. Time Resolved Spectra

In addition to the high speed video, the time resolved spectra can be used to estimate the shock stand-off along the stagnation line. As evident in table 5.3, the Phantom which recorded the spectral images has a long exposure time compared to the HPV-1, so while the measurements still give a trend over the test time, they are not as temporally resolved as the high speed imaging, because of the exposure. Two different wavelength regions were examined for both the 1:5 scale model and the full scale model; a nominal centre wavelength of 450nm and a nominal centre wavelength of 640nm with the total wavelength range of each image being approximately 150nm. Filters for both setups were used to eliminate the influence of second order features from smaller wavelengths (e.g. a 250nm feature which has a second order at 500nm).

Figure 5.36 is a summary of spectral features which has been assembled by Bose et al. [164] which presents an overall measured spectrum across a range of shots performed at NASA's EAST tunnel. The lines with the most intensity are present in the near IR region (700nm+) and there are some smaller features present in the visible region. Although the initial intention was to examine the near-IR region with the intensifier/Phantom setup, a combination of issues experienced during the experimental campaign meant that two separate visible regions were measured instead. More details about some of the encountered issues are elaborated upon in the Conclusions and Recommendations chapter 6. The two spectral regions in question are 365nm – 515nm and 555nm – 705nm and multiple experiments were performed for both spectral regions across both the 1:5 scale model and full scale model.

Overall, the quality of the spectroscopic measurements are not of the standard that would be obtained with an appropriate ICCD (intensified charge coupled device) camera, the main reason being that the regions being examined were not ideal for air, and secondly, there were several quirks, to using the intensifier with high speed camera that need to be quantified and examined in more detail. There are still some identifiable lines however, unfortunately most are due to contaminants. More importantly, the spectra gives another method to measure shock stand-off at the stagnation line which can be compared

to the high speed video obtained with the HPV-1. Firstly, the spectra of each shot will be presented with main features identified and the shock stand-off comparison will occur later in this sub section.

## Spectral Measurements

For each experiment a series of sample images were taken for calibration purposes of a Labsphere integrating sphere (a source of known intensity) supplied by Lastek [165] with the intensifier and Phantom using the same settings as during the experiments. The intensifier itself contains a micro channel plate with a gain applied which results in a noisy output, so a median filter was applied to each frame with a 3x3 window to smooth the data. The mean value of each pixel across the calibration frames was taken as the representative value and the standard deviation was taken to represent the variance of each pixel's measured intensity. The calibrated intensity from the experiments could then be calculated by multiplying the ratio of measured intensity from the experiment and calibration with the inverse ratio of exposure times and the intensity value of the integrating sphere which is shown in eq. (5.8). The error for the measured intensity was taken to be the standard deviation calculated from the calibrated data. It is unknown how much the standard deviation changes for different intensity levels for each pixel, so while using the calibration standard deviation for the experiments may not be the best estimate of error, it gives a reasonable estimate.

$$I_{final} \pm \Delta I_{final} = \frac{I_m}{I_{cal}} \times \frac{E_{cal}}{E_m} \times I_{sphere} \pm I_{final} \sqrt{\left(\frac{\sigma_{I_m}}{I_m}\right)^2 + \left(\frac{\sigma_{I_{cal}}}{I_{cal}}\right)^2} \quad (5.8)$$

Where  $I$  is the measured intensity,  $E$  is the total time the intensifier is exposed, subscripts *final*, *m*, *cal* and *sphere* are the final calibrated intensity, experimental measured intensity, calibration intensity and reference value from the integrating sphere respectively. The error is simply the propagation of the standard deviation for both the experimental and calibration measurements. An example of spectra obtained from the 1:5 scale model for both wavelength regions can be seen in fig. 5.37, and it is evident that prominent features consist mainly of the H- $\alpha$  line at 656.28nm and CN violet bands at 388nm and 415nm, other features present are identified in fig. 5.40 and fig. 5.41. Similar spectral images of the stagnation line for the full scale model are shown in fig. 5.38, it should be noted that all the spectral images have been filtered and resolution reduced for the purpose of presentation (in fig. 5.37 and fig. 5.38) by removing every second row and column using median values for the remaining coordinates. The shock and model boundaries are also indicated in fig. 5.37 and fig. 5.38 based on the change in intensity in the spatial direction. For the shock boundary, the sum of each row was taken and a threshold of 20% – 50% of the maximum value of the summed rows was deemed to be a reasonable range for the shock location, as it captures the rise in intensity but not any non zero measurements that arise due to noise or smearing in images, especially for images with low maximum intensity (see x3s694 in fig. 5.37). The location of the model was taken from calibration images taken before each

## 5. Radiation Experiments

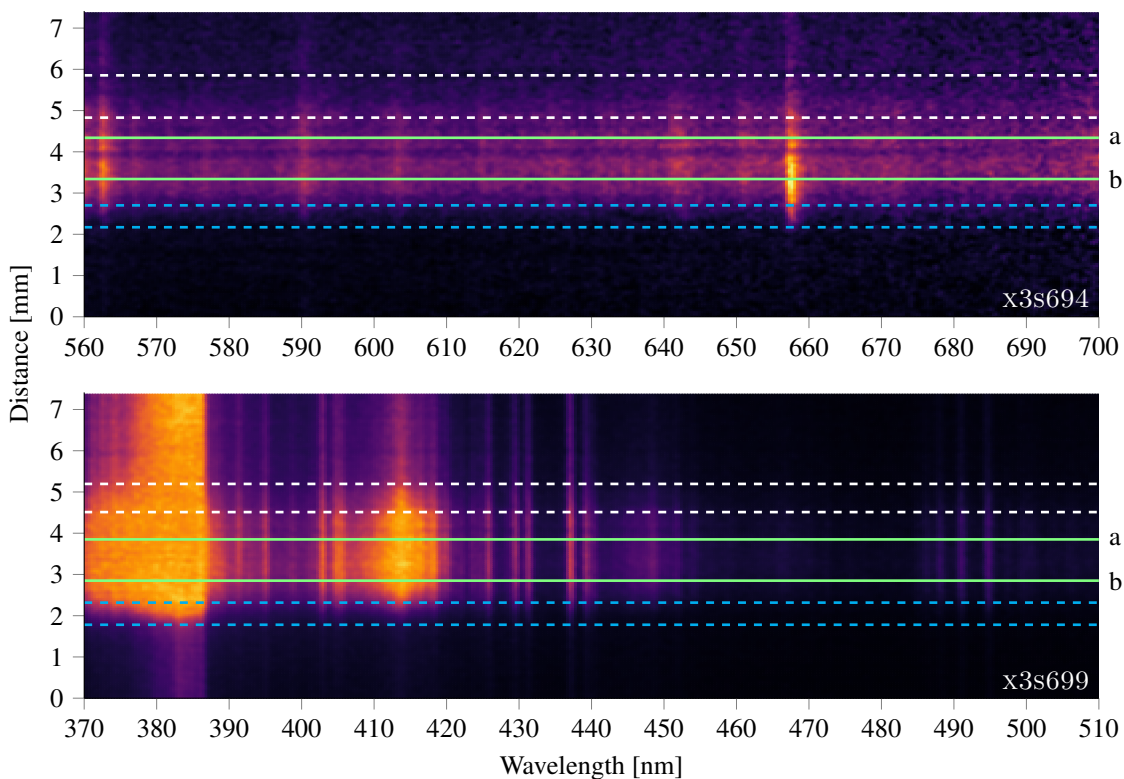


Figure 5.37.: Examples of spectral images for the 1:5 scale model, the flow direction is bottom to top. The model edge is indicated by the bounds of the dashed white lines and the shock stand-off is indicated by the dashed blue lines. The colour scale for each plot has been scaled for the purpose of illustration.

experiment and both of these methods were used to calculate the measured shock stand-off along the stagnation line later in this section.

### Shot to shot variation

As the experimental flow condition and method of measuring spectra were both newly designed, the variation in the intensity was compared for multiple regions between shots for the nominal test time. For consistency, the model boundary was taken as the reference and shock layer locations for comparison were taken as a distance from the model location. The green lines labelled "a" and "b" in fig. 5.37 and fig. 5.38 were used for measuring the consistency of each shot. In fig. 5.37 and fig. 5.38, the region between the dashed blue line identify the location of the shock based on the region of rising intensity and the region between the two white dashed lines identify the location of the model using a reference image taken before each experiment. The width of the model location varies due to the instrument settings used when taking the sample image. Figure 5.39 shows the comparison of line "b" for shots x3s693, x3s694 and x3s696, the 1:5 scale model, which consists of the H- $\alpha$  line at 656.28nm and what is believed to be a carbon line at 589.2nm and what is most likely additional contamination from carbon and iron arising later in the flow, although air species may be present but

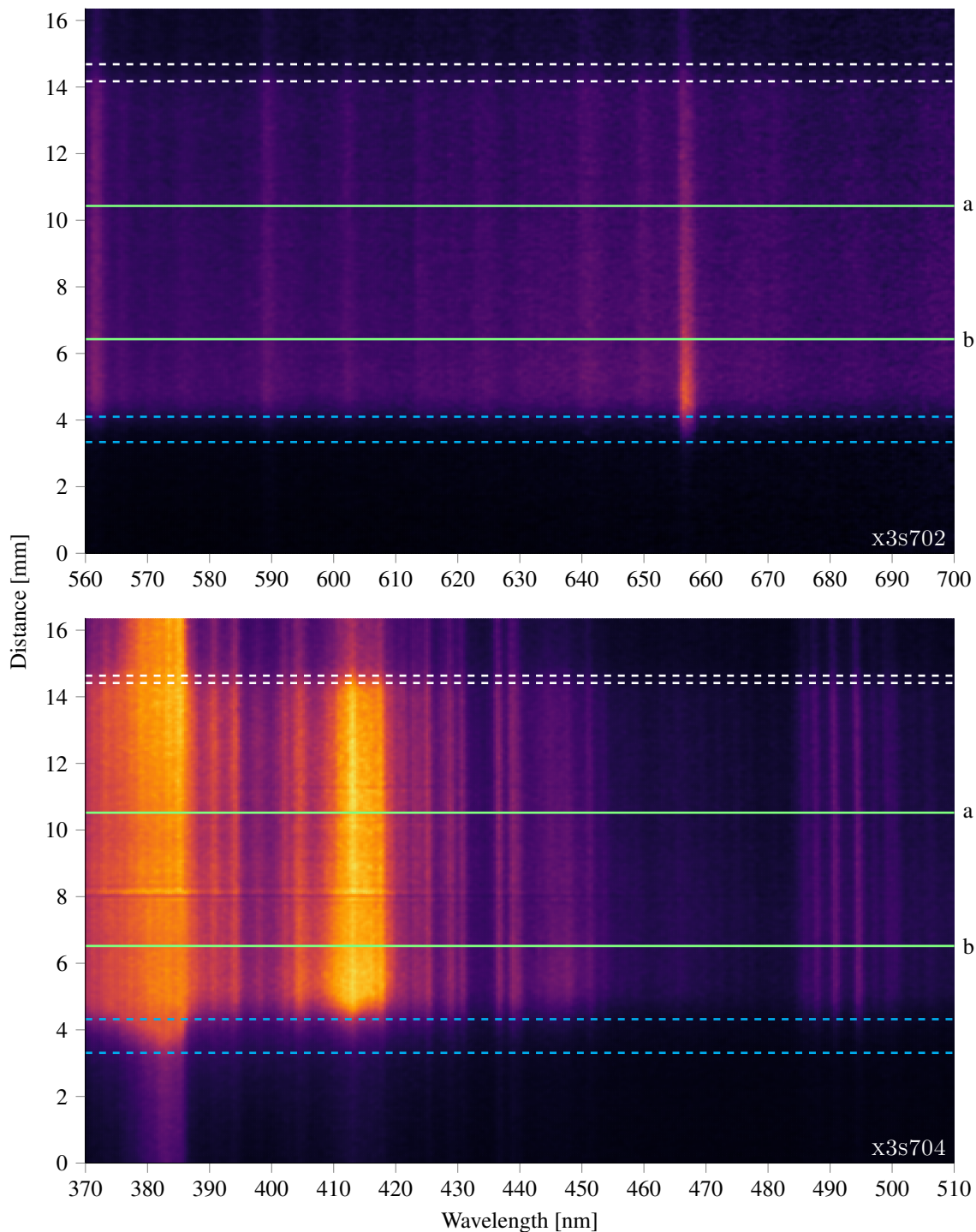


Figure 5.38.: Examples of spectral images for the full scale model, the flow direction is bottom to top. The model edge is indicated by the bounds of the dashed white lines and the shock stand-off is indicated by the dashed blue lines. The colour scale for each plot has been scaled for the purpose of illustration.

## 5. Radiation Experiments

coincide with features attributed to contaminants. Similar plots for other shots and locations are shown in appendix D. For the case shown in fig. 5.39, there is good agreement for x3s693 and x3s696 and intensities from x3s694 appear to be an underestimate with the clarity of spectral lines diminishing in frames 7–10, although the exposures for x3s693 are out of phase with the other two shots. Throughout the experiment there is also the development of three peaks around 560nm which may be due to iron (557.28nm, 558.68nm, 561.56nm), atomic oxygen (557.73nm) and carbon (561.48nm), although the presence of other unidentified species is also a possibility. An enlarged version of frame 9 is shown in fig. 5.40 with relevant spectral lines identified, with a similar plot in fig. 5.41 for the lower wavelength region examined in x3s699 and x3s700. The optical setup required manual wavelength calibration for both centre wavelength and wavelength resolution per pixel (typically spectroscopic systems have well defined wavelength resolutions) so identified species were limited to air species from the test gas, carbon, hydrogen and cyanogen from the diaphragm or grease in the tunnel, and iron from the tube wall, model or possibly primary diaphragm. Features in fig. 5.40 and fig. 5.41 have been identified by selecting a spectral feature of the aforementioned species from the NIST atomic spectra database [166] with the nearest wavelength and largest relative intensity.

The consistency of the spectral measurements between shots can also be examined in fig. 5.40 and fig. 5.41. Referring to fig. 5.40, good agreement exists between x3s693 and x3s696, while the measurements taken during x3s694 appear to underestimate the spectral radiance. The frames in fig. 5.39 show that the measured radiance for x3s694 is more consistent with x3s693 and x3s696 earlier in the test time, before the intensities start to differ later in the test time and the frames after the test time. As a lot of prominent features have been found to align with iron emissions, this suggests that contaminants from the primary diaphragm may be introduced to the test gas slug but are not consistently present in the test flow. The iron contaminants may also be particles coming off the wall of the tunnel as the test gas travels along the shock and acceleration tubes, or particles being emitted from the surface of the model, which is constructed of steel near the stagnation line. The two shots (x3s699 and x3s700) presented in fig. 5.41 also exhibit a difference in intensities, with significant disagreement at lower wavelengths. The exact reason why different intensities are measured have not been investigated but it is suspected that the behaviour of the intensifier affected the quality of the measurements. During the experimental campaign, it was observed that an artificial ceiling of measured intensity was present in the spectral measurements and as the intensifier's sensitivity varied across the wavelength regions examined, calibration images may not accurately reflect the response of the optical system because the measured intensity at wavelengths with higher sensitivity may have hit the artificial ceiling before an intensity was recorded at lower sensitivity regions. For the case of fig. 5.41, the sensitivity of the intensifier below wavelengths 400nm (where the CN (B-X)  $\Delta v = 0$  band is located) decreases considerably, and the large discrepancy between shots may arise during calibration or as a consequence of low sensitivity, although, the features between 480nm and 500nm also exhibit a similar discrepancy. A complete set of data can be seen in Appendix D and while it is less evident for the lower wavelength region and the large model, the presence of iron in the test flow

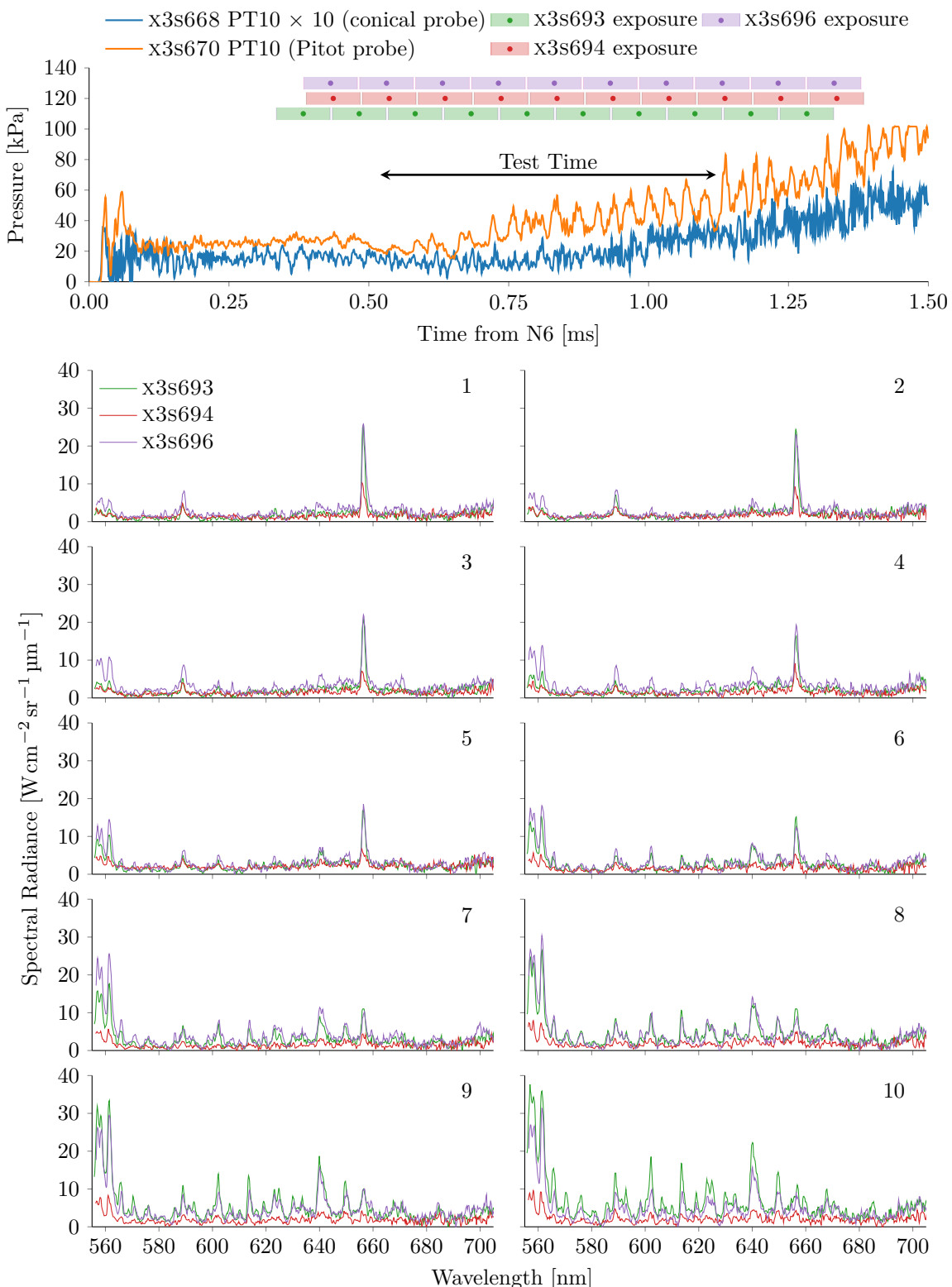


Figure 5.39.: Comparison of shots x3s693, x3s694 and x3s696 *line a* (from fig. 5.37). The top plot shows the timing of each exposure relative to the shock arrival at tube wall static pressure transducer N6 for the corresponding shock. Sample traces for the Pitot probes and conical probes are shown to put the timing of each exposure into perspective, the arrival of the flow at the probes from N6 was found to have a variation of approximately 7.5μs. Each plot below is labelled in chronological order and colours are consistent with the exposure timings in the top plot.

## 5. Radiation Experiments

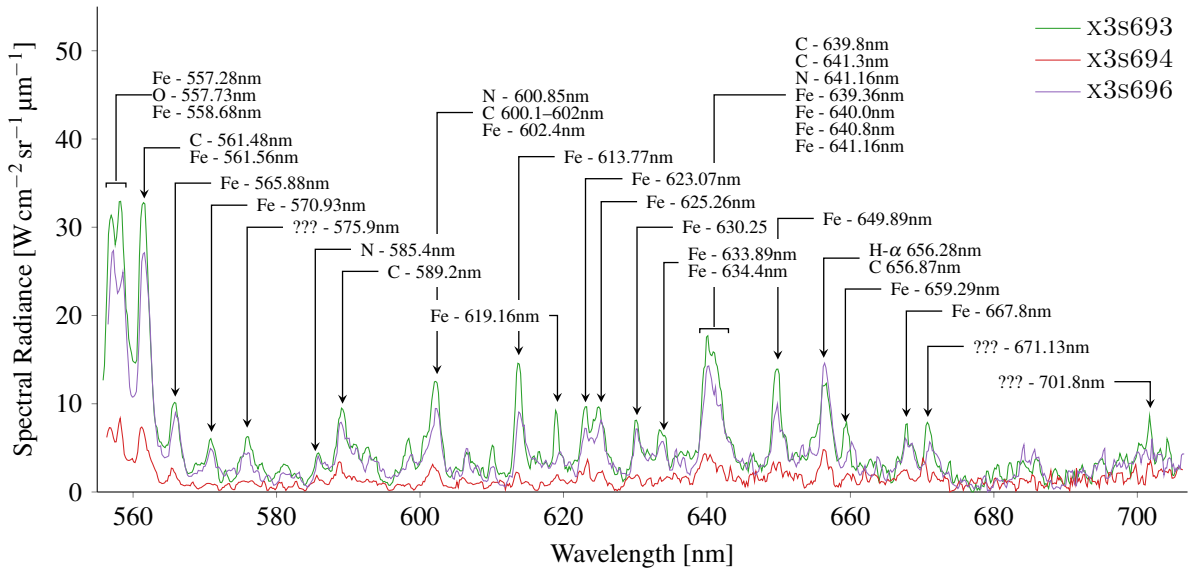


Figure 5.40.: Spectral comparison of frame 9 for shots x3s693, x3s694 and x3s696 with prominent features labelled with likely gas species or possible contaminants. Features labelled ??? were found not to have any logical identifications.

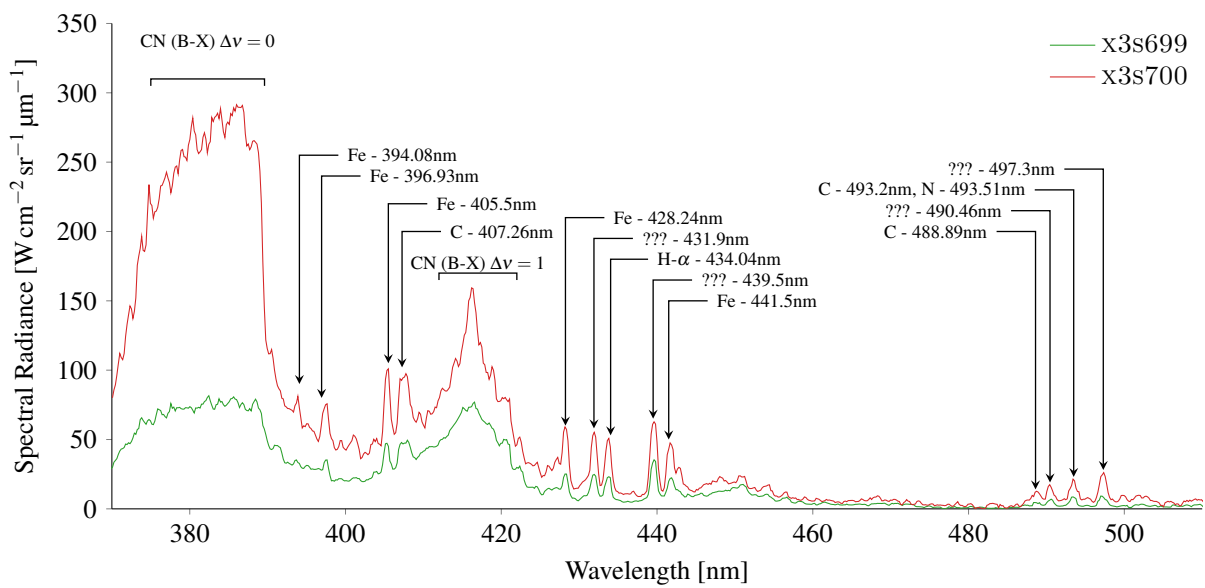


Figure 5.41.: Spectral comparison of frame 10 for shots x3s699 and x3s700 with prominent features labelled with likely gas species or possible contaminants. Features labelled ??? were found not to have any logical identifications.

consistently appears in the 7<sup>th</sup> frame which effectively truncates the test time by approximately 100 $\mu$ s if contaminants are considered detrimental to the experiment.

#### 5.7.4. Shock Stand-off Comparisons

An important part of this study was to examine the difference of shock behavior for different size models and the variation of shock shape due to high temperature effects. The full scale model has a shock stand-off ratio ( $\delta/D$ ) of approximately 0.25 through the test time whereas the 1:5 scale model has a stand-off of approximately 0.25, an increase of 40%. This is larger than the estimated shock stand-off increase of 16–27% estimated in table 5.4, although this does not include the effect of the model boundary on the density profile. A comparison of shock stand-off measurements between the two optical systems for the two models sizes are shown in fig. 5.42 and fig. 5.43 where the blue shaded region in each figure is the HPV-1 measurements with uncertainty being represented by the light blue region. In both figures, the HPV-1 and spectroscopic measurements show consistency across all experiments performed and while there is some shot to shot variation with both model sizes no measurement results in any outliers in the data. The larger error regions for the HPV-1 are due to the smaller spatial resolution of the shock stand-off: the HPV-1 measures shock stand-off across approximately 10 pixels whereas the spectroscopic measurements measure the shock stand-off across regions of over 100 pixels. Additionally, the spectral measurements do not capture unsteadiness in the flow because of the long exposure times used to record the images.

Included in fig. 5.43 are measured and quoted values from the 1:5 scaled model used by Fahy [77]. The measured values fall into two discrete regions, approximately 0.035 and 0.030, which is a limitation of the resolution as the difference in the two stand-offs is effectively one pixel difference. It is difficult to see in fig. 5.43 but x2s2317 and x2s2323 have similar shock stand-offs, as do x2s2321 and x2s2325. The quoted value for shock stand-off is within the error bounds of the reprocessed data and it is assumed that the quoted value has been calculated from spectral data with a higher resolution resulting in a more accurate measure than the high speed video, which is typically taken as a gauge for the test time rather than precise measurements. Given the availability of data, it can be said that the shock stand-offs between the full scale model in X3 and the scaled condition with a 1:5 scale model in X2 agree well, although the shock stand-off measurements in X3 result in a slightly smaller normalised stand-off distance.

## 5. Radiation Experiments

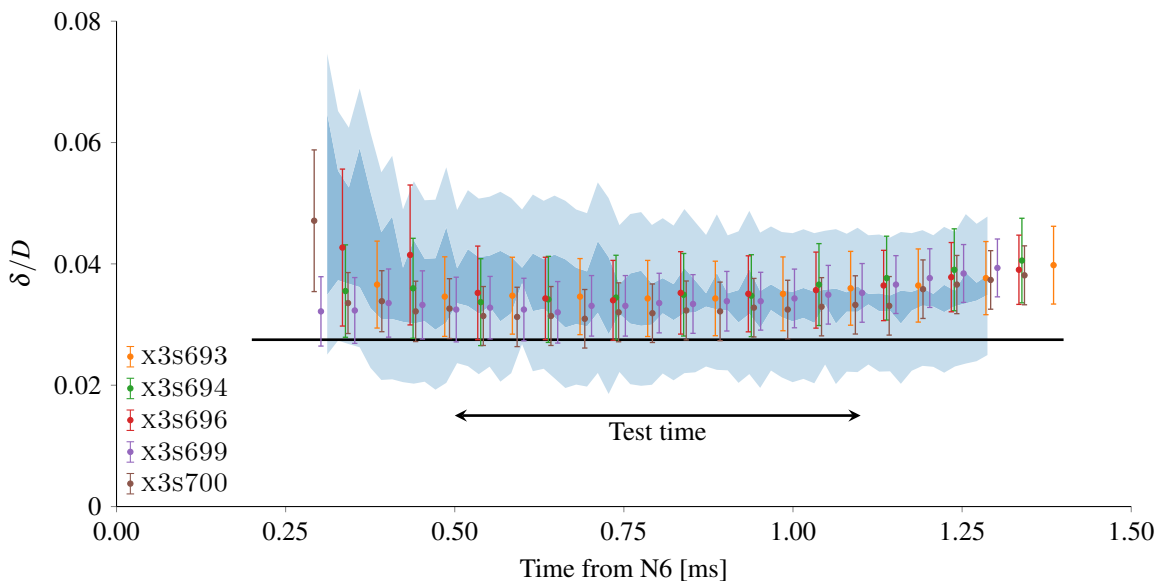


Figure 5.42.: Comparison of shock stand-offs for 1:5 scale model. The darker blue shaded region is the range of shock stand-offs measured by the HPV-1 in fig. 5.32 and the lighter shaded area is the uncertainty. The datapoints are the shock stand-off calculated from the spectral measurements, and the error bars the uncertainty in locating the shock and model edge. The black line is the shock stand-off measured by Fahy [77] which is a 1:5 scale model with binary scaling applied.

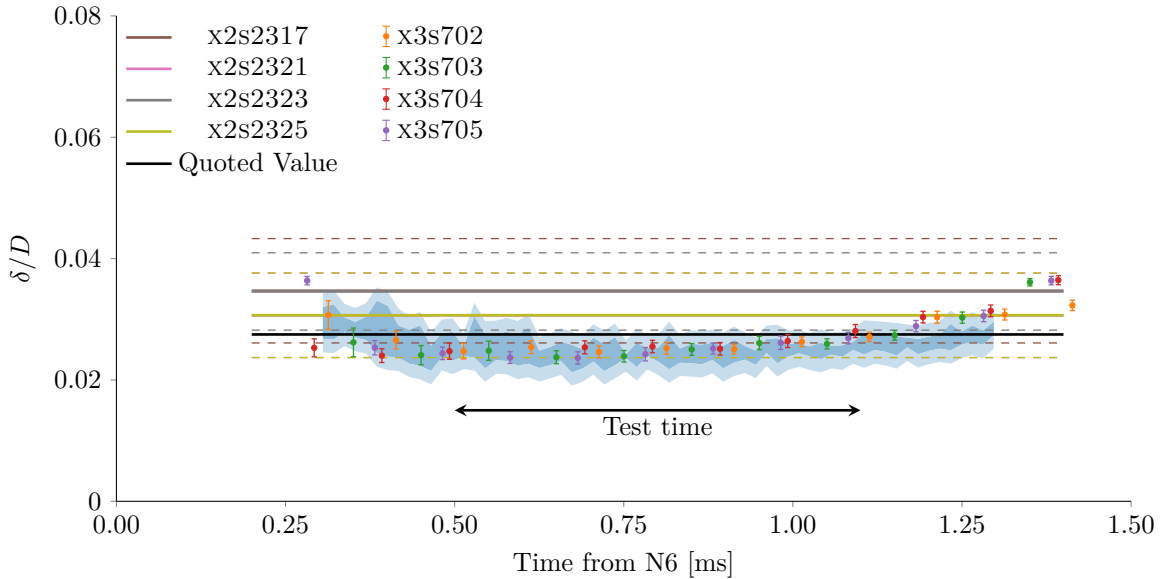


Figure 5.43.: Comparison of shock stand-offs for full scale model. The darker blue shaded region is the range of shock stand-offs measured by the HPV-1 in fig. 5.34 (shots x3s701–x3s705) and the lighter shaded area is the uncertainty. The datapoints are the shock stand-off calculated from the spectral measurements, and the error bars the uncertainty in locating the shock and model edge. The black line is a non-dimensional shock stand-off of 0.0275 quoted by Fahy [77] for the 1:5 scale model with binary scaling applied. Solid lines are stand-offs of scaled shots performed by Fahy measured using the method described in section 5.7.2 and the dashed lines are uncertainties.

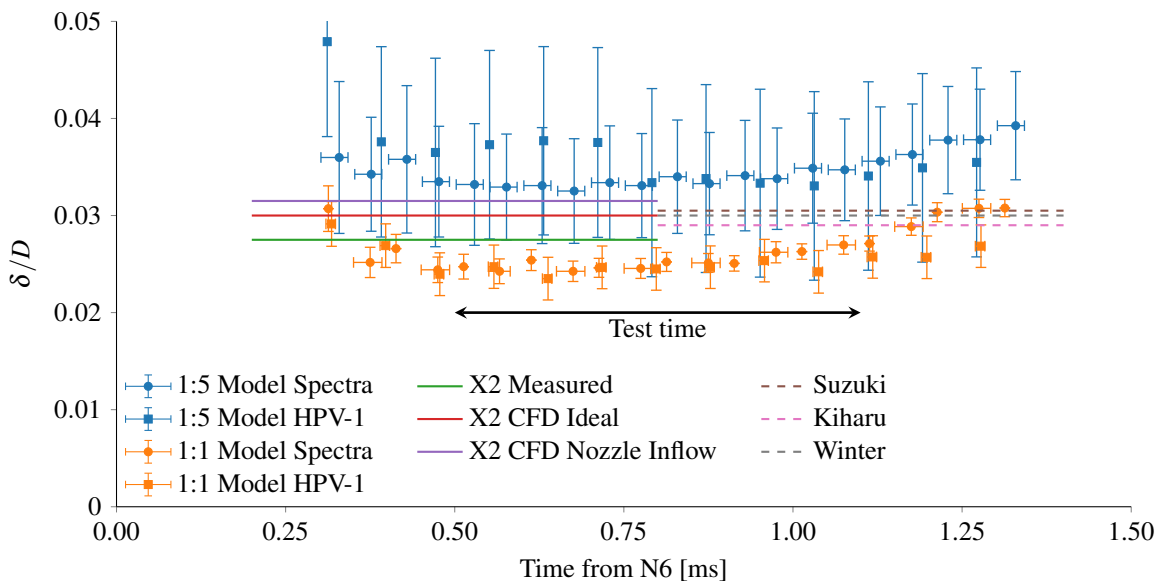


Figure 5.44.: Comparison of shock stand-off in X3 with X2 results and CFD calculations. Experiments in X3 were performed using the unscaled flow conditions with the 1:5 scale model (blue markers) and the full scale model (orange markers). The X2 results are taken from Fahy [77] using a 1:5 scale model with binary scaling applied, whereas the CFD calculations have been performed by Suzuki et al. [79], Kihara et al. [78] and Winter et al. [80].

The unscaled experiments in X3 measured a shock-stand-off of  $\delta/D = 0.025$  compared to the 1:5 scaled experiments in X2 which recorded a shock stand-off of 0.0275, a 10% increase. When regarding the limitations in matching the conditions (see table 5.2), it can be concluded that the experimental flow conditions generated by X3 are representative of the unscaled Hayabusa trajectory point at peak radiative heating. A complete summary of all measured values in X3, compared with X2 measurements and some CFD estimates is shown in fig. 5.44.

The CFD results in fig. 5.44 all converge around 0.03 for full scale model simulations by Suzuki et al. [79], Kihara et al. [78] and Winter et al. [80]. The X2 CFD using the nozzle inflow was conducted with the 1:5 scale model using the flow properties exiting the nozzle on X2 which predicts a higher shock stand-off as it uses the equilibrium flow field as the inflow to the simulation rather than the ideal air conditions. For the experimental cases, the measured shock stand-off on both X2 and X3 are consistently lower than the numerical results but they agree well with each other. The X3 results for the full scale model tend towards the CFD calculation towards the end of, and after, the test time, which may be a result of increased density in the flow as the unsteady expansion arrives, but it is unknown whether the gas properties at these times are more representative of the actual conditions or if it is just coincidence.

## 5.8. Binary Scaling Assessment

This section will examine the flow conditions and experimental measurements and discuss some of the observed phenomena with reference to binary scaling theory. For comparative purposes, there are four different conditions that can be examined: the peak radiative heating trajectory point, the condition used in X3, and the nominal and scaled flight conditions examined by Fahy in X2 [77]. Supporting numerical simulations have been conducted using Poshax [162] and all simulations use 11-species air and the reaction scheme from Park [163]. A recap of the freestream conditions is presented in table 5.5, along with the immediate post shock densities (from Poshax) and shock stand-offs. The temperatures presented in table 5.5 have been used for both the translational-rotation and vibrational-electronic temperature inputs in Poshax. The shock stand-off for the flight condition has been taken from CFD simulations in literature [77–80]. When examining the density length products ( $\rho_\infty D$  and  $\rho_2 D$ ), the condition used in X3 has a lower value due to the lower density calculated for the condition. The X3 condition both shows a reduced value for  $\rho_2 D$  compared to the two flight conditions (Peak Radiation and X2 Unscaled) due to the high inflow temperature, lower freestream density and the use of an equilibrium gas state as the freestream.

When comparing the nominal and scaled conditions used by Fahy in X2 [77], the post shock properties calculated by Poshax suggest that for both conditions, the nonequilibrium region occupies approximately the initial 15% of the shock layer; the remaining region is in equilibrium, which is counter to the requirement that the shock layer should predominantly be dominated by nonequilibrium binary reactions for binary scaling to apply. It should be reiterated that the presence of the model is not included in this analysis and changes to the post-shock flowfield due to the model have not been considered. Figure 5.45 displays the density profile behind the shock for the nominal and scaled conditions used by Fahy [77]. The density profiles have been normalised by the freestream density and the spatial coordinate has been normalised by the shock stand-off  $\delta$ , so  $x_n = 0$  is the shock and  $x_n = 1$  is the effective body of the model. For the scaled condition, the high inflow temperature reduces the post shock density ratio below the hypersonic limit (8.35 for  $\gamma = 1.271$ ), but there is still a small discrepancy observed immediately behind the shock. Aside from this the density profiles at the start of the nonequilibrium regions agree although they start to diverge at  $x_n = 0.05$ .

Stalker [167] defines the binary scaling parameter  $\xi$  as

$$\xi = \int_0^s \frac{\rho}{q} ds \quad (5.9)$$

where  $q$  is the post-shock velocity and  $s$  is the distance to some point in the shock layer. By evaluating the integral through the shock layer, an estimate of the similarity of the two flow fields can be obtained, with regards to binary reactions.

Table 5.5.: Freestream flow properties used when analysing the application of binary scaling for the operating condition. Equilibrium mole fractions calculated using CEA are presented, species with mole fractions several orders of magnitude lower than those presented have been omitted from this table. The reference condition is the peak radiative heating trajectory point while the X2 unscaled and scaled conditions are representative of a trajectory point just after the flight condition (see fig. 5.25), the scaled condition was obtained by applying binary scaling to the unscaled condition.

	X3 Condition	Peak Radiation	X2 Unscaled [77]	X2 Scaled [77]	Units
Pressure	210	34.5	38.5	1387	Pa
Temperature	2226	256	258	1860	K
Density ( $\times 10^{-3}$ )	0.33	0.46	0.52	2.6	$\text{kg m}^{-3}$
Flight Velocity	10.76	10.75	10.44	10.41	$\text{km s}^{-1}$
Altitude	58.9	56.1	55.0	55.0	km
$X_{N_2}$	0.761	—	—	0.765	—
$X_{NO}$	0.013	—	—	0.005	—
$X_{O_2}$	0.209	—	—	0.230	—
$X_O$	0.017	—	—	0.001	—
$\rho_\infty D (\times 10^{-4})$	1.32	1.84	2.08	2.08	$\text{kg m}^{-2}$
$\rho_2 (\times 10^{-3})$	1.82	2.79	3.11	14.9	$\text{kg m}^{-3}$
$\rho_2 / \rho_\infty$	5.50	6.07	5.95	5.75	—
$\rho_2 D (\times 10^{-3})$	0.73	1.12	1.24	1.20	$\text{kg m}^{-2}$
$D$	400	400	400	80	mm
Shock Stand-off ( $\delta/D$ )	0.025	0.030	0.030	0.0275	—

$X_i$  are mole fractions,  $\rho_\infty$  and  $\rho_2$  are the freestream and immediate post shock densities respectively,  $D$  is the diameter of the vehicle or model and  $\delta$  is the shock stand-off distance.

## 5. Radiation Experiments

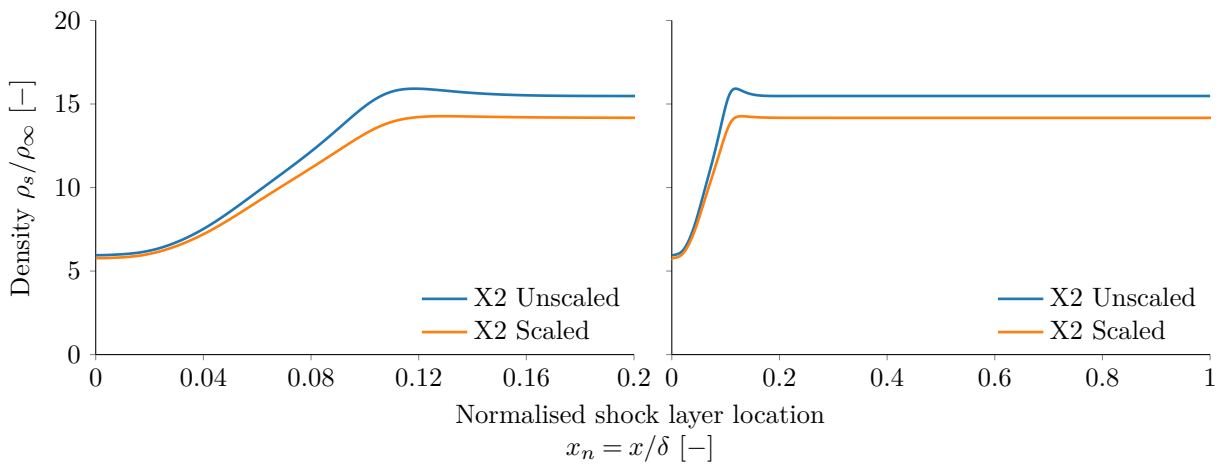


Figure 5.45.: Density ratio behind the shock for the nominal and scaled condition used in X2 by Fahy [77]. The density has been normalised by the freestream density and spatial coordinate normalised by the thickness of the shock layer. The left plot shows the detail of the nonequilibrium region.

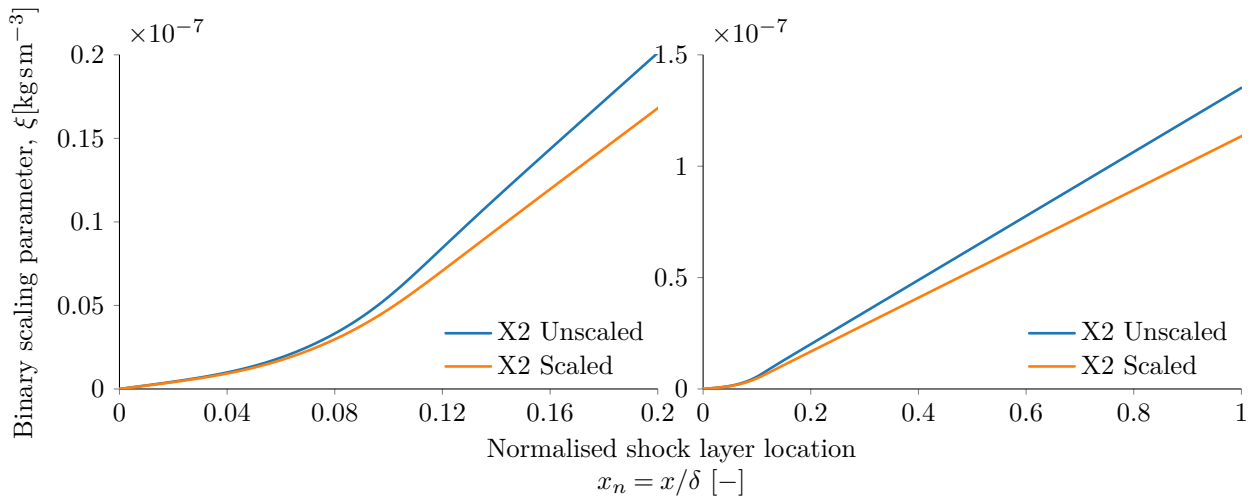


Figure 5.46.: Binary scaling parameter calculated behind the shock for the two conditions in fig. 5.45 using the calculated density and velocity from Poshax [162]. The left plot shots the detail of the nonequilibrium region.

The binary scaling parameter (plotted in fig. 5.46) begins to diverge for the two conditions at  $x_n = 0.05$  which is consistent with the divergence of densities in fig. 5.45. This suggests that the two conditions stop being similar at this location with the influence of three-body reactions and recombination reactions becoming significant. The scaled experiments in X2 had a higher absolute pressure which favours three-body recombination reactions over binary dissociation; the recombination reactions scale with  $\rho^2$  whereas the binary dissociation reactions scale with  $\rho$  [168], which explains the different equilibrium densities in fig. 5.45. In fig. 5.47, the mole fractions,  $X_i$ , and mole concentrations for the unscaled and scaled conditions used by Fahy [77] are presented. The mole fractions agree well between the two conditions (left plot in fig. 5.47) but the unscaled condition results in more moles of

atomic nitrogen and oxygen. The divergence in mole concentration begins at  $x_n = 0.05$  which agrees with the divergence in binary scaling parameter in fig. 5.46.

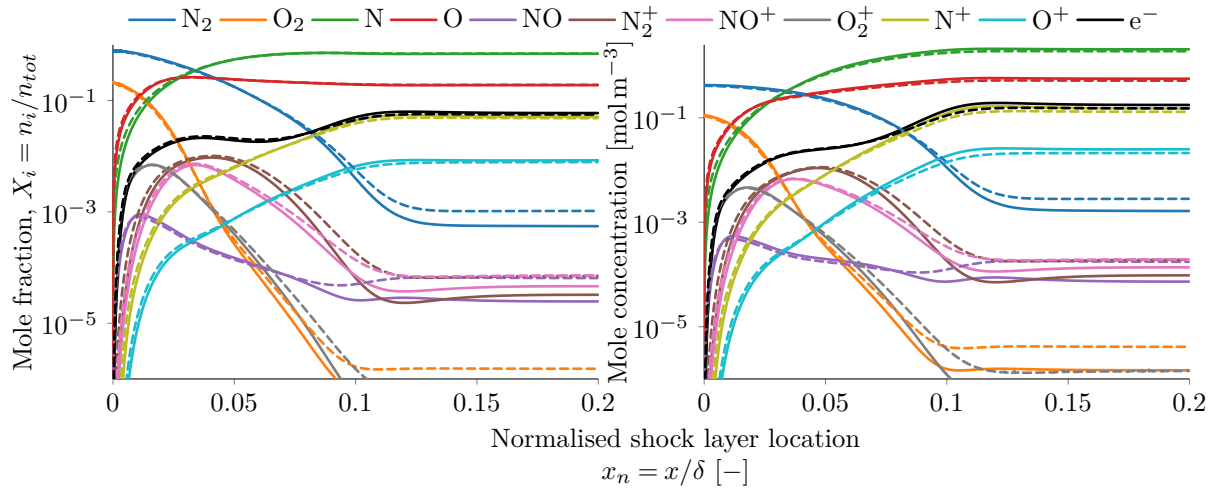


Figure 5.47.: Mole fraction (left) and mole concentration (right) calculated behind the shock for the two conditions in fig. 5.45, the scaled condition is represented by the dashed lines. The mole concentrations (right figure) have been multiplied by a factor of five for the unscaled conditions (solid lines).

Although the nonequilibrium region appears to have the same relative thickness as the unscaled condition, the increased pressure can increase the effect of three-body recombinations, thereby effectively reducing the level of dissociation in the flow, as well as the shock layer thickness, which is apparent in fig. 5.47. While there are some differences in the binary scaling parameter and equilibrium mole concentrations, the final scaled condition used on X2 [76] had already diverged from the nominal condition, but given that the condition was only scaled by a factor of 5 (compared to the Apollo capsule which would require a scaling factor on the order of 100), the two conditions are similar with reasonable confidence. A similar analysis can be applied between the true flight condition at peak radiative heating and the operating condition used in X3. From table 5.5, the estimated freestream density of the experimental condition is approximately 70% of the density of the flow during flight, and if binary scaling was to be applied, a model with a diameter of 550mm should be used instead of the 400mm (full scale) model used. For the case of X3, the flow calculated in PITOT is assumed to be at equilibrium at the exit of the nozzle, which predicts some oxygen dissociation before the flow reaches the model and will affect reaction rates in the nonequilibrium region. Using the equilibrium condition for X3 and the atmospheric conditions at the peak radiative heating trajectory point, the normalised density profiles behind the shock for each condition is presented in fig. 5.48 along with the unscaled condition from fig. 5.45.

## 5. Radiation Experiments

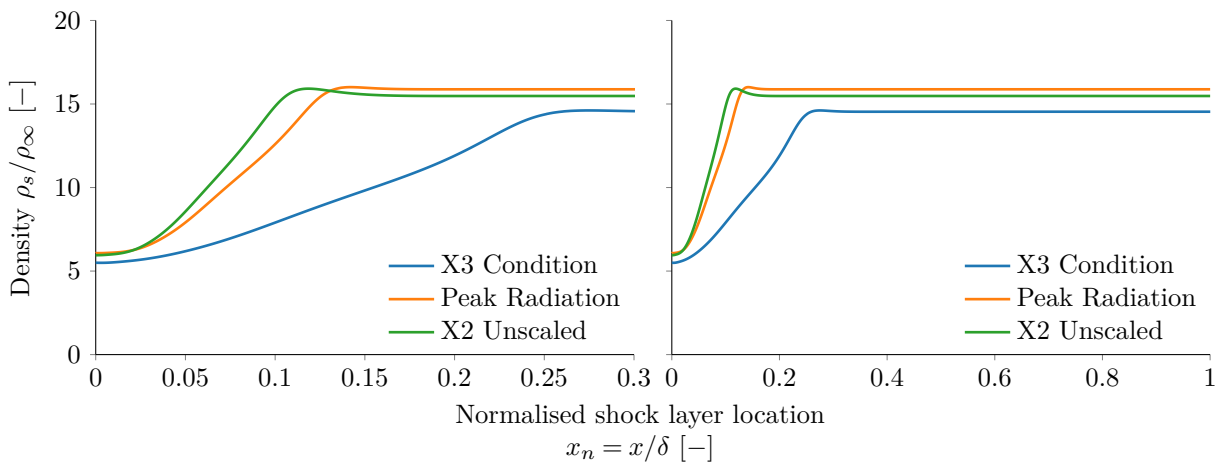


Figure 5.48.: Post-shock density profile for the X3 condition and the peak radiative heating trajectory point. Densities have been normalised by the freestream densities in table 5.5 and the unscaled condition used by Fahy [77] has been included for reference. The left plot shows the detail of the nonequilibrium region.

The condition used in X3 has a nonequilibrium region approximately twice as large as the unscaled X2 and flight conditions. This may be a product of the reduced density of the freestream, as dissociation rate is generally proportional to density [167] and a reduced rate of dissociation will be expected for the X3 condition compared the unscaled X2 and flight conditions. When examining the binary scaling parameter in fig. 5.49, it is evident that the values of  $\xi$  for the X3 condition do not match well for the flight condition at the normalised shock layer location by a factor of about half. This suggests that the two conditions are not similar, but the results in fig. 5.44 showed good agreement between experimental results and several CFD shock stand-off measurements. Theoretical work by Inger et al. [169] show that as the post-shock conditions tend from chemically frozen to equilibrium, the density scaled shock stand-off (analogous with shock stand-off measurements presented in the previous section) decreases. The density profile for the X3 condition suggests that the shock stand-off should be larger than that predicted during flight, but the difference in the freestream flow properties needs to be considered.

Increasing the density of X3's flow condition would serve to increase the binary scaling parameter and increase the similarity to the flight condition, albeit no model scaling was applied in X3. The assumption that the nozzle exit flow is at equilibrium will also have an effect on the binary scaling parameter, but it is deemed to be necessary to estimate the state of the flow until further simulations of the facility can be performed. Alternatively, another location along Hayabusa's trajectory can be considered, fig. 5.25 has been redrawn in fig. 5.50 with the addition of a third point (diamond) in the zoomed in area which is representative of the trajectory point with an equivalent altitude of the X3 condition (i.e. a density of  $0.33 \times 10^{-3} \text{ kg m}^{-3}$ ). The altitude of the new trajectory point is approximately 58.9km, which is in the lower part of the highlighted region of fig. 5.50, but this is because density does not scale linearly with altitude and the density selected is the average of the

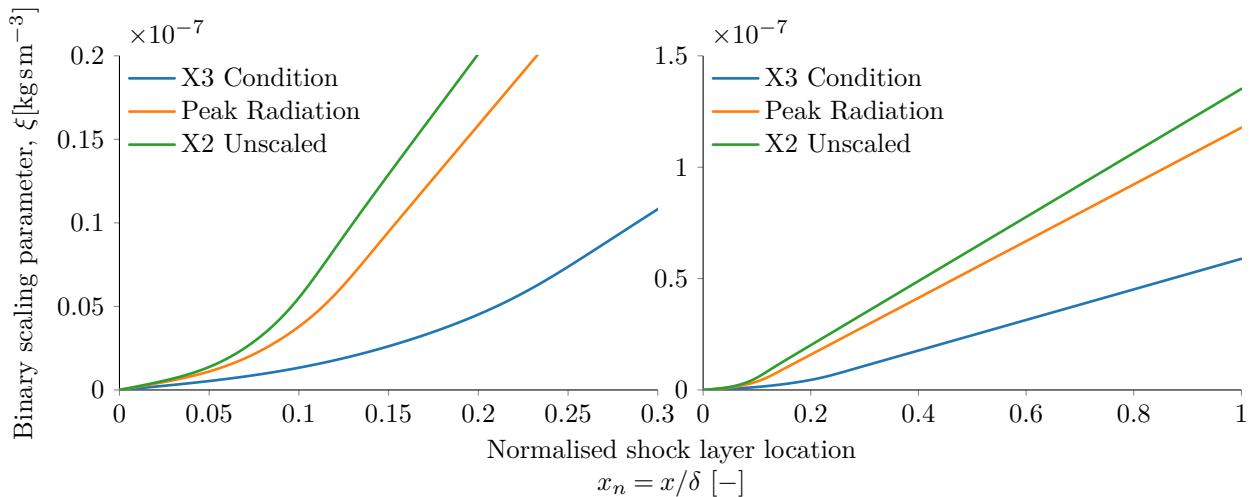


Figure 5.49.: Binary scaling parameter calculated behind the shock for the condition used in X3 and the peak radiative heating trajectory point, the unscaled condition used by Fahy [77] has been included for reference. The left plot shows the detail of the nonequilibrium region.

minimum and maximum calculated densities from table 5.2, rather than the average of all the possible conditions.

The equivalent altitude trajectory point has been compared with the X3 condition and peak radiative heating trajectory point in table 5.6. For the purpose of comparison, the shock stand-off ( $\delta/D$ ) for the new trajectory point has been assumed to be equal to the measurements taken during experiments in X3, so the distance  $x_n$  will be normalised by the same distance for both cases, while the peak radiative point will continue to use the larger shock stand-off taken from literature. When considering the freestream and post-shock density of the equivalent altitude condition, the density values, as well as density length products match the X3 condition much better than the peak radiative heating, despite the difference in flight velocity between the two conditions.

A comparison of the post-shock density profile and binary scaling parameter for the equivalent altitude trajectory point is presented in fig. 5.51 and fig. 5.52. Although the density at equilibrium for the equivalent altitude condition is still larger than for the X3 condition, the density profile through the nonequilibrium region agrees much better than for the peak radiative heating condition. Similarly, the binary scaling parameter throughout the shock layer lines up quite well, only slightly diverging at equilibrium due to the different densities. The velocity for the new trajectory point is only approximately 5% larger than the equivalent flight velocity in X3, and when considering the uncertainty of the X3 condition and shot to shot variation, this is a small discrepancy. For future similarity studies, either in X3 or involving this operating condition, the trajectory point at 58.9km altitude and  $11.17 \text{ km s}^{-1}$  should be used as a reference trajectory point, as a much higher similarity between the two conditions has been found compared to the peak radiative heating trajectory point.

## 5. Radiation Experiments

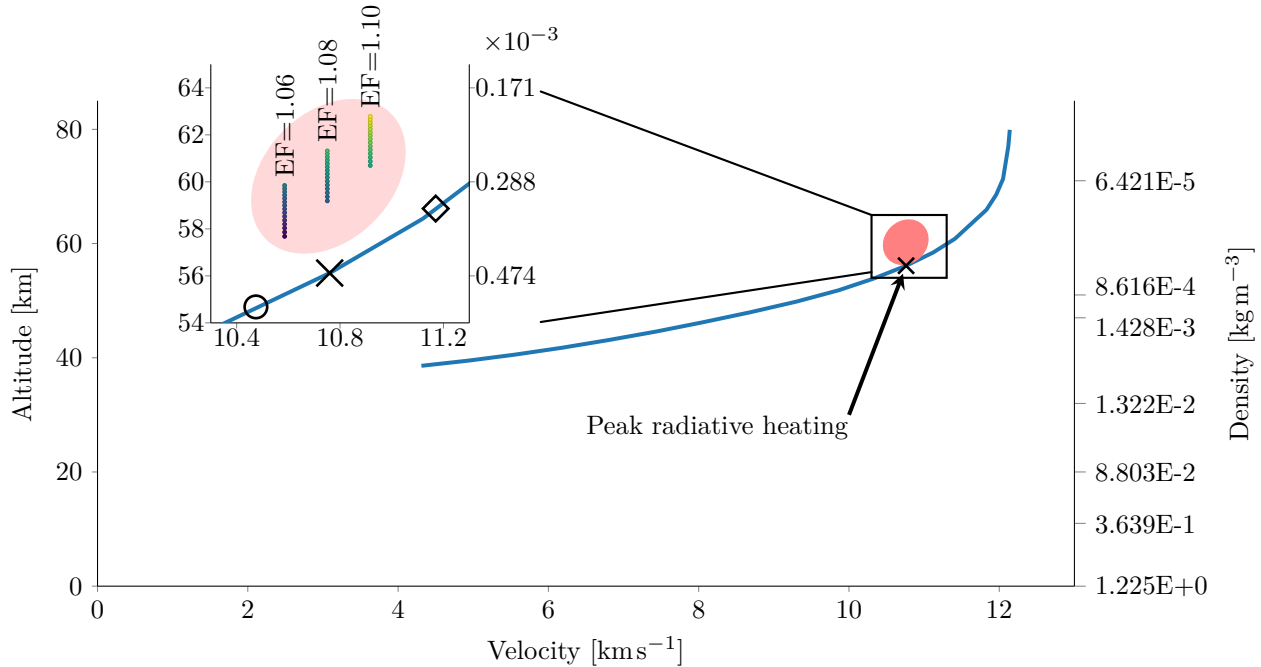


Figure 5.50.: Hayabusa trajectory from fig. 5.25 with an additional trajectory point, located at the diamond marker, which has the same equivalent altitude as the X3 condition in table 5.5.

Table 5.6.: Comparison of the equivalent altitude trajectory point with the X3 condition and peak radiative heating trajectory point.

	X3 Condition	Flight Condition	Equivalent Altitude Condition	Units
Pressure	210	34.5	23.6	Pa
Temperature	2226	256	249	K
Density ( $\times 10^{-3}$ )	0.33	0.46	0.33	$\text{kg m}^{-3}$
Flight Velocity	10.76	10.75	11.17	$\text{km s}^{-1}$
Altitude	58.9	56.1	58.9	km
$\rho_\infty D (\times 10^{-4})$	1.32	1.84	1.32	$\text{kg m}^{-2}$
$\rho_2 (\times 10^{-3})$	1.82	2.79	1.96	$\text{kg m}^{-3}$
$\rho_2 / \rho_\infty$	5.50	6.07	5.96	—
$\rho_2 D (\times 10^{-3})$	0.73	1.12	0.79	$\text{kg m}^{-2}$
Shock Stand-off ( $\delta/D$ )	0.025	0.030	—	—

$\rho_\infty$  and  $\rho_2$  are the freestream and immediate post shock densities respectively,  $D$  is the diameter of the vehicle or model and  $\delta$  is the shock stand-off distance.

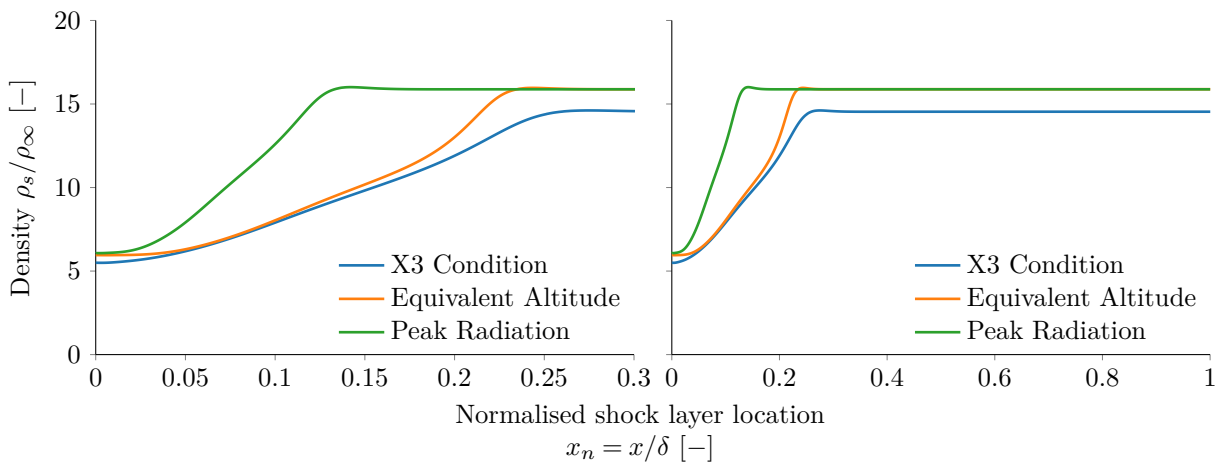


Figure 5.51.: Post-shock density for the equivalent altitude condition compared the X3 condition and peak radiative heating condition. The densities have been normalised by the freestream densities. The left plot shows the detail of the nonequilibrium region.

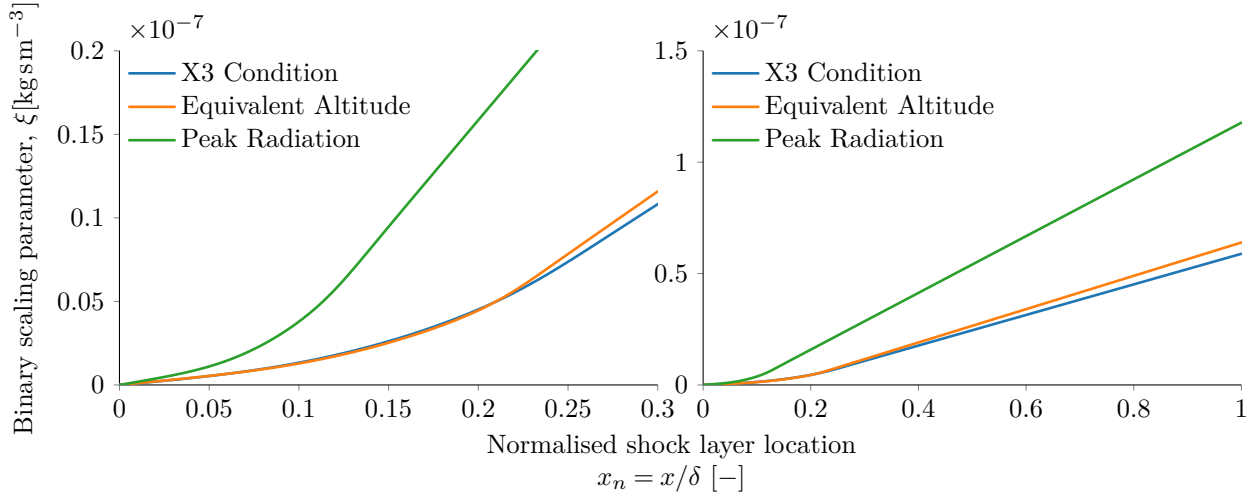


Figure 5.52.: Binary scaling parameter calculated behind the shock for the equivalent altitude condition with comparisons to the X3 condition and peak radiative heating condition. The left plot shows the detail of the nonequilibrium region.

## 5.9. Chapter Conclusion

In this chapter a new operating condition for X3 was developed with supporting analysis to suggest that the flow conditions near the peak radiation point of Hayabusa's trajectory was reproduced. A test time of 500 $\mu$ s was measured for the new condition, with limitations being the initial nozzle start up time and the introduction of iron contaminants at the end of the test flow. Radiation experiments were performed with a 1:5 scale and full scale Hayabusa model using this new operating condition, with high speed video and time resolved spectra being taken for each model. From the high speed video, the shock stand-off was able to be measured over the test time and high temperature effects on shock layer

## *5. Radiation Experiments*

thickness were demonstrated. The time resolved spectra methodology is a new technique, and within the experimental uncertainties, the images agree with the high speed camera regarding shock stand-off. The development of the time resolved spectra system removes the usual limitations associated with these types of measurements and much more information can be acquired per shot for a facility like X3 with a test time on the order of 1ms. Though, the system does come with its own difficulties that still need to be solved. The response of the intensifier/Phantom combination still needs to be examined, especially in wavelength regions where intensifier sensitivity is reduced. There also appeared to be a maximum intensity that could be recorded well below the number of counts the Phantom can record and it remains unknown why this phenomena was observed.

The shock stand-offs measured in X3 were compared to experiments performed in X2 and a selection of CFD results: the X2 experiments measured a shock stand-off ( $\delta/D$ ) of 0.0275 and the CFD results have consistently calculated shock stand-offs of 0.03. These values are 10% and 20% larger than the shock stand-off measured in X3 during this study, which measured a shock stand-off of 0.025. When investigating the binary scaling parameter and the similarity between the operating experimental flow and points on Hayabusa's trajectory, it was found that the flow was more representative of the trajectory location with a velocity of  $11.2\text{km s}^{-1}$  and altitude of 58.9km, corresponding to an equal freestream density. For future experiments, either in X3 or comparative ones in another facility, the condition should be defined by this trajectory point (slightly before peak radiative heating) as the experimental flow has a higher level of similarity compared to the peak radiative trajectory point.

# Conclusions and Recommendations

Performing experiments of high enthalpy radiating flows remains critically important to further our understanding of the gas dynamics experienced during atmospheric entry. But ground testing remains typically limited to using small scale models with limitations how well time resolved measurements taken during the experiments are. The final objective of this thesis was to perform radiation experiments with a full scale Hayabusa model in the X3 expansion tube and take time-resolved spectroscopic measurements. To accomplish the final objective significant advancements to the operating potential of X3 were made which enabled the production of high enthalpy flows and consequently spectral measurements of the flowfield in front of a full scale model were taken.

## 6.1. Research Goals

### 6.1.1. Facility Development

*An L1d model that can accurately predict the behaviour of the piston in X3's driver for a given reservoir and compression tube fill pressure.* L1d can now be used as a tool to predict the behaviour of the lightweight piston as well as the compression tube pressure during an experiment reliably and without having to change empirical parameters once they are established. To achieve this, the geometry of X3 was reproduced in one dimension and an exploration of existing L1d model parameters was performed as well as the implementation of new ones. The model was first verified with blank-off shots, which showed that the model could accurately estimate the timing of pressure waves and the stroke of the piston to an accuracy of 50mm. The same model was used to design conditions with a rupturing diaphragm, and a soft landing condition was obtained for two thicknesses of diaphragm. The L1d model has since been used by Toniato [96] to perform numeric simulation of a Mach 12 scramjet condition and Stennet et al. [146], who used it to design driver conditions for a reflected shock tunnel version of X3 using a 280kg piston, where only minor changes to the model due to buffer length were required.

*The new lightweight piston was successfully used to generate a range of driver conditions.* The implementation of the lightweight piston to X3 was performed using L1d as the main numerical tool

## 6. Conclusions and Recommendations

to predict the piston's trajectory. A range of driver operating conditions were realised using a 2mm diaphragm which ruptures at 19.5MPa with a compression ratio of 36.3 and a 3mm diaphragm that ruptures at 29MPa with a compression ratio of 47.8. Orifice plates allowed the helium concentration of the driver gas to be increased and were validated for helium partial pressures of 0.6, 0.75, 0.85 and 1.0. While the driver condition did not have the required performance to reproduce the target condition used in X2, it was capable of producing an unscaled condition with the 3mm diaphragm and 100% helium driver gas. Toniato [96] also used the 2mm diaphragm with 0% and 60% helium configuration to produce a nominal and pressure-scaled Mach 12 scramjet flow condition.

### 6.1.2. Radiation Experiments

*An unscaled flow condition representative to a point on Hayabusa's trajectory near peak radiative heating was developed.* Prior to performing the final experiments the diaphragm static test rig was used to tailor the score depth and the rupture pressure of diaphragms with different material properties. The final developed condition was representative of the peak radiation point of the Hayabusa capsule. An analytical estimation of the test condition resulted in an equivalent flight velocity of  $10.76 \pm 0.12 \text{ km s}^{-1}$  and density of  $0.33 \times 10^{-3} \pm 0.11 \times 10^{-3} \text{ kg m}^{-3}$  compared to flight values of  $11.17 \text{ km s}^{-1}$  and  $0.33 \times 10^{-3} \text{ kg m}^{-3}$ , which is slightly before peak radiative heating (velocity of  $10.75 \text{ km s}^{-1}$  and density of  $0.46 \times 10^{-3} \text{ kg m}^{-3}$ ). The test condition has test time of 600 $\mu\text{s}$  although the measured pressure was constantly rising throughout; the beginning of the test time is limited by nozzle start up processes. Measurements of Pitot and conical impact pressure indicated a core flow diameter of 400mm with a reduction in Pitot pressure of 20% at the edge of the core flow compared to the centre.

*Time resolved spectroscopic measurements were taken in front of a full scale model and 1:5 scale model.* A HiCATT high speed image intensifier and Phantom v611 high speed camera were combined with a Princeton Instruments SP2300 spectrometer with 150grooves/mm grating. Using this setup multiple spectral images were taken for single experiments which gives a greater understanding of the flow behaviour and addresses a key limitation of expansion tube flow, regarding flow contamination and steadiness. While the signal at wavelengths where air species radiate strongly could not be captured, contaminants most likely from the diaphragms were identified. From the spectral results it appears that contaminants from the tertiary diaphragm — hydrogen and carbon — are present at the beginning of the test gas while iron contaminants, probably from the primary diaphragm, appear towards the end of the test time.

*Shock stand-off in front of the full scale model was found to agree well with literature.* stand-off was measured for both the 1:5 scale model and full scale model, both taken using the full scale flow condition. The ratio of shock stand-off distance to model diameter was used to quantify shock layer thickness: a shock stand-off of 0.025 was measured for the full scale model compared to 0.035 for

the 1:5 scale model, an increase of 40%. CFD calculations from literature have found the shock stand-off for Hayabusa at the peak radiation point to be 0.03, which is 20% larger than the experimental findings in this thesis. Similarly binary scaled measurements for a 1:5 scale model in X2 by Fahy [77] had a measured shock stand-off of 0.0275, only 10% larger than the measurements in X3, with the lower shock stand-off distance measured in X3 possible due to the slightly lower density of the flow condition.

## 6.2. Future Work and Recommendations

Recommendations for future work that stem directly from this thesis and improvements to both the work covered in this thesis and that which has arisen during experimental periods are discussed here. Recommendations that require significant hardware upgrades or are focussed on making the experimental process in X3 easier will not be discussed here.

### 6.2.1. The Driver and Condition Development

#### Refine the L1d model

While the model is currently sufficient for predicting the behaviour of the piston, and, for the purposes of this thesis, the L1d model performed adequately, there are still improvements that can be made for better flow predictions. First of all there is still a slight discrepancy in the piston stroke; improving the heat loss model incorporated in the code, or enabling variations in constants used in heat transfer coefficients (e.g. Prandtl number), may result in extra refinement of the driver. Of greater importance is the continued work in improving the model's capability to predict flow conditions. As seen in section 4.4, L1d does not match the shock tube pressure after diaphragm rupture as well as it does in the driver nor does it accurately predict shock speed and to lesser extent post shock pressure in the shock tube. While not discussed in this thesis attempts were made to improve the compatibility of the numerical calculations, these include but are not limited to varying orifice plate area, driver gas fill temperature, diaphragm rupture pressure and loss factor strength and location. Additional features were added: temperature scaling after primary diaphragm rupture and the capacity to change diameter, but the best estimate was still the one provided from the vanilla model. All these changes influence the piston trajectory which may result in different driver gas behaviour, especially with wave propagation, so tinkering with L1d is definitely a non-trivial exercise and significant improvement to expansion tube condition quality and predictive capability can potentially be made.

## 6. Conclusions and Recommendations

### Improve starting point for driver conditions

The driver design in this thesis started from a 100% argon driver gas with no orifice plate, which was based on what seemed feasible given the available hardware. By changing the starting point in the condition drive process, it is feasible that one could arrive at a driver condition with a higher performance than the ones designed in this thesis. For example, if the starting driver condition comprised 20% helium and 80% argon instead of 100% argon, it would be expected that faster shock speeds could be driven through the shock tube. The rupture pressures of both diaphragms were also higher than first thought and the fill conditions were calculated using the nominal pressures. The analysis could be performed again for the actual rupture pressures and improvements to the operating conditions may result.

### Complete performance envelope

The shots performed in chapter 4 were all conducted with the same fill conditions, which were an attempt to match a scaled X2 condition. With the exception of the final operating condition, which is for a full scale Hayabusa model, and Mach 12 scramjet conditions, experiments for a full range of flows have not been performed and the full limitations of the facility with the new driver upgrades are not known, although a good idea of the performance limitations can be extrapolated from chapter 4.

### A lighter piston

As with the lightweight piston in this thesis, an even lighter piston would enable driver conditions with higher compression ratios and therefore higher temperatures to be used on X3. The faster piston velocities in the tube would also enable increased helium concentrations to be used in the driver as the higher velocities will be able to match the rate the driver gas vents from the compression tube. The development of the L1d model in this thesis means that the challenge goes towards designing a piston structure that can withstand the large forces at a lower mass.

### Another nozzle

To quote a passage of Gildfind's thesis [86]:

*"Contoured hypersonic nozzles are optimised for a single Mach number, and subsequently their performance can increasingly deteriorate at off-design conditions."*

The nozzle used for the radiation experiments in this thesis was optimised for Mach 12 scramjet flow conditions, and along with temporal variation of test gas properties entering the nozzle, it was apparent that flow startup issues occurred which severely reduced the length of steady flow and the quality of the flow. Designing a nozzle more suitable for high enthalpy flows, and one that is suitable for the temporal variation in test gas properties, could result in an increased test time, possibly over 1ms, and potentially larger core flows. This would increase the advantages of using a large facility like X3 for these kinds of experiments.

### **6.2.2. The diaphragm problem**

Although the diaphragms were scored, which reduced the amount of shrapnel travelling down the tube, the surface of the models still has substantial wear and impacts, especially the full scale model. It would be beneficial to investigate ways to reduce the amount of shrapnel that travels down the tube to prevent damage to models.

### **6.2.3. Radiating flow experiments**

#### **CFD of the condition**

X3 is spatially large and as such performing CFD of the facility to obtain accurate flow properties in the test section is a significant undertaking. Part of the computational load can be reduced by performing L1d, but for the conditions in this thesis a sufficiently accurate estimate of the flow could not be obtained, with analytical estimates and a binary scaling analysis being performed to quantify the condition. The test gas was assumed to be in equilibrium after the unsteady expansion into the acceleration tube and expansion through the nozzle. For the measurements taken in this thesis, this assumption was shown to be adequate but analysis using a nonequilibrium gas should be performed when conducting experiments that are sensitive to different species concentrations. Additionally, moving mesh updates in Eilmer3 and Eilmer4 could be used to simulate the piston, and therefore perform axisymmetric simulations of the entire facility, although this would be a computationally expensive procedure.

#### **Instrumented model**

The full scale model used for experiments in this thesis had no instrumentation. Extra information of the test flow, primarily test gas arrival and end could be obtained by instrumenting the surface of the model, as well as other flow properties which can be used to perform more analysis with optical data.

## *6. Conclusions and Recommendations*

### **Use more suitable optical components**

Time, and access to instrumentation, were big limitations in setting up and taking optical measurements. The grating used was blazed to 300nm whereas initial spectral measurements were taken at 500–700nm, a region of low efficiency, to the point where it was impossible to view anything in the near infrared region, which is important for air. Using a different grating or spectrometer would result in improved optical measurements in the near infrared and also the regions examined in this thesis.

### **Characterise the intensifier**

Although the technique was proved to work and time resolved spectra was obtained, a lot is still to be learnt regarding the behaviour of the intensifier coupled with the camera as the settings were set mainly as corrections from the previous shot. During calibration, there appeared to be a maximum intensity that could be recorded — at approximate 25% the maximum sensor intensity — and it was not clear whether it was an intensifier or a camera issue. It would be worthwhile to use the setup on a smaller facility and learn the limitations of the setup and also obtain a greater understanding of the behaviour of the system.

### **Develop new flows**

The flow condition used in this thesis is just one condition of many that can potentially be used for radiation experiments. The facility is not limited to air as the test gas, as there is potential to develop flows that represent the atmosphere of other bodies in the solar system. Flows such as one simulating Titan entry may be more suitable for the intensifier as it is more sensitive in the visible region.

## **6.3. A Final Point**

A significant part of the work in this thesis has gone towards knocking down the brick wall that has stood in the way of many performing high enthalpy radiation flow experiments on X3. While the operating difficulties of using a large facility still exist, there are now a range of driver conditions that are usable for a wide variety of test flows. Already, the driver conditions have been used for Mach 12 scramjet flows [96] and Magnetohydrodynamic experiments [170]. While there is still work to be done to remove operational uncertainties and further understand the freestream gas properties, X3's large flow diameter and long test time presents a unique opportunity to perform experiments that have previously been limited by duration and size, and it is envisioned that X3 will be used more frequently for different types of experiments in the years to come.

---

# Bibliography

- [1] A. Andrianatos, D. Gildfind, and R. Morgan. “A study of radiation scaling of high enthalpy flows in expansion tubes”. In: *7th Asia-Pacific International Symposium on Aerospace Technology Conference*. 2015. DOI: 10.1007/978-3-319-91017-8\_37 (cit. on p. v).
- [2] A. Andrianatos, D. Gildfind, and R. Morgan. “Preliminary Development of High Enthalpy Conditions for the X3 Expansion Tube”. In: *20th Australasian Fluid Mechanics Conference, 20AFMC*. 2016 (cit. on p. v).
- [3] A. Andrianatos, D. Gildfind, and R. G. Morgan. “Driver Condition Development for High Enthalpy Operation of the X3 Expansion Tube”. In: *31st International Symposium on Shock Waves*. 2017. DOI: 10.1007/978-3-319-91017-8\_37 (cit. on p. v).
- [4] T. Hermann, S. Löhle, S. Fasoulas, and A. Andrianatos. “Tomographic optical emission spectroscopy of a high enthalpy air plasma flow”. In: *Applied optics* 55.36 (2016), pp. 10290–10298. DOI: 10.1364/AO.55.010290 (cit. on p. v).
- [5] T. Hermann, S. Löhle, R. Öfele, S. Fasoulas, and A. Andrianatos. “Tomographic optical emission spectroscopy for plasma wind tunnel testing”. In: *32nd AIAA Aerodynamic Measurement Technology and Ground Testing Conference*. 2016, p. 3203 (cit. on p. v).
- [6] P. Toniato, D. E. Gildfind, A. Andrianatos, and R. G. Morgan. “Full Free-stream Mach 12 Scramjet testing in expansion tubes”. In: *2018 Applied Aerodynamics Conference*. 2018, p. 3818. DOI: 10.2514/6.2018-3818 (cit. on p. v).
- [7] D. E. Gildfind, P. A. Jacobs, R. J. Gollan, P. Toniato, T. J. McIntyre, A. Andrianatos, C. M. James, and R. G. Morgan. “Flow characterization and modeling of the X2 and X3 expansion tubes”. In: *VKI Lecture Series* (2018) (cit. on p. v).
- [8] D. Preller and M. Smart. “Spartan: Scramjet powered accelerator for reusable technology advancement”. In: *Proceedings of the 12th Reinventing Space Conference*. Springer. 2017, pp. 139–147 (cit. on p. 1).
- [9] Rocket Lab. *Electron*. URL: <https://www.rocketlabusa.com/electron/> (cit. on p. 1).
- [10] Gilmour Space Technologies. *Eris*. URL: <http://www.gspacetech.com/launch> (cit. on p. 1).

## 6. Conclusions and Recommendations

- [11] S. Watanabe, Y. Tsuda, M. Yoshikawa, S. Tanaka, T. Saiki, and S. Nakazawa. “Hayabusa2 mission overview”. In: *Space Science Reviews* 208.1-4 (2017), pp. 3–16 (cit. on p. 1).
- [12] K. Berry, B. Sutter, A. May, K. Williams, B. W. Barbee, M. Beckman, and B. Williams. “OSIRIS-REx touch-and-go (TAG) mission design and analysis”. In: *36th Annual AAS Guidance and Control Conference* (2013) (cit. on p. 1).
- [13] J. Zhao, L. Xiao, L. Qiao, T. D. Glotch, and Q. Huang. “The Mons Rümker volcanic complex of the Moon: A candidate landing site for the Chang’E-5 mission”. In: *Journal of Geophysical Research: Planets* 122.7 (2017), pp. 1419–1442. DOI: 10.1002/2016JE005247 (cit. on p. 1).
- [14] J. Anderson Jr. “An engineering survey of radiating shock layers.” In: *AIAA Journal* 7.9 (Sept. 1969), pp. 1665–1675 (cit. on p. 1).
- [15] S. P. Sharma and E. E. Whiting. “Modeling of nonequilibrium radiation phenomena - An assessment”. In: *Journal of Thermophysics and Heat Transfer* 10.3 (July 1996), pp. 385–396. DOI: 10.2514/3.802. URL: <http://dx.doi.org/10.2514/3.802> (cit. on pp. 1, 2).
- [16] R. Morgan, T. McIntyre, D. Buttsworth, P. Jacobs, D. Potter, A. Brandis, R. Gollan, C. Jacobs, B. Capra, M. McGilvray, et al. “Impulse facilities for the simulation of hypersonic radiating flows”. In: *38th Fluid Dynamics Conference and Exhibit, Seattle, Washington*. 2008 (cit. on p. 2).
- [17] S. P. Sharma and W. Gillespie. “Nonequilibrium and equilibrium shock front radiation measurements”. In: *Journal of Thermophysics and Heat transfer* 5.3 (1991), pp. 257–265 (cit. on pp. 2, 10).
- [18] M. J. Wright, D. Bose, and J. Olejniczak. “Impact of flowfield-radiation coupling on aeroheating for Titan aerocapture”. In: *Journal of Thermophysics and Heat Transfer* 19.1 (2005), pp. 17–27 (cit. on pp. 2, 3).
- [19] A. Feldick, M. Modest, and D. Levin. “Closely Coupled Flowfield-Radiation Interactions for Flowfields Created During Hypersonic Reentry”. In: *40th Thermophysics Conference, Seattle, WA, Jun.* 2008, pp. 23–26 (cit. on p. 2).
- [20] P. Leyland, T. McIntyre, R. Morgan, P. Jacobs, F. Zander, U. Sheikh, T. Eichmann, E. Fahy, O. Joshi, G. Duffa, et al. “Radiation-Ablation Coupling for Capsule Reentry Heating via Simulation and Expansion Tube Investigations”. In: *Proceedings of the 5th European Conference for Aeronautics and Space Sciences (EUCASS)*. EPFL-CONF-200443. 2013 (cit. on p. 3).
- [21] M. E. Tauber and K. Sutton. “Stagnation-point radiative heating relations for Earth and Mars entries”. In: *Journal of Spacecraft and Rockets* 28.1 (1991), pp. 40–42. DOI: 10.2514/3.26206 (cit. on p. 3).
- [22] D. Gildfind, R. Morgan, and J. Sancho. “Design and commissioning of a new lightweight piston for the X3 Expansion Tube”. In: *29th International Symposium on Shock Waves*. Springer. 2014. DOI: 10.1007/978-3-319-16835-7\_58 (cit. on pp. 4, 27, 28, 30, 53–55).

- [23] R. Morgan. “Development of X3, a superorbital expansion tube”. In: *38th Aerospace Sciences Meeting and Exhibit*. 2000, p. 558. DOI: 10.2514/6.2000-558 (cit. on pp. 4, 25).
- [24] D. Potter. “Modelling of radiating shock layers for atmospheric entry at Earth and Mars”. PhD thesis. 2011 (cit. on pp. 8, 103).
- [25] C. Park. *Nonequilibrium hypersonic aerothermodynamics*. New York: Wiley, 1989 (cit. on pp. 8, 19).
- [26] J. Wilson. “Ionization Rate of Air behind High-Speed Shock Waves”. In: *The Physics of Fluids* 9.10 (1966), pp. 1913–1921. DOI: 10.1063/1.1761543 (cit. on p. 8).
- [27] R. Breene Jr and M. C. Nardone. “Radiant emission from high temperature equilibrium air”. In: *Journal of Quantitative Spectroscopy and Radiative Transfer* 2.3 (1962), pp. 273–292. DOI: 10.1016/0022-4073(62)90003-1 (cit. on p. 9).
- [28] M. Nardone, R. G. Breene, S. Zeldin, and T. Riethof. *Radiance of species in high temperature air*. Tech. rep. GENERAL ELECTRIC CO PHILADELPHIA PA MISSILE and SPACE DIV, 1963 (cit. on p. 9).
- [29] R. E. Meyerott, J. Sokoloff, and R. Nicholls. *Absorption coefficients of air*. Tech. rep. LOCKHEED MISSILES and SPACE CO INC SUNNYVALE CA, 1960 (cit. on pp. 9, 11).
- [30] B. Kivel and K. Bailey. *Tables of radiation from high temperature air*. Avco Manufacturing Corporation, Avco Research Laboratory, 1957 (cit. on p. 9).
- [31] R. Allen, J. Camm, and J. C. Keck. “Radiation from hot nitrogen”. In: *Journal of Quantitative Spectroscopy and Radiative Transfer* 1.3-4 (1961), 269–IN2. DOI: 10.1016/0022-4073(61)90027-9 (cit. on pp. 9, 10, 13).
- [32] R. A. Allen, J. C. Keck, and J. Camm. *Non-equilibrium radiation from shock heated nitrogen and a determination of the recombination rate*. Tech. rep. AVCO EVERETT RESEARCH LAB EVERETT MASS, 1961. DOI: 10.1016/0022-4073(65)90084-1 (cit. on pp. 9, 10).
- [33] R. A. Allen. “Nonequilibrium shock front rotational, vibrational and electronic temperature measurements”. In: *Journal of Quantitative Spectroscopy and Radiative Transfer* 5.3 (1965), pp. 511–523 (cit. on pp. 9, 13).
- [34] W. A. Page. “Shock-layer radiation of blunt bodies traveling at lunar return entry velocities”. In: *IAS PAPER 63-41* (1963) (cit. on p. 9).
- [35] W. A. Page. “Shock layer radiation of blunt bodies at reentry velocities”. In: *NASA TR R-193* (1964) (cit. on pp. 9–11).
- [36] C. Wittliff. “Hypersonic shock tunnel heat transfer tests of the Space Shuttle SILTS pod configuration”. In: *18th Thermophysics Conference*. 1983, p. 1535. DOI: 10.2514/6.1983-1535 (cit. on p. 10).

## 6. Conclusions and Recommendations

- [37] R. Hiers, W. Loubsky, and D. Stewart. “Performance of a Combustion Driven Shock Tunnel with Application to the Tailored-Interface Operating Conditions”. In: *Third Conference on Performance of High Temperature Systems* (1964) (cit. on p. 10).
- [38] J. Belanger and H. Hornung. “A combustion driven shock tunnel to complement the free piston shocktunnel T5 at GALCIT”. In: *28th Joint Propulsion Conference and Exhibit*. 1992, p. 3968. DOI: 10.2514/6.1992-3968 (cit. on p. 10).
- [39] R. Stalker. *An investigation of free piston compression of shock tube driver gas*. Tech. rep. National Research Council Canada, 1961 (cit. on p. 10).
- [40] R. Stalker. “Two developments with free piston drivers”. In: *Proc. 7th Int. Symp. on Shock Tubes and Waves*. 1971, pp. 242–258 (cit. on p. 10).
- [41] J. C. Camm and P. H. Rose. *Electric shock tube for high velocity simulation*. Tech. rep. AVCO EVERETT RESEARCH LAB EVERETT MASS, 1962 (cit. on p. 10).
- [42] S. P. Sharma and C. Park. “Operating characteristics of a 60-and 10-cm electric arc-driven shock tube. I-The driver. II-The driven section”. In: *Journal of thermophysics and heat transfer* 4.3 (1990), pp. 259–265. DOI: 10.2514/3.175 (cit. on p. 10).
- [43] J. Grinstead, M. Wilder, J. Olejniczak, D. Bogdanoff, G. Allen, K. Dang, and M. J. Forrest. “Shock-heated air radiation measurements at lunar return conditions”. In: *AIAA paper 1244* (2008), p. 2008. DOI: 10.2514/6.2008-1244 (cit. on pp. 10, 11).
- [44] C. Johnston. “A comparison of EAST shock-tube radiation measurements with a new air radiation model”. In: *46th AIAA Aerospace Sciences Meeting and Exhibit*. 2008, p. 1245. DOI: 10.2514/6.2008-1245 (cit. on p. 12).
- [45] K. Fujita, S. Sato, T. Abe, and Y. Ebinuma. “Experimental investigation of air radiation from behind a strong shock wave”. In: *Journal of thermophysics and heat transfer* 16.1 (2002), pp. 77–82. DOI: 10.2514/6.1998-2467 (cit. on p. 12).
- [46] C. G. Miller III. *A comparison of measured and predicted sphere shock shapes in hypersonic flows with density ratios from 4 to 19*. Tech. rep. NASA Langley Research Center, 1975 (cit. on p. 12).
- [47] H. Hornung. “Non-equilibrium dissociating nitrogen flow over spheres and circular cylinders”. In: *Journal of Fluid Mechanics* 53.1 (1972), pp. 149–176. DOI: 10.1017/S0022112072000084 (cit. on p. 12).
- [48] G. Laufer and R. McKenzie. “Temperature measurements in hypersonic air flows using laser-inducedO2 fluorescence”. In: *Sensor and Measurements Techniques for Aeronautical Applications*. 1988, p. 4679. DOI: 10.2514/6.1988-4679 (cit. on p. 12).
- [49] J. A. Wilkes, D. W. Alderfer, S. B. Jones, and P. M. Danehy. “Portable Fluorescence imaging system for hypersonic flow facilities”. In: (2003) (cit. on p. 12).

- [50] B. McMillin, M. Lee, and R. Hanson. “Planar laser-induced fluorescence imaging of shock-tube flows with vibrational nonequilibrium”. In: *AIAA journal* 30.2 (1992), pp. 436–443. DOI: 10.2514/3.10935 (cit. on p. 13).
- [51] C. Park. “Assessment of a two-temperature kinetic model for dissociating and weakly ionizing nitrogen”. In: *Journal of Thermophysics and Heat Transfer* 2.1 (1988), pp. 8–16. DOI: 10.2514/3.55 (cit. on p. 13).
- [52] C. Park. “Assessment of two-temperature kinetic model for ionizing air”. In: *Journal of Thermophysics and Heat Transfer* 3.3 (1989), pp. 233–244. DOI: 10.2514/3.28771 (cit. on pp. 13, 14).
- [53] C. Park. “Nonequilibrium air radiation (Nequair) program: User’s manual”. In: (1985) (cit. on p. 13).
- [54] K. Sutton. “Air radiation revisited”. In: *19th Thermophysics Conference*. Fluid Dynamics and Co-located Conferences (June 1984). DOI: 10.2514/6.1984-1733 (cit. on p. 14).
- [55] A. Balakrishnan, C. Park, and M. Green. “Radiative viscous-shock-layer analysis of Fire, Apollo, and PAET flight data”. In: *20th Thermophysics Conference*. 1985, p. 1064. DOI: 10.2514/6.1985-1064 (cit. on p. 14).
- [56] A. Brandis, C. Johnston, B. Cruden, D. Prabhu, and D. Bose. “Uncertainty Analysis and Validation of Radiation Measurements for Earth Reentry”. In: *Journal of Thermophysics and Heat Transfer* 29.2 (2015), pp. 209–221. DOI: 10.2514/1.T4000 (cit. on pp. 15, 16).
- [57] A. Feldick, M. Modest, D. Levin, P. Gnoffo, and C. Johnston. “Examination of Coupled Continuum Fluid Dynamics and Radiation in Hypersonic Simulations”. In: *47th AIAA Aerospace Sciences Meeting including The New Horizons Forum and Aerospace Exposition*. 2009, p. 475. DOI: 10.2514/6.2009-475 (cit. on pp. 14, 16).
- [58] P. A. Gnoffo and F. M. Cheatwood. *User’s manual for the Langley aerothermodynamic upwind relaxation algorithm (LAURA)*. Tech. rep. NASA Langley Research Center, 1996 (cit. on p. 14).
- [59] C. O. Johnston. “Nonequilibrium shock-layer radiative heating for Earth and Titan entry”. PhD thesis. Virginia Tech, 2006 (cit. on p. 14).
- [60] M. J. Wright, G. V. Candler, and D. Bose. “Data-parallel line relaxation method for the Navier-Stokes equations”. In: *AIAA journal* 36.9 (1998), pp. 1603–1609. DOI: 10.2514/2.586 (cit. on pp. 14, 19).
- [61] K. Fujita and T. Abe. *SPRADIAN, structured package for radiation analysis: Theory and application*. Tech. rep. The Institute of Space and Astronautical Science, 1997, p. 1 (cit. on p. 16).
- [62] D. F. Potter. *A High Temperature Gas Radiation Module for Compressible Flow CFD: Theory and User’s Guide*. 2013 (cit. on p. 16).

## 6. Conclusions and Recommendations

- [63] A. Smith, T. Gogel, P. Vandevelde, and L. Marraffa. “Plasma radiation database PARADE final report”. In: *ESTEC contract 11148* (1996), p. 94 (cit. on p. 16).
- [64] M. Fertig and G. Herdrich. “The advanced URANUS Navier-Stokes code for the simulation of nonequilibrium re-entry flows”. In: *Transactions of the Japan Society for Aeronautical and Space Sciences, Space Technology Japan* 7.ists26 (2009), Pe\_15–Pe\_24. DOI: 10.2322/tstj.7.Pe\_15 (cit. on p. 16).
- [65] D. L. Cauchon. *Project FIRE flight 1 radiative heating experiment*. 1966 (cit. on p. 16).
- [66] D. L. Cauchon. “Radiative heating results from the FIRE II flight experiment at a reentry velocity of 11.4 kilometers per second”. In: *NASA TM X-1402* (1967) (cit. on pp. 16, 17).
- [67] D. B. Lee and M. S. Center. *Apollo experience report: aerothermodynamics evaluation*. Vol. 6843. National Aeronautics and Space Administration, 1972 (cit. on pp. 17, 18).
- [68] D. Buttsworth, R. Morgan, and P. Jenniskens. “Near-Ultraviolet Emission Spectroscopy of the Hayabusa Reentry”. In: *Journal of Spacecraft and Rockets* 50.6 (June 2013), pp. 1109–1120. DOI: 10.2514/1.A32500 (cit. on pp. 17–19, 106, 109).
- [69] J. Grinstead, P. Jenniskens, A. Cassell, J. Albers, and M. Winter. “Airborne observation of the Hayabusa sample return capsule re-entry”. In: *42nd AIAA Thermophysics Conference*. 2011, p. 3329. DOI: 10.2514/6.2011-3329 (cit. on p. 17).
- [70] T. J. McIntyre, R. Khan, T. N. Eichmann, B. Upcroft, and D. Buttsworth. “Visible and Near Infrared Spectroscopy of Hayabusa Reentry Using Semi-Autonomous Tracking”. In: *Journal of Spacecraft and Rockets* 51.1 (2013), pp. 31–38. DOI: 10.2514/1.A32497 (cit. on pp. 17, 19, 106, 109).
- [71] P. Jenniskens. “Observations of the Stardust Sample Return Capsule entry with a slitless echelle spectrograph”. In: *Journal of Spacecraft and Rockets* 47.5 (2010), pp. 718–735. DOI: 10.2514/1.37518 (cit. on p. 17).
- [72] F. Harms, J. Wolf, G. Raiche, and P. Jenniskens. “Imaging and Slitless Spectroscopy of the Stardust Capsule Reentry Radiation”. In: *Journal of Spacecraft and Rockets* 47.6 (Nov. 2010), pp. 868–872. DOI: 10.2514/1.38054 (cit. on p. 17).
- [73] S. Löhle, R. Wernitz, G. Herdrich, M. Fertig, H.-P. Röser, and H. Ritter. “Airborne re-entry observation experiment SLIT: UV spectroscopy during STARDUST and ATV1 re-entry”. In: *CEAS Space Journal* 1.1-4 (2011), pp. 59–69 (cit. on p. 17).
- [74] P. Jenniskens, M. Kozubal, R. Dantowitz, J. Breitmeyer, M. Winter, J. Grinstead, and S. Loehle. “Time-Resolved Absolute Irradiance of the Hayabusa Sample Return Capsule Reentry”. In: *50th AIAA Aerospace Sciences Meeting including the New Horizons Forum and Aerospace Exposition*. 2012, p. 1294. DOI: 10.2514/6.2012-1294 (cit. on p. 18).

- [75] D. Buttsworth, M. D’Souza, D. Potter, T. Eichmann, N. Mudford, M. McGilvray, T. J. McIntyre, P. Jacobs, and R. Morgan. “Expansion tunnel radiation experiments to support hayabusa re-entry observations”. English. In: *48th AIAA Aerospace Sciences Meeting Including the New Horizons Forum and Aerospace Exposition* (2010). DOI: 10.2514/6.2010-634 (cit. on p. 19).
- [76] E. J. Fahy, R. J. Gollan, D. R. Buttsworth, P. A. Jacobs, and R. G. Morgan. “Expansion Tube and Computational Fluid Dynamics Studies of Superorbital Earth Re-entry”. In: *46th AIAA Thermophysics Conference* (2016). URL: <https://doi.org/10.2514/6.2016-3532> (cit. on pp. 19, 45, 58, 66, 67, 69, 73, 86, 93, 109, 111, 135).
- [77] E. J. Fahy. “Superorbital Re-Entry Shock Layers: Flight and Laboratory Comparisons”. PhD thesis. University of Queensland, 2017 (cit. on pp. 19, 20, 59, 109, 129–134, 136, 137, 143).
- [78] H. Kihara, N. Hirata, and K.-i. Abe. “A Study of Thermal Response and Flow Field Coupling Simulation around Hayabusa Capsule Loaded with Light-Weight Ablator”. In: *Open Journal of Fluid Dynamics* 3.02 (2013), p. 100. DOI: 10.4236/ojfd.2013.32A016 (cit. on pp. 19, 131, 132).
- [79] T. Suzuki, M. Furudate, and K. Sawada. “Unified calculation of hypersonic flowfield for a reentry vehicle”. In: *Journal of Thermophysics and Heat Transfer* 16.1 (2002), pp. 94–100. DOI: 10.2514/2.6656 (cit. on pp. 19, 131, 132).
- [80] M. W. Winter, R. D. McDaniel, Y.-K. Chen, D. Saunders, and P. Jenniskens. “Radiation Modeling for Reentry of Hayabusa Sample Return Capsule”. In: *Journal of Spacecraft and Rockets* (2019), pp. 1–13. DOI: 10.2514/1.A34381 (cit. on pp. 19, 131, 132).
- [81] P. Jacobs and R. Gollan. *The Eilmer3 Code: user guide and example book. Mechanical Engineering Report 2008/07*. Australia: Department of Mechanical Engineering, University of Queensland, 2008 (cit. on p. 20).
- [82] C. Park, R. L. Jaffe, and H. Partridge. “Chemical-kinetic parameters of hyperbolic earth entry”. In: *Journal of Thermophysics and Heat transfer* 15.1 (2001), pp. 76–90. DOI: 10.2514/2.6582 (cit. on p. 20).
- [83] E. Resler and D. Boxsom. *Very high mach number principles by unsteady flow principle*. Cornell University Graduate School of Aerodynamic Engineering, 1952 (cit. on p. 20).
- [84] R. Morgan. “A Review of the Use of Expansion Tubes for Creating Superorbital Flows”. In: *AIAA 35th Aerospace Sciences Meeting and Exhibit*. Reno, NV, Jan 6-10, 1997. DOI: 10.2514/6.1997-279 (cit. on p. 20).
- [85] U. S. N. A. Trimpi Robert L. and S. Administration. *A preliminary theoretical study of the expansion tube, a new device for producing high-enthalpy short-duration hypersonic gas flows*. Washington, D. C.; Springfield, Va.: National Aeronautics, Space Administration ; for sale by the Clearinghouse for Federal Scientific, and Technical Information, 1962 (cit. on p. 20).

## 6. Conclusions and Recommendations

- [86] D. Gildfind. “Development of High Total Pressure Scramjet Flows Conditions Using the X2 Expansion Tube”. PhD thesis. St. Lucia, Australia: the University of Queensland, 2012 (cit. on pp. 20, 21, 31, 34, 36, 41, 56, 144).
- [87] J. J. Jones. “Some performance characteristics of the LRC 3 3/4-inch pilot expansion tube using an unheated hydrogen driver”. In: *NASA Langley Research Centre* (1965) (cit. on p. 20).
- [88] J. J. Givens, W. A. Page, and R. M. Reynolds. “Evaluation of flow properties in a combustion-driven expansion tube operating at 7.5 km/sec.” In: (1966) (cit. on p. 20).
- [89] C. G. Miller. “Operational experience in the Langley expansion tube with various test gases”. In: *AIAA Journal* 16.3 (1978), pp. 195–196. DOI: 10.2514/3.60877 (cit. on p. 20).
- [90] A. Paull, R. Stalker, and I. Stringer. “Experiments on an expansion tube with a free piston driver”. In: *15th Aerodynamic Testing Conference*. 1988, p. 2018. DOI: 10.2514/6.1988-2018 (cit. on p. 22).
- [91] A. Neely, R. Stalker, and A. Paull. “High enthalpy, hypervelocity flows of air and argon in an expansion tube”. In: *The Aeronautical Journal* 95.946 (1991), pp. 175–186. DOI: 10.1017/S0001924000023885 (cit. on p. 22).
- [92] A. Paull and R. Stalker. “Test flow disturbances in an expansion tube”. In: *Journal of Fluid Mechanics* 245 (1992), pp. 493–521. DOI: 10.1017/S0022112092000569 (cit. on pp. 22, 23).
- [93] H. Mirels. “Test Time Limitation Due to Turbulent-Wall Boundary Layer”. In: *AIAA Journal* 2 (1963), pp. 84–93. DOI: 10.2514/3.2218 (cit. on pp. 22, 100).
- [94] R. E. Duff. “Shock-tube performance at low initial pressure”. In: *The Physics of Fluids* 2.2 (1959), pp. 207–216. DOI: 10.1063/1.1705910 (cit. on p. 22).
- [95] D. Gildfind, P. Jacobs, R. Morgan, W. Chan, and R. Gollan. “Scramjet test flow reconstruction for a large-scale expansion tube, Part 2: axisymmetric CFD analysis”. In: *Shock Waves* 28.4 (2018), pp. 899–918 (cit. on pp. 22, 72, 81, 100).
- [96] P. Toniato. “Free-jet testing of a Mach 12 scramjet in an expansion tube”. PhD thesis. St. Lucia, Australia: the University of Queensland, 2018 (cit. on pp. 22, 23, 27, 81, 82, 85, 86, 94, 96, 98, 100, 101, 103, 141, 142, 146).
- [97] R. Morgan and R. Stalker. “Double diaphragm driven free piston expansion tube”. In: *Shock waves; Proceedings of the 18th International Symposium*. Vol. 1. 1992, pp. 1031–1038 (cit. on pp. 22, 23).
- [98] D. Gildfind, C. James, P. Toniato, and R. Morgan. “Performance considerations for expansion tube operation with a shock-heated secondary driver”. In: *Journal of Fluid Mechanics* 777 (2015), pp. 364–407. DOI: 10.1017/jfm.2015.349 (cit. on p. 23).
- [99] C. Doolan and R. Morgan. “A two-stage free piston driver”. In: *Shock Waves* 9 (1999), pp. 239–248. DOI: 10.1007/s001930050 (cit. on p. 23).

- [100] R. Morgan. “A compound isentropic free piston driver for expansion tunnels”. In: *Proc 11th Australian Fluid Mechanics Conference*. 1992 (cit. on p. 23).
- [101] R. A. Palmer. “Measurement of heat transfer in superorbital flows”. PhD thesis. University of Queensland, 2000 (cit. on p. 24).
- [102] R. Palmer, K. Hannemann, and R. Morgan. “Experimental and numerical blunt body heat transfer in an expansion tube”. In: *Proc 21th Int Symp on Shock Tubes and Waves, Springer-Verlag*. 1997 (cit. on p. 24).
- [103] M. Abdel-Jawad, D. Mee, R. Morgan, P. Jacobs, and J. Philpot. “Transient force measurements at superorbital speeds”. In: *23rd International Symposium on Shock Waves* (2002) (cit. on p. 24).
- [104] M. Scott, R. Morgan, and P. Jacobs. “A new single stage driver for the X2 expansion tube”. In: *43rd AIAA Aerospace Sciences Meeting and Exhibit*. 2005, p. 697. DOI: 10.2514/6.2005-697 (cit. on p. 24).
- [105] D. E. Gildfind. “Development of high total pressure scramjet flow conditions using the X2 expansion tube”. PhD thesis. University of Queensland, 2012 (cit. on p. 24).
- [106] C. M. James, T. G. Cullen, H. Wei, S. W. Lewis, S. Gu, R. G. Morgan, and T. J. McIntyre. “Improved test time evaluation in an expansion tube”. In: *Experiments in Fluids* 59.5 (2018), p. 87 (cit. on pp. 25, 113, 115).
- [107] C. M. James, D. R. Smith, C. McLean, R. G. Morgan, S. W. Lewis, and P. Toniato. “Improving High Enthalpy Expansion Tube Condition Characterisation Using High Speed Imagery”. In: *2018 Aerodynamic Measurement Technology and Ground Testing Conference*. 2018, p. 3805. DOI: 10.2514/6.2018-3805 (cit. on p. 25).
- [108] C. James, D. Gildfind, R. Morgan, P. Jacobs, and F. Zander. “Designing and Simulating High Enthalpy Expansion Tube Conditions”. In: *2013 Asia-Pacific International Symposium on Aerospace Technology*. Takamatsu, Japan, 2013 (cit. on pp. 25, 44, 102).
- [109] T. N. Eichmann. “Radiation measurements in a simulated Mars atmosphere”. PhD thesis. University of Queensland, 2012 (cit. on p. 25).
- [110] S. Gu, R. Morgan, and T. McIntyre. “Study of Afterbody Radiation during Mars Entry in an Expansion Tube”. In: *55th AIAA Aerospace Sciences Meeting, AIAA SciTech Forum*. Grapevine, TX, U.S.A, January 9-13, 2017. DOI: 10.2514/6.2017-0212 (cit. on p. 25).
- [111] G. de Crombrugghe, D. Gildfind, F. Zander, T. McIntyre, and R. Morgan. “Design of Test Flows to Investigate Binary Scaling in High Enthalpy CO<sub>2</sub> – N<sub>2</sub> Mixtures”. In: *19th Australasian Fluid Mechanics Conference*. Melbourne, Australia, 2014 (cit. on p. 25).

## 6. Conclusions and Recommendations

- [112] C. James, D. Gildfind, R. Morgan, S. Lewis, E. Fahy, and T. McIntyre. “On the Current Limits of Simulating Gas Giant Entry Flows in an Expansion Tube”. In: *20th AIAA International Space Planes and Hypersonic Systems and Technologies Conference*. Glasgow, Scotland, 2015. DOI: 10.2514/6.2015-3501 (cit. on p. 25).
- [113] Y. Liu, C. M. James, R. G. Morgan, and T. J. McIntyre. “Experimental study of saturn entry radiation with higher amount of diluent in an expansion tube”. In: *2018 Joint Thermophysics and Heat Transfer Conference*. [publishername] American Institute of Aeronautics and Astronautics Inc, AIAA. 2018. DOI: 10.2514/6.2018-4070 (cit. on p. 25).
- [114] B. Capra and R. Morgan. “Radiative and Total Heat Transfer Measurements to a Titan Explorer Model”. In: *Journal of Spacecraft and Rockets* 49 (1 2012), pp. 12–23. DOI: 10.2514/6.2006-7934 (cit. on p. 25).
- [115] H. Porat, F. Zander, R. G. Morgan, and T. J. McIntyre. “Emission spectroscopy of a Mach disk at Titan atmospheric entry conditions”. In: *29th International Symposium on Shock Waves 1*. Springer. 2015, pp. 593–598. DOI: 10.1007/978-3-319-16835-7\_94 (cit. on p. 25).
- [116] U. A. Sheikh, R. G. Morgan, and T. J. McIntyre. “Vacuum Ultraviolet Spectral Measurements for Superorbital Earth Entry in X2 Expansion Tube”. In: *Aiaa Journal* (2015). DOI: 10.2514/1.J054027 (cit. on p. 25).
- [117] H. Wei, R. Morgan, T. McIntyre, A. Brandis, and C. Johnston. “Experimental and Numerical Investigation of Air Radiation in Superorbital Expanding Flow”. In: *47th AIAA Thermophysics Conference*. Denver, CO, U.S.A., June 5-9, 2017. DOI: 10.2514/6.2017-4531 (cit. on p. 25).
- [118] F. Zander. “Hot Wall Testing in Hypersonic Impulse Facilities”. PhD thesis. St. Lucia, Australia: University of Queensland, 2013 (cit. on p. 25).
- [119] S. W. Lewis, C. James, R. G. Morgan, T. J. McIntyre, C. R. Alba, and R. G. Greendyke. “Carbon Ablative Shock-Layer Radiation with High Surface Temperatures”. In: *Journal of Thermophysics and Heat Transfer* 31.1 (2017), pp. 193–204. DOI: 10.2514/1.T4902 (cit. on p. 25).
- [120] T. Cullen, C. James, R. Gollan, and R. Morgan. “Development of a Total Enthalpy and Reynolds Number Matched Apollo Re-entry Condition in the X2 Expansion Tunnel”. In: *31st International Symposium on Shock Waves*. Nagoya, Japan, July 9-14, 2017. DOI: 10.1007/978-3-319-91017-8\_24 (cit. on p. 25).
- [121] T. Eichmann. “Radiation Measurements in a Simulated Mars Atmosphere”. PhD thesis. St. Lucia, Australia: the University of Queensland, 2012 (cit. on pp. 25, 26).
- [122] M. Abdel-Jawad. “Stability assessment of planetary entry vehicles in the X3 superorbital expansion tube”. PhD thesis. University of Queensland, 2005 (cit. on p. 25).

- [123] B. R. Capra. “Aerothermodynamic simulation of subscale models of the FIRE II and Titan Explorer vehicles in expansion tubes”. PhD thesis. University of Queensland, 2007 (cit. on p. 25).
- [124] B. R. Capra and R. G. Morgan. “Radiative and total heat transfer measurements to a Titan explorer model”. In: *Journal of Spacecraft and Rockets* 49.1 (2012), pp. 12–23. DOI: 10.2514/6.2006-7934 (cit. on p. 25).
- [125] A. Dann, R. Morgan, D. Gildfind, P. Jacobs, M. McGilvray, and F. Zander. “Upgrade of the X3 super-orbital expansion tube”. In: *Proceedings of the 18th Australasian Fluid Mechanics Conference, AFMC 2012*. Australasian Fluid Mechanics Society. 2012 (cit. on pp. 25, 27).
- [126] M. P. Scott. “Development and modelling of expansion tubes”. PhD thesis. University of Queensland, 2007 (cit. on p. 27).
- [127] M. G. Davey. “A hypersonic nozzle for the X3 expansion tube”. In: *University of Queensland* (2006) (cit. on p. 27).
- [128] P. Jacobs and R. Stalker. “Mach 4 and Mach 8 axisymmetric nozzles for a high-enthalpy shock tunnel”. In: *The Aeronautical Journal* 95.949 (1991), pp. 324–334. DOI: 10.1017/S0001924000024209 (cit. on p. 27).
- [129] D. Gildfind, J. Sancho, and R. Morgan. “High Mach number scramjet test flows in the X3 expansion tube”. In: *International Symposium on Shock Waves*. Springer. 2013, pp. 373–378. DOI: 10.1007/978-3-319-16835-7\_58 (cit. on p. 27).
- [130] J. Sancho Ponce. “Scramjet testing at high total pressure”. PhD thesis. University of Queensland, 2016 (cit. on pp. 27, 30, 31, 58, 82).
- [131] B. Wheatley. “Tunable Diode Laser Absorption Spectroscopy of Aerospace Flows”. PhD thesis. University of Queensland, 2017 (cit. on p. 27).
- [132] P. Jacobs. *L1d: A computer program for the simulation of transient-flow facilities. Report 1/99*. Australia: Department of Mechanical Engineering, University of Queensland, 1999 (cit. on pp. 28, 46).
- [133] R. Stalker. “A study of the free-piston shock tunnel.” In: *AIAA Journal* 5.12 (1967), pp. 2160–2165. DOI: 10.2514/3.4402 (cit. on pp. 29, 33, 34).
- [134] D. Gildfind, P. Jacobs, R. Morgan, W. Chan, and R. Gollan. “Scramjet test flow reconstruction for a large-scale expansion tube, Part 1: quasi-one-dimensional modelling”. In: *Shock Waves* 28.4 (2018), pp. 877–897. DOI: 10.1007/s00193-017-0785-x (cit. on pp. 30–32).
- [135] K. Itoh, S. Ueda, T. Komuro, K. Sato, M. Takahashi, H. Miyajima, H. Tanno, and H. Muramoto. “Improvement of a free piston driver for a high-enthalpy shock tunnel”. In: *Shock Waves* 8.4 (1998), pp. 215–233. DOI: 10.1007/s001930050115 (cit. on pp. 31, 34, 41).
- [136] H. Hornung. “The piston motion in a free-piston driver for shock tubes and tunnels”. In: *GALCIT Report FM* (1988), pp. 88–1 (cit. on pp. 33, 36–40, 42).

## 6. Conclusions and Recommendations

- [137] D. Gildfind, C. James, and R. Morgan. “Free-piston driver performance characterisation using experimental shock speeds through helium”. In: *Shock Waves* 25 (2 2015), pp. 169–176. DOI: 10.1007/s00193-015-0553-8 (cit. on p. 43).
- [138] P. A. Jacobs. *Using l<sub>script</sub> to define L1d simulations*. Tech. rep. University of Queensland, 2005 (cit. on p. 47).
- [139] D. Gildfind, T. Hines, P. Jacobs, S. Stennett, and I. Dimitrijevic. “Use of acceleration and optical waypoint measurements to estimate piston trajectory in an impulse facility”. In: *Shock Waves* (2019), pp. 1–27. DOI: 10.1007/s00193-018-0877-2 (cit. on p. 53).
- [140] P. A. Jacobs. “Numerical simulation of transient hypervelocity flow in an expansion tube”. In: *Computers & fluids* 23.1 (1994), pp. 77–101. DOI: 10.1016/0045-7930(94)90028-0 (cit. on pp. 72, 100).
- [141] G. Roberts, R. Morgan, and R. Stalker. “Influence of secondary diaphragm on flow quality in expansion tubes”. In: *Shock Waves@ Marseille I*. Springer, 1995, pp. 203–208. DOI: 10.1007/978-3-642-78829-1\_32 (cit. on p. 72).
- [142] D. E. Gildfind, C. M. James, P. Toniato, and R. G. Morgan. “Performance considerations for expansion tube operation with a shock-heated secondary driver”. In: *Journal of Fluid Mechanics* 777 (2015), pp. 364–407 (cit. on pp. 76, 77).
- [143] M. McGilvray, P. Jacobs, R. Morgan, and D. Ramanah. “Boundary layer transition in an expansion tube at a low enthalpy operating condition”. In: *45th AIAA Aerospace Sciences Meeting and Exhibit*. 2011, p. 1328. DOI: 10.2514/6.2007-1328 (cit. on pp. 81, 82).
- [144] E. L. Petersen and R. K. Hanson. “Improved turbulent boundary-layer model for shock tubes”. In: *AIAA journal* 41.7 (2003), pp. 1314–1322. DOI: 10.2514/2.2076 (cit. on p. 81).
- [145] P. Toniato, D. Gildfind, P. A. Jacobs, and R. G. Morgan. “Optimisation and design of a fully instrumented Mach 12 nozzle for the X3 expansion tube”. In: *31st International Symposium on Shock Waves*. Nagoya, Japan: Springer, July 10, 2017. DOI: 10.1007/978-3-319-91017-8\_108 (cit. on p. 86).
- [146] S. J. Stennett, D. E. Gildfind, P. A. Jacobs, and R. G. Morgan. “Performance optimization of X3R: A new reflected shock tunnel mode for the X3 expansion tube”. In: *2018 Aerodynamic Measurement Technology and Ground Testing Conference*. 2018, p. 3563. DOI: 10.2514/6.2018-3563 (cit. on pp. 86, 141).
- [147] A. Sasoh, Y. Ohnishi, D. Ramjaun, K. Takayama, H. Otsu, and T. Abe. “Effective test time evaluation in high-enthalpy expansion tube”. In: *AIAA journal* 39.11 (2001), pp. 2141–2147. DOI: 10.2514/2.1210 (cit. on p. 100).
- [148] D. McBride and G. Gordian. *Computer Program for Calculations of Complex Chemical Equilibrium Compositions and Applications II. Users Manual and Program Description*. Tech. rep. Cleveland, OH, U.S.A.: NASA Lewis Research Center, 1996 (cit. on p. 102).

- [149] B. J. McBride and S. Gordon. *Computer Program for Calculation of Complex Chemical Equilibrium Compositions and Applications II. Users Manual and Program Description. 2; Users Manual and Program Description*. Tech. rep. NASA Lewis Research Center, 1996 (cit. on p. 102).
- [150] D. Potter, R. Gollan, T. Eichmann, T. McIntyre, R. Morgan, and P. Jacobs. “Simulation of CO<sub>2</sub>-N<sub>2</sub> expansion tunnel flows for the study of radiating shock layers”. In: *46th AIAA Aerospace Sciences Meeting and Exhibit*. Reno, NV, USA, Jan 7-10, 2008 (cit. on p. 103).
- [151] K. Ohnishi, J. Watanabe, M. Sato, T. Ohkawa, and N. Ebizuka. “Spectroscopic Observation of the Re-Entry Capsule of HAYABUSA Spacecraft”. In: *Publications of the Astronomical Society of Japan* 63.5 (2011), pp. 987–993. DOI: 10.1093/pasj/63.5.987 (cit. on pp. 106, 109).
- [152] Wikipedia. *Barometric Formula*. URL: [https://en.wikipedia.org/wiki/Barometric\\_formula](https://en.wikipedia.org/wiki/Barometric_formula) (cit. on p. 109).
- [153] Photonics. *Shimadzu HPV-1 High Speed Camera*. URL: [https://www.photonics.com/Products/Hyper\\_Vision\\_HPV-1\\_High-Speed\\_Video\\_Camera/pr22689](https://www.photonics.com/Products/Hyper_Vision_HPV-1_High-Speed_Video_Camera/pr22689) (cit. on p. 111).
- [154] Lambert Instruments. *HiCatt*. URL: <https://www.lambertinstruments.com/hicatt> (cit. on p. 111).
- [155] Adept. *Phantom v611*. URL: <http://www.adept.net.au/cameras/visionresearch/Phantomv61x.shtml> (cit. on p. 111).
- [156] F. Zander, R. Gollan, P. Jacobs, and R. Morgan. “Hypervelocity shock standoff on spheres in air”. In: *Shock Waves* 24.2 (2014), pp. 171–178. DOI: 10.1007/s00193-013-0488-x (cit. on p. 113).
- [157] J. Canny. “A computational approach to edge detection”. In: *Readings in computer vision*. Elsevier, 1987, pp. 184–203. DOI: 10.1109/TPAMI.1986.4767851 (cit. on pp. 113, 115).
- [158] F. S. Billig. “Shock-wave shapes around spherical-and cylindrical-nosed bodies.” In: *Journal of Spacecraft and Rockets* 4.6 (1967), pp. 822–823. DOI: 10.2514/3.28969 (cit. on p. 115).
- [159] D. Umbach and K. N. Jones. “A few methods for fitting circles to data”. In: *IEEE Transactions on instrumentation and measurement* 52.6 (2003), pp. 1881–1885 (cit. on p. 115).
- [160] H. Hornung and C. Wen. “Nonequilibrium dissociating flow over spheres”. In: *33rd Aerospace Sciences Meeting and Exhibit*. 1995, p. 91. DOI: 10.1017/S0022112095003545 (cit. on p. 119).
- [161] K. R. Lobb. “Experimental measurement of shock detachment distance on spheres fired in air at hypervelocities”. In: *AGARDograph*. Vol. 68. Elsevier, 1964, pp. 519–527. DOI: 10.1016/B978-1-4831-9828-6.50031-X (cit. on p. 119).
- [162] R. Gollan. *poshax: Computing post-shock thermochemically relaxing flow behind a steady normal shock*. Tech. rep. University of Queensland, 2007 (cit. on pp. 120, 132, 134).

## 6. Conclusions and Recommendations

- [163] C. Park. “Review of chemical-kinetic problems of future NASA missions. I-Earth entries”. In: *Journal of Thermophysics and Heat transfer* 7.3 (1993), pp. 385–398 (cit. on pp. 120, 132).
- [164] D. Bose, E. McCorkle, C. Thompson, D. Bogdanoff, D. Prabhu, G. Allen, and J. Grinstead. “Analysis and model validation of shock layer radiation in air”. In: *VKILS Course on hypersonic entry and cruise vehicles, Palo Alto, California, USA* (2008) (cit. on p. 122).
- [165] Lastek Pty Ltd. *Lastek Photonics Technology Solutions*. URL: <https://www.lastek.com.au/> (cit. on p. 123).
- [166] R. J. Kramilda A. Ralchenko Y. and N. A. Team. *NIST Atomic Spectra Database (version 5.6.1)*. 2018 (cit. on p. 126).
- [167] R. Stalker. “Approximations for nonequilibrium hypervelocity aerodynamics”. In: *AIAA journal* 27.12 (1989), pp. 1761–1769. DOI: 10.2514/3.10332 (cit. on pp. 132, 136).
- [168] N. Freeman. “Non-equilibrium flow of an ideal dissociating gas”. In: *Journal of Fluid Mechanics* 4.4 (1958), pp. 407–425 (cit. on p. 134).
- [169] G. R. Inger, C. Higgins, and R. Morgan. “Shock standoff on hypersonic blunt bodies in nonequilibrium gas flows”. In: *Journal of thermophysics and heat transfer* 16.2 (2002), pp. 245–250 (cit. on p. 136).
- [170] D. R. Smith, D. E. Gildfind, C. M. James, T. McIntyre, and V. Wheatley. “Magnetohydrodynamic drag force measurements in an expansion tube”. In: *2018 Flow Control Conference*. 2018, p. 3755. DOI: 10.2514/6.2018-3755 (cit. on p. 146).

# A

---

## Experiment List

In this Appendix a list of shots which have been discussed in the body of the thesis are listed. Where relevant the fill pressure and gas composition of each section of tube is presented. For the shots conducted in chapter 5 details about the optical setup are also included. Shots performed that are not mentioned in this thesis are not included, as well as shots where the measurement technique failed. The tables in this appendix are as follows:

- Table A.1 contains the shots performed with a 2mm thick diaphragm for a variation of driver gas compositions.
- Table A.2 contains the shots performed with a 3mm thick diaphragm for a variation of driver gas compositions.
- Table A.3 contains shots performed with a secondary driver. This includes both thicknesses of primary diaphragm.
- Table A.4 contains shots performed with a shortened shock tube.
- Table A.5 contains shots performed with 3mm diaphragms of different material.
- Table A.6 contains shots performed comparing the piston repairs and new diaphragms with the previous arrangement and shots done to quantify the full scale condition.
- Table A.7 contains all the shots which resulted in optical data.

Table A.1.: Shots performed with a 2mm thick primary diaphragm discussed in section 4.5.

Shot	Reservoir	Compression Tube			Shock Tube		Acceleration Tube	
	Fill MPa	Fill kPa	He %	Ar %	Fill kPa	Gas —	Fill Pa	Gas —
x3s505	6.7	49.0	0	100	13.5	Air	21.0	Air
x3s508	6.7	49.0	75	25	13.5	Air	28.0	Air
x3s509	6.7	49.0	75	25	13.5	Air	25.0	Air
x3s510	6.7	49.0	60	40	13.5	Air	17.0	Air
x3s511	6.7	49.0	85	15	13.5	Air	17.0	Air
x3s512	6.7	49.0	100	0	13.5	Air	40.0	Air

Table A.2.: Shots performed with a 3mm thick primary diaphragm discussed in section 4.5.

Shot	Reservoir	Compression Tube			Shock Tube		Acceleration Tube	
	Fill MPa	Fill kPa	He %	Ar %	Fill kPa	Gas —	Fill Pa	Gas —
x3s526	8.8	46.0	0	100	13.5	Air	17.0	Air
x3s527	8.8	46.0	60	40	13.5	Air	17.0	Air
x3s528	8.8	46.0	75	25	13.5	Air	17.0	Air
x3s529	8.8	46.0	75	25	13.5	Air	17.0	Air
x3s530	8.8	46.0	85	15	13.5	Air	17.0	Air
x3s531	8.8	46.0	100	0	13.5	Air	17.0	Air
x3s532	8.8	46.0	100	0	13.5	Air	17.0	Air

Table A.3.: Shots that used a secondary driver with both 2mm and 3mm thick primary diaphragms, discussed in section 4.7.

Shot	Reservoir	Compression Tube			Secondary Driver		Shock Tube		Acceleration Tube		Diaphragms	
	Fill MPa	Fill kPa	He %	Ar %	Fill kPa	Gas —	Fill Pa	Gas —	Fill kPa	Gas —	Primary (Steel)	Secondary (Mylar)
x3s514	6.7	49.0	100	0	100	He	13.5	Air	17.0	Air	2mm	70µm
x3s515	6.7	49.0	100	0	80	He	13.5	Air	17.0	Air	2mm	2 × 25µm
x3s516	6.7	49.0	100	0	120	He	13.5	Air	17.0	Air	2mm	70µm
x3s535	8.8	46.0	100	0	100	He	13.5	Air	17.0	Air	3mm	50µm
x3s536	8.8	46.0	100	0	150	He	13.5	Air	17.0	Air	3mm	70µm
x3s537	8.8	46.0	100	0	225	He	13.5	Air	17.0	Air	3mm	50 + 70µm

Table A.4.: Shots performed with a short shock tube, discussed in section 4.8.

Shot	Reservoir	Compression Tube			Shock Tube		Acceleration Tube	
	Fill MPa	Fill kPa	He %	Ar %	Fill kPa	Gas —	Fill Pa	Gas —
x3s533	8.8	46.0	100	0	13.5	Air	17.0	Air
x3s534	8.8	46.0	100	0	13.5	Air	17.0	Air

Table A.5.: Shots performed with the stronger 3mm diaphragms, discussed in section 4.9.

Shot	Reservoir	Compression Tube			Shock Tube		Acceleration Tube	
	Fill MPa	Fill kPa	He %	Ar %	Fill kPa	Gas —	Fill Pa	Gas —
x3s546	8.8	46.0	100	0	13.5	Air	17.0	Air
x3s553	9.8	46.0	100	0	13.5	Air	17.0	Air
x3s554	9.4	46.0	100	0	13.5	Air	17.0	Air
x3s555	9.4	46.0	100	0	13.5	Air	17.0	Air

Table A.6.: Shots performed when developing and quantifying the full scale condition

Shot	Reservoir Fill MPa	Compression Tube			Shock Tube		Acceleration Tube		Note
		Fill kPa	He %	Ar %	Fill kPa	Gas —	Fill Pa	Gas —	
x3s663	8.8	46.0	85	15	13.5	Air	17.0	Air	
x3s664	8.8	46.0	85	15	13.5	Air	17.0	Air	
x3s665	8.8	46.0	100	0	13.5	Air	17.0	Air	
x3s666	8.8	46.0	100	0	2.5	Air	5.5	Air	
x3s667	8.8	46.0	100	0	2.5	Air	3.5	Air	
x3s668	8.8	46.0	100	0	2.5	Air	3.5	Air	15° conical probes at nozzle exit
x3s669	8.8	46.0	100	0	2.5	Air	3.5	Air	15° conical probes at nozzle exit
x3s670	8.8	46.0	100	0	2.5	Air	3.5	Air	Pitot pressure probes at nozzle exit
x3s673	8.8	46.0	100	0	2.5	Air	3.5	Air	Pitot pressure probes at nozzle exit
x3s682	8.8	46.0	100	0	2.5	Air	3.5	Air	15° conical probes at nozzle inlet
x3s683	8.8	46.0	100	0	2.5	Air	3.5	Air	15° conical probes at nozzle inlet

Table A.7.: Shots performed when taking optical measurements in front of a model. Shots x3s693–x3s700 were performed using the 1:5 scale model and shots x3s701 – x3s705 were performed using the full scale Hayabusa model.

Shot	Reservoir	Compression Tube				Shock Tube		Acceleration Tube				Optics					
	Fill MPa	Fill kPa	He %	Ar %	Fill kPa	Gas —	Fill Pa	Gas —	HSC <sup>1</sup>	f <sup>2</sup> kHz	Ex. <sup>3</sup> μs	F <sup>4</sup> nm	Sp. <sup>5</sup> nm	C.W. <sup>6</sup> nm	F <sup>7</sup> nm	f <sup>8</sup> kHz	Ex. <sup>9</sup> μs
x3s693	8.8	46.0	100	0	2.5	Air	3.5	Air	—	—	—	—	✓	640	550	10	95
x3s694	8.8	46.0	100	0	2.5	Air	3.5	Air	—	—	—	—	✓	640	550	10	95
x3s696	8.8	46.0	100	0	2.5	Air	3.5	Air	—	—	—	—	✓	640	550	10	95
x3s698	8.8	46.0	100	0	2.5	Air	3.5	Air	✓	62.5	8	740	—	—	—	—	—
x3s699	8.8	46.0	100	0	2.5	Air	3.5	Air	✓	62.5	8	780	✓	450	315 <sup>7a</sup>	20	45
x3s700	8.8	46.0	100	0	2.5	Air	3.5	Air	✓	62.5	8	780	✓	450	315 <sup>7a</sup>	20	45
x3s701	8.8	46.0	100	0	2.5	Air	3.5	Air	✓	62.5	8	740	✓	640	550	10	95
x3s702	8.8	46.0	100	0	2.5	Air	3.5	Air	✓	62.5	8	740	✓	640	550	10	95
x3s703	8.8	46.0	100	0	2.5	Air	3.5	Air	✓	62.5	8	740	✓	640	550	10	95
x3s704	8.8	46.0	100	0	2.5	Air	3.5	Air	✓	62.5	8	780	✓	450	315 <sup>7a</sup>	10	95
x3s705	8.8	46.0	100	0	2.5	Air	3.5	Air	✓	62.5	8	780	✓	450	315 <sup>7a</sup>	10	95

<sup>1</sup> Two-dimensional high speed camera imaging. <sup>2</sup> Frequency of the high speed camera. <sup>3</sup> Exposure time of the high speed camera. <sup>4</sup> Centre wavelength of the ±5nm bandpass filter. <sup>5</sup> Time resolved spectroscopy. <sup>6</sup> Centre wavelength of the spectrometer. <sup>7</sup> Cutoff wavelength of the highpass filter. <sup>7a</sup> 315–700nm bandpass filter used. <sup>8</sup> Frequency of the imaging system for spectroscopy. <sup>9</sup> Exposure time of the imaging system for spectroscopy.

# B

## Shock Tube Wall Static Pressures

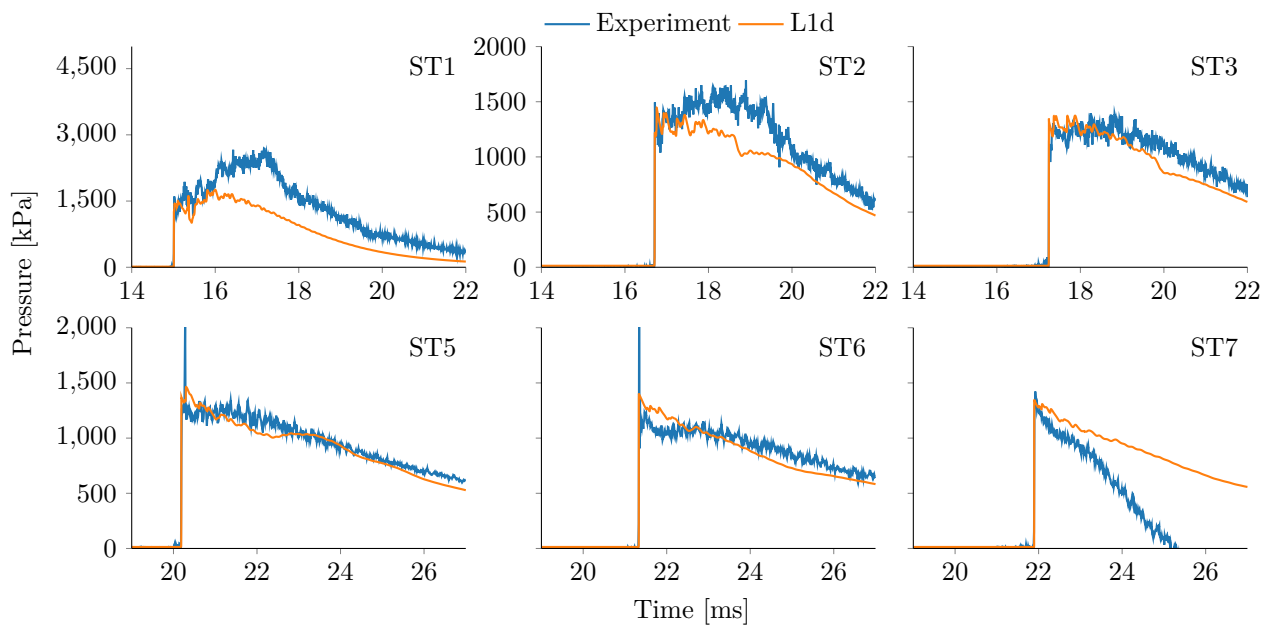


Figure B.1.: Shock tube wall static pressure traces for x3s508 with L1d data centred on the experimental data for each wall sensor. Experimental data has been filtered with a 5<sup>th</sup> order Butterworth filter with a 250kHz cutoff.

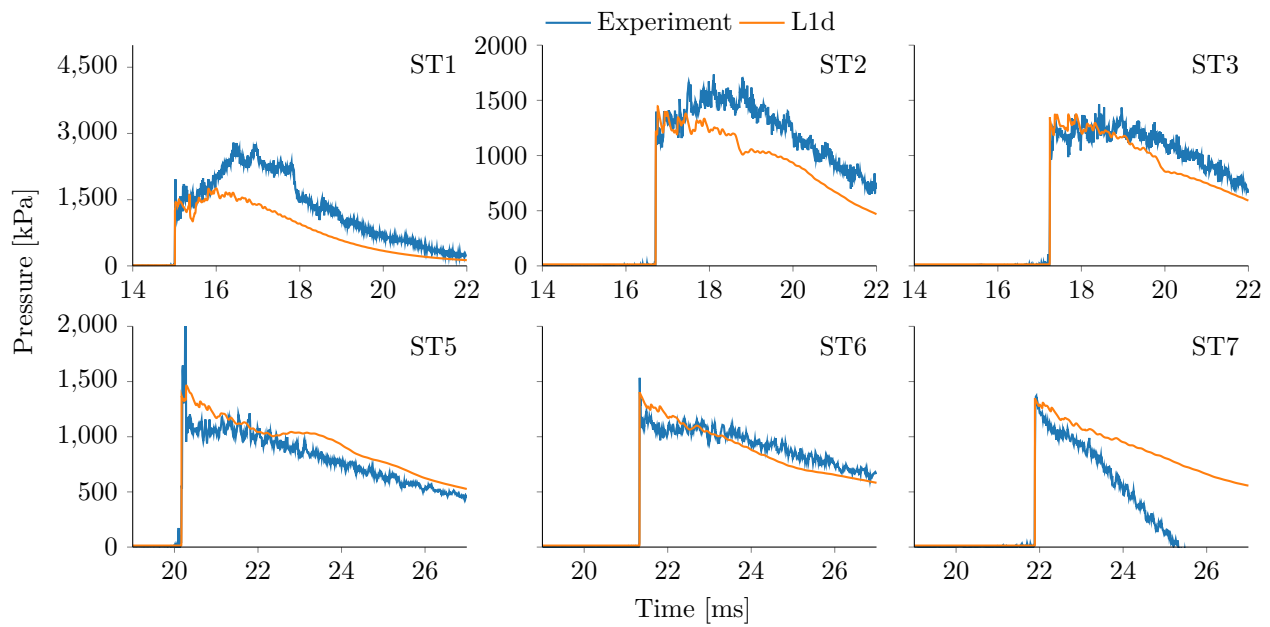


Figure B.2.: Shock tube wall static pressure traces for x3s509 with L1d data centred on the experimental data for each wall sensor. Experimental data has been filtered with a 5<sup>th</sup> order Butterworth filter with a 250kHz cutoff.

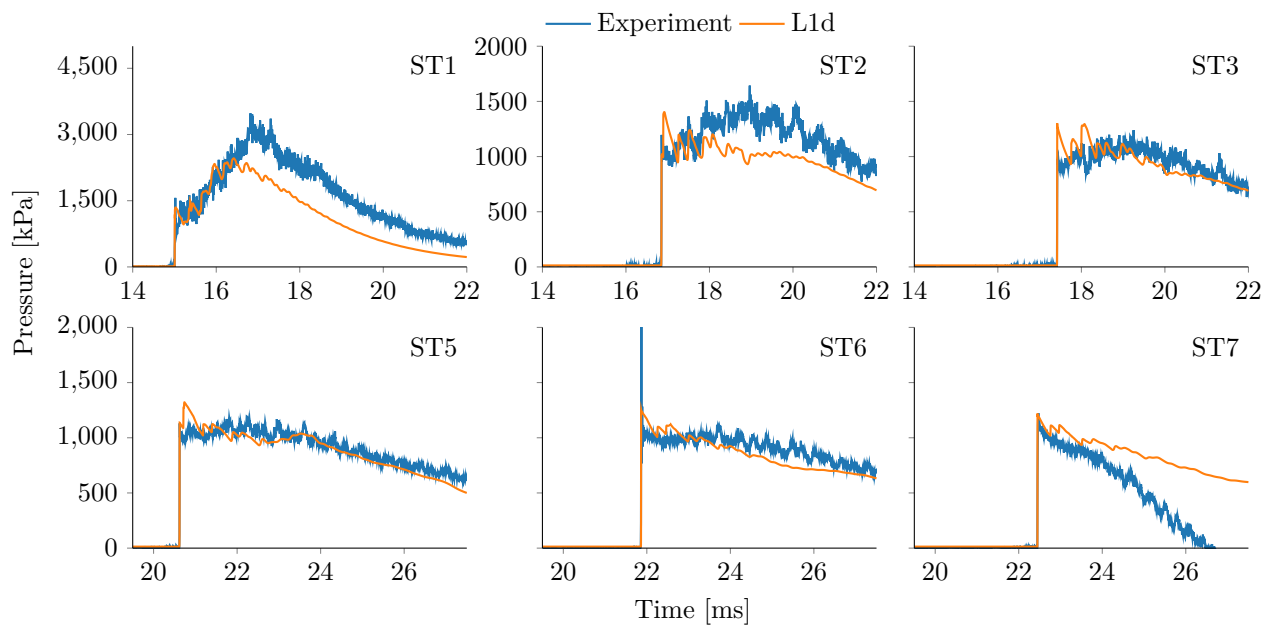


Figure B.3.: Shock tube wall static pressure traces for x3s510 with L1d data centred on the experimental data for each wall sensor. Experimental data has been filtered with a 5<sup>th</sup> order Butterworth filter with a 250kHz cutoff.

## B. Shock Tube Wall Static Pressures

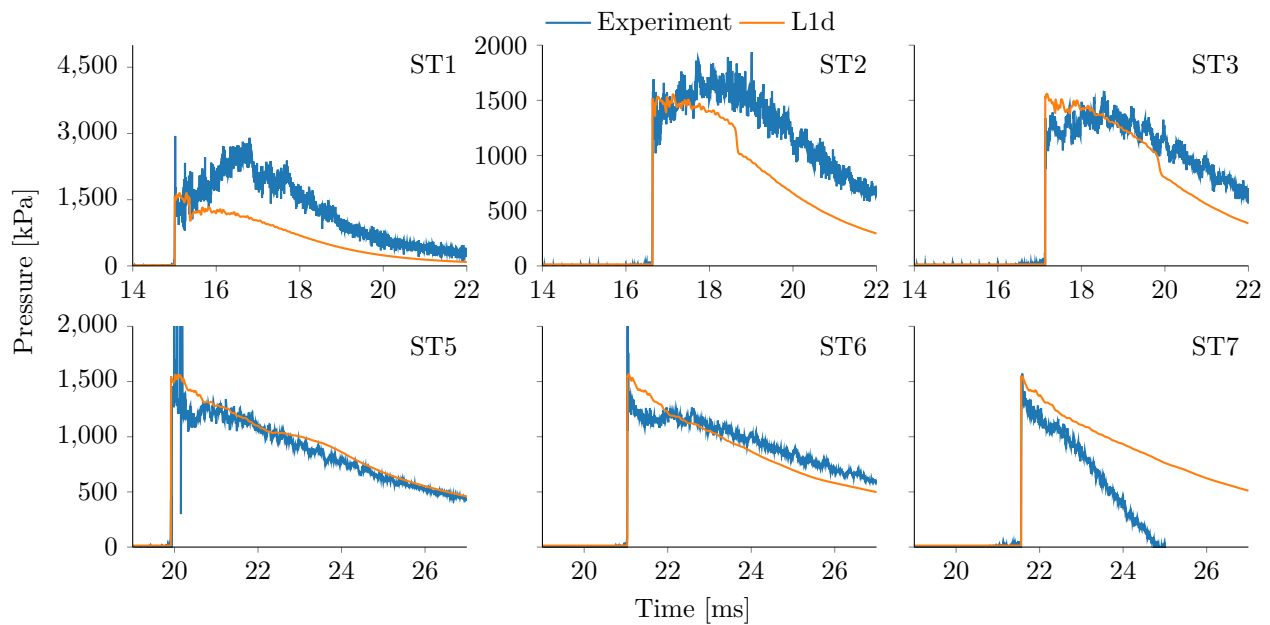


Figure B.4.: Shock tube wall static pressure traces for x3s511 with L1d data centred on the experimental data for each wall sensor. Experimental data has been filtered with a 5<sup>th</sup> order Butterworth filter with a 250kHz cutoff.

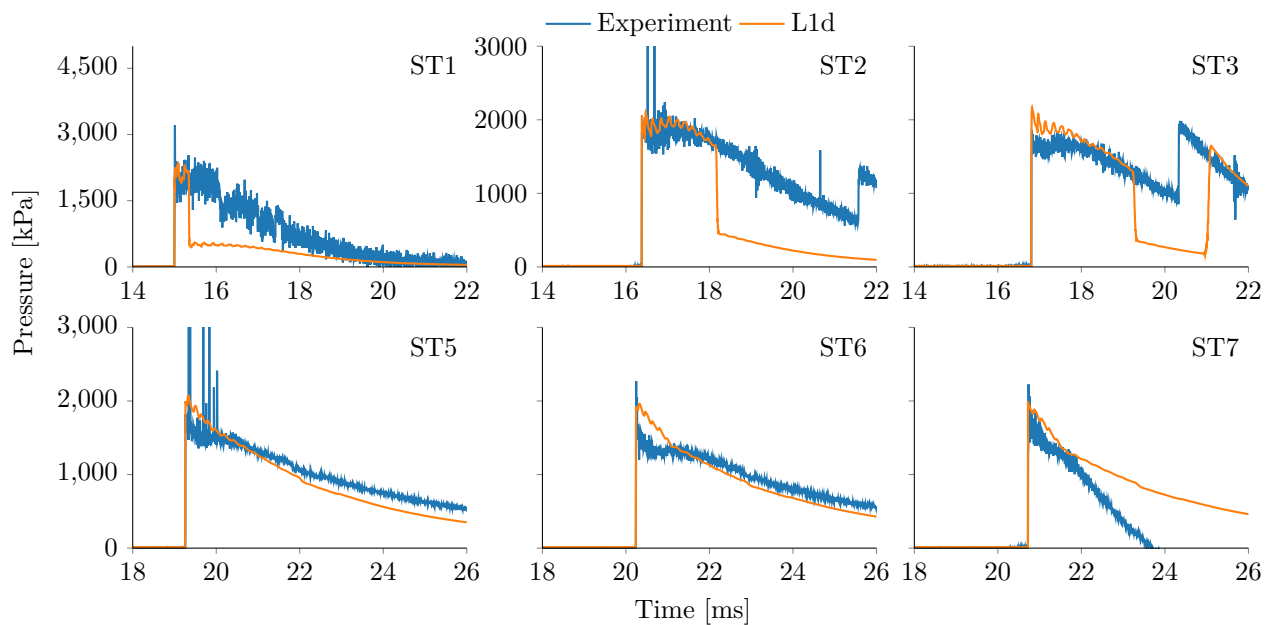


Figure B.5.: Shock tube wall static pressure traces for x3s512 with L1d data centred on the experimental data for each wall sensor. Experimental data has been filtered with a 5<sup>th</sup> order Butterworth filter with a 250kHz cutoff.

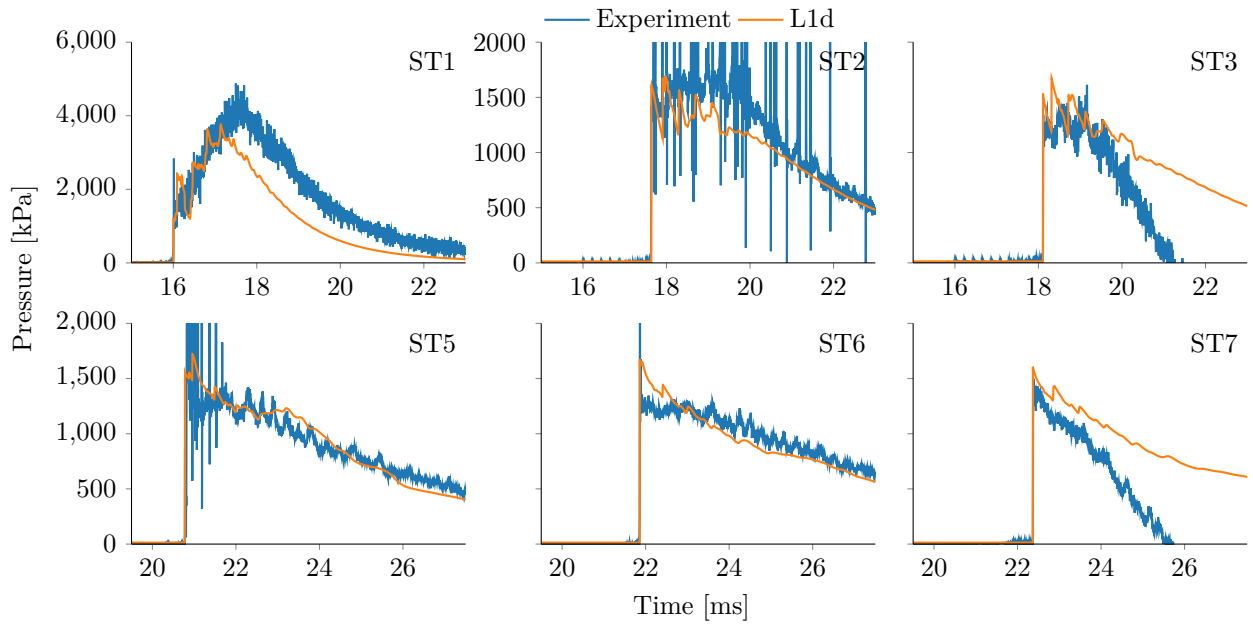


Figure B.6.: Shock tube wall static pressure traces for x3s527 with L1d data centred on the experimental data for each wall sensor. Experimental data has been filtered with a 5<sup>th</sup> order Butterworth filter with a 250kHz cutoff.

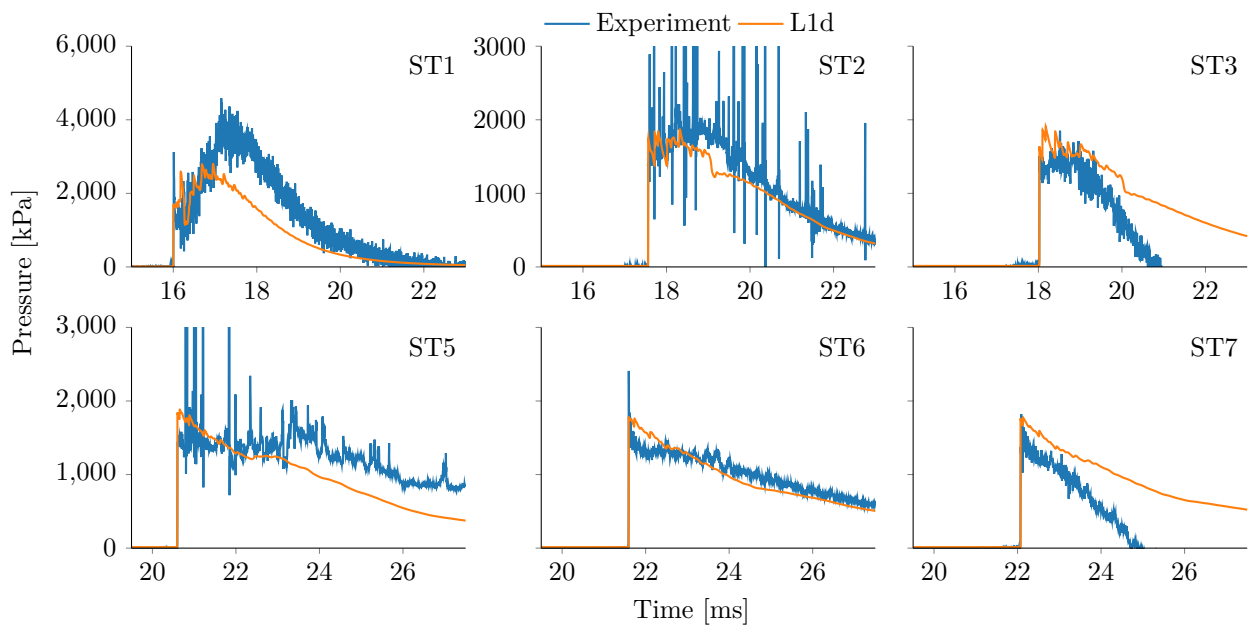


Figure B.7.: Shock tube wall static pressure traces for x3s528 with L1d data centred on the experimental data for each wall sensor. Experimental data has been filtered with a 5<sup>th</sup> order Butterworth filter with a 250kHz cutoff.

## B. Shock Tube Wall Static Pressures

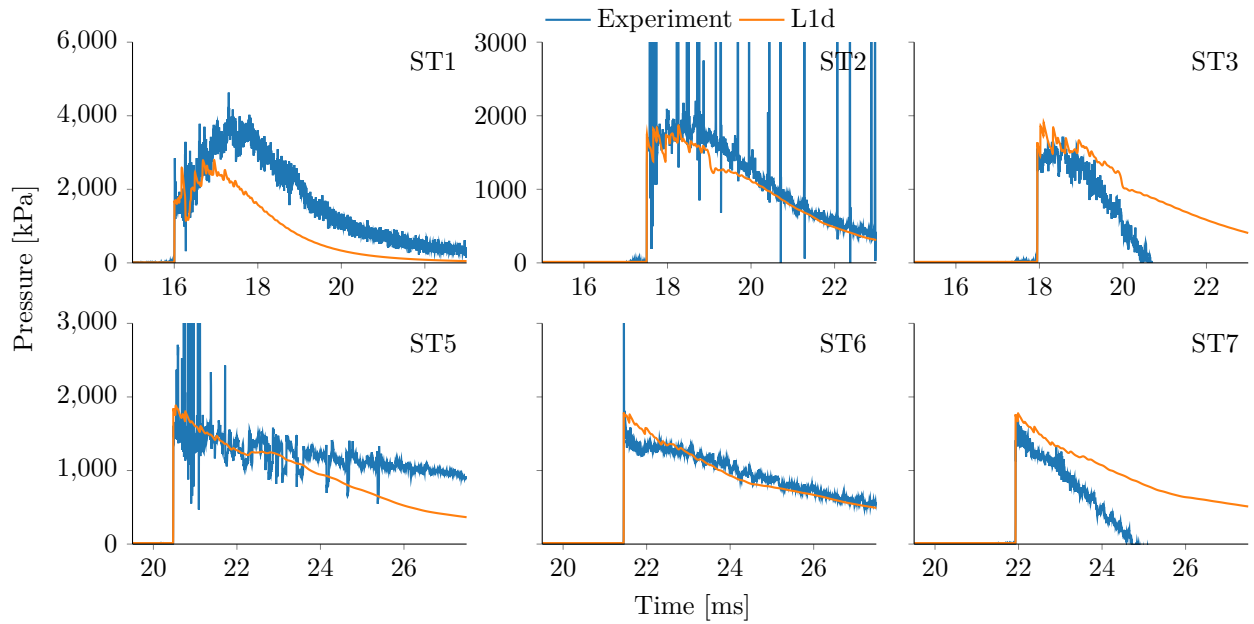


Figure B.8.: Shock tube wall static pressure traces for x3s529 with L1d data centred on the experimental data for each wall sensor. Experimental data has been filtered with a 5<sup>th</sup> order Butterworth filter with a 250kHz cutoff.

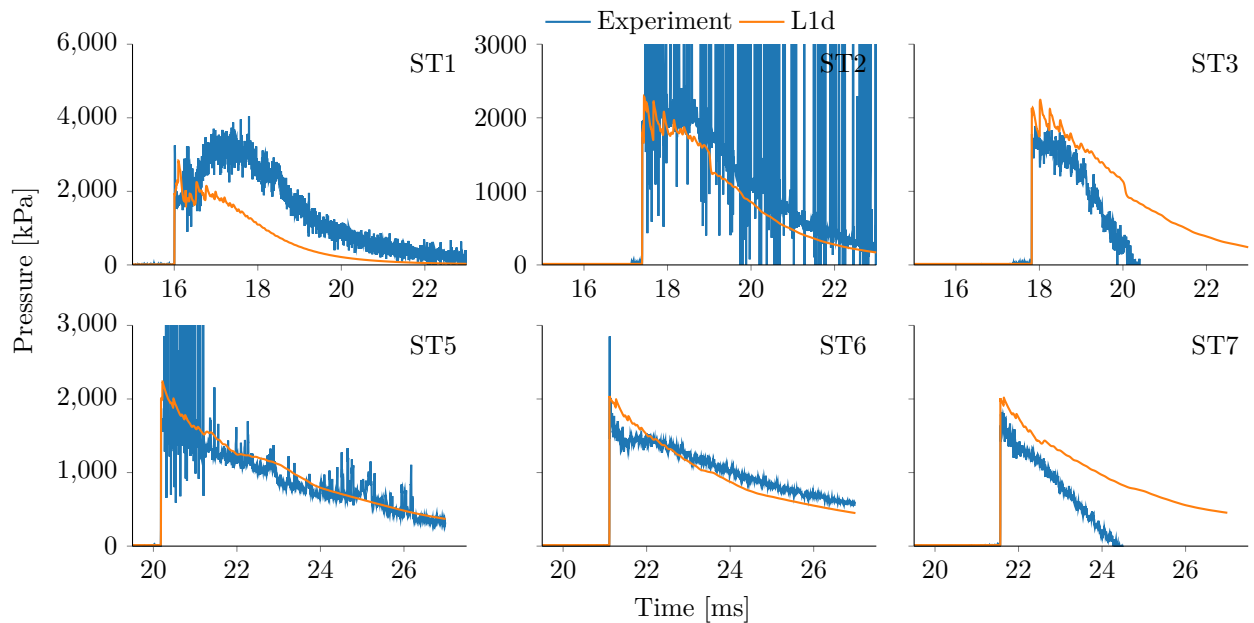


Figure B.9.: Shock tube wall static pressure traces for x3s530 with L1d data centred on the experimental data for each wall sensor. Experimental data has been filtered with a 5<sup>th</sup> order Butterworth filter with a 250kHz cutoff.

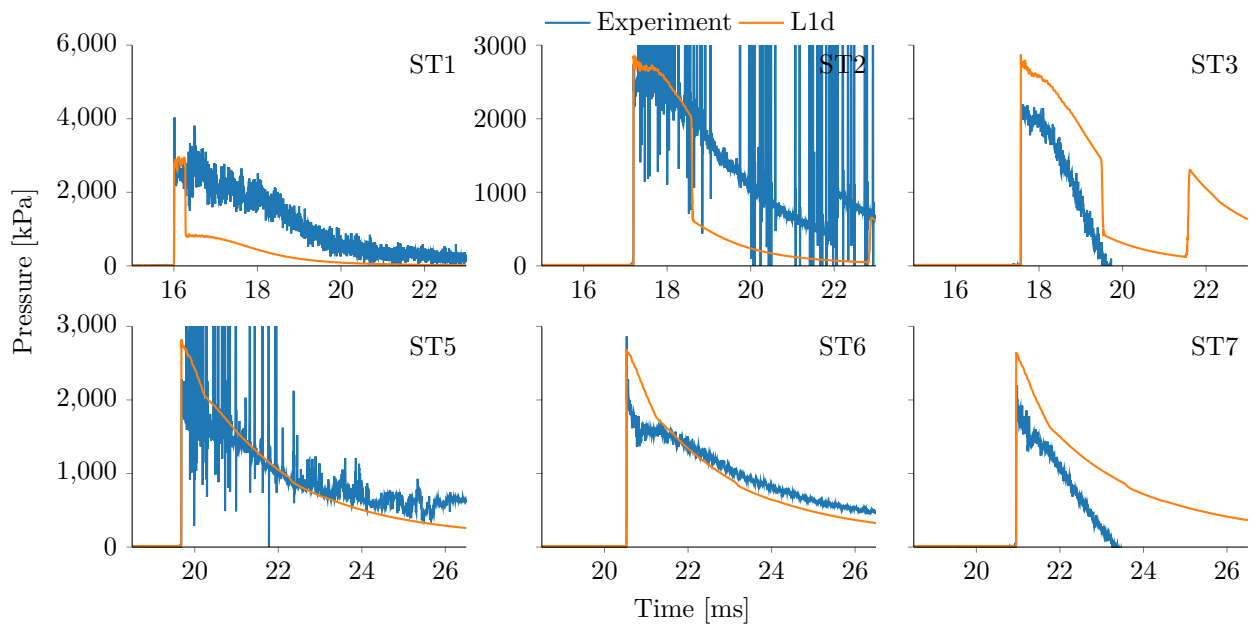


Figure B.10.: Shock tube wall static pressure traces for x3s531 with L1d data centred on the experimental data for each wall sensor. Experimental data has been filtered with a 5<sup>th</sup> order Butterworth filter with a 250kHz cutoff.

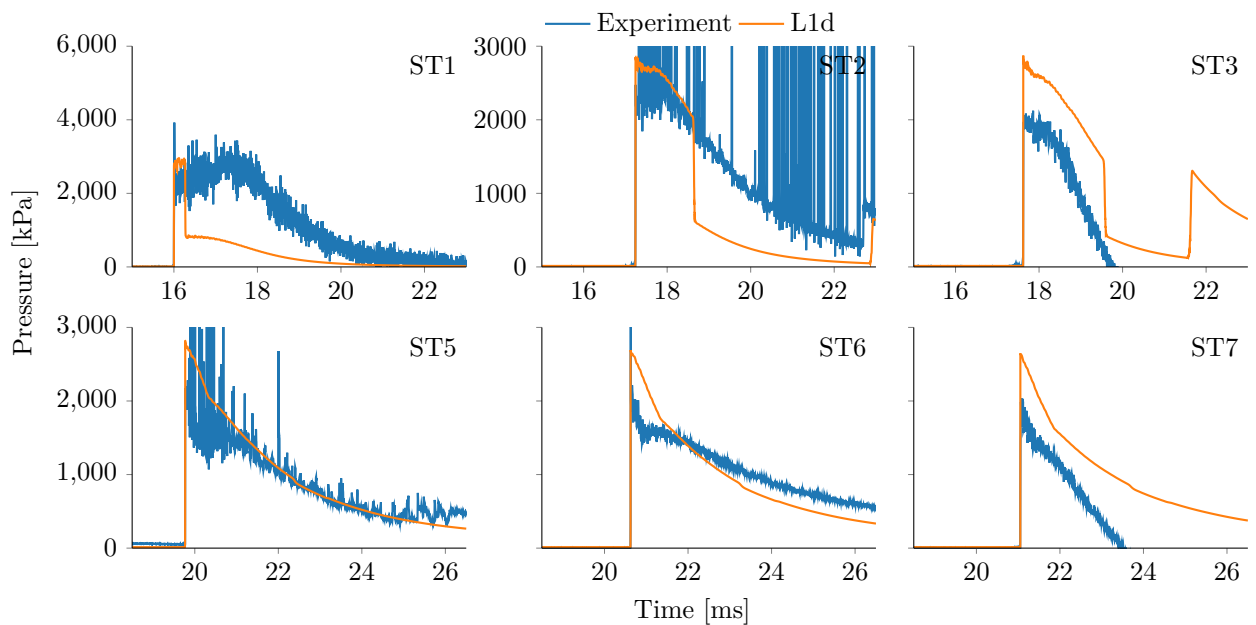


Figure B.11.: Shock tube wall static pressure traces for x3s532 with L1d data centred on the experimental data for each wall sensor. Experimental data has been filtered with a 5<sup>th</sup> order Butterworth filter with a 250kHz cutoff.

# C

---

## Acceleration Tube Wall Static Pressures

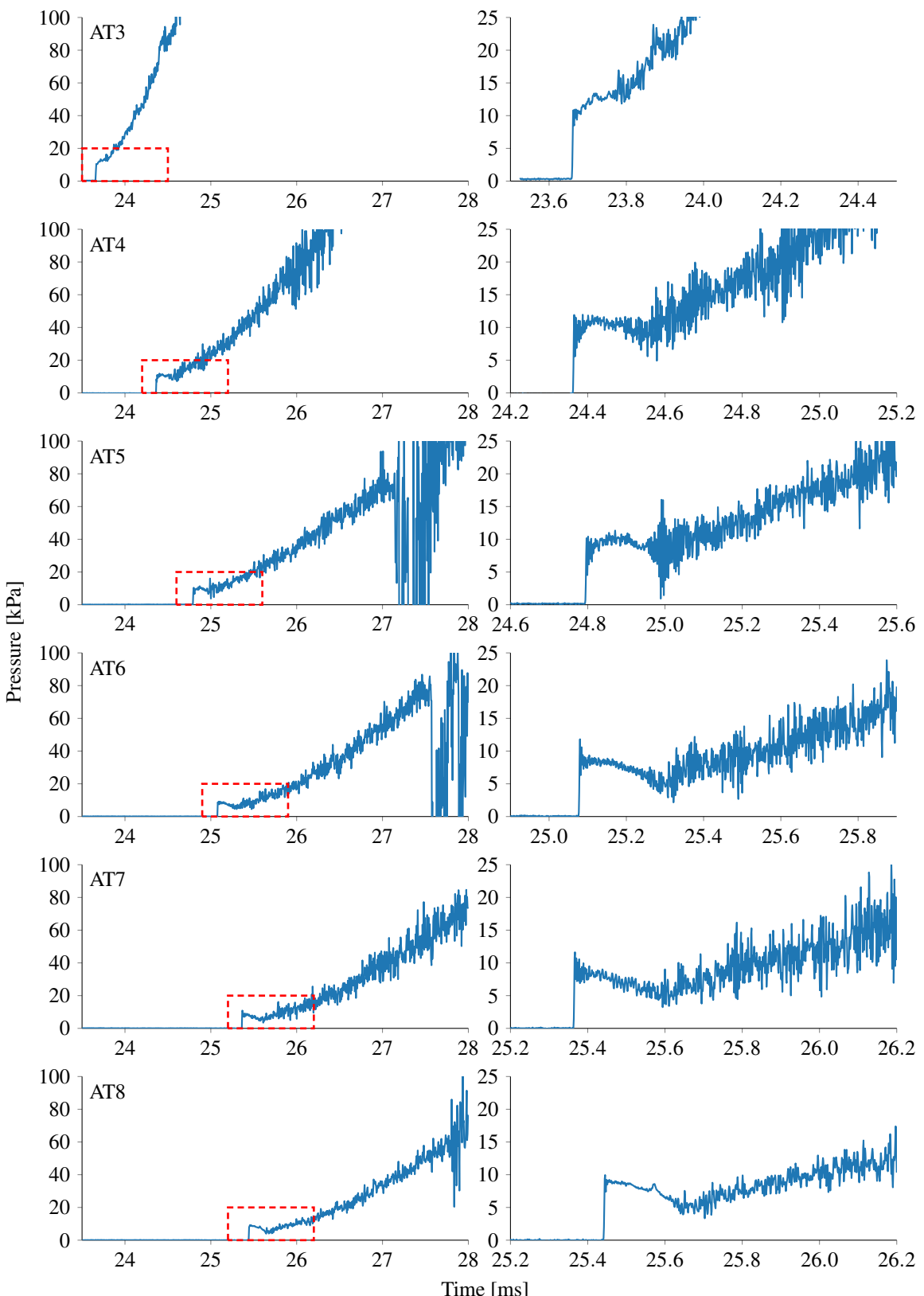


Figure C.1.: Acceleration tube wall static pressure traces for x3s508. Data is filtered with a 5<sup>th</sup> order Butterworth filter with a 250kHz cutoff.

### C. Acceleration Tube Wall Static Pressures

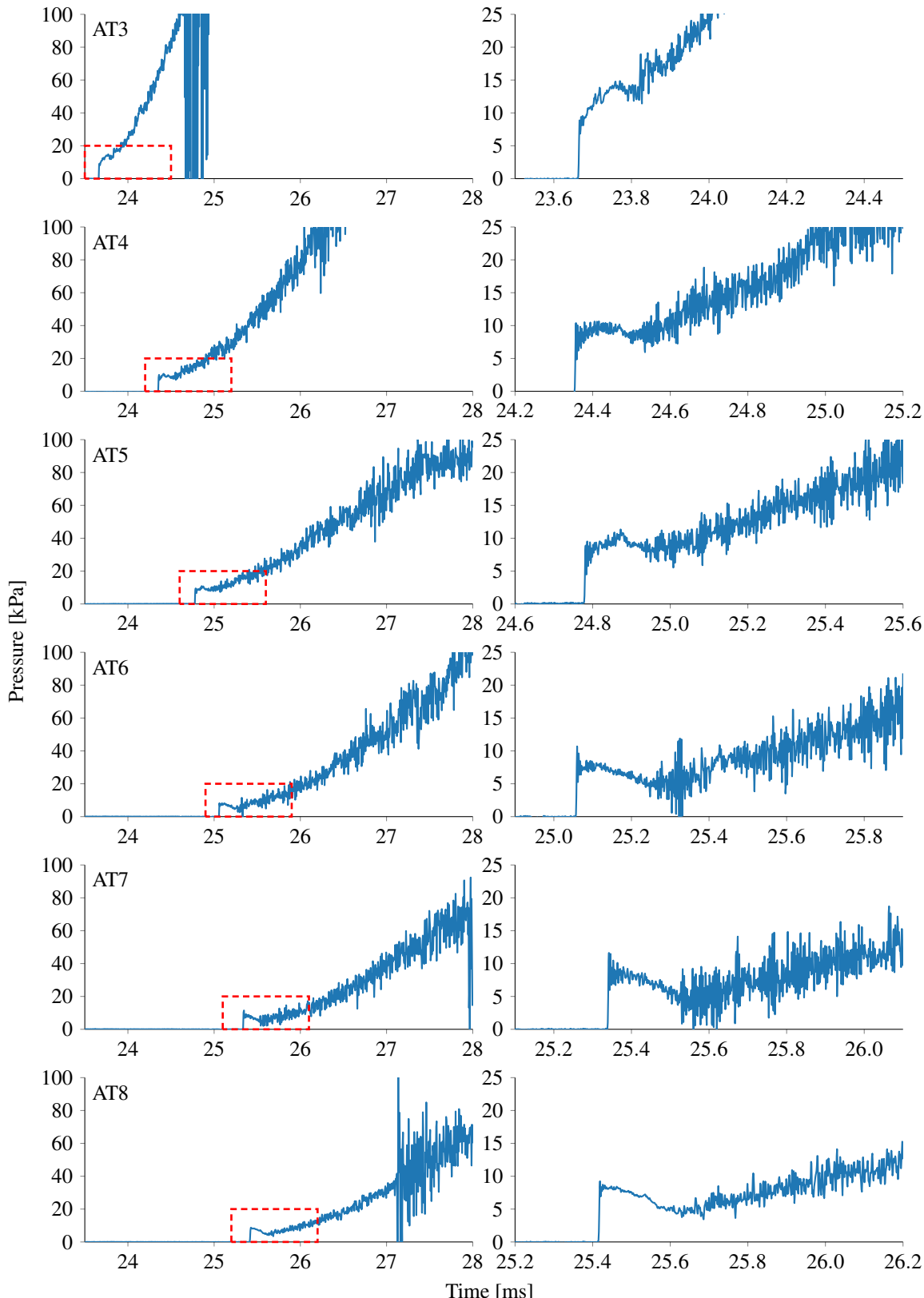


Figure C.2.: Acceleration tube wall static pressure traces for x3s509. Data is filtered with a 5<sup>th</sup> order Butterworth filter with a 250kHz cutoff.

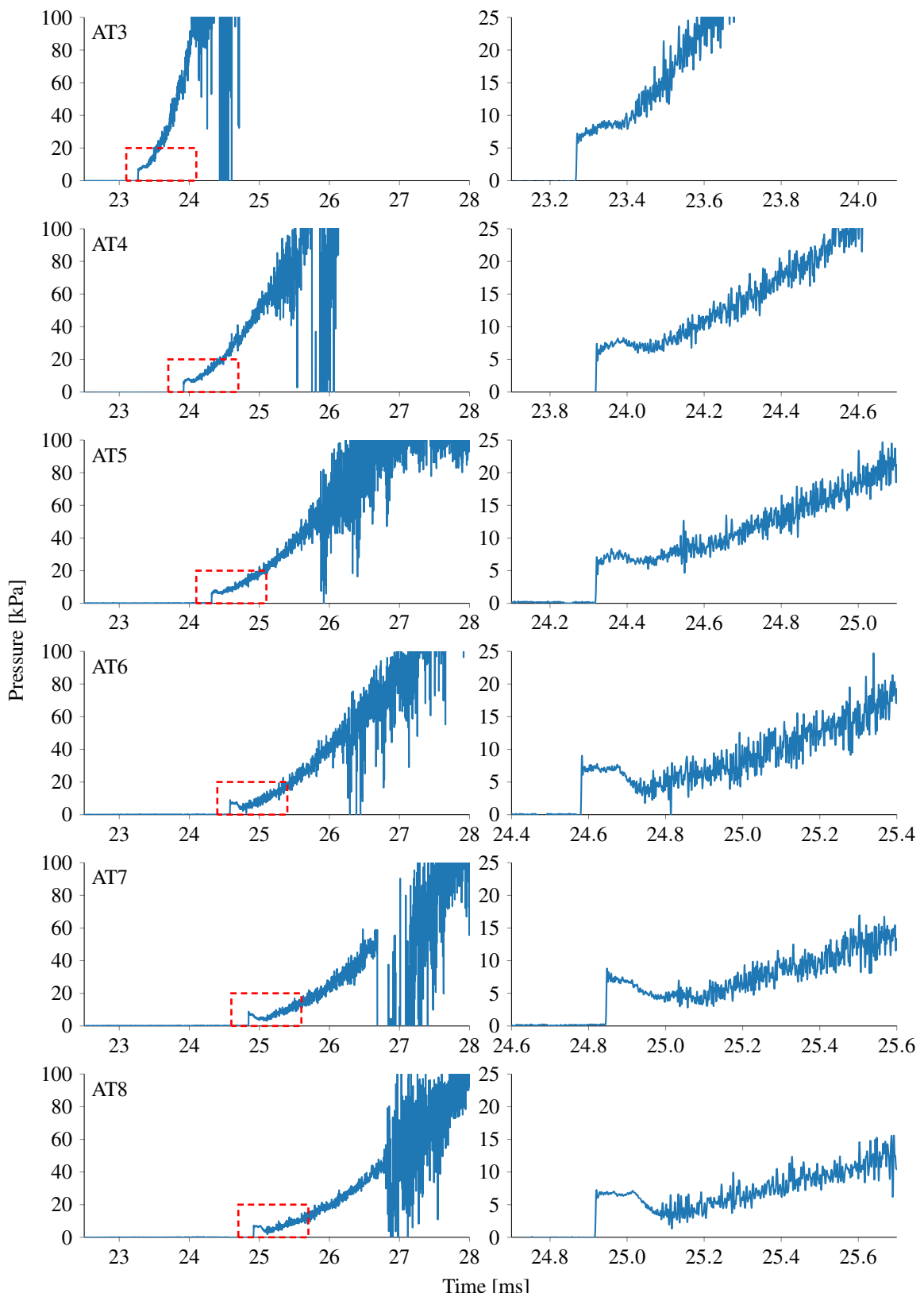


Figure C.3.: Acceleration tube wall static pressure traces for x3s511. Data is filtered with a 5<sup>th</sup> order Butterworth filter with a 250kHz cutoff.

### C. Acceleration Tube Wall Static Pressures

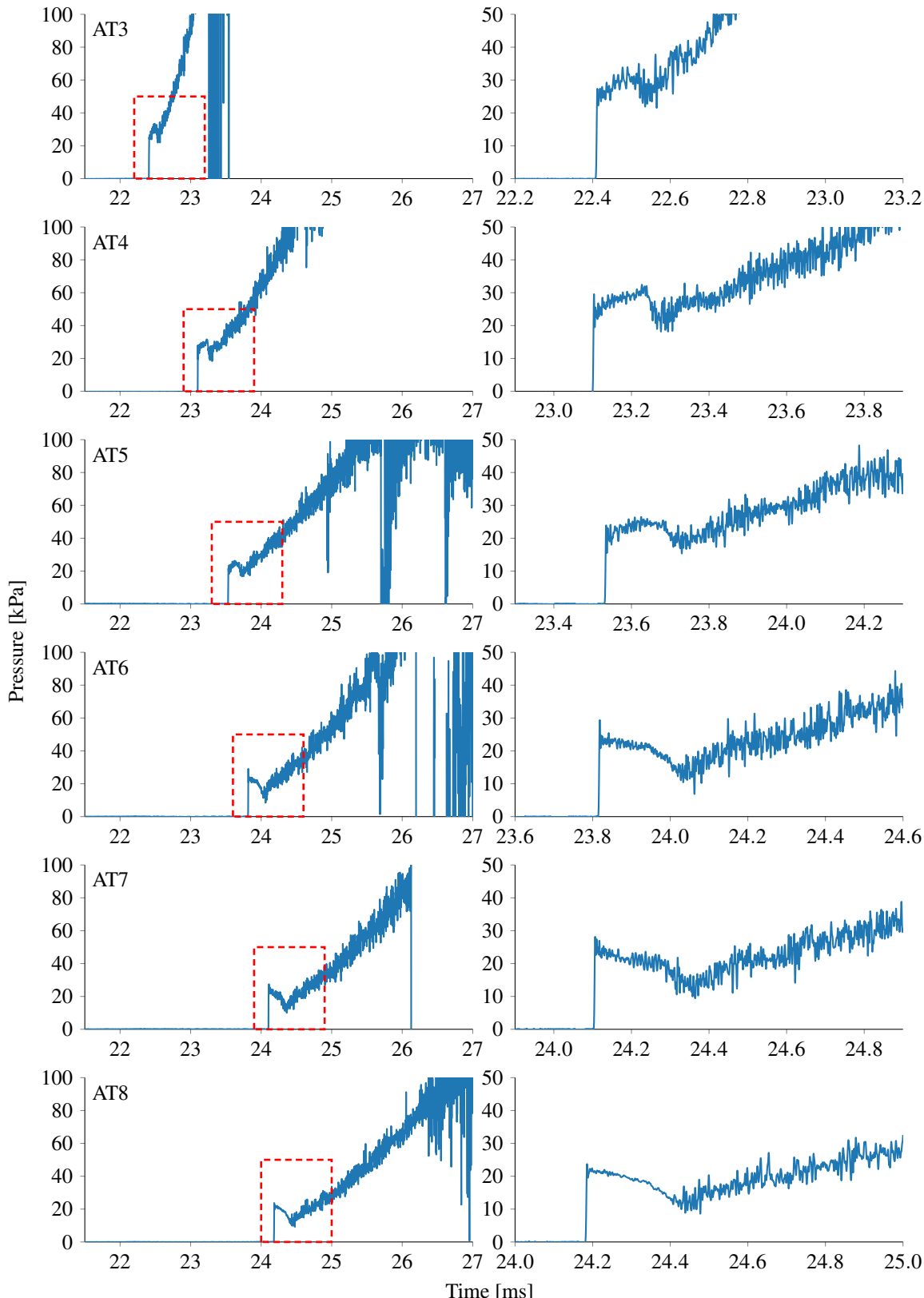


Figure C.4.: Acceleration tube wall static pressure traces for x3s512. Data is filtered with a 5<sup>th</sup> order Butterworth filter with a 250kHz cutoff.

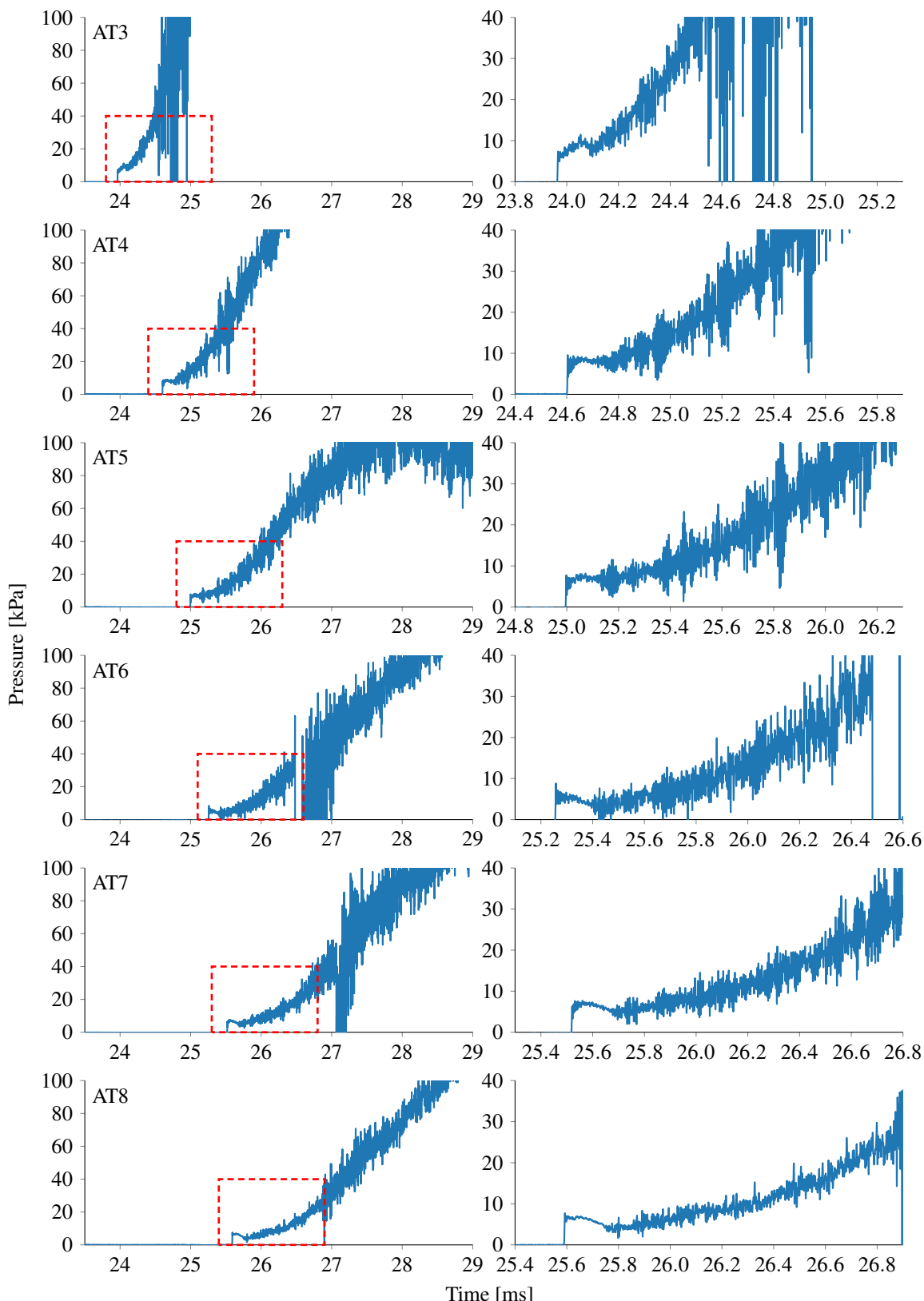


Figure C.5.: Acceleration tube wall static pressure traces for x3s527. Data is filtered with a 5<sup>th</sup> order Butterworth filter with a 250kHz cutoff.

### C. Acceleration Tube Wall Static Pressures

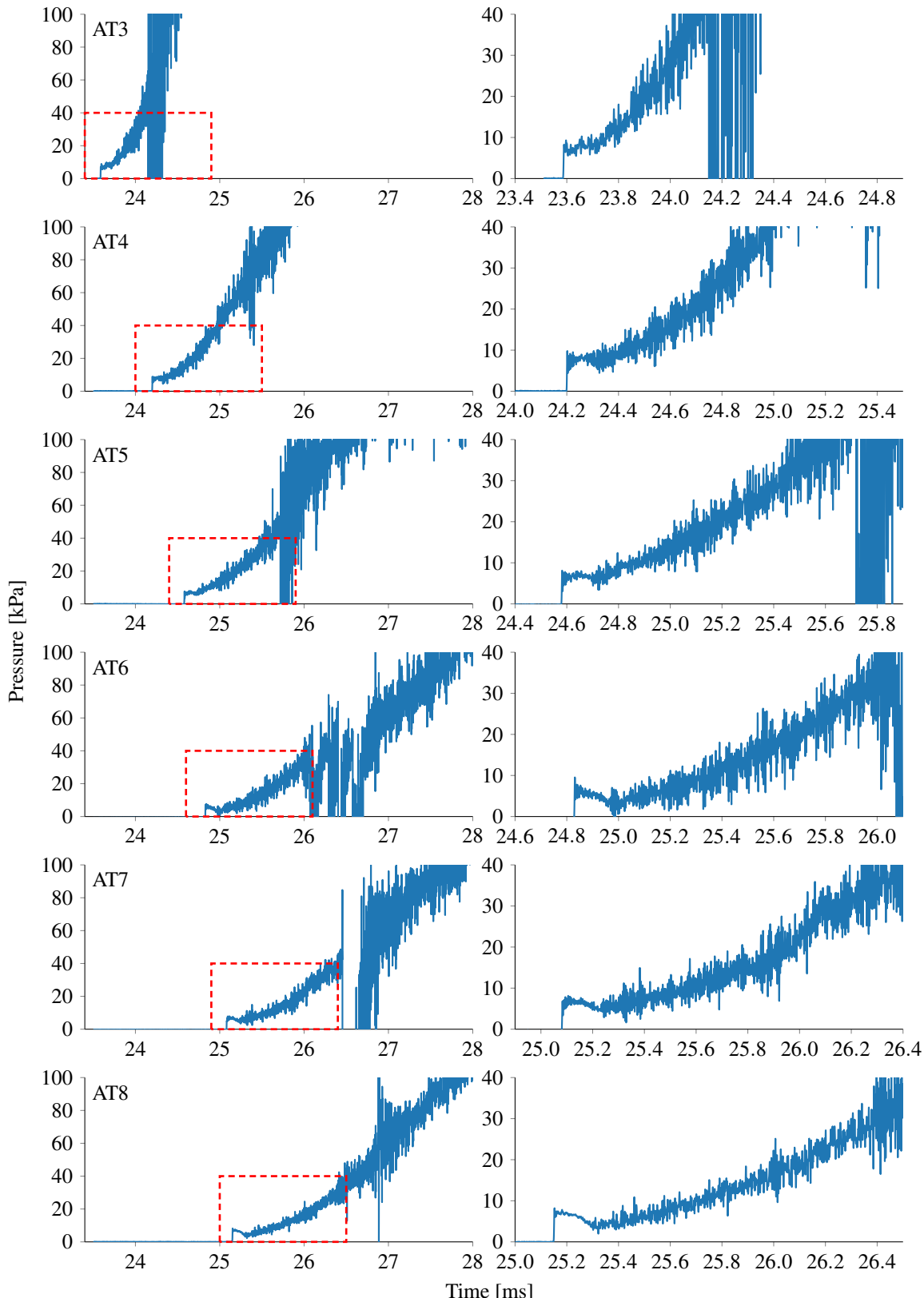


Figure C.6.: Acceleration tube wall static pressure traces for x3s528. Data is filtered with a 5<sup>th</sup> order Butterworth filter with a 250kHz cutoff.

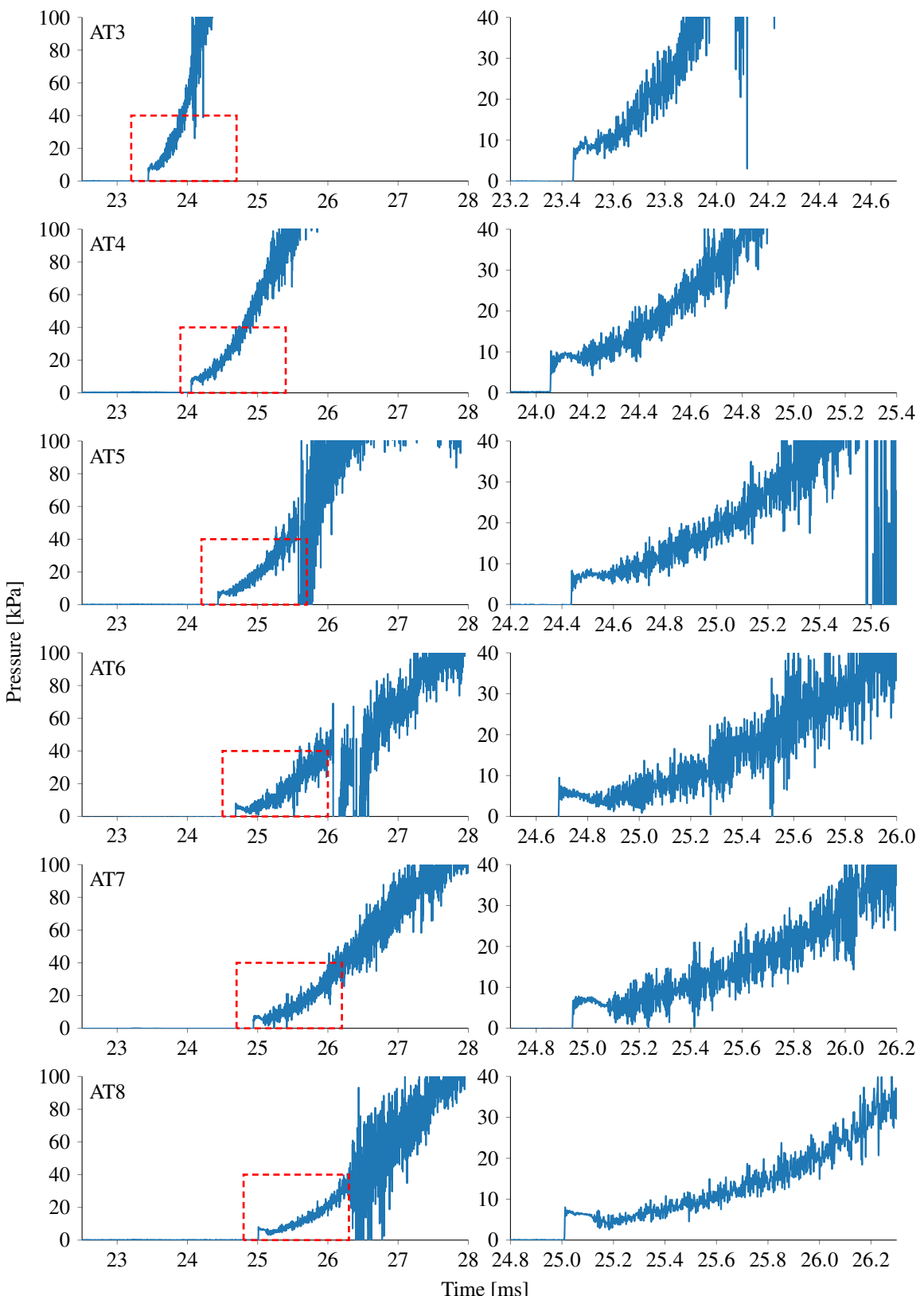


Figure C.7.: Acceleration tube wall static pressure traces for x3s529. Data is filtered with a 5<sup>th</sup> order Butterworth filter with a 250kHz cutoff.

### C. Acceleration Tube Wall Static Pressures

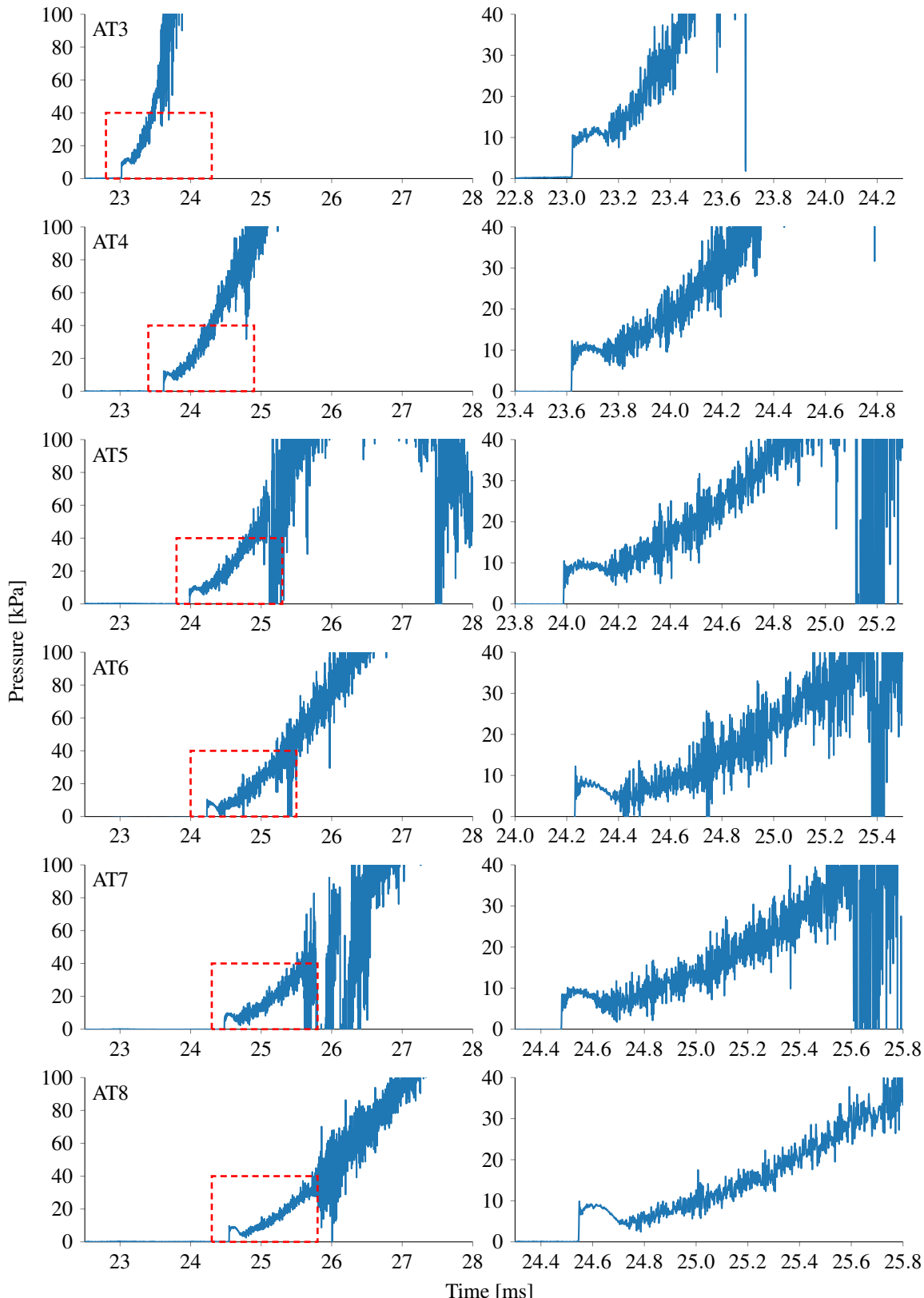


Figure C.8.: Acceleration tube wall static pressure traces for x3s530. Data is filtered with a 5<sup>th</sup> order Butterworth filter with a 250kHz cutoff.

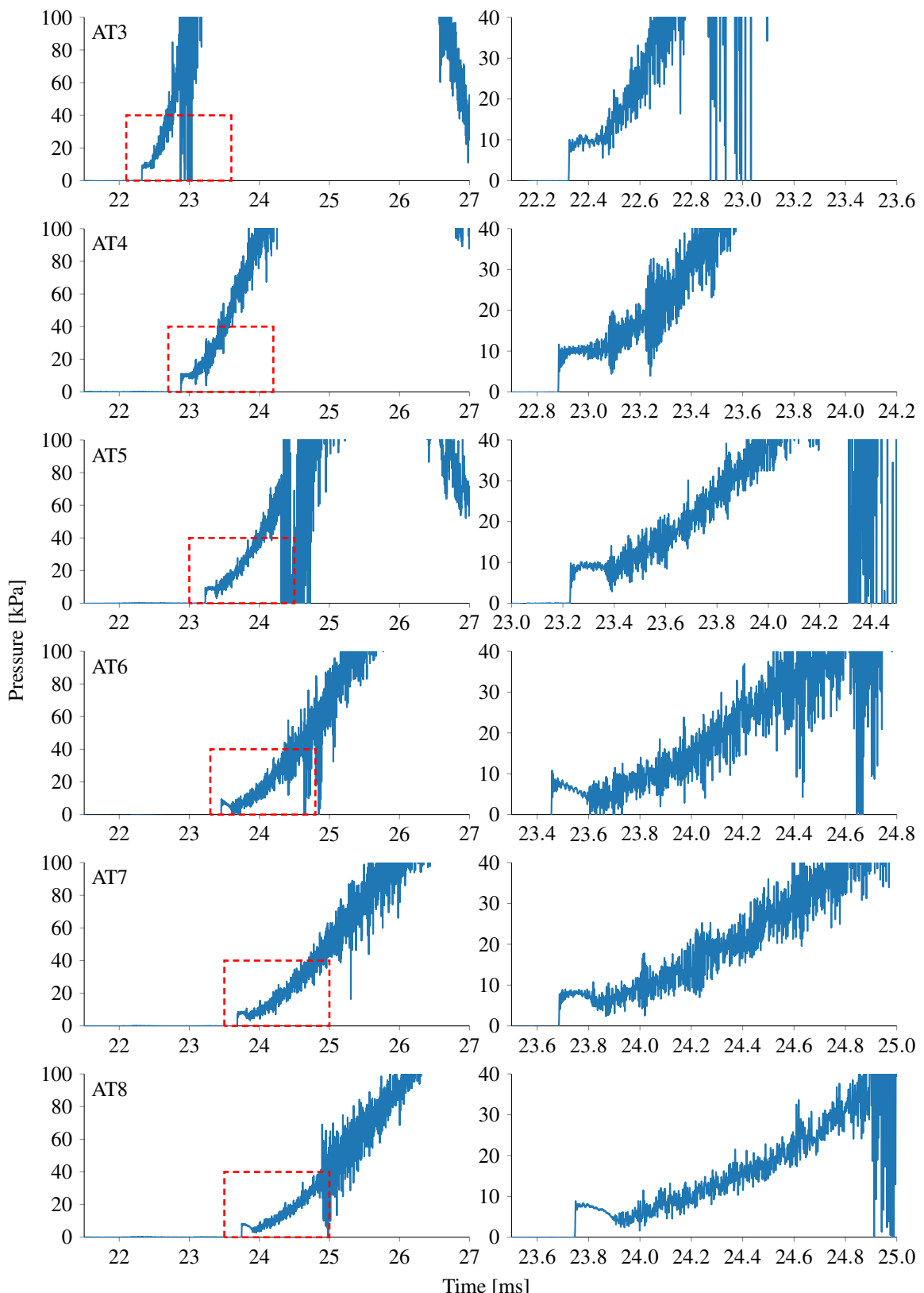


Figure C.9.: Acceleration tube wall static pressure traces for x3s531. Data is filtered with a 5<sup>th</sup> order Butterworth filter with a 250kHz cutoff.

### C. Acceleration Tube Wall Static Pressures

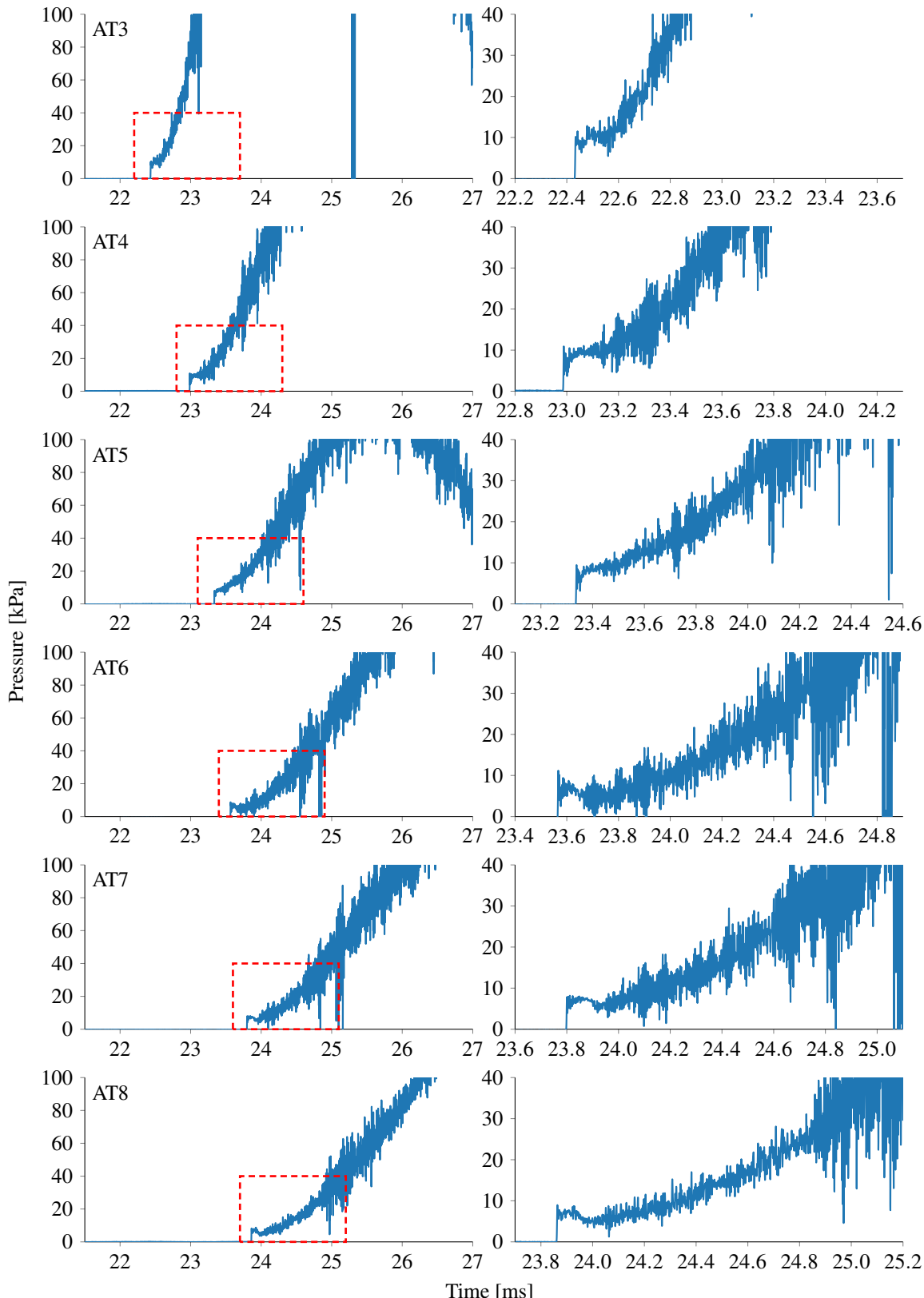


Figure C.10.: Acceleration tube wall static pressure traces for x3s532. Data is filtered with a 5<sup>th</sup> order Butterworth filter with a 250kHz cutoff.

# D

---

## Spectral Line Comparisons

This appendix presents all the spectral data taken along the stagnation line for both the 1:5 and full-scale model. An optical filter was used for each experiment to remove second order effects arising at the diffraction grating. For measurements taken over the wavelength region 560–700nm, a 550nm longpass filter was used, similarly for the wavelength region 380–500nm and 315–700nm bandpass filter was used. The timing of the spectral images is shown at the top of each figure, with the frames presented on each page identified by the darker colour and referenced to the timing of shots x3s668 and x3s670, with the pressure measured after a conical shock multiplied by a factor of 10 for visualisation. It was found that the timing has an error of  $\pm 7.5\mu\text{s}$  which is the variation in time the flow took to travel from N6 (last wall static pressure sensor in the nozzle) to the Pitot rake at the exit of the nozzle. A list of figures in this appendix is presented in table D.1.

Table D.1.: Descriptions of figures in this appendix.

Figure Label	Description
Figure D.1	1:5 scale model, 560–700nm, <i>line a</i> from fig. 5.37
Figure D.2	1:5 scale model, 560–700nm, <i>line b</i> from fig. 5.37
Figure D.3	1:5 scale model, 380–500nm, <i>line a</i> from fig. 5.37
Figure D.4	1:5 scale model, 380–500nm, <i>line b</i> from fig. 5.37
Figure D.5	full-scale scale model, 560–700nm, <i>line a</i> from fig. 5.38
Figure D.6	full-scale scale model, 560–700nm, <i>line b</i> from fig. 5.38
Figure D.7	full-scale scale model, 380–500nm, <i>line a</i> from fig. 5.38
Figure D.8	full-scale scale model, 380–500nm, <i>line b</i> from fig. 5.38

#### D. Spectral Line Comparisons

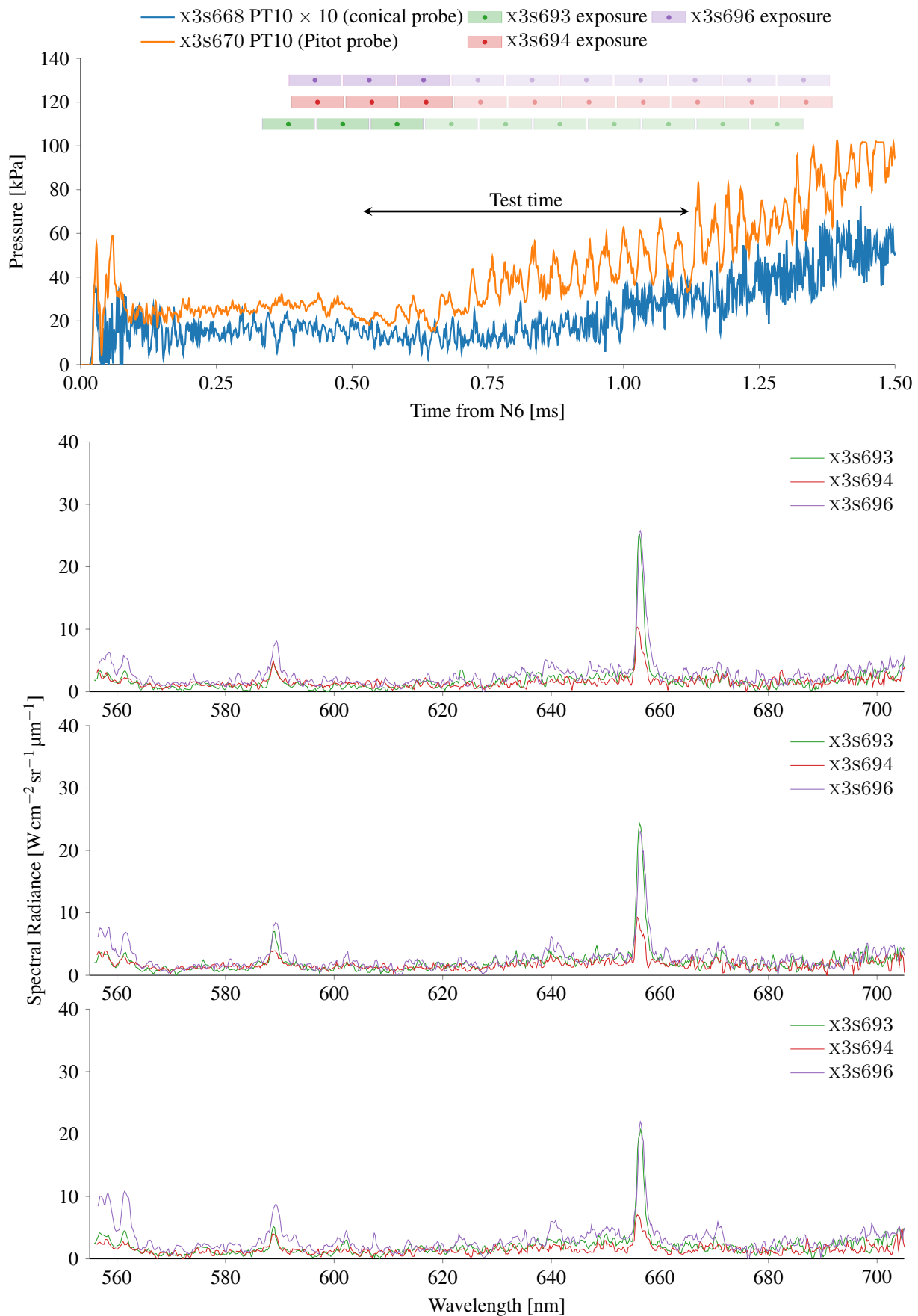


Figure D.1.: Comparison of shots x3s693, x3s694 and x3s696 line *a* for a wavelength region of 560–700nm.

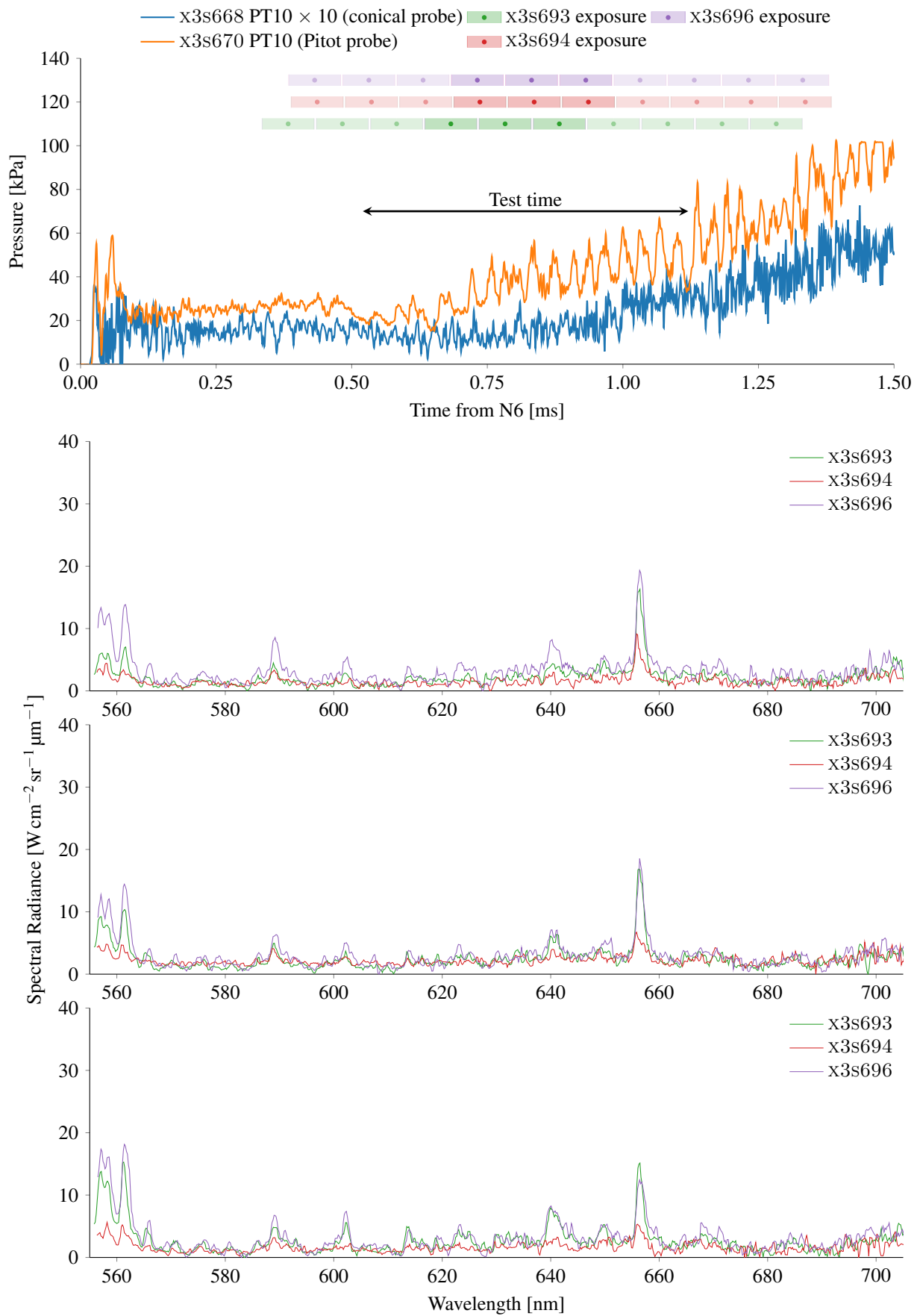


Figure D.1.: Comparison of shots x3s693, x3s694 and x3s696 line *a* for a wavelength region of 560–700nm.

#### D. Spectral Line Comparisons

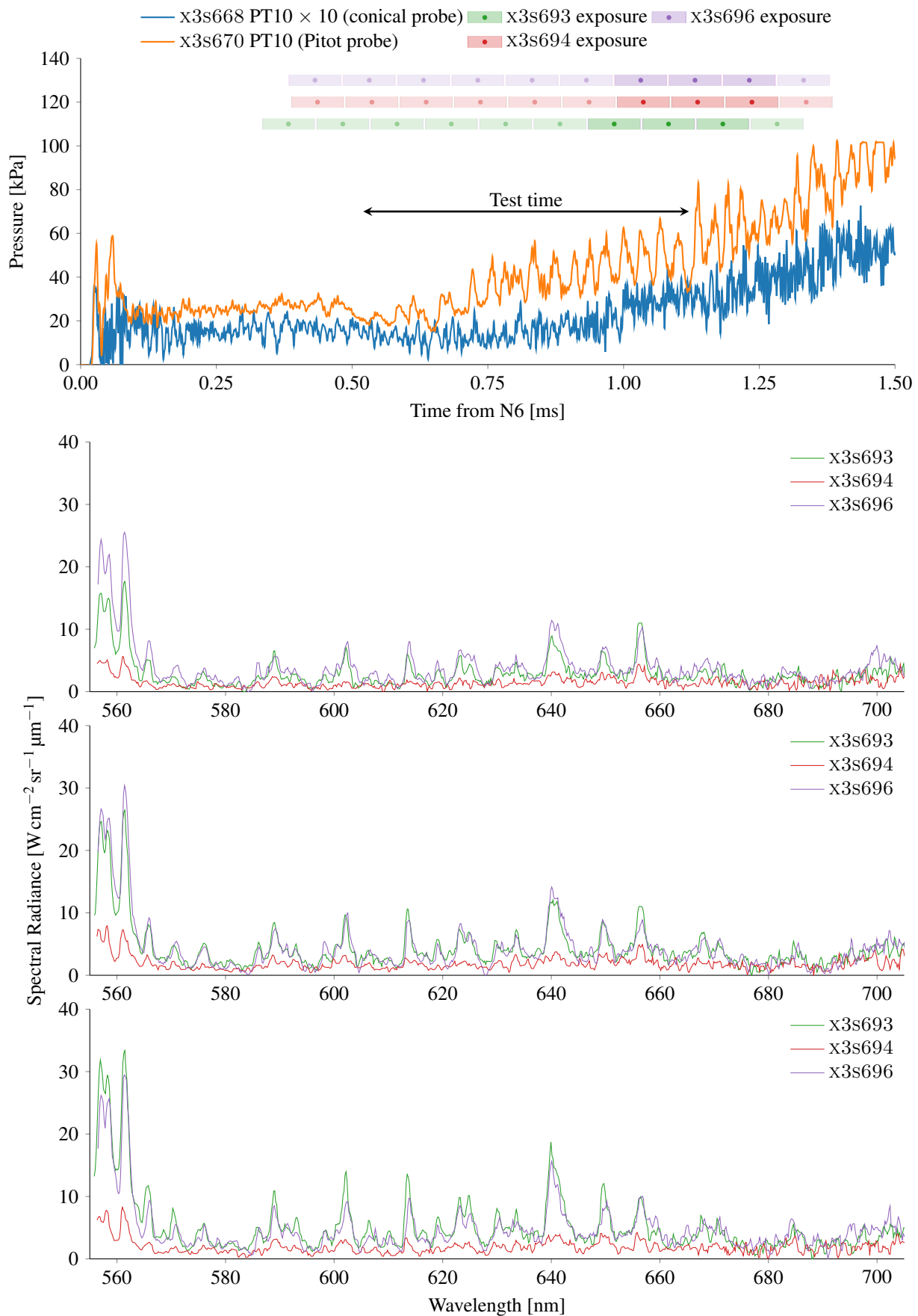


Figure D.1.: Comparison of shots x3s693, x3s694 and x3s696 line *a* for a wavelength region of 560–700nm.

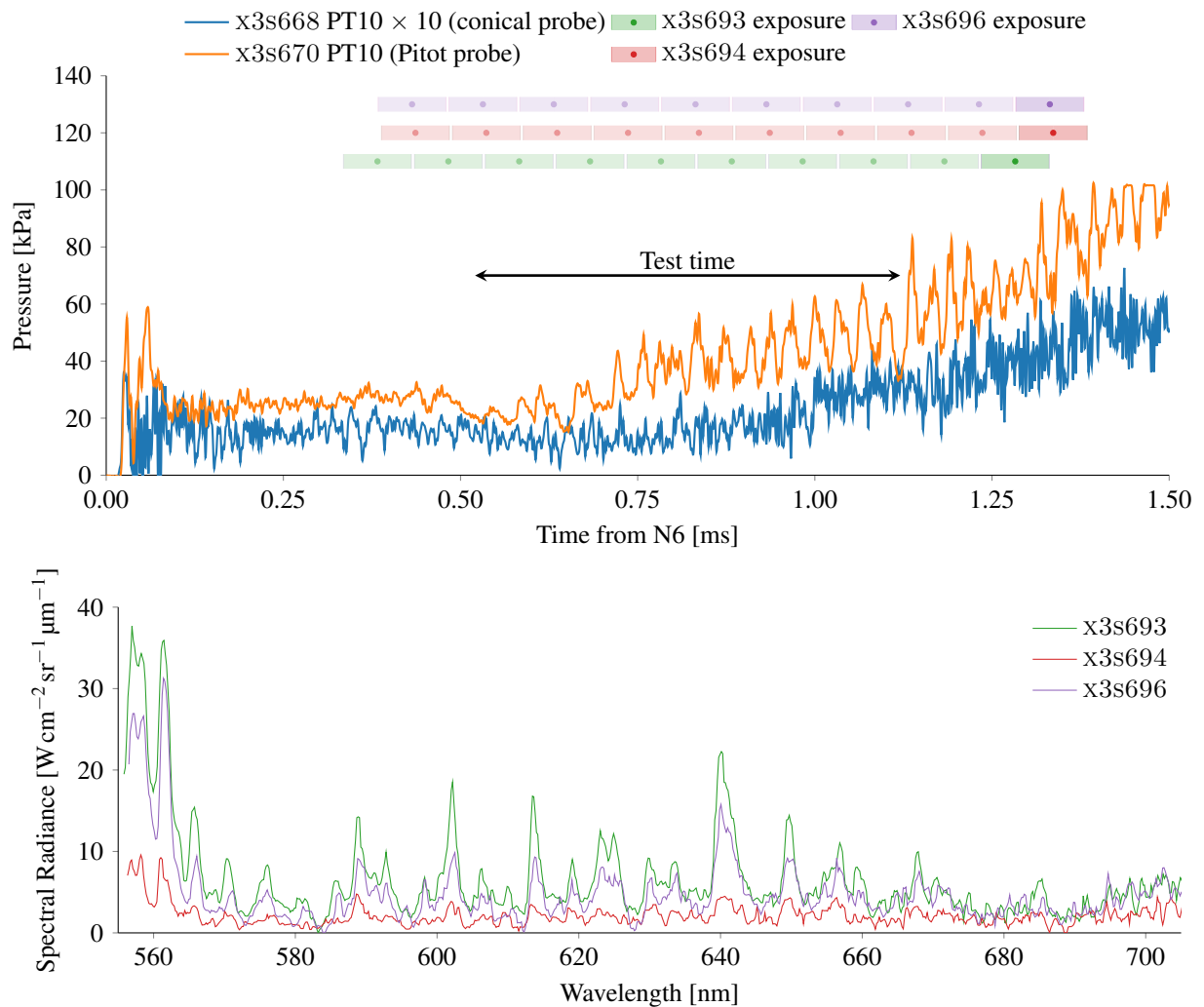


Figure D.1.: Comparison of shots x3s693, x3s694 and x3s696 line *a* for a wavelength region of 560–700nm.

#### D. Spectral Line Comparisons

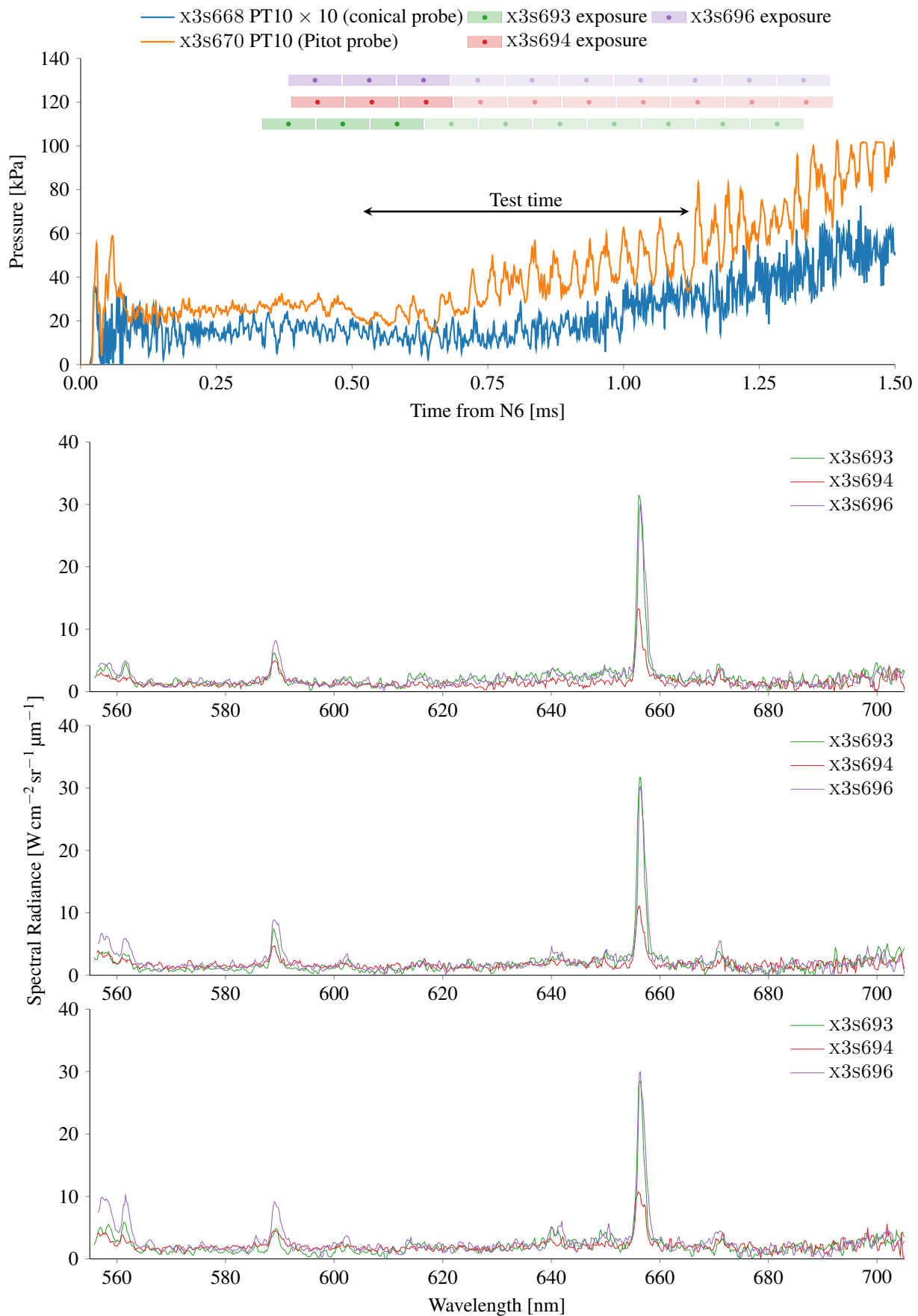


Figure D.2.: Comparison of shots x3s693, x3s694 and x3s696 line *b* for a wavelength region of 560–700nm.

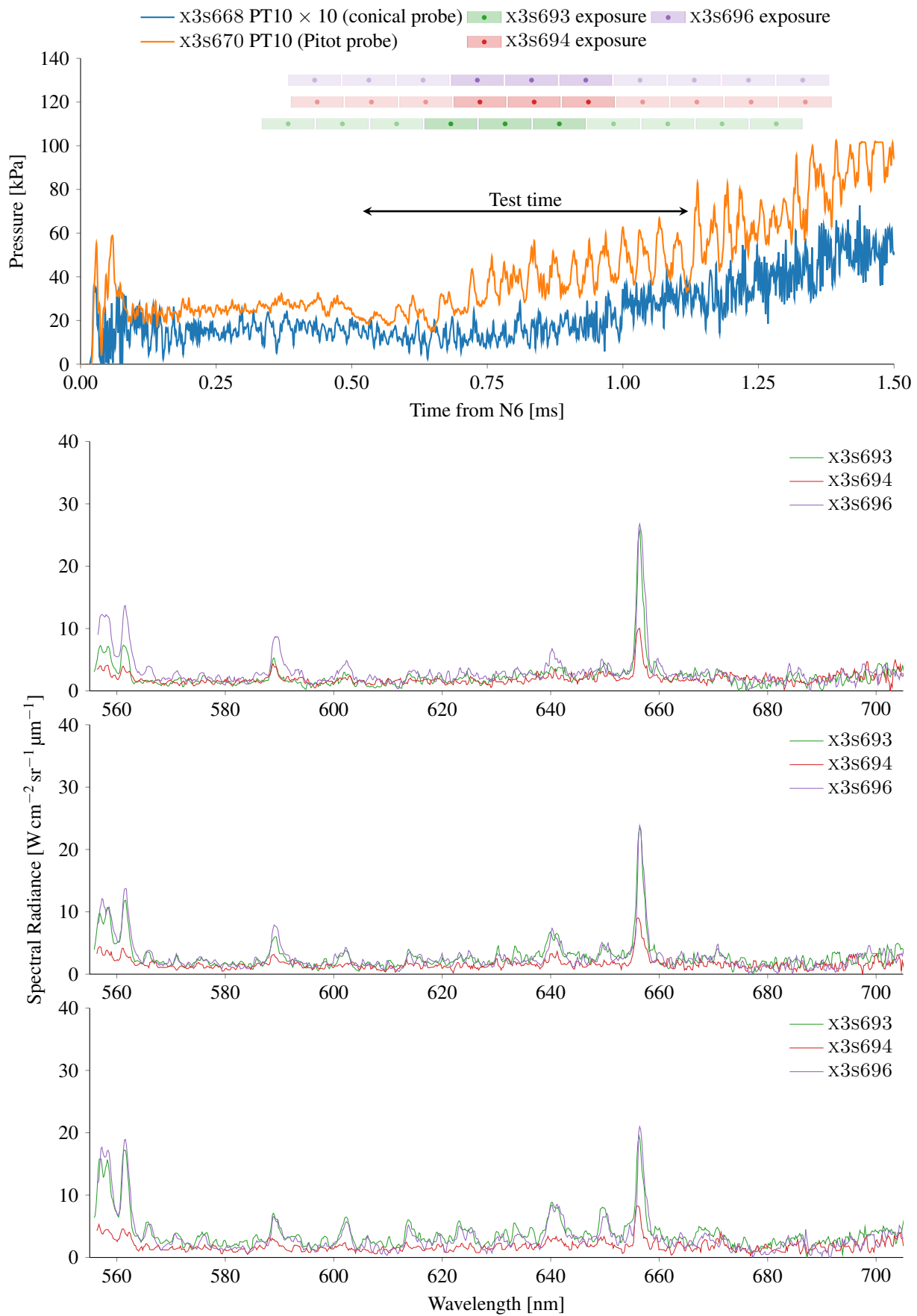


Figure D.2.: Comparison of shots x3s693, x3s694 and x3s696 line *b* for a wavelength region of 560–700nm.

#### D. Spectral Line Comparisons

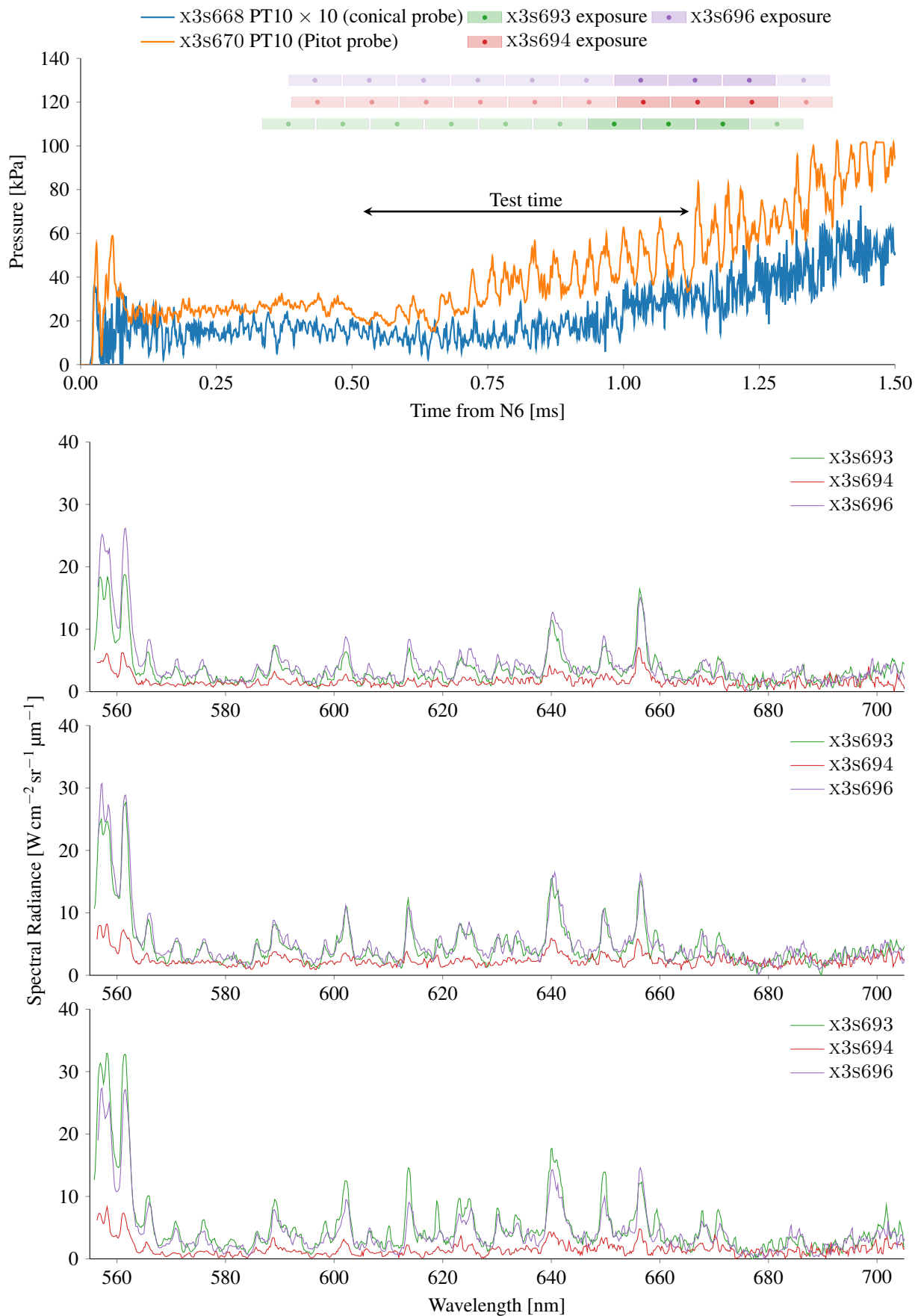


Figure D.2.: Comparison of shots x3s693, x3s694 and x3s696 line *b* for a wavelength region of 560–700nm.

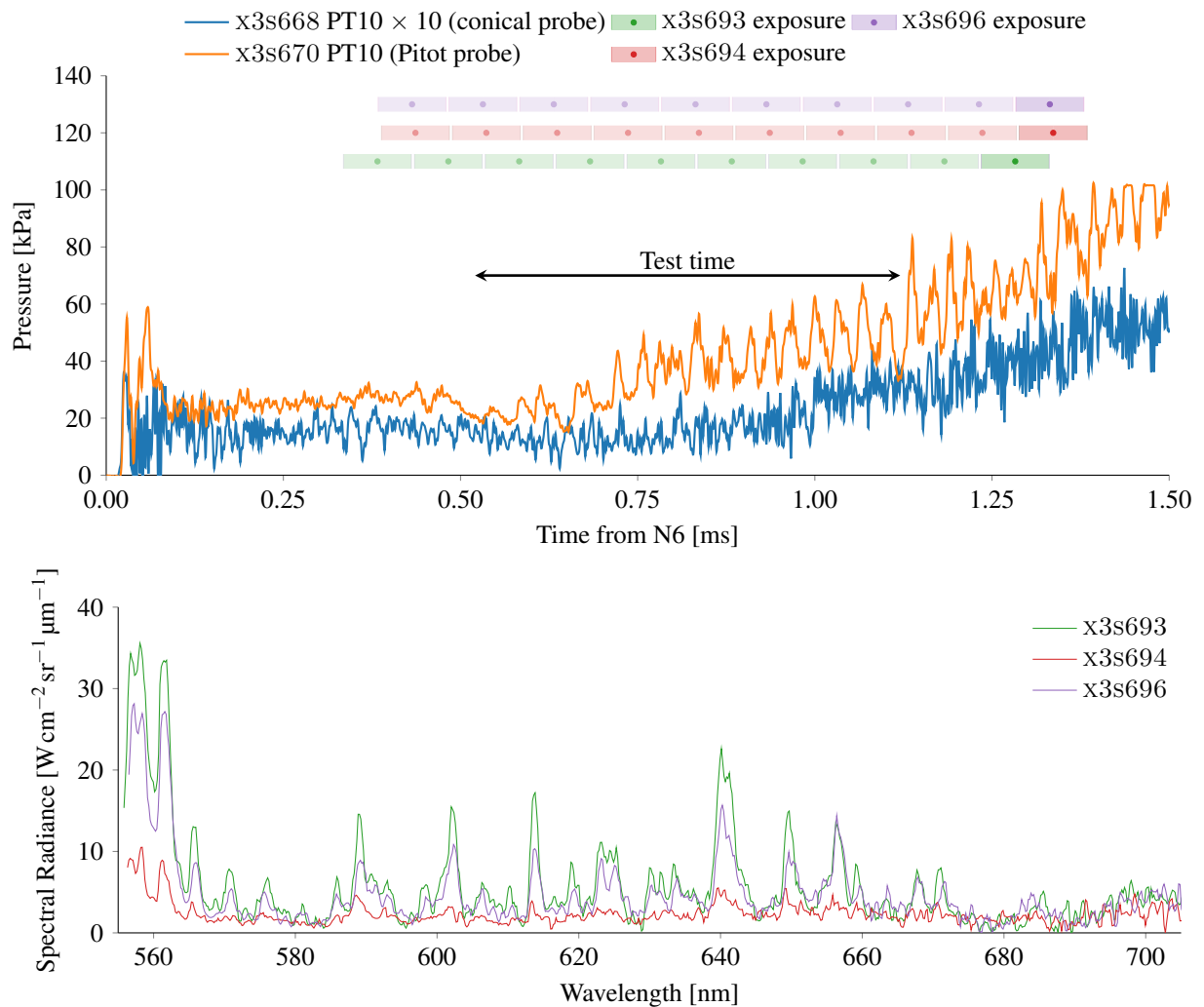


Figure D.2.: Comparison of shots x3s693, x3s694 and x3s696 line *b* for a wavelength region of 560–700nm.

#### D. Spectral Line Comparisons

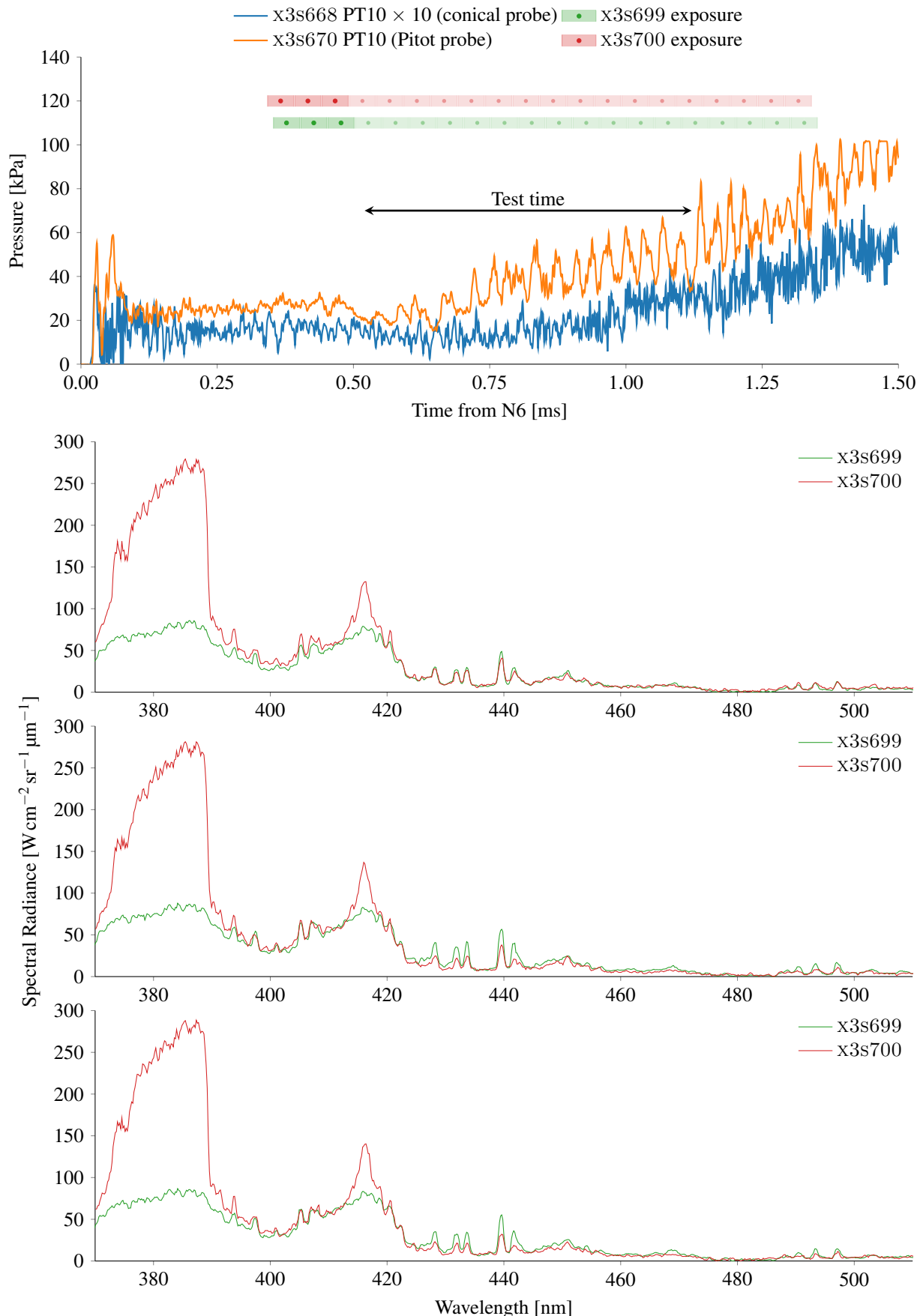


Figure D.3.: Comparison of shots x3s699 and x3s700 line *a* for a wavelength region of 380–500nm.

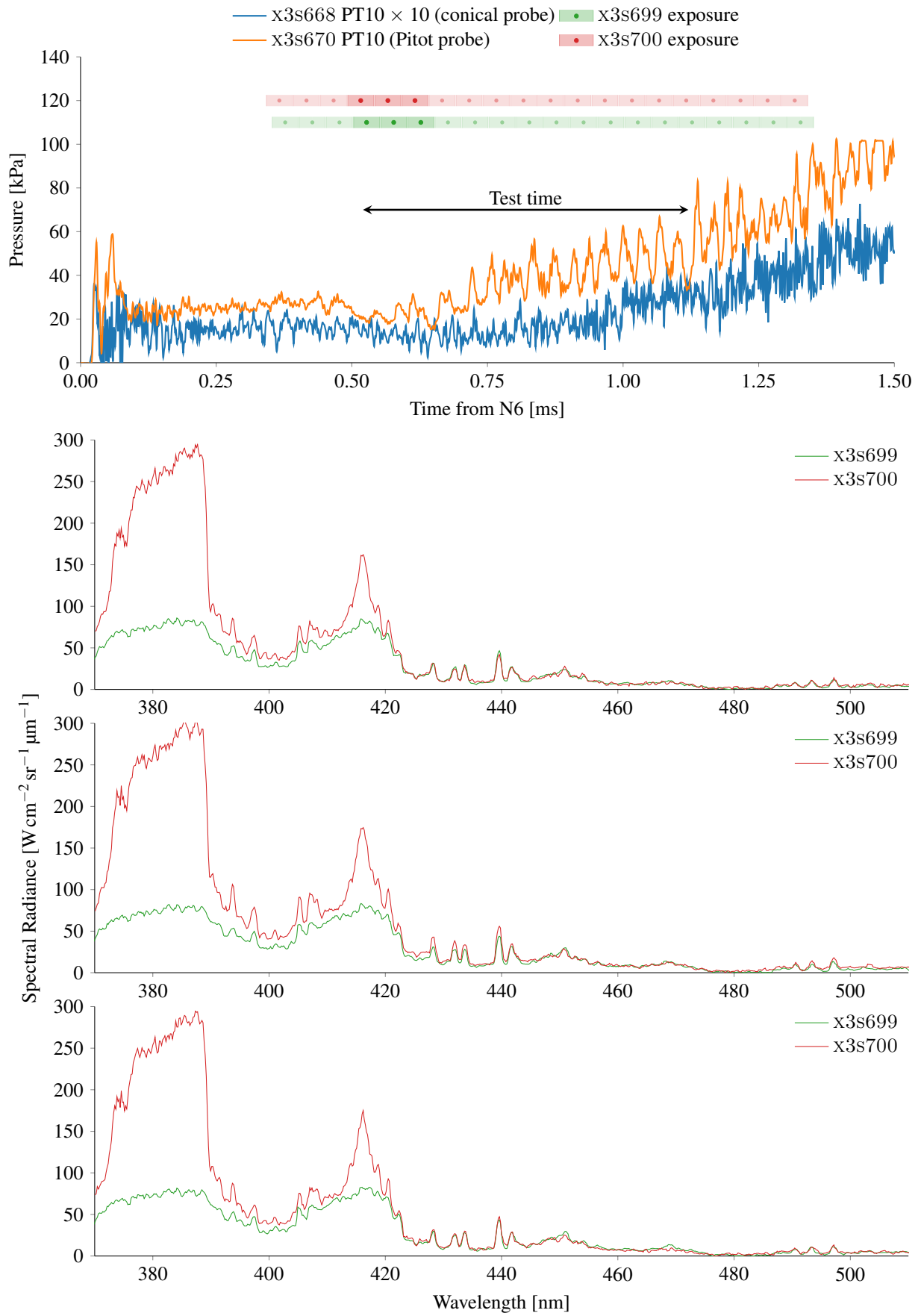


Figure D.3.: Comparison of shots x3s699 and x3s700 line *a* for a wavelength region of 380–500nm.

#### D. Spectral Line Comparisons

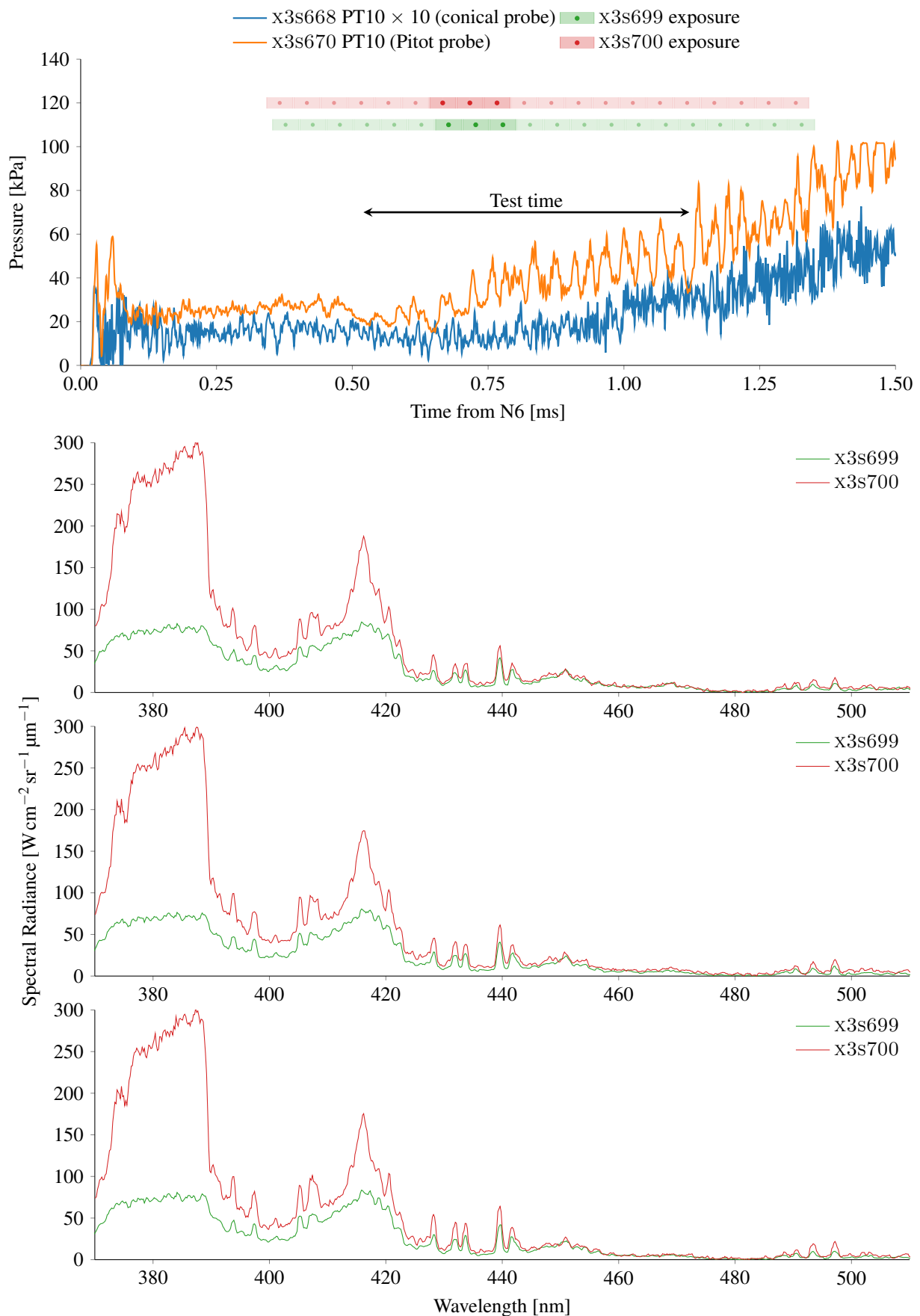


Figure D.3.: Comparison of shots x3s699 and x3s700 line *a* for a wavelength region of 380–500nm.

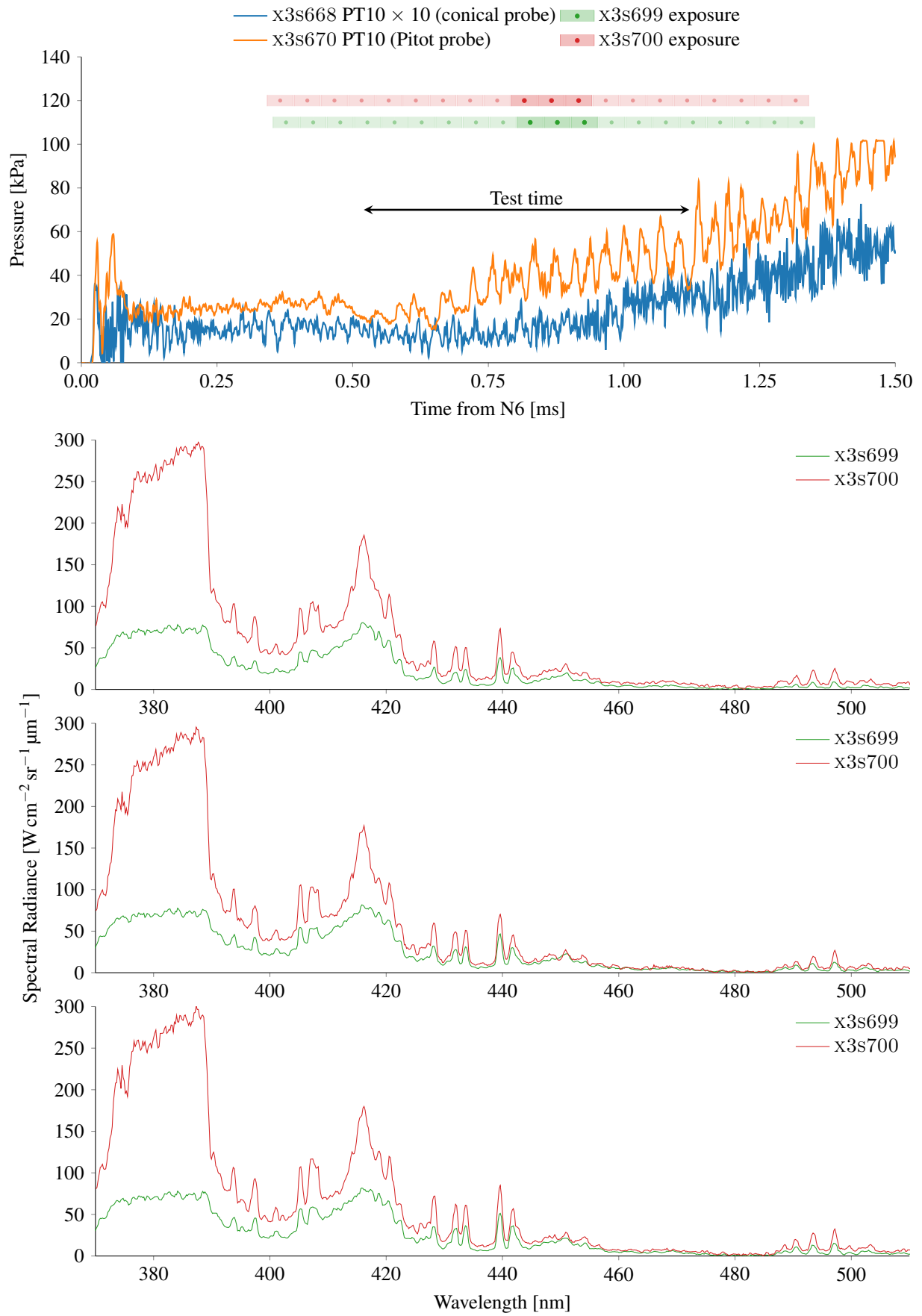


Figure D.3.: Comparison of shots x3s699 and x3s700 line *a* for a wavelength region of 380–500nm.

#### D. Spectral Line Comparisons

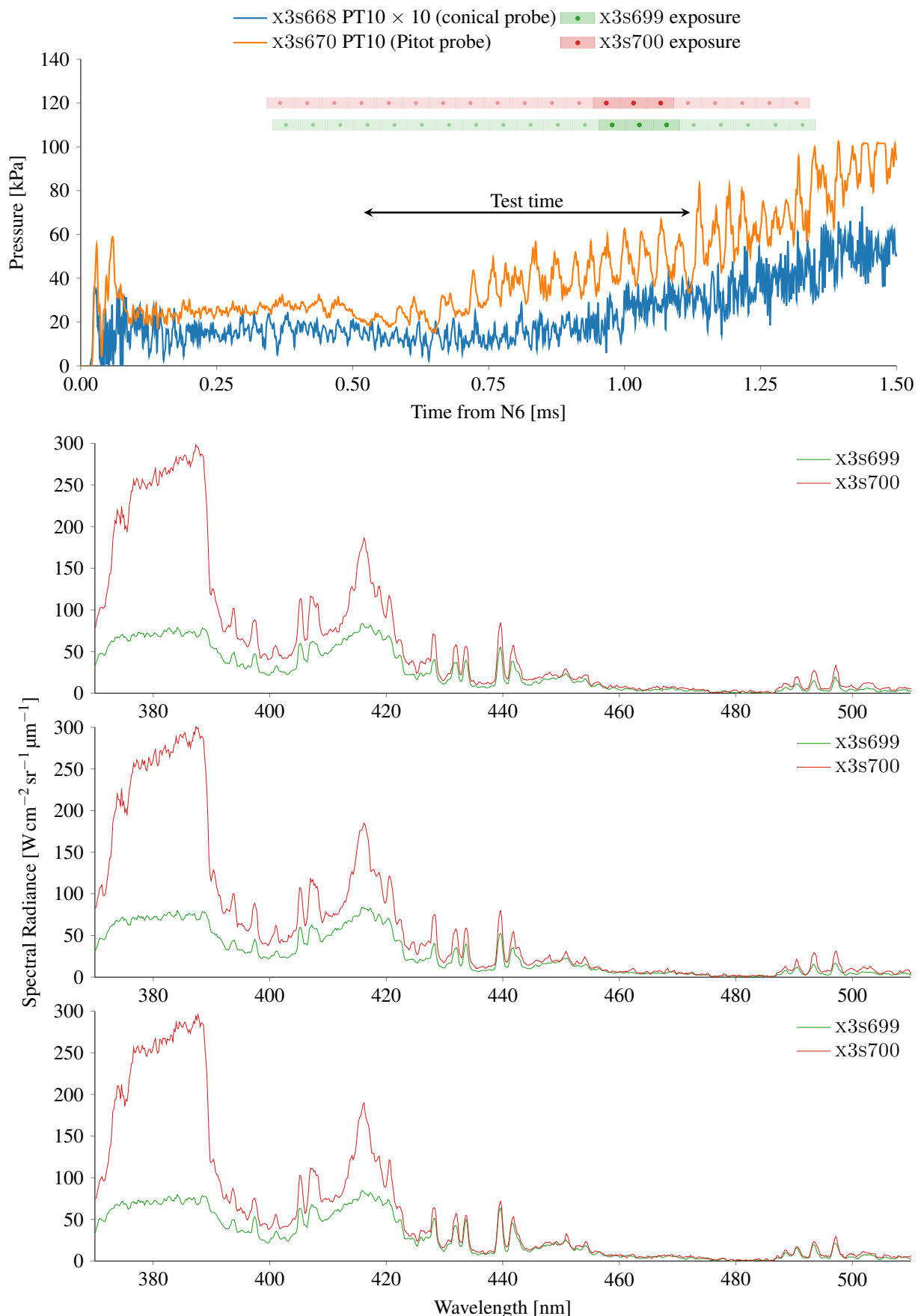


Figure D.3.: Comparison of shots x3s699 and x3s700 line *a* for a wavelength region of 380–500nm.

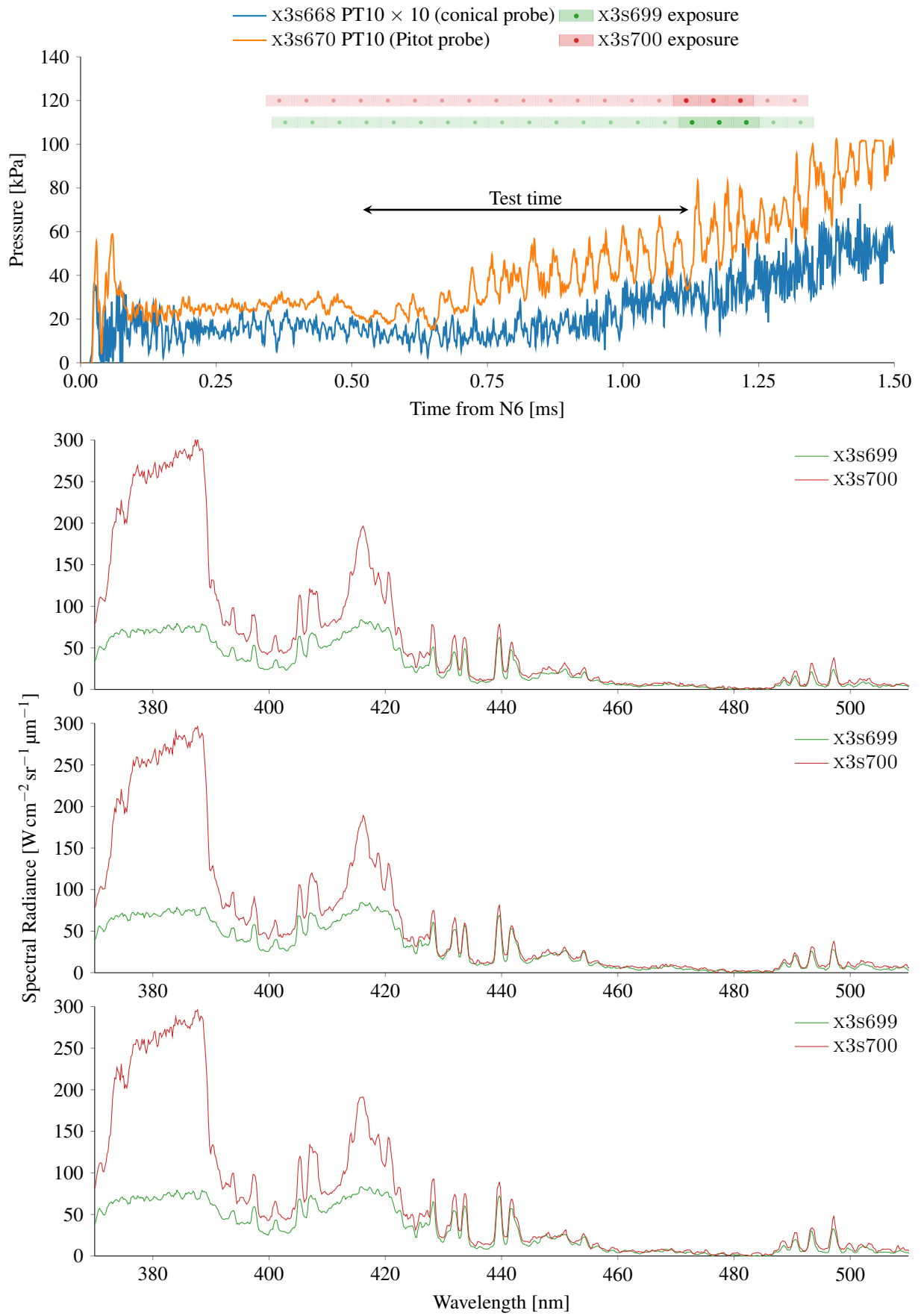


Figure D.3.: Comparison of shots x3s699 and x3s700 line *a* for a wavelength region of 380–500nm.

#### D. Spectral Line Comparisons

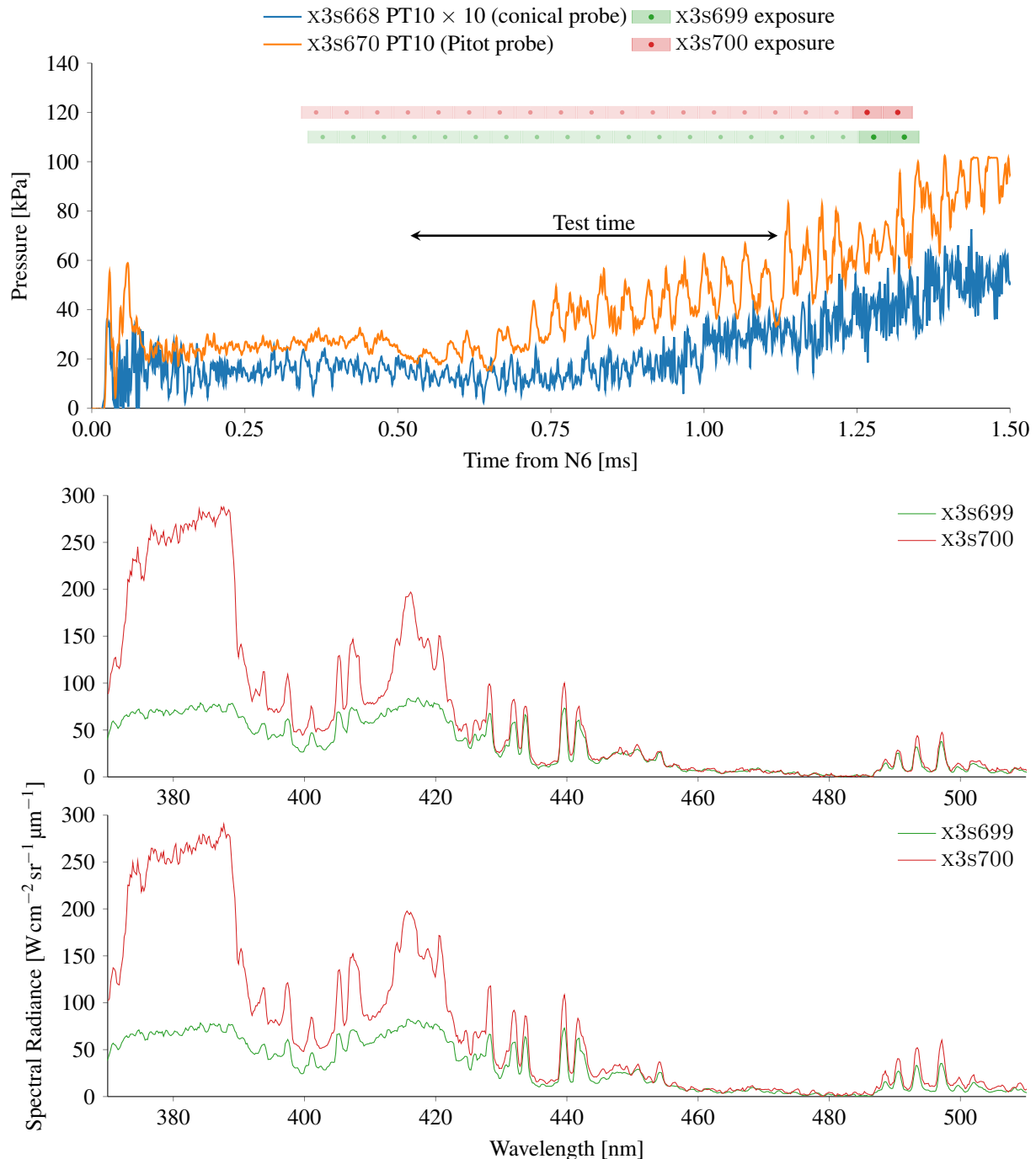


Figure D.3.: Comparison of shots x3s699 and x3s700 line *a* for a wavelength region of 380–500nm.

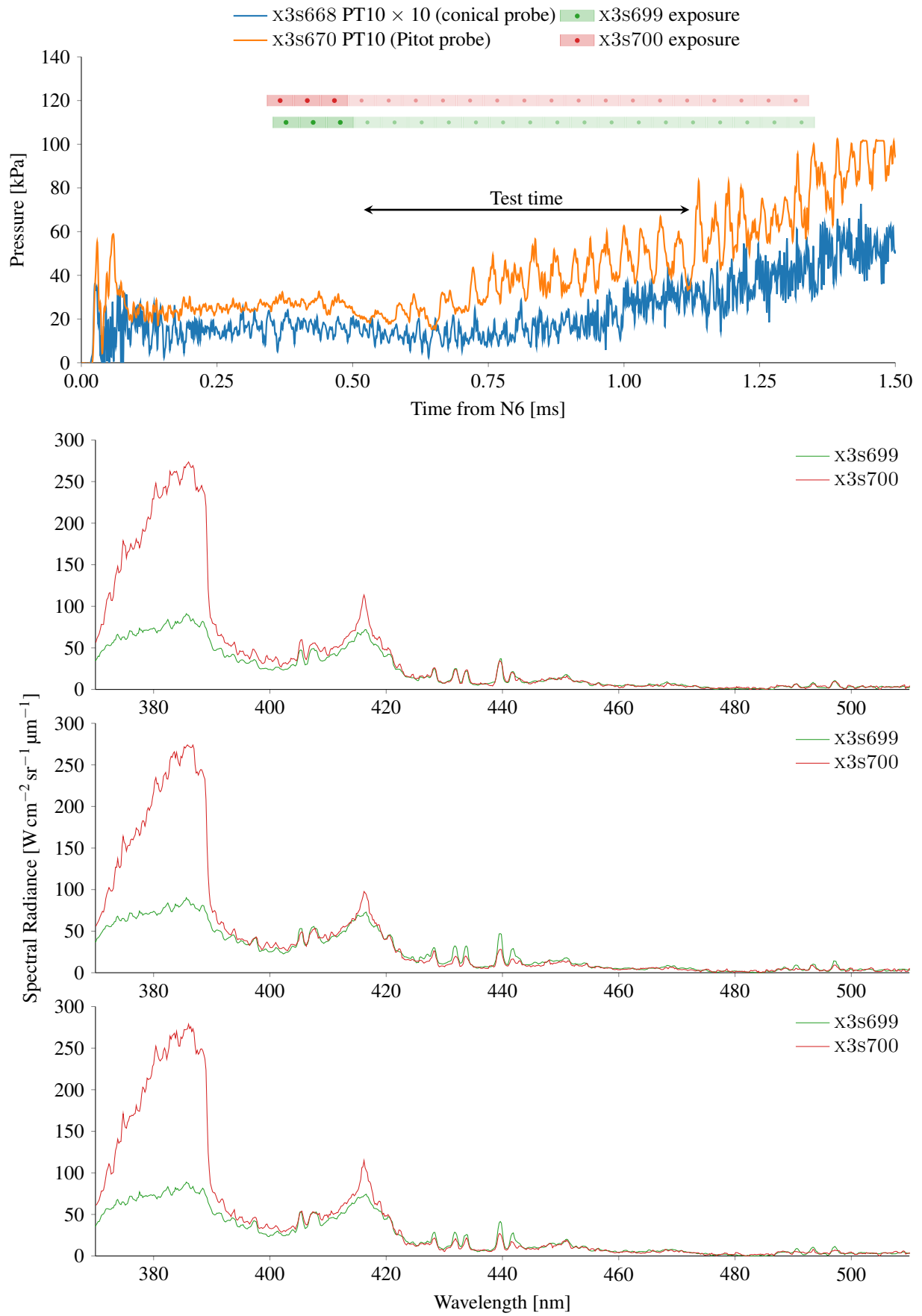


Figure D.4.: Comparison of shots x3s699 and x3s700 line *b* for a wavelength region of 380–500nm.

#### D. Spectral Line Comparisons

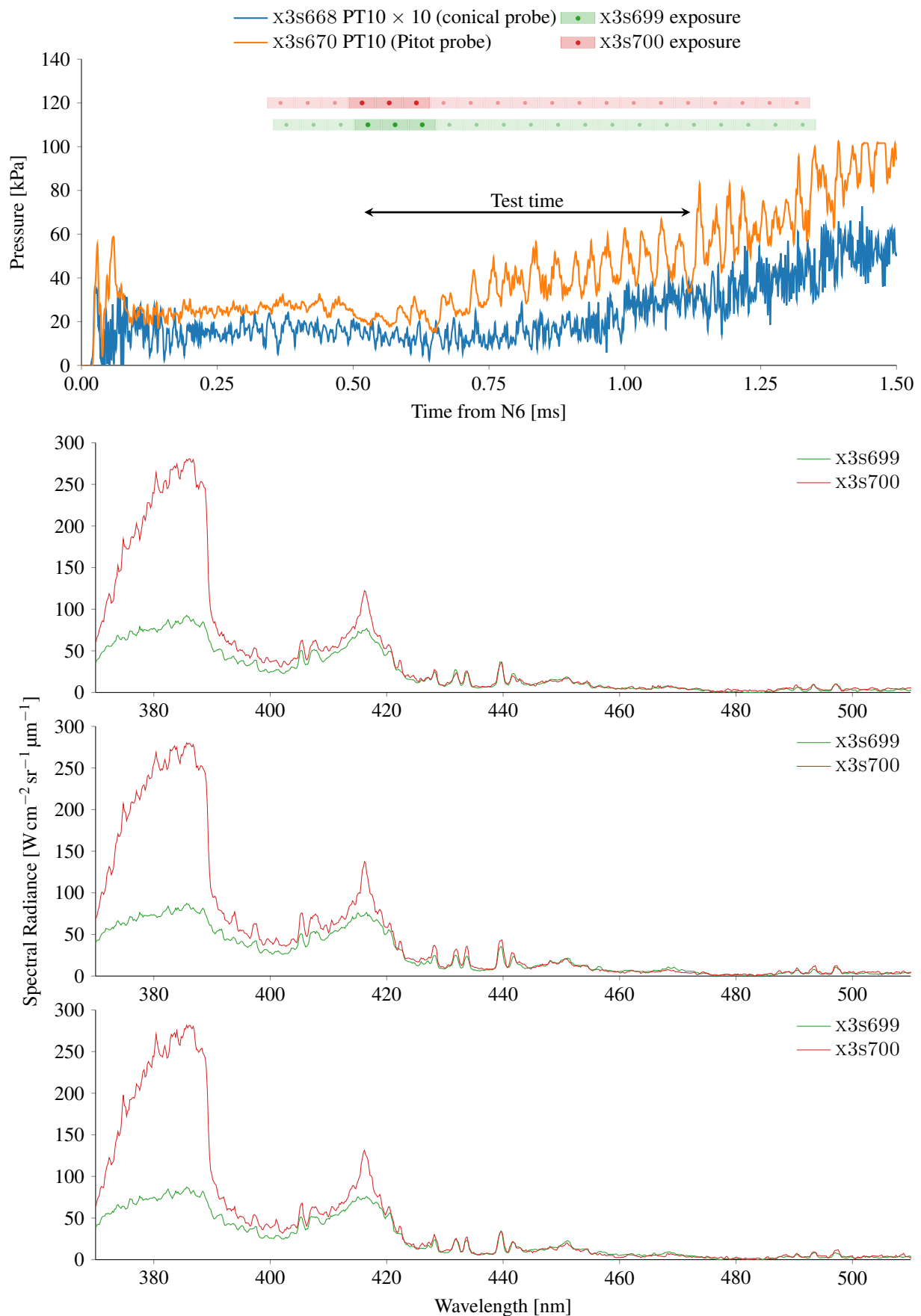


Figure D.4.: Comparison of shots x3s699 and x3s700 line *b* for a wavelength region of 380–500nm.

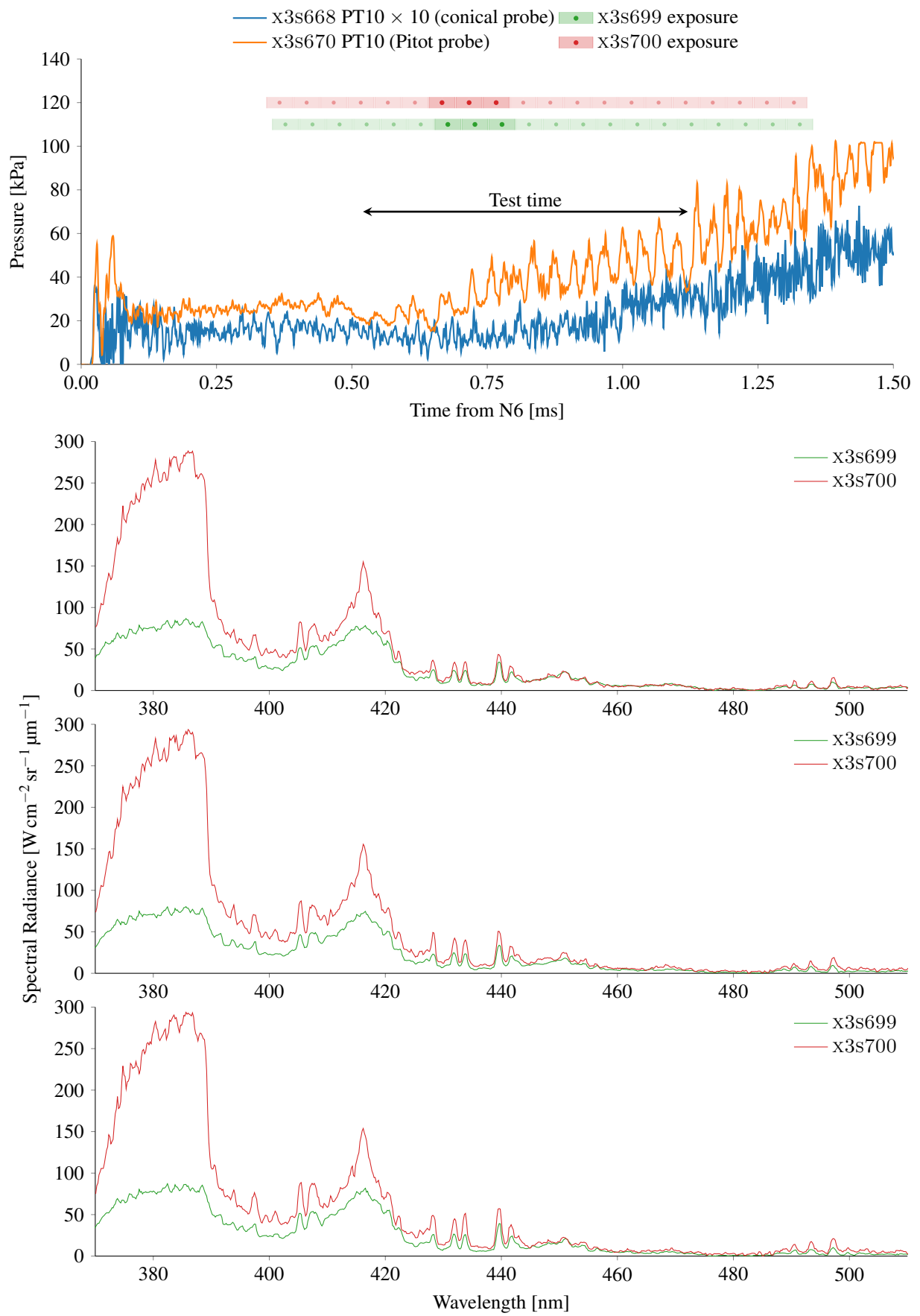


Figure D.4.: Comparison of shots x3s699 and x3s700 line *b* for a wavelength region of 380–500nm.

#### D. Spectral Line Comparisons

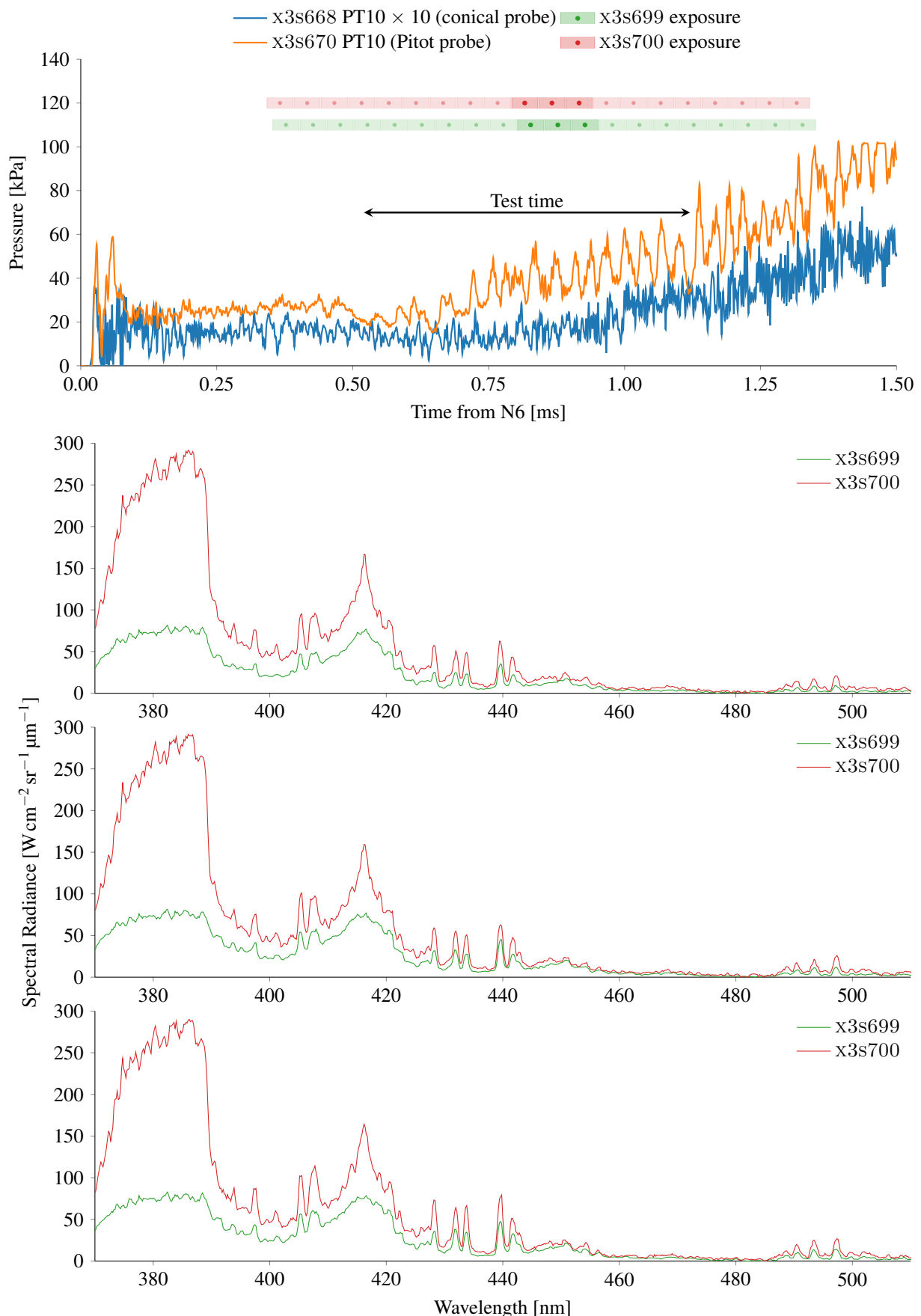


Figure D.4.: Comparison of shots x3s699 and x3s700 line *b* for a wavelength region of 380–500nm.

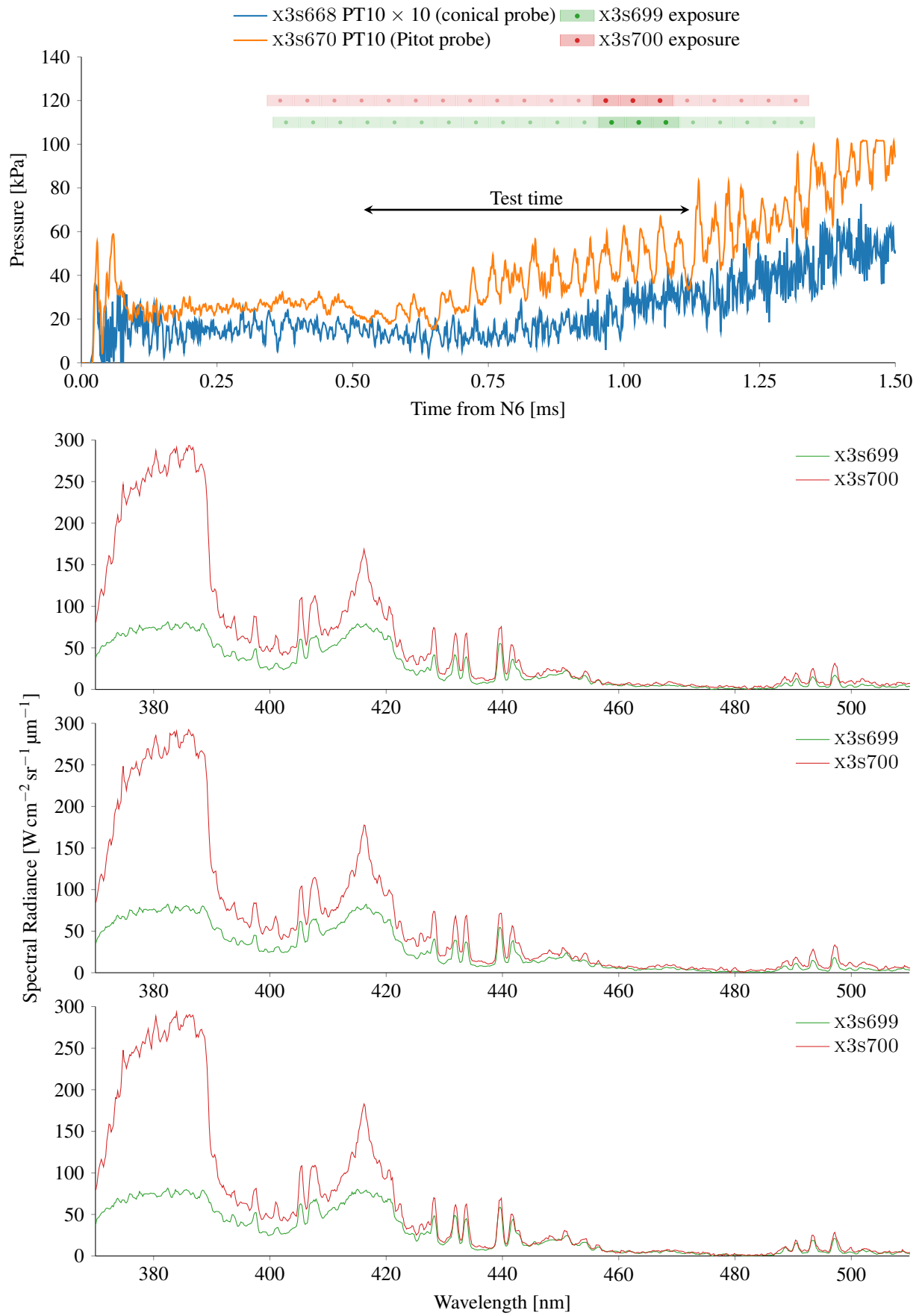


Figure D.4.: Comparison of shots x3s699 and x3s700 line *b* for a wavelength region of 380–500nm.

#### D. Spectral Line Comparisons

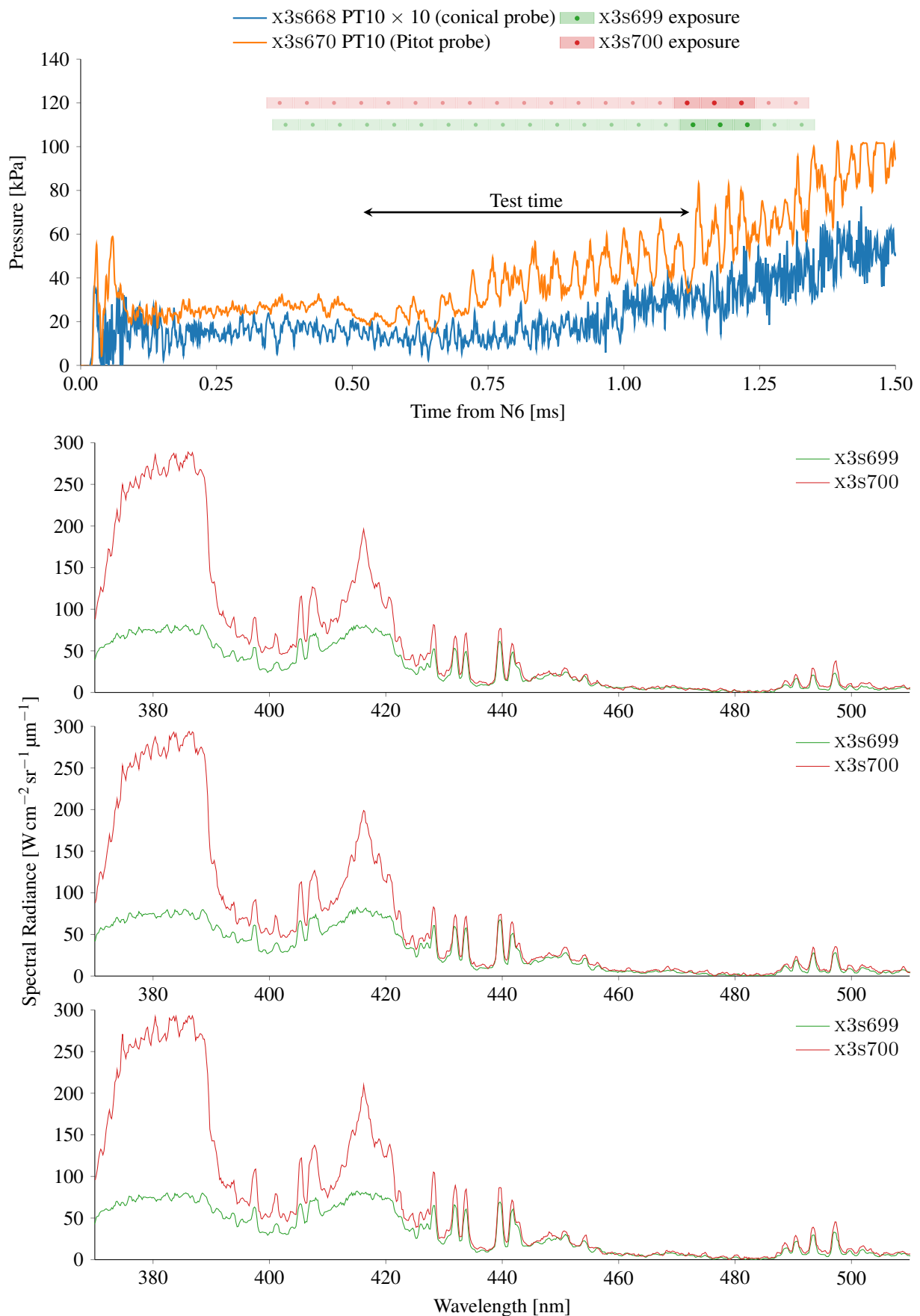


Figure D.4.: Comparison of shots x3s699 and x3s700 line *b* for a wavelength region of 380–500nm.

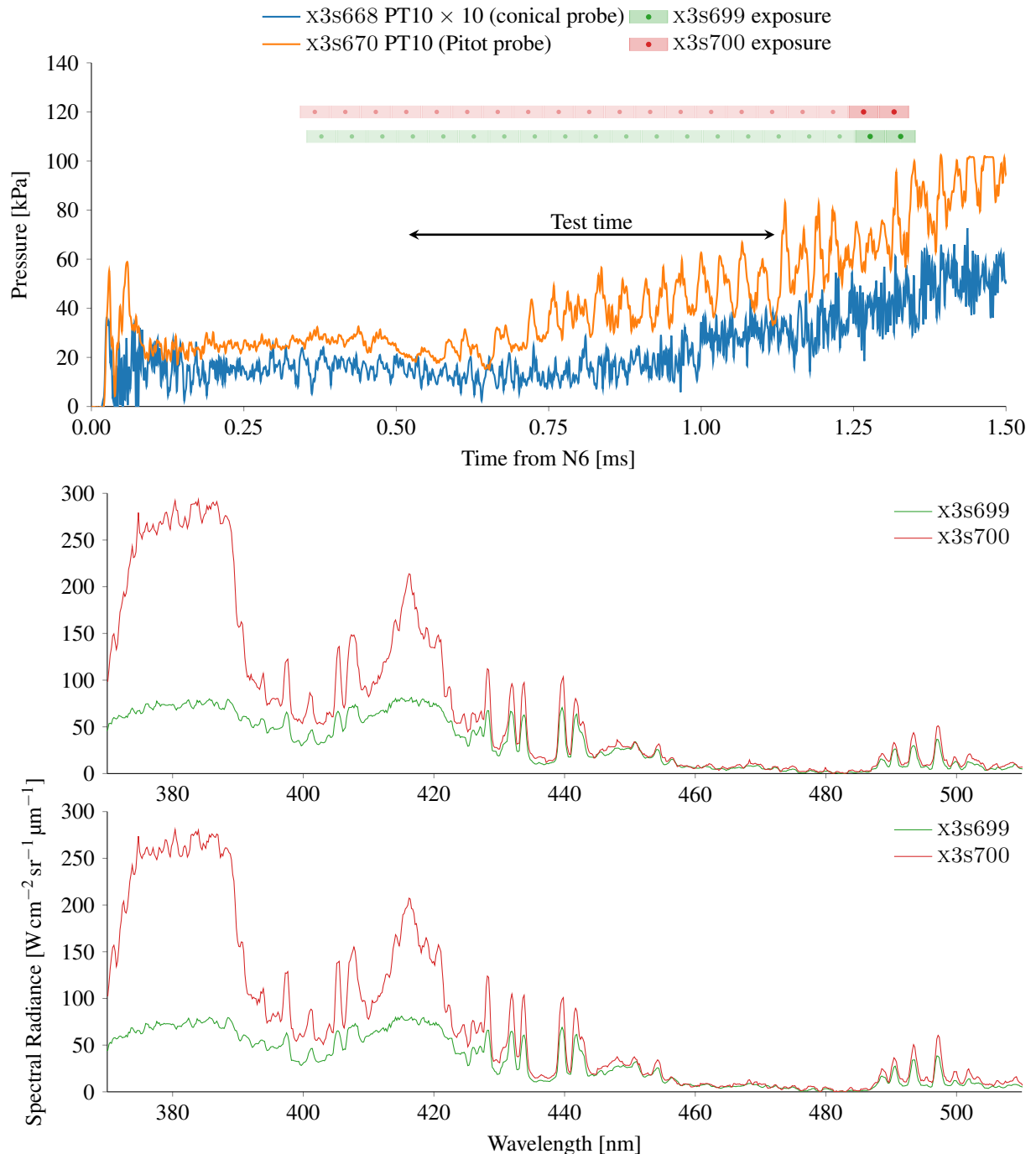


Figure D.4.: Comparison of shots x3s699 and x3s700 line *b* for a wavelength region of 380–500nm.

#### D. Spectral Line Comparisons

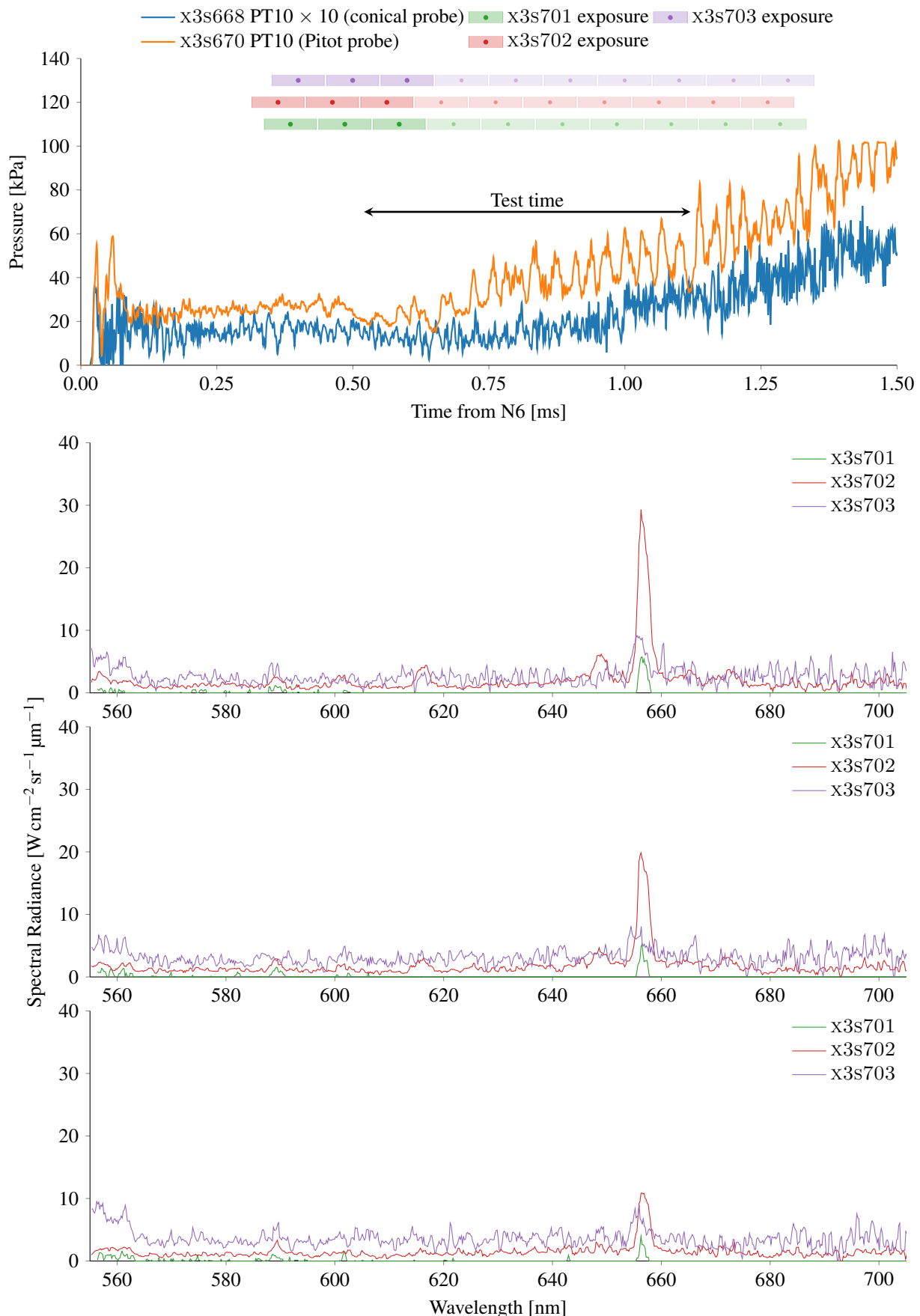


Figure D.5.: Comparison of shots x3s701, x3s702 and x3s703 line *a* for a wavelength region of 560–700nm.

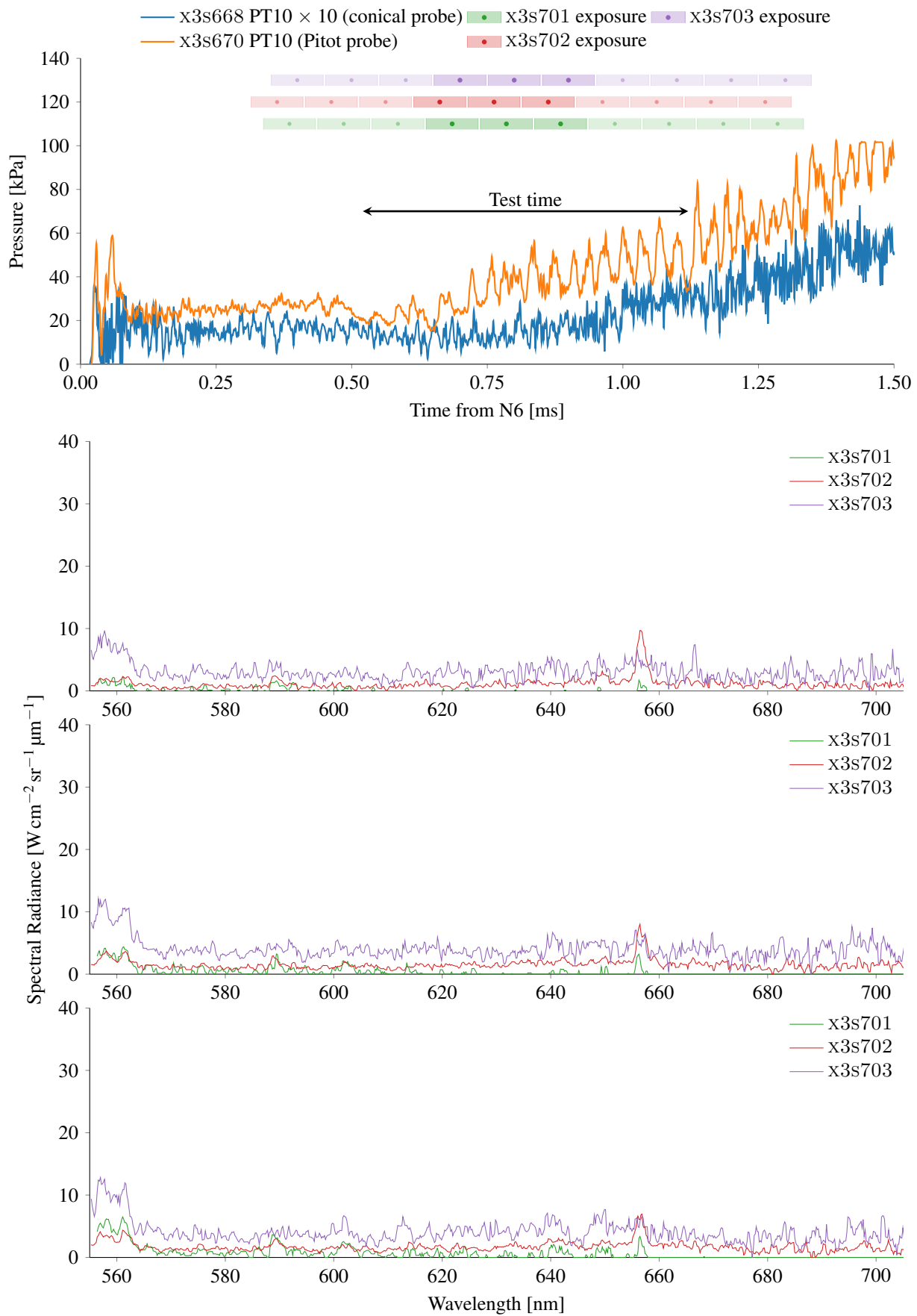


Figure D.5.: Comparison of shots x3s701, x3s702 and x3s703 line *a* for a wavelength region of 560–700nm.

#### D. Spectral Line Comparisons

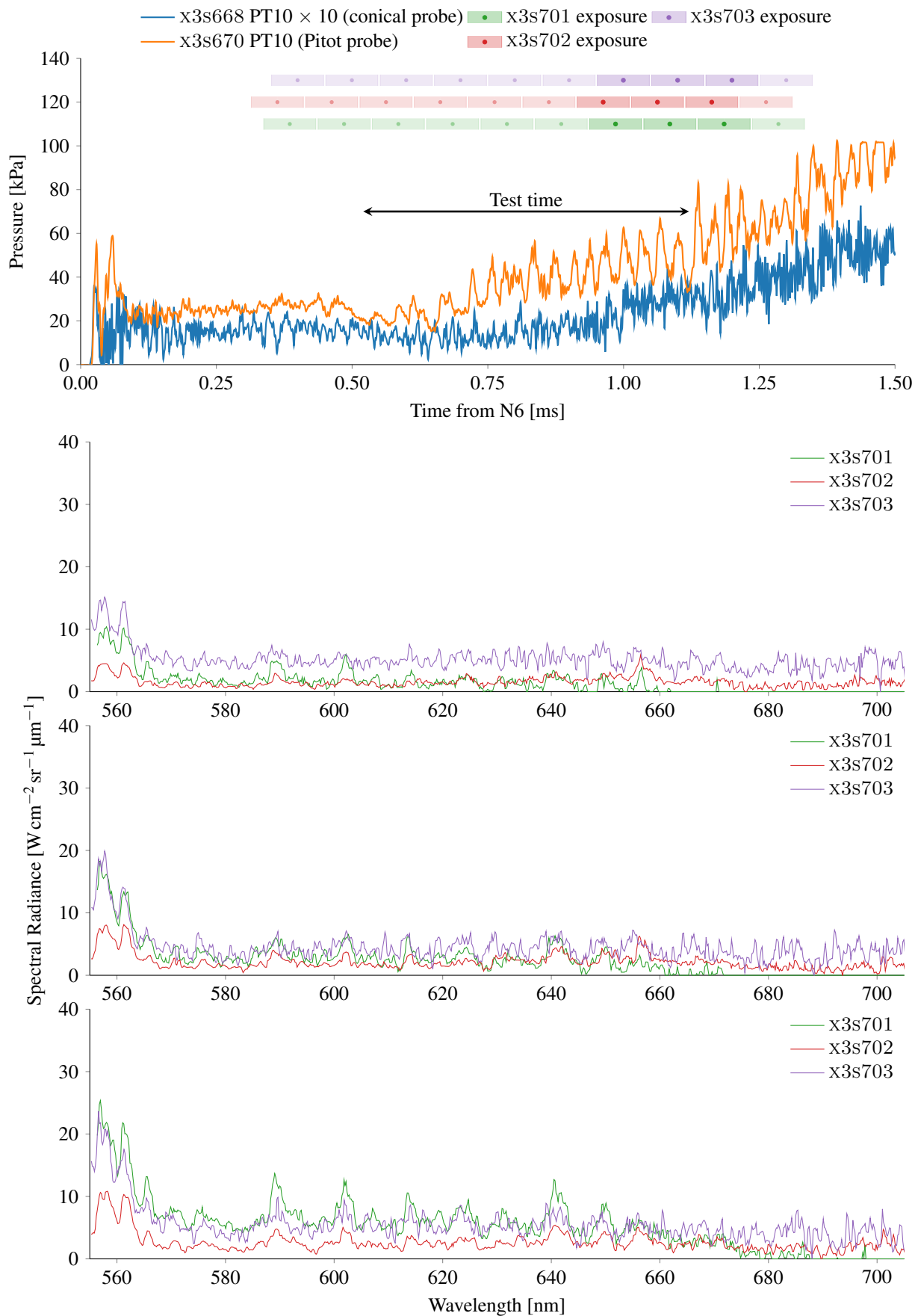


Figure D.5.: Comparison of shots x3s701, x3s702 and x3s703 line *a* for a wavelength region of 560–700nm.

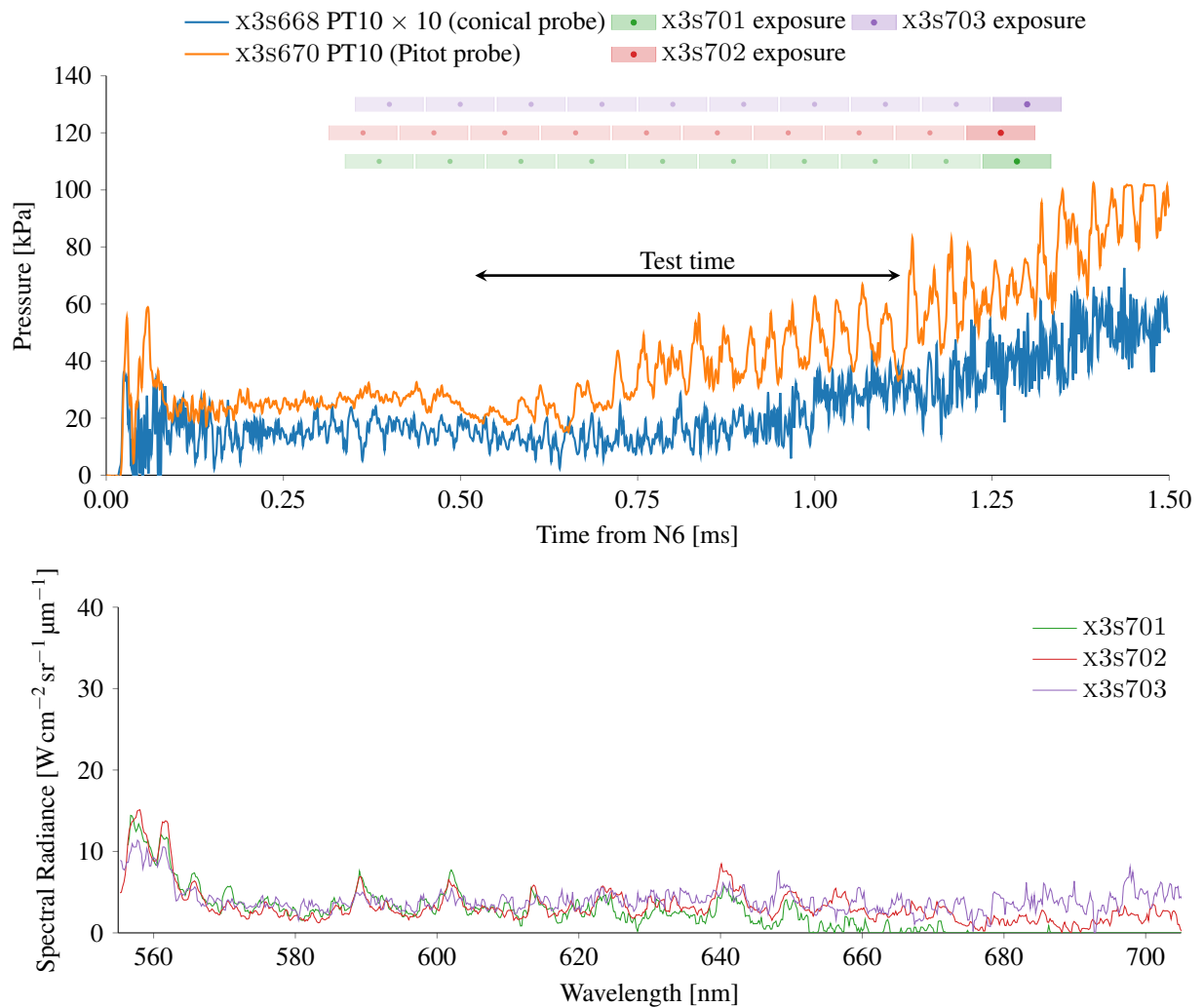


Figure D.5.: Comparison of shots x3s701, x3s702 and x3s703 line *a* for a wavelength region of 560–700nm.

#### D. Spectral Line Comparisons

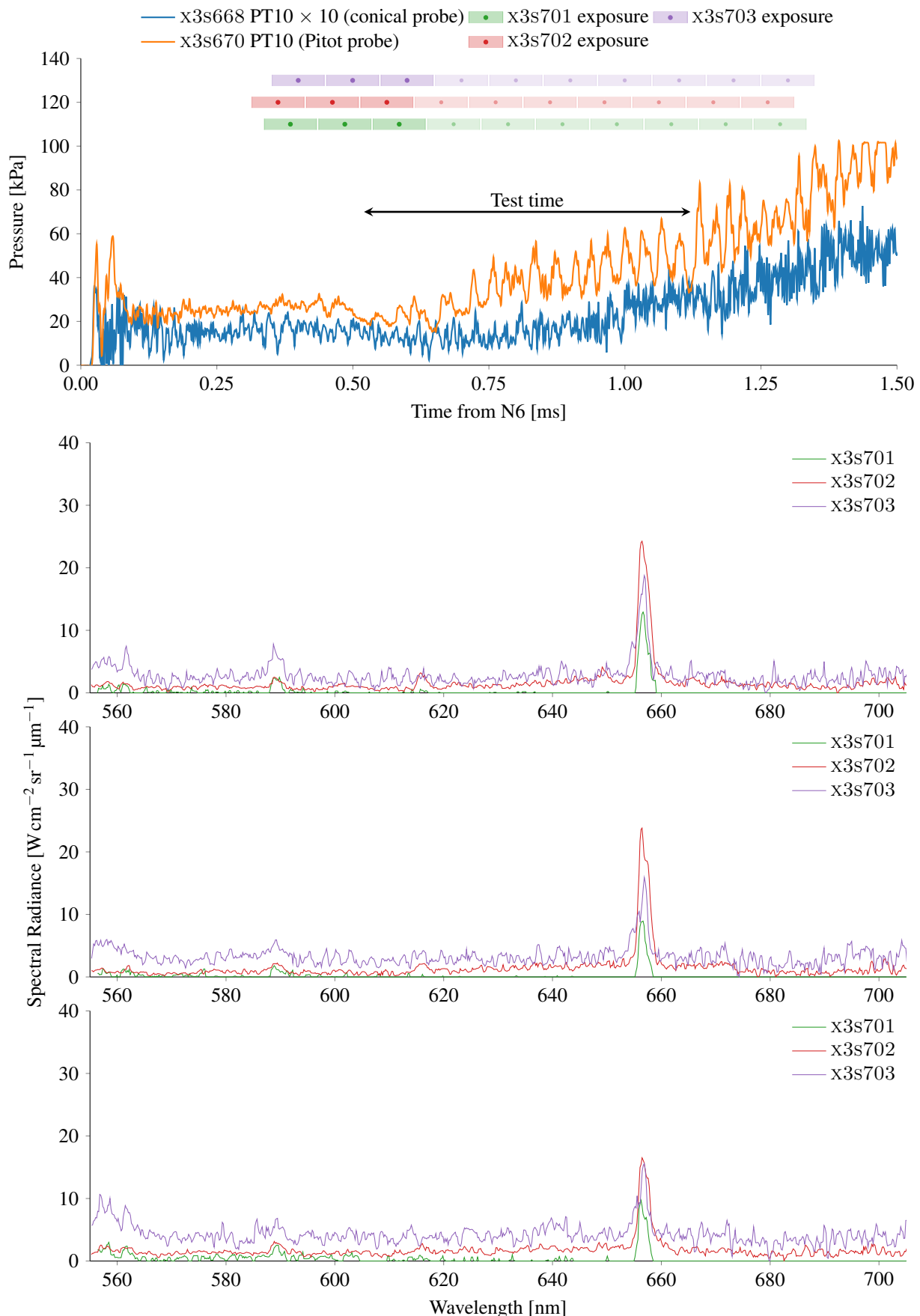


Figure D.6.: Comparison of shots x3s701, x3s702 and x3s703 line *b* for a wavelength region of 560–700nm.

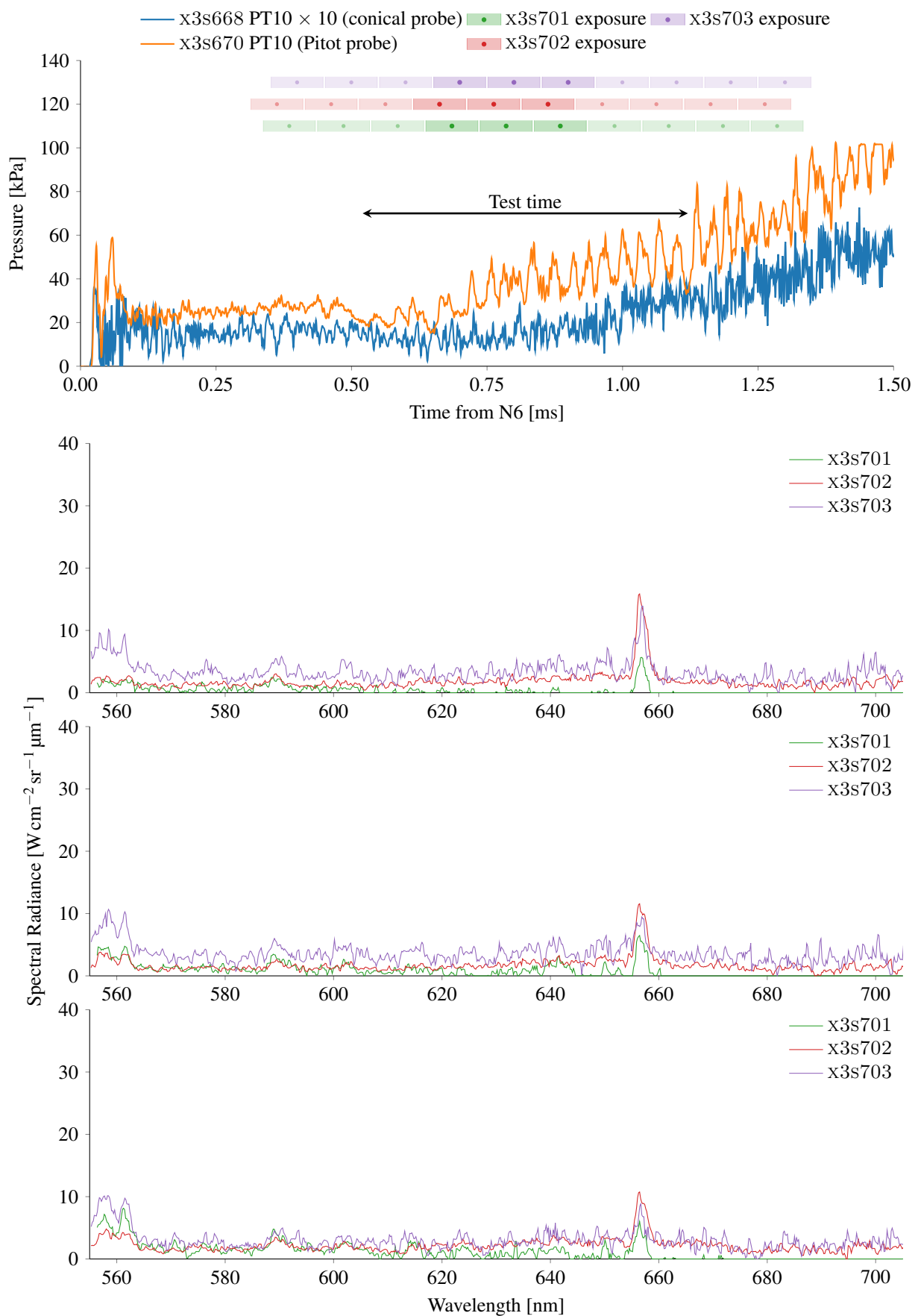


Figure D.6.: Comparison of shots x3s701, x3s702 and x3s703 line *b* for a wavelength region of 560–700nm.

#### D. Spectral Line Comparisons

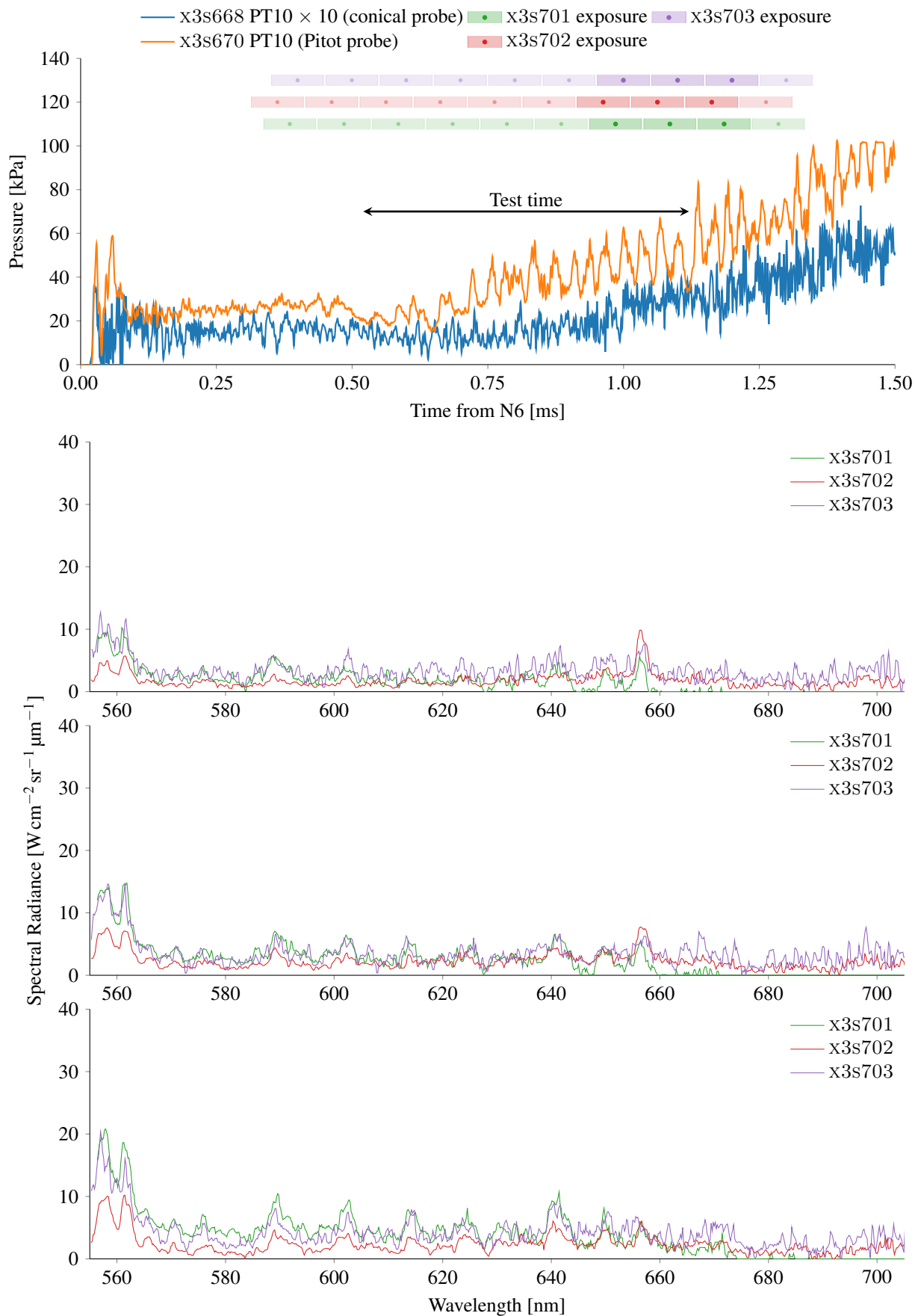


Figure D.6.: Comparison of shots x3s701, x3s702 and x3s703 line *b* for a wavelength region of 560–700nm.

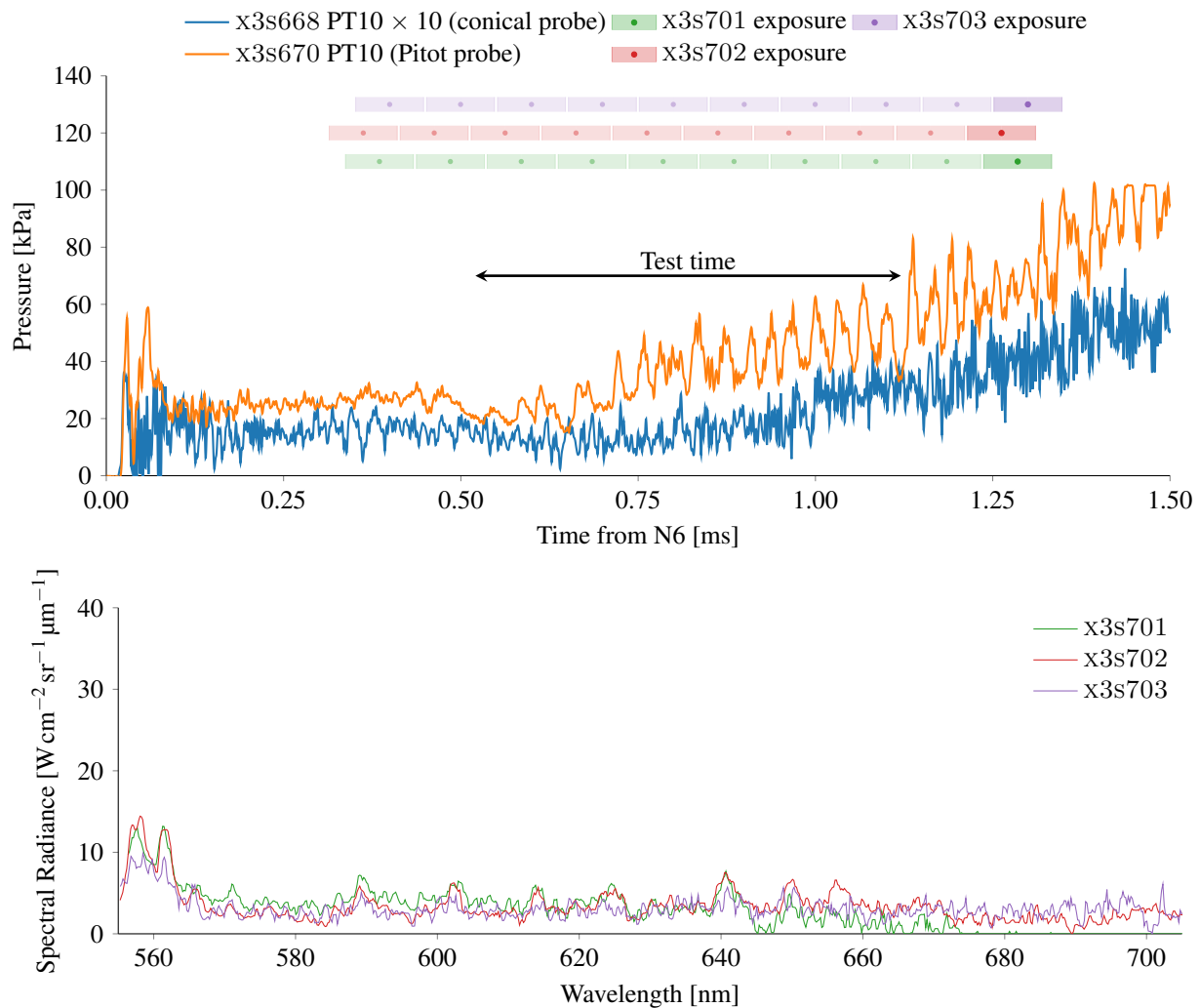


Figure D.6.: Comparison of shots x3s701, x3s702 and x3s703 line *b* for a wavelength region of 560–700nm.

#### D. Spectral Line Comparisons

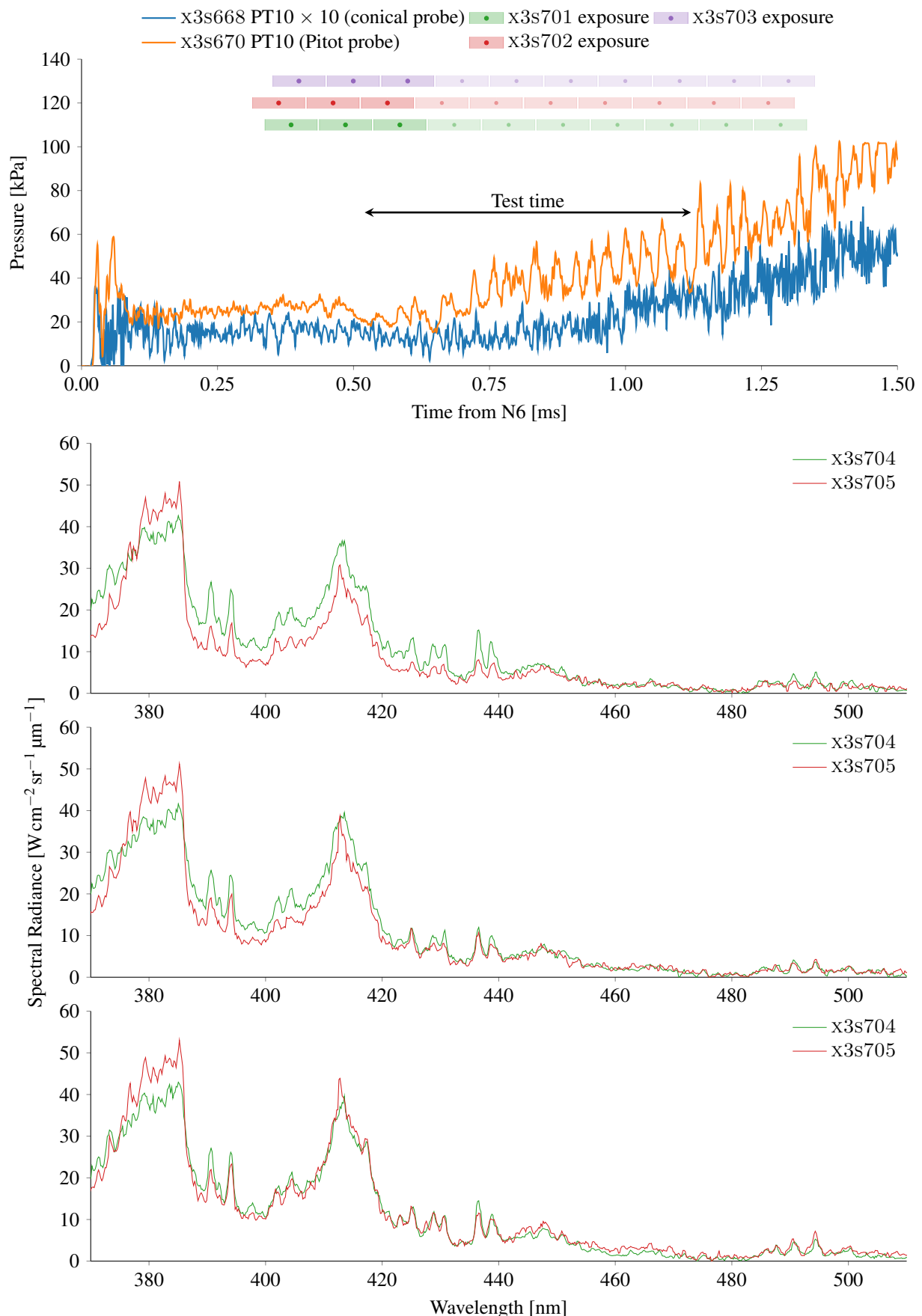


Figure D.7.: Comparison of shots x3s704 and x3s705 line *a* for a wavelength region of 380–500nm.

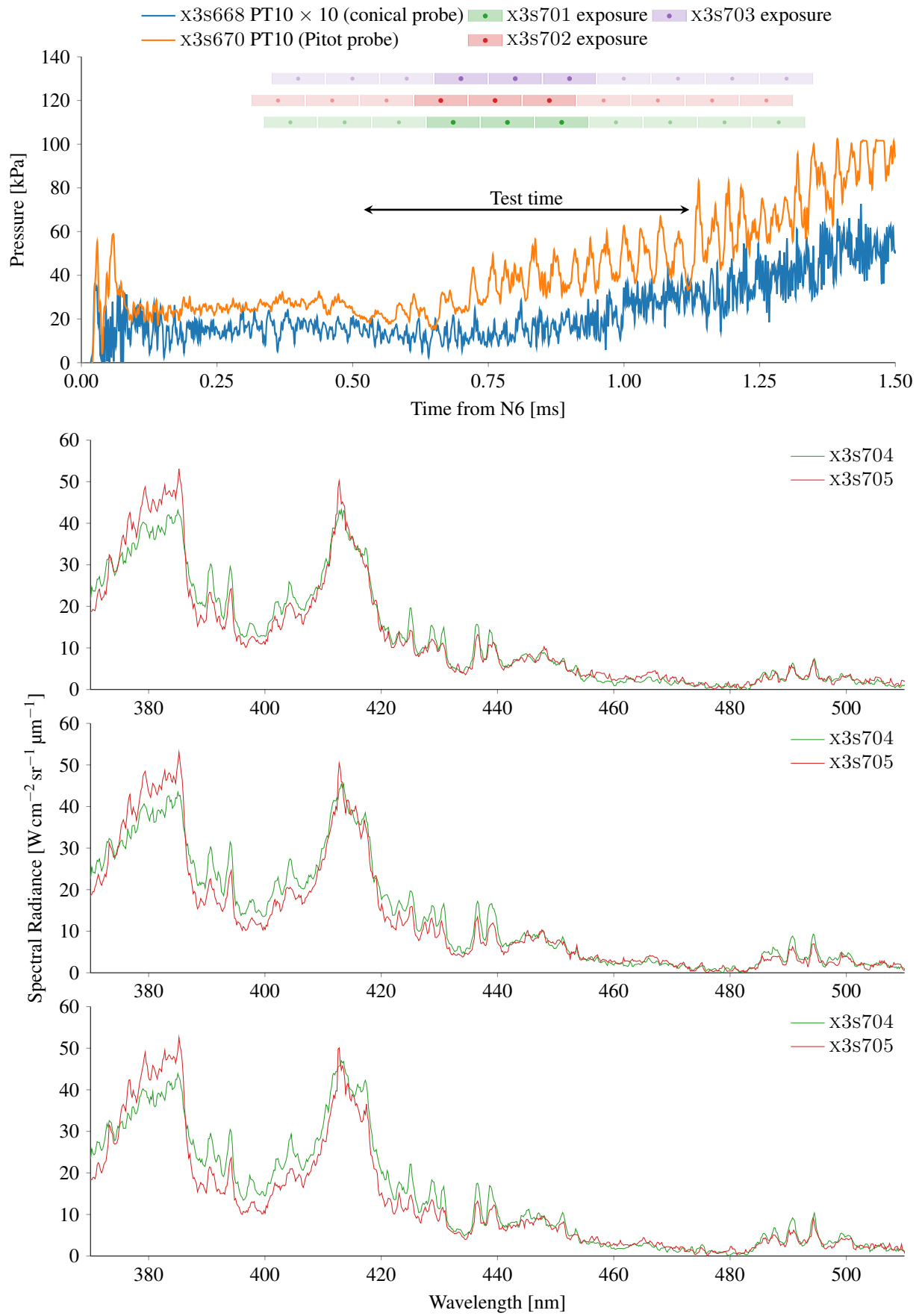


Figure D.7.: Comparison of shots x3s704 and x3s705 line *a* for a wavelength region of 380–500nm.

#### D. Spectral Line Comparisons

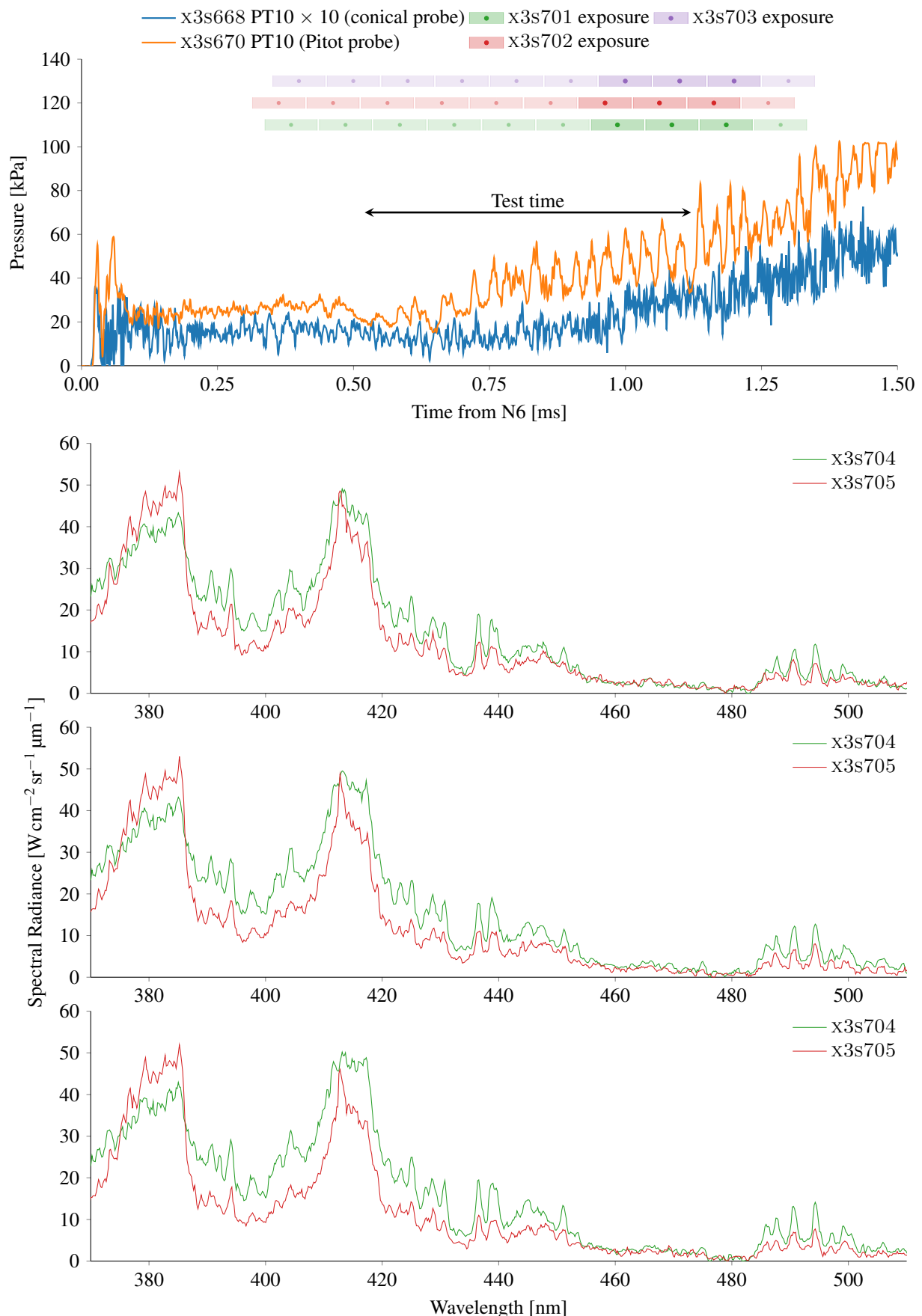


Figure D.7.: Comparison of shots x3s704 and x3s705 line *a* for a wavelength region of 380–500nm.

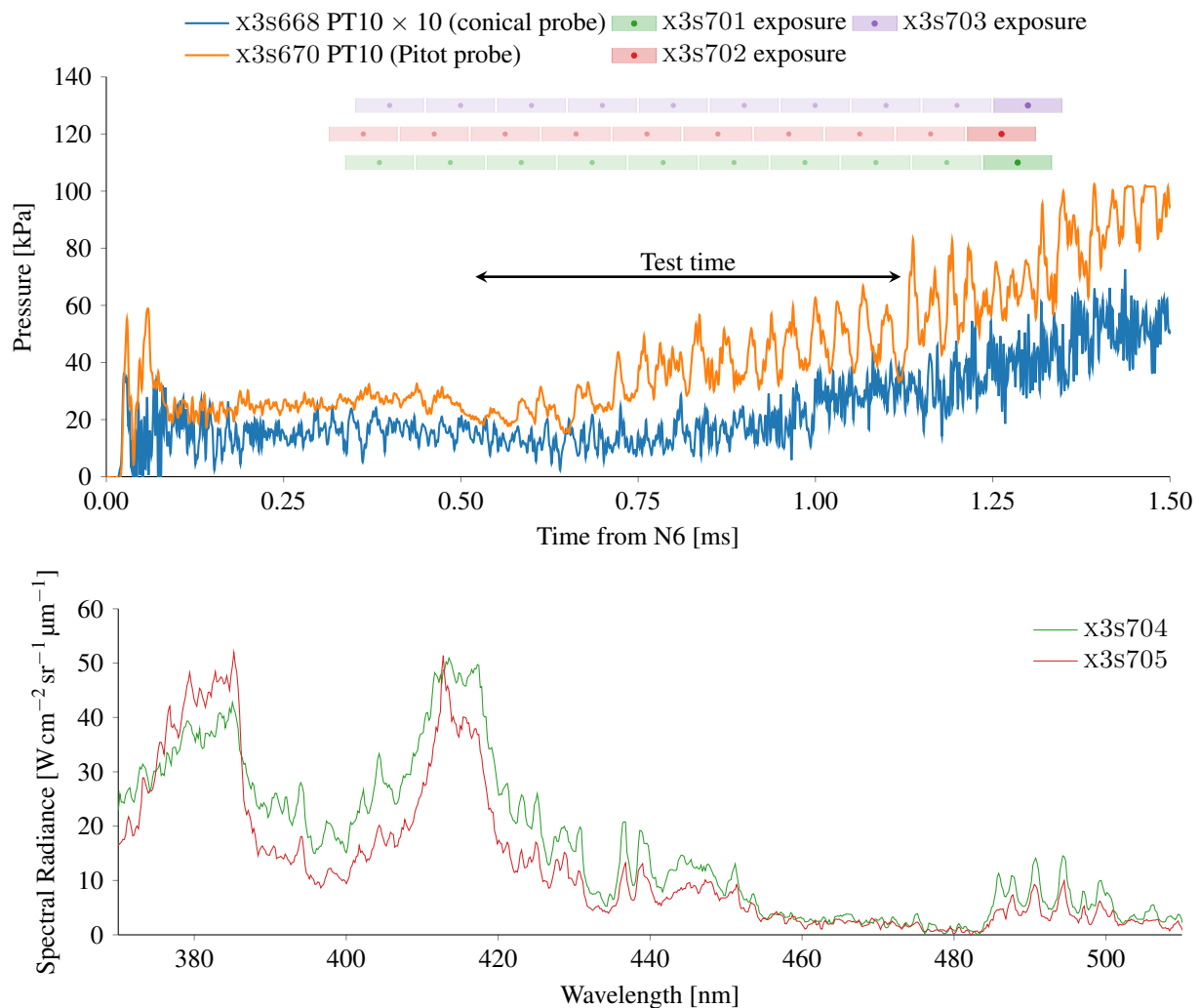


Figure D.7.: Comparison of shots x3s704 and x3s705 line *a* for a wavelength region of 380–500nm.

#### D. Spectral Line Comparisons

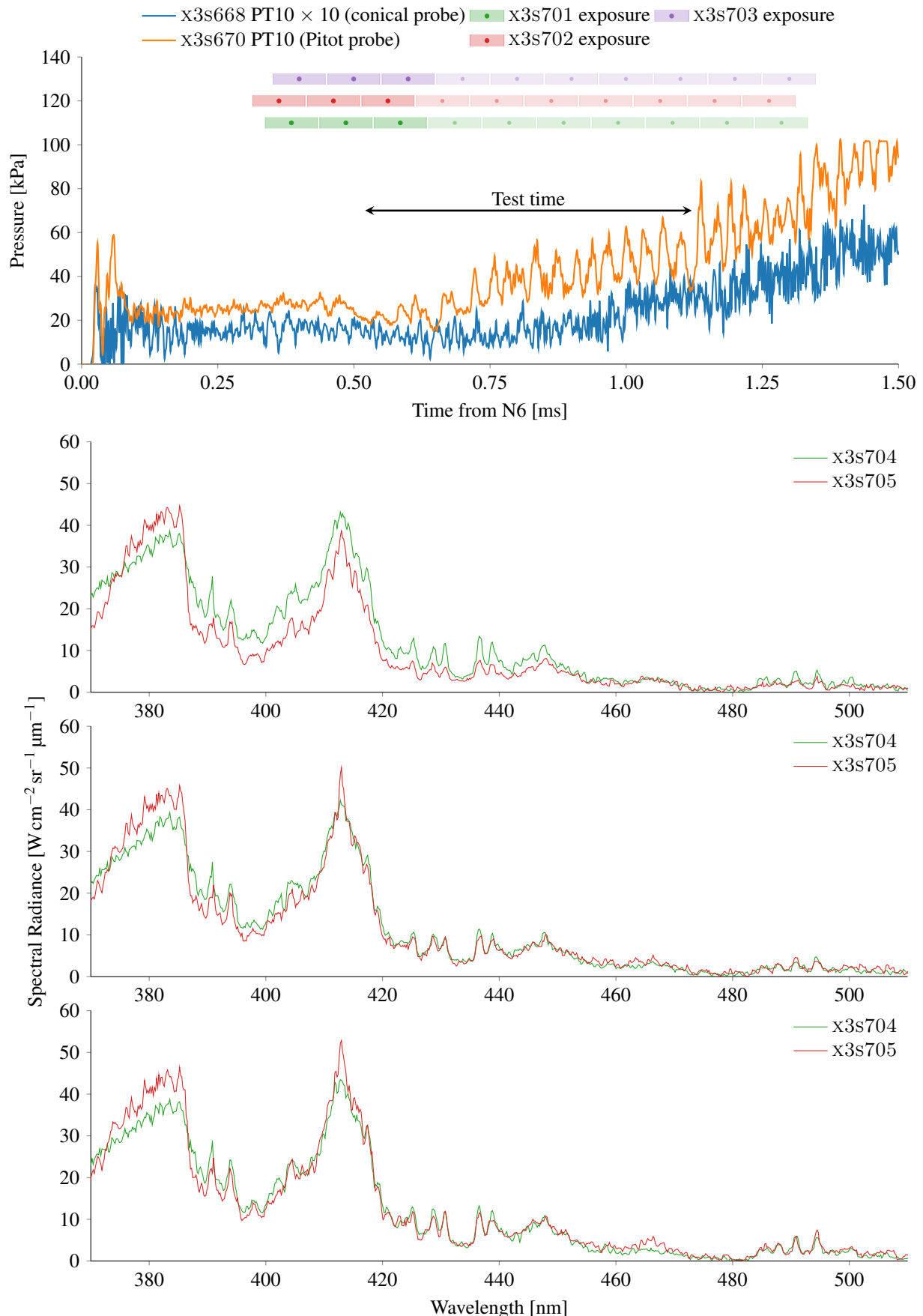


Figure D.8.: Comparison of shots x3s704 and x3s705 line *b* for a wavelength region of 380–500nm.

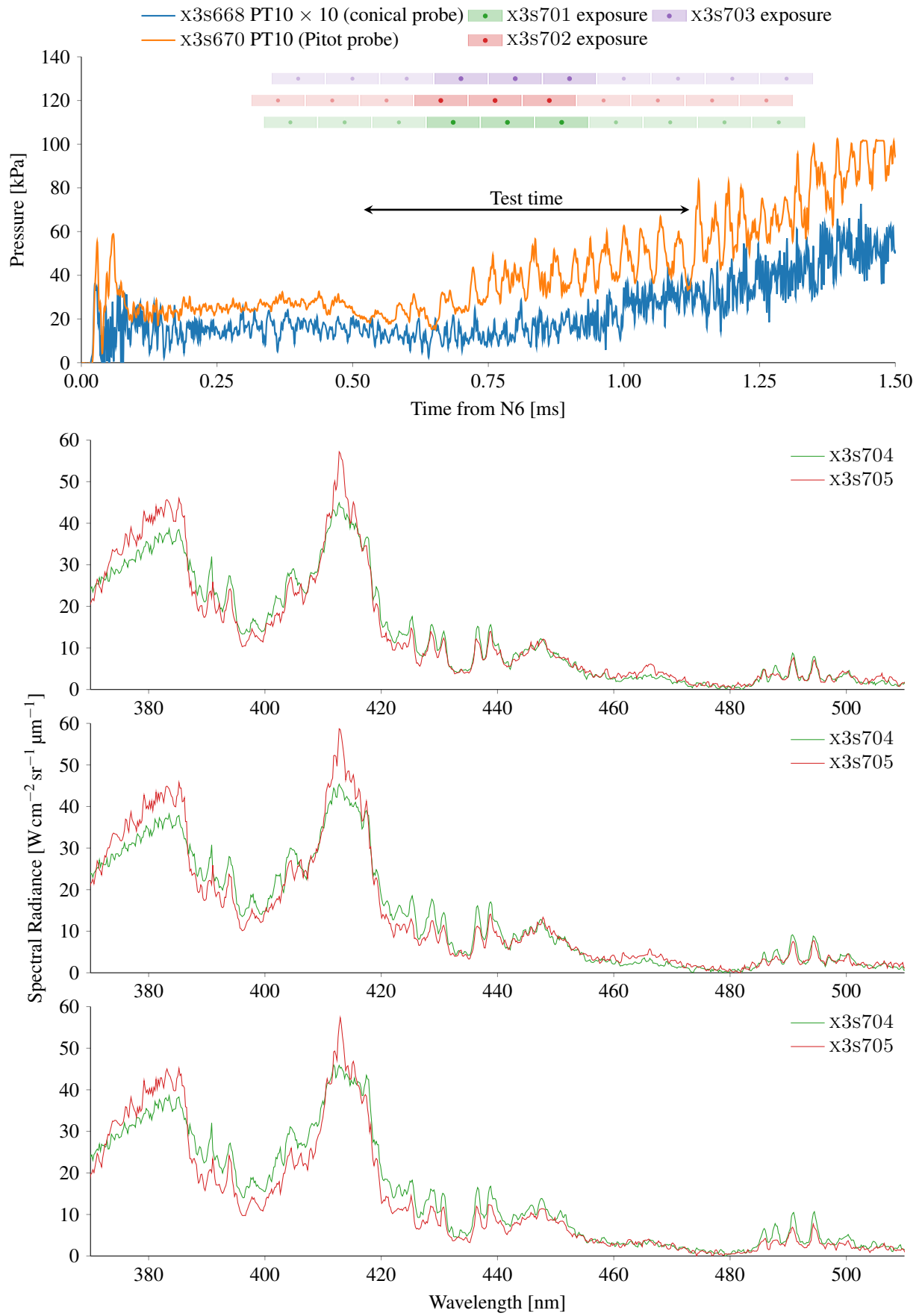


Figure D.8.: Comparison of shots x3s704 and x3s705 line *b* for a wavelength region of 380–500nm.

#### D. Spectral Line Comparisons

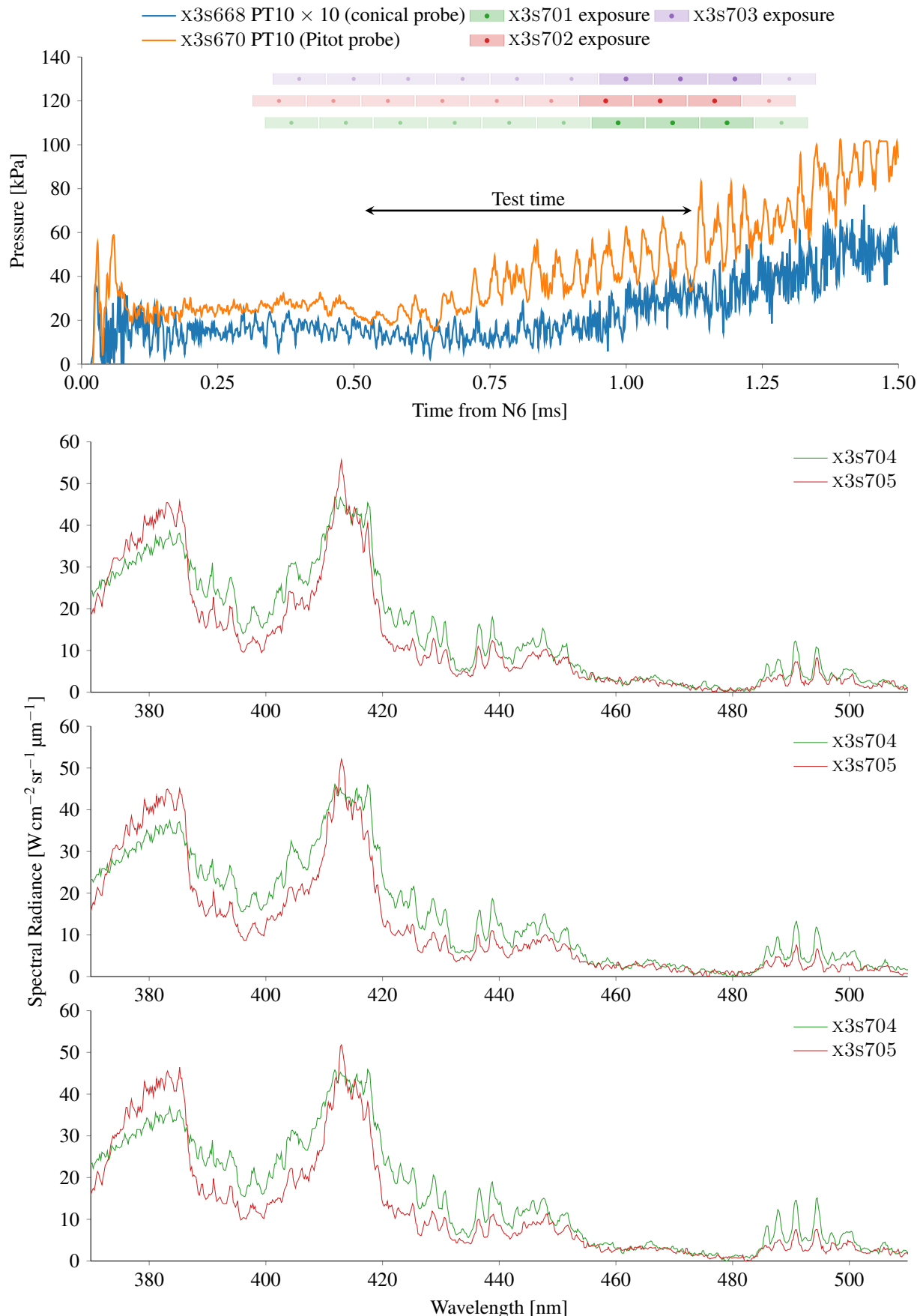


Figure D.8.: Comparison of shots x3s704 and x3s705 line *b* for a wavelength region of 380–500nm.

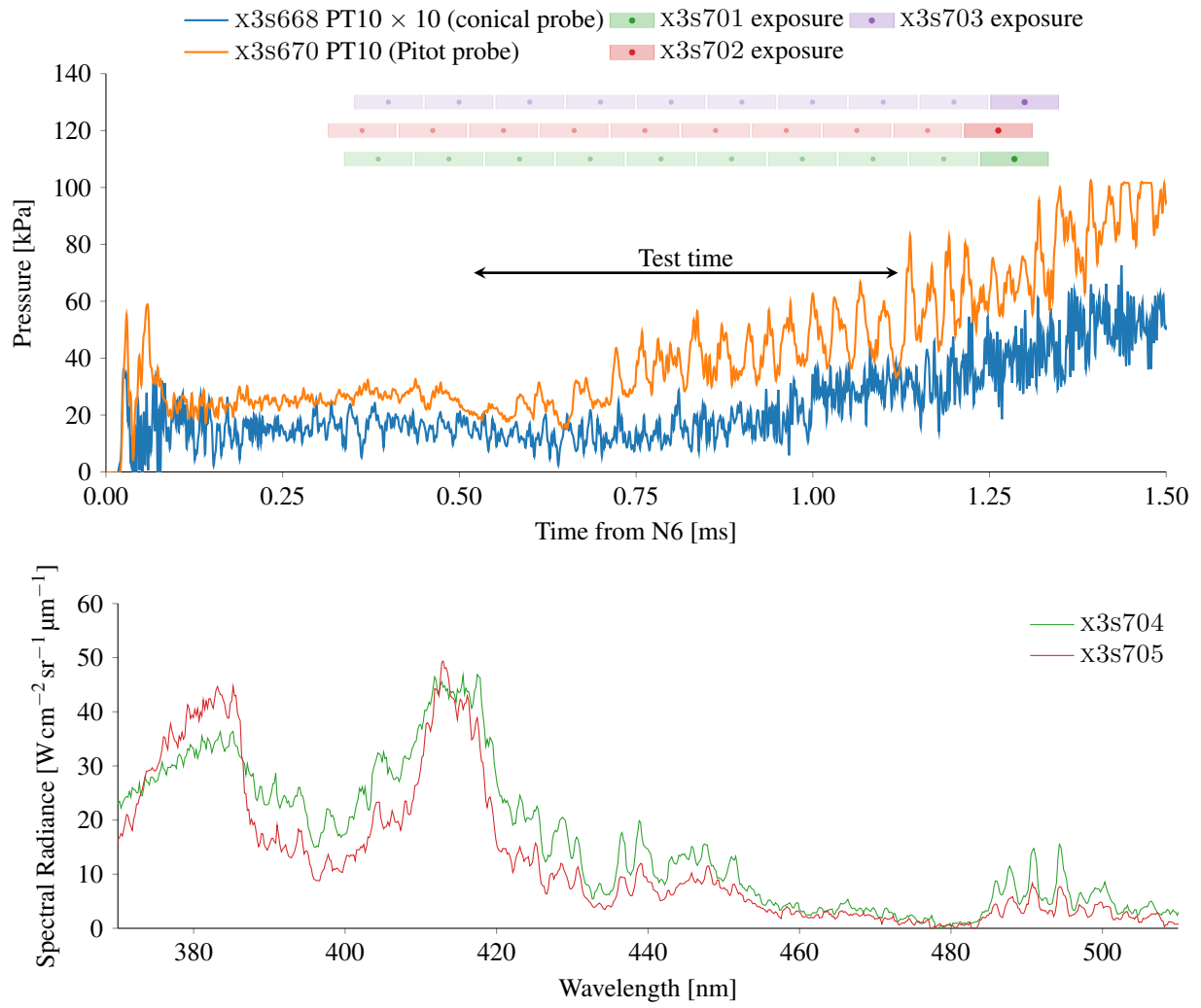


Figure D.8.: Comparison of shots x3s704 and x3s705 line *b* for a wavelength region of 380–500nm.